Kinetic Modelling of Plasma Thruster Plumes

by

Matteo Guaita

A dissertation submitted in partial fulfilment of the requirements for the degree of Doctor of Philosophy in

Aerospace Engineering

Universidad Carlos III de Madrid

Advisors:

Eduardo Ahedo
Mario Merino Martínez

Tutor:

Eduardo Ahedo

April 2026

A mamma e papá,
a Tommaso e a Giacomo.

Acknowledgements

A wise man once said that a thesis is just a very time-consuming excuse to write the acknowledgements, and he was right: the crumbs of scientific progress and technical knowledge that may be hidden in this document are just a few fruits of a deep-rooted tree of human connections. First I must thank my advisors, Eduardo and Mario, who have sown unwavering trust in my capabilities and attentive freedom of ideas and interests throughout my PhD, and have harvested by the end of it a recklessly confident researcher. Thank your for the always educational and constructive criticism and for your guidance through the bizarre world of research and academia. I would also like to thank Kristof Holste, Peter Klar and Konstantin Keil, along with the whole research group at JLU, who warmly welcomed me in Gießen and made me feel at home during the three months of my research stay.

This thesis, and the experiences that it symbolises, would look very different without every single person at EP2 that has contributed, in the past and in the present, to the enriching atmosphere that reigns in the research group. In sparse order, a deeply grateful hug goes out to Diego and Davide Maddaloni who have been a sturdy bedrock for my life in Madrid, and now represent lights of guidance towards new adventures; to Alberto Modesti, whose crystalline emotivity and grounded perspective on life have always been an invaluable moral compass; to Simone and Qi, unwaveringly joyful and tirelessly proactive; to Matteo Ripoli whose talents and company at the Matteodero will leave permanent memories; to Guille, whose mercurial emotions always represent a much-needed anchor to the important things in life; and to Alberto Marín, Tatiana, Nataša, Marco, Iñaki, Hugo, Andrés, and Borja, responsible for innumerable moments of happiness throughout these years. Finally, a brotherly embrace is reserved to Davide Poli, *de facto* a co-author of this work, who's company, support, and exasperation throughout this journey are a matter of personal pride and gratitude.

An inevitably insufficient thank you is dedicated to my guides to Spain and its culture: Elena, Álvaro, Ana, Carlos, the Pablos, Viki, María, and Arturo. Your hospitality, patience, and never-ending desire to accompany me in the discovery of this beautiful country are the reason I can confidently call Spain and Madrid home. Although it may not be evident, your support and joyful diversion have been as valuable in this thesis as any technical and academic advice.

My deepest gratitude also goes to all the friends back in Milan, who's selfless encouragement inflated my wings when pursuing my ambitions, and whose open arms welcomed me whenever vacations or necessity brought me back home. Andrea, Sergio, Ila, Massi, Gio, Marta, Marco, and Lorenzo, thank you for your unwavering affection.

Finally, I can only attempt to express my gratitude and appreciation for my parents, Monica and Paolo, and my brothers, Tommaso and Giacomo. To me our family represents a place where gravity and time abide to different laws, where responsibility and expectations become weightless, where possibilities multiply, and where any conversation can be tackled with timeless care and light-heartedness. More than any technical achievement I will consider myself satisfied if I can bring even a drop of this environment into the world.

Published and submitted content

The articles submitted and published in peer-reviewed journals during the course of this PhD thesis, and included in the present manuscript, are listed below.

- **M. Guaita**, E. Ahedo, M. Merino. PIC/Fluid Simulations of the Plasma Expansion in a Planar Magnetic Arch, *Plasma Sources Science and Technology*, 34, 015007 (2025), DOI: 10.1088/1361-6595/adab8e

  M. Guaita adapted the numerical model, run the simulations, analysed the results and wrote the manuscript. E. Ahedo and M. Merino contributed to the formulation of the research question, the analysis of the results and the review of the paper. The article has been published in the peer-reviewed journal *Plasma Sources Science and Technology*, and is included in its entirety in Chapter 3. Whenever contents of this article are included in this thesis, they are indicated by topographic means and an explicit reference.

- **M. Guaita** A. Marín-Cebrián, M. Merino, E. Ahedo, F. Cipriani, K. Dannenmayer. Electron Populations and Neutralization Process in the Plume of a Gridded Ion Thruster. *Plasma Sources Science and Technology*, 34, 045003 (2025), DOI: 10.1088/1361-6595/adc482.

  M. Guaita adapted the numerical model, run the simulations, analysed the results and wrote the manuscript. A. Marín-Cebrián developed the bulk of the numerical code and contributed to the analysis of the results and to the review of the article. M. Merino, E. Ahedo, F. Cipriani and K. Dannenmayer contributed to the formulation of the research question, and the review of the paper. The article has been published in the peer-reviewed journal *Plasma Sources Science and Technology*, and is included in its entirety in Chapter 4. Whenever contents of this article are included in this thesis, they are indicated by topographic means and an explicit reference.

- **M. Guaita**, K. Keil, K. Holste, P.J. Klar, E. Ahedo, M. Merino. Numerical and Experimental Study of Facility Effects on a Gridded Ion Engine's Plasma Plume. *Journal of Applied Physics*, 139, 093301 (2026), DOI: 10.1063/5.0315733

  M. Guaita adapted the numerical model, run the simulations, analysed the results and wrote the manuscript. K. Keil executed the experimental measurements, post-processed the resulting data, contributed to the analysis and interpretation of the results, and reviewed of the manuscript. K. Holste, P.J. Klar, E. Ahedo and M. Merino helped analyse the results and review the article. The article has been published in the peer-reviewed *Journal of Applied Physics*, and is included in its entirety in Chapter 5. Whenever contents of this article are included in this thesis, they are indicated by topographic means and an explicit reference.

The following is a list of contributions to conference proceedings reproduced within this thesis.

- **M. Guaita**, E. Ahedo, M. Merino, PIC-Informed Reduced Electron Model for Gridded Ion Engine Plumes. *10th Space Propulsion Conference*, 394 (2026).

  M. Guaita developed the numerical model, run the simulations, post-processed the results and wrote the paper. E. Ahedo and M. Merino contributed to the analysis of the results and the review of the article. The paper was exposed with an oral presentation during the *10th Space Propulsion Conference*, Bari, Italy, 18-21 May 2026. Its contents are entirely reproduced in Chapter 6, and are singled out with typographic means and an explicit reference.

Other research merits

The contributions to conferences and workshops produced during the arch of this PhD are listed below.

- **M. Guaita**, M. Merino, E. Ahedo, Hybrid PIC/Fluid Simulations of the Plume Expansion in a Magnetic Arch. *38th International Electric Propulsion Conference*, 471 (2024).

  M. Guaita adapted the numerical model, run the simulations, analysed the results and wrote the manuscript. E. Ahedo and M. Merino contributed to the formulation of the research question, the analysis of the results and the review of the paper. The paper was exposed with an oral presentation during the *38th International Electric Propulsion Conference*, Toulouse, France, 23-28 June 2024.

- **M. Guaita**, A. Marín-Cebrián, M. Merino, E. Ahedo, F. Cipriani, K. Dannenmayer, A Full PIC Study of the Neutralization of the RIT10-EVO's Plasma Plume. *38th International Electric Propulsion Conference*, 472 (2024).

  M. Guaita adapted the numerical model, run the simulations, analysed the results and wrote the manuscript. A. Marín-Cebrián developed the bulk of the numerical code and contributed to the analysis of the results and to the review of the article. M. Merino, E. Ahedo, F. Cipriani and K. Dannenmayer contributed to the formulation of the research question, and the review of the paper. The paper was exposed with an oral presentation during the *38th International Electric Propulsion Conference*, Toulouse, France, 23-28 June 2024.

- **M. Guaita**, M. Merino, E. Ahedo, K. Keil, K. Holste, P.J. Klar, Comparison Between PIC Simulations and Experimental Data of the RIT10-EVO's Plasma Plume. *39th International Electric Propulsion Conference*, 329 (2025).

M. Guaita adapted the numerical model, run the simulations, analysed the results and wrote the manuscript. K. Keil executed the experimental measurements, post-processed the resulting data, contributed to the analysis and interpretation of the results, and reviewed of the manuscript. K. Holste, P.J. Klar, E. Ahedo and M. Merino helped analyse the results and review the article. The paper was exposed with an oral presentation during the *39^th^ International Electric Propulsion Conference*, London, United Kingdom, 14-19 September 2025.

- K. Holste, K. Keil, O. Dörr, C. Winklmeier, P.J. Klar, **M. Guaita**, Towards Standardized Ion Thruster Diagnostics: Calibration of Energy Analyzers. *39th International Electric Propulsion Conference*, 310 (2025).

  K. Holste envisioned the study, assembled the experimental setup, oversaw the execution of the experimental campaign and wrote the article. K. Keil, O. Dörr contributed to the experimental campaign, the post-processing of the data and the review of the article. C. Winklmeier and K. Keil also contributed to the assembly of the RPA under study. P.J. Klar helped with the interpretation of the results and the review of the article. M. Guaita executed the simulations of the RPA, post-processed and interpreted their results, and contributed to the review of the manuscript. The paper was exposed by K. Holste with an oral presentation during the *39th International Electric Propulsion Conference*, London, United Kingdom, 14-19 September 2025.

- **M. Guaita**, J. Zhou, M. Merino, E. Ahedo, A Kinetic Study of the Electron Thermodynamics in a Plasma Plume, *29th SPINE Workshop*, Kiruna, Sweden (2022).

  Oral presentation delivered by M. Guaita on the 1st of December 2022.

- **M. Guaita**, A. Modesti, M. Merino, E. Ahedo, A Quasi-Neutral Full PIC Model for the Study of Electron Thermodynamics in a Plasma Thruster Plume, *76th Gaseous Electronics Conference*, Ann Harbour, Michigan (2023).

  Oral presentation delivered by M. Guaita on the 10th of October 2023.

- **M. Guaita**, K. Keil, A. Marín-Cebrián, M. Merino, E. Ahedo, K. Holste, P.J. Klar, Preliminary Validation of a PIC Model for Gridded Ion Thruster Plumes, *31st SPINE Workshop*, Toulouse, France (2024).

  Oral presentation delivered by M. Guaita on the 10th of October 2024.

- **M. Guaita**, M. Merino, E. Ahedo, K. Keil, K. Holste, P.J. Klar, Numerical and Experimental Calibration of an RPA Probe, *32nd SPINE Workshop*, Madrid, Spain (2025).

  Oral presentation delivered by M. Guaita on the 9th of October 2025.

- **M. Guaita**, M. Merino, E. Ahedo, K. Keil, K. Holste, P.J. Klar, Comparison Between PIC Simulations and Experimental Data of the RIT10-EVO's Plasma Plume, *32nd SPINE Workshop*, Madrid, Spain (2025).

Oral presentation delivered by M. Guaita on the 9th of October 2025.

- **M. Guaita**, M. Merino, E. Ahedo, Influence of Immersed Probes on the Charge Neutralization Process in a Gridded Ion Thruster Plume, *78th Gaseous Electronics Conference*, Seoul, Republic of Korea (2025).

  Oral presentation delivered by M. Merino on the 15th of October 2025.

Abstract

The increasingly popular use in the space sector of electric propulsion solutions requires, among other challenges, the evaluation of the interaction between the generated plasma plume and the components of the hosting spacecraft. Additionally, a confident extrapolation to in-space conditions of a thruster's propulsive performance and plume properties must pass through a detailed determination of the facility effects that alter the thruster's response during on-ground experiments. For these reasons the present thesis is dedicated to the study of plasma plumes, and to the improvement of the predictive capabilities and numerical efficiency of the models employed for their simulation.

In particular, a first part of the thesis concentrates on the simulation by means of a hybrid code of the plasma expansion within a magnetic arch, a magnetic topology generated by two electrodeless plasma thrusters (EPTs) of opposite magnetic polarity. The execution of a series of simulations elucidates the physical mechanisms that guide the merging of the plasma beams produced by each EPT, and reveal that the influence of the magnetic field intensity on the plasma discharge and propulsive properties saturates for values of the Hall parameters larger than 10. The developed hybrid model is also employed to study the effects of vacuum chamber walls and residual background pressure on the plasma properties, indicating that the former may relevantly influence the electron current pathways of magnetized electrons, while the latter generates an increase in the effective mass flux and a consequent improvement of the observed propulsive performance.

A second part of the thesis is instead dedicated to the investigation and simulation of gridded ion engine (GIE) plumes. First, a particle in cell (PIC) code is employed for the study of the neutralisation mechanisms that allow the formation of a quasi-neutral, current-free plume from the merging of the ion and electron beams emitted by thruster and neutraliser. This numerical effort evidences for the first time the importance of inelastic collisions between electrons and neutrals, that provide an energy sink for electrons causing their electrostatic trapping within the ion beam. As a consequence, the inclusion of ionisation and excitation collisions in the model allows a relevant improvement of the recovered electric potential and electron temperature maps with respect to previous PIC simulations of GIE plumes. This observation also prompts a conceptual subdivision of electrons into primary and trapped populations based on their capability to escape the ion beam's potential well, and the study of the sensitivity of these populations to the problem's parameters. Second, the results of the proposed PIC model are thoroughly compared, for different operating points, background pressures, and facility wall potentials, with the experimental measurements of the plume of Ariane's RIT10-EVO. This comparison confirms the model's capabilities in the prediction of the ion properties in the plume bulk and in the qualitative assessment of background pressure effects, but also evidences some remaining uncertainties in the determination of the maximum plume potential and electron temperature. A subsequent study of the perturbations caused by the immersion of a Langmuir probe within the plume bulk shows that it can cause a substantial shift in the plasma potential, but is unable to explain the numerical and experimental differences in the electron temperature. Finally, the gathered numerical and experimental data, and the conceptual distinction between primary and trapped electrons, are used to inform the development of an electron fluid closure to be employed in hybrid simulations of GIE plumes. The assumptions behind this novel methodology are verified by means of the PIC simulation data, and the developed closure is shown to yield results in good agreement with the PIC model, while reducing the simulation times by a factor 10 or more.

Contents

List of Figures

List of Tables

CHAPTER 1

Introduction

Since the infancy of electric propulsion (EP), when pioneering missions like SERT I[1] (1964) and ATS-4 (1968) demonstrated its applicability and value, attentive care was taken in the evaluation of its integration with the hosting spacecraft[2], [3]. While the successes of SERT II[4] (1970) and ATS-6[5] (1974) paved the way for the further development and expansion of EP, others such as SNAP-10A[6] (1965) —which likely failed due to electromagnetic interference between the propulsive subsystem and the attitude sensors— and the measurements on board of the same ATS-6 mission —that demonstrated the influence of EP on spacecraft charging— prompted caution on possible interactions between the propulsive subsystem and spacecraft. Indeed, the plume emitted by EP thrusters is host to ions (at single or multiple states of charge), electrons, and residual neutral atoms (or molecules) with a wide range of energies, along with electric and magnetic fields induced by the charged particles themselves and by the electrodes and magnets in the thruster design. The plasma environment thus produced will inevitably interact with the nearby spacecraft surfaces, potentially altering their properties and functionality. The study of plasma plumes, to which this thesis is dedicated, and their interaction with the surrounding plasma environment and material surfaces is therefore paramount for the successful integration of EP subsystems on board of hosting spacecraft.

One type of plume-spacecraft interaction that attracted the concerns of engineers regarded the electrically charged nature of the particles composing EP plumes. Indeed, the collisional processes that take place in the plume (*e.g.* charge-exchange (CEX) between ions and neutrals), and the local electric and magnetic forces cause charged particles to circle back towards the spacecraft, leading to the collection of electric currents at its surfaces. This effect is further complicated by the natural plasma environment in which the spacecraft is situated (*e.g.* the plasmasphere or the solar wind), which interacts with the thruster's plasma plume and further modulates the currents collected by the spacecraft. As a consequence, a gradual electric biasing of either the whole spacecraft with respect to the surrounding plasma environment (termed *absolute charging*), or between its separate components (*differential charging*) may occur[7], [8]. The former presents the smaller hazards, since it does not lead to abrupt currents flowing within the spacecraft, but the resulting electric fields can lead to modifications in the properties of the surrounding plasma environment, further altering the way it interacts with the spacecraft. Differential charging, on the other hand, may result harmful for the spacecraft and its mission. When potentials between isolated components exceed the local dielectric breakdown voltage, an electrostatic discharge (ESD) takes place.[9] The resulting current arc may cause electromagnetic interference with other spacecraft components, or directly damage the hardware that experienced the sharp flow of current.

Historically, the first dedicated missions demonstrated an adequate compatibility between spacecraft charging and the use of EP. ATS-6 (1974) and SCATHA P78-2[9] (1979) both observed an influence of ion beams on the spacecraft's absolute charge, but also showed that it could be heavily mitigated through a proper neutralisation of the emitted currents by means of an external neutraliser (indeed, correctly controlled, EP proved to be a solution rather than a hazard to absolute charging[3]). Studies of the telemetry of SCATHA P78-2 also pointed to a strong correlation between ESDs and the plasma environment surrounding the spacecraft, while only some of these could be traced back to the operation of ion and electron beams.[10] More recently (2009), a study of the surface charging taking place on board of 4 Intelsat and 2 SES satellites showed fluctuations in differential potentials during operations of the EP subsystem[11]. However, only very rare occurrences, mostly related to harsh space-weather conditions, of differential voltages above engineering thresholds were recorded.

In the context of scientific missions dedicated to the study of the space plasma environment, absolute and differential charging pose another hurdle for the mission objectives. Indeed, the potential difference between the spacecraft components and the surrounding plasma alter the particle trajectories and electromagnetic fields under investigation, and thus modify the measurements of the scientific payload. For example, measurements of low energy ion fluxes taken by Rosetta (2004)[12], and the moments of the electron distribution measured by BepiColombo (2016)[13] during its Mercury flyby, were found to be convoluted by spacecraft potentials and had to be corrected through complex simulation efforts. In general, numerous on-board algorithms for the de-convolution of the measured electron properties from the effects of spacecraft charging are proposed in the literature[14], highlighting the interest of the scientific community in this topic.

A second type of plume-spacecraft interaction of important concern regards the large energies possessed by the particles emitted by EP thrusters. The impingement of these particles onto spacecraft surfaces eventually leads to their erosion and to the consequent degradation of their optical, electrical, and thermal properties[15]. Moreover, the sputtered material generated by these interactions or from the erosion of internal thruster components, may later deposit on other surfaces, leading to a further deterioration of their properties[16]. This deposition of material is vastly accentuated when dealing with thrusters that operate with alternative propellants (*e.g.* mercury, used on board of SERT I and II, or iodine considered for modern designs[17]), which contrary to the commonly employed inert noble gases may bind chemically and mechanically with exposed surfaces. Note also that reducing the deterioration of surface properties results even more important for the very common case of EP powered by solar panels, since the conservation of their optical and electric properties is paramount for efficient power generation. As a result, many space missions have dedicated scientific payloads to the study of the impinging energy of EP-produced particles and contamination rates due to sputtered material. NASA's Deep Space 1[18], [19] (1998), propelled by the NSTAR gridded ion engine (GIE), was equipped with a specifically designed EP diagnostics package including — among other sensors— a retarding potential analyser (RPA) and a planar Langmuir probe (LP) for plasma diagnostics, and a quartz crystal microbalance (QCM) and a calorimeter pair (CAL) for contamination studies. The RPA and LP data, complemented by the readings of the Plasma Experiment for Planetary Exploration (PEPE) scientific payload, pointed to the presence of artificially produced plasma well outside of the plume bulk. The resulting plasma densities, energies, and currents at the spacecraft surfaces were observed to be strongly dependent on the thruster's operating point, with PEPE (located at the opposite side of the spacecraft) registering measurement interferences only at specific thrust levels[19]. Similarly, the QCM and CAL readings showed a modulation of the collection rate of Molybdenum sputtered from the ion thruster grids that depended on the thrust level, with sensors not in line of sight of the thruster collecting relevant fluxes when the plume densities and potentials increased[18]. ESA also contributed to this line of research by mounting similar EP dedicated diagnostics first on STENTOR[20] (failed launch in 2002) and then on SMART-1[21] (2003), that employed a Hall effect thruster (HET) for its propulsion. Interestingly, the QCM on board of SMART-1 recorded negligible material deposition, consistent with the minor decline of solar panel efficiency, and the LP and RPA measurements pointed to a modulation of the plume potential that resulted in the limitation of the thruster ground voltage with respect to the surrounding ambient plasma.[22]

The last form of undesired plume-spacecraft interaction consists in parasitic forces and torques induced by the momentum flux of plume particles reaching spacecraft surfaces, that modify its nominal trajectory and attitude. While these torques and forces are very small, and can be easily corrected by the propulsive and ADCS subsystems, they can lead to a faster saturation of reaction wheels and to an increased use of propellant. This was the case for the Russian Express-A2 and A3 telecommunication satellites, where the particles emitted by the SPT-100 used for orbit keeping and collected by the solar panels produced torques that had to be compensated by the reaction wheels of the attitude control subsystem[23], [24].

The issue of the interactions between EP plume and spacecraft remains today a topic of active attention and research, as demonstrated by the recent launch of ESA's Heinrich Hertz satellite (2023) equipped with an EP diagnostics package analogous to the ones of Deep Space 1 and SMART-1[25]. Nevertheless, the multi-scale and multi-physics nature of the problem complicates immensely its examination. In-space measurements are expensive, logistically complex, and limited to punctual locations that preclude a holistic view of the problem. Similarly, experimental investigations of the integrated spacecraft-thruster system in on-ground facilities are prohibitive due to the large scales involved; but even accurate on-ground testing of an isolated thruster presents open challenges. Indeed, replicating precisely the space environment in test facilities is impracticable, and experiments are inevitably conducted under conditions that alter the response of the thruster and its plume[26], [27]. The differences between the space environment and the one generated in ground facilities, together with the variations that they produce in the thruster discharge, are typically grouped under the term "facility effects" and may differ in entity and magnitude depending on the thruster design and operating conditions. Because of this complexity, the theoretical investigation of plasma plumes and facility effects through the development of accurate numerical models for their simulation is paramount for the prediction of the plume properties in space and for the evaluation of its interaction with the hosting spacecraft.

1.1. Facility Effects

As mentioned, facility effects are diverse and thruster and facility dependent. We distinguish here between three categories based on the fundamental differences between the in-space and on-ground environments that generate them: background effects, wall effects, and probing effects.

Background effects: Background effects stem from the impossibility of reproducing in vacuum vessels the densities and characteristics of the space plasma that surrounds the thruster during its in orbit operation. During experiments, in fact, state of the art vacuum chambers are capable of reaching background pressures of the order of 10^{-6} mbar[28], while typical pressures in space can be orders of magnitude lower (*e.g.* around 10^{-10} mbar at an altitude of 1000 km). The chemical nature and energy of the particles composing the background plasma are also very different, but this represents a secondary effect compared to the differences in density. Indeed, most of the observed variations in thruster discharges may be attributed to the increased collision frequencies that the facility background density provokes. Primary among these, and common to all EP thrusters, is the generation of a cloud of low energy ions, much denser than the one generated in space, that surrounds the plume bulk and is formed mostly by CEX collisions between plume ions and background neutrals[29], [30]. These ions, and the electrons that they attract electrostatically, may lead to a premature truncation of the plume's ambipolar expansion, which stops when the bulk density becomes comparable with the background one[31].

Additionally, because of their reduced kinetic energy, CEX ions also respond more readily to the small electric fields present in the plume, causing an increase in the currents that return to the thruster's exhaust plane (*i.e.* where the spacecraft would be in a fully integrated system) compared to what occurs in space[29], [32]. Another issue that affects thrusters with relevant magnetic fields in their plume is the increase in classical electron cross-field transport. For thrusters employing magnetic nozzles (MNs), this may cause an earlier plasma detachment from magnetic lines and a reduction of the magnetic thrust[33]; while in HETs it modifies the dynamics with which electrons flow from the neutraliser to the discharge chamber. In the case of thruster designs with a strong backwards coupling between plume and discharge chamber (*e.g.* HETs and electrodeless plasma thrusters, as opposed to GIEs), larger background pressures can lead to the ingestion of neutral atoms into the thruster's discharge chamber, effectively providing an increased mass flow rate with respect to the nominal one. As a result, many studies on the performance of HETs (although not all, as this effect is sometimes opposed by a shift in the ionization region) reported a larger thrust as the background pressure increased[27], [34]. In the case of electrodeless plasma thrusters (EPTs) equipped with a MN, neutral ingestion is overshadowed by the increase in electron inelastic collisions, which deplete the thermal energy employed for the plasma acceleration and thrust production in the MN. As a result, the propulsive performance of EPTs has often been observed to decrease as the facility background pressure was raised[35]. Finally, variations in neutral densities have been shown to affect discharge oscillations, modifying the frequency and amplitude of the breathing mode in HETs[36], and influencing oscillations, mode transitions, and general discharge properties in hollow cathodes[37].

Wall effects: The walls of the vacuum vessels in which experiments are carried out may influence the response of a thruster's plume by delimiting its expansion, prompting the formation of Debye sheaths at the plasma-wall interface, and emitting additional particles into the discharge through secondary electron emission (SEE) and sputtering. In particular, the conductive nature of facility walls generates additional low resistance current paths that are not present in space. While an obvious mitigation of this issue is achieved by isolating the thruster assembly from facility ground, conductive chamber walls have still been shown to modify the current distributions in the plume. Indeed, studies on HET discharges have pointed to a preferred electron flow to the closer radial walls (in place of the axial flow expected in space)[38], [39], while works on EPTs and MNs hypothesize that the geometry and conductive properties of chamber walls may explain some important variations in thrust and efficiency observed when testing the same thruster in different facilities[40], [41]. In the case of GIEs, on the other hand, it is known that SEE from facility walls can contribute to the plume neutralisation, to the extent that ground tests of low power thrusters sometimes rely on this mechanism —rather than the use of an external neutraliser— for the charge neutralisation of the ion beam[42]. Nevertheless, the influence and importance of SEE when a larger electron flux is provided from an external neutraliser is yet to be quantified. Finally, the highly energetic ion beam of a GIE can cause the erosion and sputtering of the beam target and chamber walls, hindering the experimental determination of material deposition from the sputtering of the thruster grids, and complicating on-ground lifetime assessments[43].

Probing effects: The insertion of probes within a thruster's plume for the evaluation of the local plasma properties may lead to a perturbation of the plume equilibrium, especially if the probe is electrically biased or if it can constitute a relevant current path to ground. In the case of HETs, the insertion of probes in the very near plume (at distances shorter than a channel width) was shown to alter the potential profiles in the acceleration region, the ion velocity distribution function (VDF) in the plume, and the average value and amplitude of oscillations of the discharge current[44]. These perturbations were enhanced for a positively biased probe (*e.g.* for the electron collecting branch of a Langmuir probe sweep). More concerningly, several experimental studies on the plumes of GIEs have reported a strong sensitivity of the plume potential to invasive probing techniques[42], [45]. This is attributed to the delicate charge neutralisation mechanism of the ion beam, that involves the slow formation of a trapped electron population which is prone to depletion if presented with additional current paths to ground. In case of an imperfect coupling between the neutraliser and the ion beam (or in total absence of a neutraliser), dramatic global increases in the plume potential are observed when probing the denser regions of the plume, with consequent increases in the plume divergence[42]. Although it has yet to be proven experimentally, the presence of a trapped electron population has also been theorized in MNs[46], [47], leading to the conjecture that they may be prone to similar perturbing mechanisms when subjected to invasive probing.

1.2. Thesis Objectives and Structure

This thesis aims to improve our capabilities in the numerical simulation of EP plasma plumes, identifying the most opportune modelling strategies, determining their shortcomings and strong points, and enhancing their accuracy and computational efficiency. In doing so, it provides insight on the physics that governs the simulated plasma plumes, and on the influence of design parameters and operating conditions on the plumes' characteristics. Concerning this latter point, particular attention is dedicated to the determination and description of facility effects, promoting a more confident extrapolation of experimental measurements to in space conditions. In practice, the thesis first provides a propaedeutic overview of the state on the art of plasma plume modeling in Chapter 2, and then delves into the characterization of the plumes of two distinct propulsive devices.

1. Chapter 3 is dedicated to the investigation of the plasma expansion in a magnetic arch topology generated by the clustering of two EPTs. Because of the novelty of this architecture and the limited related research available in the literature, this part of the thesis intends to consolidate the understanding of the principal physical

processes that govern the plume equilibrium, and provide a qualitative study of the effects of design parameters and operating conditions such as the magnetic field strength, and the influence of facility walls and background pressure. To this end a planar version of the in-house hybrid code EP2PLUS was implemented and applied to the case under study. Chapter 3 reproduces entirely the contents of the peer-reviewed journal article published in *Plasma Sources Science and Technology*[48].

2. The following chapters, instead, concentrate on the analysis and simulation of GIE plumes. Contrary to magnetic arches, these thrusters are well established and can count on a long history of research dedicated to their characterization, allowing a more detailed and specific investigation line with the following objectives.

    - The tailoring and application of a Particle in Cell (PIC) code to the simulation of GIE plumes, and to the study of the mechanisms that allow an efficient neutralisation of the emitted ion beam. This process should allow the identification of the components of the problem that require particular attention (*e.g.* collisional processes, plasma bridge, approach to steady-state), and those that can be acceptably simplified.
    - The validation of the previously developed model by a thorough comparison with dedicated experimental measurements, and the consequent application of the gathered numerical and experimental data to the study of background, wall, and probing facility effects.
    - The identification, by comparison with the validated PIC code, of accurate closures to the electron fluid equations for the case of GIE plumes. In particular, the identified fluid closure should permit an accurate retrieval of the plume characteristics when employed in hybrid or fluid models, while granting a relevant mitigation of computational costs compared to the PIC code.

The first two objectives are respectively tackled in Chapters 4 and 5, that reproduce the peer-reviewed articles published in *Plasma Sources Science and Technology*[49], and in the special issue dedicated to facility effects on the *Journal of Applied Physics*[50]. Chapter 6, instead, covers the third objective, reprinting the conference article presented at the *10th Space Propulsion Conference*[51].

As a final note, Chapters 3, 4, 5, and 6 reproduce published articles, that are reported here without modifications. These chapters therefore result self-contained, including their own introduction, motivation, methodology and conclusions. The author's apologies for any repetitions or changes in notation across these chapters.

CHAPTER 2

Overview of Numerical Models for Plasma Plumes

This chapter provides an overview of the most common models employed in the EP community for the simulation of plasmas. The objective here is not to provide a detailed description of each model implementation, but rather to outline the underlying assumptions, advantages and limitations of each methodology. This is propaedeutic to an informed comparison between models when choosing which is more suitable for the problem under consideration. The next two sections will tackle the different approaches for the description of the species composing a plasma, and the alternatives for the computation of the electric forces acting on these species. Finally, Section 2.3 provides a critical analysis of the most commonly employed models for plume simulations.

2.1. Description of the Plasma Species

In a plasma, the conservation in phase-space of the particles of a species α may be expressed by means of the Boltzmann equation

$$\frac{\partial f_\alpha}{\partial t} + \mathbf{v} \cdot \nabla_x f_\alpha + \frac{q_\alpha}{m_\alpha}(\mathbf{E} + \mathbf{v} \times \mathbf{B}) \cdot \nabla_v f_\alpha = S, \tag{2.1}$$

where $f_\alpha(t, \mathbf{x}, \mathbf{v})$ is the species' VDF, ∇_x and ∇_v are the gradients in space and velocity coordinates, and q_α and m_α are respectively the charge and mass of the species' particles. The term $q_\alpha(\mathbf{E}+\mathbf{v}\times\mathbf{B})$ expresses the forces due to the electric and magnetic fields (respectively $\mathbf{E}$ and $\mathbf{B}$), while $S(t, \mathbf{x}, \mathbf{v})$ is a source term linked to the injection of new particles into the domain or to particle-particle collisional processes. If the forces acting on the species and the source term S are known, Equation (2.1) may be discretized and integrated numerically to yield f_α at each moment in time. However, models that employ this approach —named Vlasov solvers— are limited by the computational burden linked to the six-dimensional discretization and integration in phase-space (three dimensions in space and three in velocity). As a consequence, while Vlasov solvers can be very accurate even in regions of low plasma density, they are seldom used for full-scale applications[52].

An alternative to the direct integration of the Boltzmann equation is the Particle in Cell (PIC) methodology[53], [54], in which the VDF of a species is discretized as a set of N_p "macro-particles" (each representing a cloud of numerous physical particles belonging to an infinitesimal volume of phase-space), so that

$$f_\alpha(t, \mathbf{x}, \mathbf{v}) \approx \sum_{p=1}^{N_p} w_p S_x(\mathbf{x}_p, \mathbf{x}) S_v(\mathbf{v}_p, \mathbf{v}), \tag{2.2}$$

where w_p is the weight of macro-particle p (the number of physical particles it represents), $\mathbf{x}_p$ and $\mathbf{v}_p$ are its position and velocity in function of time, and S_x and S_v are its shape functions in physical and velocity space[55] (typically a Heaviside step function in space and a Dirac delta in velocity, although higher order alternatives have been proposed[56]). Assuming that the forces acting on each macro-particle are known, PIC codes then propagate their trajectories in time through the integration of their equations of motion to retrieve f_α at each simulation time-step. Collisional events can also be included in the model by perturbing the particle velocities through stochastic algorithms such as Monte Carlo Collisions (MCC)[57] or Direct Simulation Monte Carlo (DSMC)[58] collisional models. The macroscopic quantities describing the species (*e.g.* density, velocities, and temperature) are then retrieved by integrating the discretized VDF over the velocity space, as formally defined later. Since particle orbits in phase-space coincide with the characteristics of Equation (2.1), this approach is equivalent to integrating the Boltzmann equation along N_p characteristics[59]. PIC codes thus benefit of an intrinsically adaptive discretisation of phase-space: more macro-particles will cluster in regions of higher density and fewer —or none— will be present where the densities drop, leading to a more efficient use of computational resources with respect to the more structured discretization employed in Vlasov solvers. On the other hand, when the macro-particles are too few to provide an accurate description of f_α in Equation (2.2), PIC codes become prone to numerical noise, leading to numerical thermalization of the species' VDF and an inaccurate reconstruction of its macroscopic properties[60].

Yet another approach to the resolution of the Boltzmann equation is the fluid methodology. Its formal derivation starts by defining the macroscopic fluid quantities describing a species as moments of its VDF:

$$\begin{aligned} n_\alpha &= \iiint f_\alpha \, d^3\mathbf{v}, & n_\alpha \mathbf{u}_\alpha &= \iiint \mathbf{v} f_\alpha \, d^3\mathbf{v}, \\ \overline{\overline{M}}_\alpha &= m_\alpha \iiint \mathbf{v}\mathbf{v} f_\alpha \, d^3\mathbf{v}, & \mathbf{P}''_\alpha &= \frac{m_\alpha}{2} \iiint \mathbf{v} v^2 f_\alpha \, d^3\mathbf{v}, \end{aligned} \tag{2.3}$$

where n_α, $\mathbf{u}_\alpha$, $\overline{\overline{M}}_\alpha$, and $\mathbf{P}''_\alpha$ are respectively the species' density, bulk velocity, momentum tensor, and energy flux vector. Related to these fundamental quantities are the pressure tensor $\bar{\bar{p}}_\alpha = \bar{\bar{M}}_\alpha - m_\alpha n_\alpha \mathbf{u}_\alpha \mathbf{u}_\alpha$ and the temperature tensor $\bar{\bar{T}}_\alpha = \bar{\bar{p}}_\alpha / n_\alpha$. The transport equations for each of these macroscopic quantities, and of any desired higher-order moment of the VDF, are then obtained by taking the corresponding moment of Equation (2.1) (multiplying it an appropriate amount of times by $\mathbf{v}$, and integrating it over the velocity space), yielding the continuity, momentum and energy equations:

$$\frac{\partial n_\alpha}{\partial t} + \nabla \cdot (n_\alpha \mathbf{u}_\alpha) = S_\alpha, \tag{2.4}$$

$$m_\alpha \frac{\partial (n_\alpha \mathbf{u}_\alpha)}{\partial t} + \nabla \cdot \bar{\bar{M}}_\alpha = q_\alpha n_\alpha (\mathbf{u}_\alpha \times \mathbf{B} + \mathbf{E}) + \mathbf{R}_\alpha, \tag{2.5}$$

$$\frac{1}{2} \frac{\partial \, \mathrm{tr}(\bar{\bar{M}}_\alpha)}{\partial t} + \nabla \cdot \mathbf{P}''_\alpha = -q_\alpha n_\alpha \mathbf{u}_\alpha \cdot \mathbf{E} + W_\alpha, \tag{2.6}$$

when truncating the derivation at the second order moment. Here tr(·) stands for the trace of the underlying tensor, and the terms S_α, $\mathbf{R}_\alpha$, and W_α represent respectively the effects of collisions on particle production, momentum exchange, and energy loss. Note that these equations are exact, and make no assumption on the underlying VDF. However, the system of Equations (2.4–2.6) is undetermined, since each transport equation depends on the value of the next moment of the VDF. As a result, to be able to solve the fluid system, a closure must be imposed to relate the highest VDF moment considered (for which the transport equation isn't solved) to the lower order ones. This is equivalent to making an assumption on the shape of the species' VDF, which in the most common fluid formulations is taken to be a drifted Maxwellian (the species is assumed at thermal equilibrium) and as a consequence the pressure and temperature tensors become diagonal and isotropic ($\bar{\bar{p}}_\alpha = p_\alpha \bar{\bar{I}}$ and $\bar{\bar{T}}_\alpha = T_\alpha \bar{\bar{I}}$), and the heat flux and gyro-stress tensor are null, so that the energy flux vector reduces to $\mathbf{P}''_\alpha = (1/2) n_\alpha \mathbf{u}_\alpha (m_\alpha u_\alpha^2 + 5T_\alpha)$[61].

2.2. Computation of the Electromagnetic Forces

The previous section assumed that the electric and magnetic forces acting on the plasma are known. However, the electromagnetic fields present in the domain depend on the distributions of electric charge and current, and are therefore coupled with the plasma dynamics. As a consequence, schemes that provide values of $\mathbf{E}$ and $\mathbf{B}$ consistent with the state of the plasma are required. The plume studies presented in this thesis are carried out in the electrostatic limit, meaning that the magnetic field induced by the plasma currents is assumed to be negligible with respect to the one applied externally by the thruster, so that the magnetic field map can be taken constant in time and the only remaining concern is the computation of the electric fields. While this is a common assumption in plasma plume simulations due to the relevant reduction in computational costs that it entails[29], [62], [63], some studies suggest that, although small, the plasma induced magnetic field may not always be negligible, especially for the case of MNs where it may constitute an important plasma detachment mechanism[64], [65].

The self-consistent determination of the electric potential ϕ in the domain may be carried out in two ways. The first is to couple the description of the plasma species with Poisson's equation:

$$\nabla^2 \phi = -\frac{\rho_{el}}{\varepsilon_0}, \tag{2.7}$$

where $\rho_{el} = \sum_\alpha q_\alpha n_\alpha$ is the net electric charge density, and ε_0 is the electric permittivity of vacuum. This approach allows the consistent resolution of non-neutral regions (*e.g.* Debye sheaths), but introduces the Debye length λ_D and plasma frequency ω_e as fundamental scales of the problem. These minute scales must be resolved by the cell size and time-step for the stability of commonly employed explicit integrating schemes, and since λ_D and ω_e are much smaller than the largest dimension of the problem (by up to 5 or 6 orders of magnitude), codes relying on the resolution of Poisson's equation can become extremely computationally expensive[66]. As a result, non-neutral codes must often make other simplifying assumptions to allow an affordable computational treatment of the problem, such as reducing the number of spatial dimensions[67], neglecting the slower temporal scales (typically those linked to neutrals)[68], or artificially modifying some parameters of the problem (*e.g.* the vacuum permittivity[68], the mass of ions[63], or rescaling the problem's geometry[69]).

Alternatively, one can assume that the scale of the non-neutral regions is infinitely smaller than the other characteristic scales of the problem, and that the plasma in the plume is quasi-neutral. As a consequence, rather than solving Equation (4.2) one may impose $\sum_\alpha q_\alpha n_\alpha = 0$, and use this additional condition to retrieve ϕ. This approach removes the stability constraints typical of non-neutral codes, and permits discretizations of time and space that abundantly over-step the plasma frequency and Debye length. This obviously allows for much lighter codes from the computational standpoint, but also introduces some modelling challenges that should be taken into consideration. The assumption of quasi-neutrality, in fact, does not allow an accurate resolution of those regions of the domain where charge separation is important (*e.g.* plasma sheaths, oscillations driven by non-neutrality, *etc.*). Since Debye sheaths nearly always develop at the boundary between material walls and the plasma, this also complicates the imposition of boundary conditions, which are most naturally given at material walls, after a sheath. This issue is typically settled through semi-analytical models of a mono-dimensional Debye sheath that connect the quasi-neutral domain with the material boundaries[29], at the price of introducing into the model additional hypotheses required to close these simplified sheath models[70] (*e.g.* mono-dimensionality, undrifted Maxwellian electron VDFs, isotropic electron temperature, Bohm condition, *etc.*).

2.3. Types of Models

The different approaches to the description of plasma species and electric fields described in the previous section can be combined into various modelling strategies, summarized below.

2.3.1. Fluid Codes

These models employ the fluid methodology for the description of all the species composing the plasma, and have been proposed both in the quasi-neutral[64], [71], [72] and non-neutral[73], [74] forms. Their main limitations are the requirement of a heuristic closure to the system of fluid equations (which are often truncated at the energy level)[75], a non-trivial determination of the boundary conditions for higher order VDF moments such as the energy flux vector, and the numerical stability of the integration scheme which often requires some level of numerical diffusion[76]. On the other hand, fluid codes are highly flexible, allowing for large variations in their complexity and computational cost depending on the assumptions made in their derivation. They are also particularly indicated for large-scale numerical parallelization, as the resulting algorithms are not prone to conditional branching or load imbalances between computing nodes.

2.3.2. Hybrid Codes

Models that employ a particle methodology for some of the plasma species, and a fluid one for others are termed “hybrid”. In most cases, these codes describe ions and neutrals as particles, and employ a drift-diffusion approximation for electrons (assuming them to be inertialess and with an isotropic VDF)[29], [62], [77], [78]. The use of a fluid description for electrons allows for a trivial imposition of quasi-neutrality (which is not as straight-forward when a particle formalism is employed, as discussed later), while the particle description of the heavier species does not force any assumptions on their VDFs. As a result hybrid codes are computationally light, provide a kinetic description of the heavier species, and are often employed for full scale simulations of propulsive devices and their plumes. Nevertheless, the drift-diffusion approximation and the fluid closures employed for the description of electrons have been shown to have a limited applicability range[79], [80], [81]. Similarly, some works have found the quasi-neutral assumption to be inaccurate at the outer edges of the plume, where the plasma densities become very low[82], or in regions of large electric charge density such as in proximity of a cathode or in front of the grids of a GIE[32]. More complex fluid descriptions for electrons and the inclusion of a non-linear Poisson solver have been proposed to overcome these issues[29], [83], but these approaches quickly negate the computational advantages of the classical hybrid scheme. As a result, the detailed study of physical phenomena that still elude our understanding are often tackled with higher-fidelity but more cumbersome models, although hybrid codes are still widely regarded as the models of choice for full-scale simulations of thrusters and their plumes.

2.3.3. Particle in Cell Codes

Electrostatic PIC models employ a particle description for ions and electrons, coupled with a Poisson solver for the determination of the electric potential[63], [68], [84], [85],

[86]. As such, they make no assumption of the VDFs of charged particles and require no fluid closures, but are computationally cumbersome because of the limitations on cell size and time-step imposed by the resolution of the Poisson equation. Recently, implicit and energy conserving schemes have been proposed to relax these constraints at the cost of an increase in the complexity of the code[87], [88], [89], but the traditional explicit approach remains to date the most employed. Because their computational burden these models are typically used for detailed simulations of a subsection of the global problem by either reducing its dimensionality (invoking symmetries or assuming no gradients in the neglected dimensions), disregarding the longer time-scales (usually linked to the dynamics neutral, which are therefore described through reduced models)[68], or artificially altering the characteristic scales of the problem[69].

The PIC methodology does not permit a straight forward imposition of quasi-neutrality, since one does not have a direct control on a species' density, which is instead obtained as a function of the instantaneous position of millions of macro-particles. Nevertheless, during the initial phases of this thesis substantial effort was dedicated to the development of a quasi-neutral, bi-dimensional, PIC code. The idea being that instead of retrieving the electric potential from the resolution of Poisson's equation one could assume quasi-neutrality *a priori*, and obtain ϕ from the continuity and momentum equations of electrons with the density of the ion macro-particles substituted in place of the electron density[90], [91]. These equations could be closed with the temperature provided by the electron macro-particles, and the resulting electric fields would then be used to advance the electrons and ions along their orbits in phase-space. This approach would overcome the constraints on cell size and time-step characteristic of non-neutral codes, while making no assumption on the VDFs of ions and and electrons. However, when checking *a posteriori* the assumption of quasi-neutrality it was found that the numerical system quickly diverged from this condition: the density of electron macro-particles gradually depleted, falling well below the one of ions. It was therefore necessary to develop dedicated injection and outflow boundaries for electron macro-particles that enforced through a PID controller a zero global electric charge in the domain[92]. Although this approach allowed us to reach a quasi-neutral steady-state for a simple plume scenario, it was not deemed sufficiently rigorous, and the development of the quasi-neutral PIC code was discontinued.

CHAPTER 3

PIC/Fluid Simulations of the Plasma Expansion in a Planar Magnetic Arch

This chapter reproduces the contents of Ref. [48], published in the peer-reviewed journal Plasma Sources Science and Technology. The typography has been adapted to the style of this thesis.

Abstract

Magnetic arches (*i.e.* the magnetic topology that emerges when placing two magnetic nozzles with opposite polarities side by side) are an attractive option for the clustering of multiple electrodeless plasma thrusters, as they are characterized by a zero magnetic dipole moment and thus allow a reduction of perturbing magnetic forces on the spacecraft. This work employs the hybrid code EP2PLUS to simulate and study the plasma expansion for such a magnetic topology in the planar limit. First, a reference simulation is used to analyze the leading physical mechanisms that govern the plume properties. Ions are thus found to be characterized by a double peaked VDF close to the symmetry plane, where the plasma beams emitted by the two thrusters merge, while the magnetic force acting on electrons is shown to shape both the lateral confinement of the plume, and the thrust profile provided. Second, a parametric sweep on the strength of the magnetic field shows that its influence on the propulsive properties and on the characteristics of the plume saturates for values of the Hall parameter larger than around 10. Beyond this value of the Hall parameter, only the in-plane electron currents are found to be particularly sensitive both to the magnetization levels and the boundary conditions employed, although they are also largely decoupled from the rest of plasma properties. Finally, background

pressure effects were considered by including collisions with neutral atoms in the simulations, highlighting the relevance of neutral entrainment in the modification of the plume properties and in the propulsive performance of the magnetic arch.

3.1. Introduction

Electrodeless plasma thrusters (EPTs) are a rapidly emerging technology in the electric propulsion community because of their simplicity, scalability, and absence of plasma-immersed electrodes[93], [94]. This family of thrusters most notably includes the helicon plasma thruster [95], [96], [97] and the electron-cyclotron resonance thruster [98], [99], [100], in which the plasma generation is guaranteed by exciting the electron population through electro-magnetic waves. A key component of these architectures is the magnetic nozzle (MN)[71], [101], [102], used to externally accelerate the plasma and increase the provided thrust. A traditional MN consists of a diverging magnetic field **B**, applied by the thruster's magnetic circuit, which confines the plasma in the perpendicular direction and accelerates it axially. In fact, in the common case of an 'electron-pressure-driven' MN (where the electron temperature is much larger than the ions') the orthogonal electron pressure gradient, combined with the $\mathbf{E} \times \mathbf{B}$ drift, gives rise to an azimuthal and diamagnetic electron current $j_{\theta e}$. This generates a magnetic force density that pushes electrons axially, and by reaction contributes relevantly to the total thrust provided by the EPT.[103], [104] To maintain a current free plume in the presence of the axial magnetic force acting on electrons, an ambipolar potential drop must also develop, confining electrons and generating an increase in the axial momentum of ions equivalent to the magnetic thrust provided. [71], [105]

A single MN produces a non-zero magnetic dipole moment that can give rise, in presence of terrestrial or planetary magnetic fields, to disruptive torques for the control of a spacecraft's attitude. However, with the aim of easily scaling the generated thrust and providing a form of thrust control, the idea of clustering multiple EPTs has been recurrently proposed in the literature[64], [106], [107], [108], [109]. It becomes therefore intuitive to envision the pairing of EPTs with opposite magnetic polarities, so as to cancel out the total dipole moment[110]. In such a configuration the gradually diverging magnetic topology of a MN is modified into a magnetic arch (MA), in which a portion of the magnetic field lines emitted by one of the EPTs curves and connects with those of the other[106]. These field lines are termed *closed magnetic lines*, while the outer lines of each EPT, which do not connect with those of the neighbouring one and close back on themselves are termed *open magnetic lines*. These definitions also allow the identification of a separatrix, the magnetic surface that lays on the boundary between open and closed lines, whose position and geometry depends on the details of the MA topology.

The magnetic topology of a MA implies important variations in the plasma response with respect to the traditional MN. Amongst these the most relevant are the coupling between the two plasma sources, which now become directly connected by the arching magnetic lines, and the interaction and merging of the two plasma beams emitted by each EPT[107]. Additionally, in a MA the plasma must eventually move across some closed magnetic lines in order to expand downstream. While ions typically are unmagnetized because of their large mass, electrons must either move along the open magnetic lines present at the edges of the plume or undergo magnetic detachment from the closed ones to reach infinity[64] and create a current-free plume. The failure to do so would eventually cause an electrostatic deceleration of ions and a reduction in the propulsive efficiency of the MA. This causes a design trade-off in the choice of the strength of the magnetic field. In fact, at lower magnetic flux densities the lateral confinement of the plasma decreases, and the propulsive force generated by the diamagnetic electron currents also drops. On the other hand, as the magnetic field is increased, electrons injected on one of the closed magnetic field lines will find it more and more complex to reach infinity, eventually decreasing the propulsive performance.[111], [112]

Although these differences with respect to traditional MNs are important, their investigation and treatment in the literature remains for the moment very limited. As a first approach to understand the physics of a MA, Merino *et al.*[64], [106] explored an expansion in a planar MA (constituted by two infinitely elongated plasma sources) by means of a quasi-neutral, full-fluid approach, that considered perfectly magnetized and polytropic electrons and a single and cold ion fluid. This allowed a first description of the general plasma and propulsive properties of a MA, highlighting the presence of a magnetic drag force in the region where the magnetic lines become perpendicular to the plasma flow, and the consequent importance of detachment in the propulsive performance. Indeed, it was found that a relevant role was played in this direction by the magnetic field induced by the electron currents in the plume, that caused an opening of the magnetic lines and an effective detachment of the plasma from the applied magnetic field. This model, however, also had important restrictive assumptions in the physical description that it offered. First, the ions injected from the two EPT sources, were modeled by means of a single, cold fluid, which, as this work aims to show, misrepresents the complex double-peaked velocity distribution function (VDF) that develops at the intersection between the two plasma beams. Second, collisional events were fully neglected, so electrons were perfectly magnetized (*i.e.* the Hall parameter was infinity). Thus, electrons were forced to remain within the initial magnetic surface and only energetic electrons emitted on open magnetic lines could flow downstream and cancel the ion current to form a current-free plume. A non-trivial point was that conditions imposed at the downstream boundary of the domain had to be compatible with that electron behavior.

The case of a 3D MA, created by two circular plasma sources, has been first simulated by Di Fede[107] and Cescon[113], who have investigated multiple architectures for EPT clusters by means of a Particle in Cell (PIC) approach, highlighting for the case of the MA a strong exchange of electron currents between the magnetically linked EPT sources. With respect to the case of two MNs, this was found to decrease the total electron current reaching infinity, and consequently reduced the total ambipolar potential drop that developed in the plume. Despite the relevance of those works, various open points were left pending. First, collisions were neglected in the principal study cases (marginal collisions were commented in an appendix, having no effect on the solution), thus having electrons fully magnetized, exactly as in Ref. [64]. Second, in order to reduce the computational time, the vacuum permittivity was increased by a factor of 45^2, thus increasing the plasma non-neutrality and inverting the hierarchy of the Debye length with the electron Larmor radius. Some studies have suggested that in the case of magnetized plasmas a strong artificial scaling of the vacuum permittivity, such as the one employed in these works, may alter the plasma response and reduce the reliability of the results.[63], [68]

Finally, a first experimental investigation of a MA was carried out by Boyé *et al.*[114], [115], and proved the feasibility of the concept by detecting the flow of plasma across the closed magnetic lines as well as the theorized reduction of the plume divergence with respect to a MN configuration. This investigation also noted, in accordance with the previous numerical studies[64], [107], a reduction in the ion velocity in the far plume when the MA configuration was employed instead of two distinct MNs.

None of the publications mentioned so far have provided any insight into the effects of testing a MA inside experimental facilities, which in the case of MNs are responsible for relevant differences between the plasma response obtained in a vacuum chamber and in space. These effects are predominantly linked to the larger background pressure of neutral gas found in a testing facility, which can lead to: (i) the modification of the plasma density map and an increase of the plume divergence due to resonant charge exchange (CEX) collisions between ions and neutrals[116], (ii) an increased perceived mass flux due to the entrainment of ionized background neutrals in the plume expansion[35], [117], [118], (iii) a reduction of the ion acceleration due to collisional drag forces[119] and the electron cooling caused by inelastic collisions[35], [117], and (iv) an increased diffusion of electrons across magnetic lines caused by collisional events[33]. Additionally, it has been suggested that the finite extension of the plume expansion permitted in a vacuum chamber, and the presence of conductive facility walls, may alter the map of electron currents[120] and in some cases strongly influence the value of the magnetic thrust provided by a MN[41].

This work aims to investigate the open points identified in the literature with regards to the MA and its application for clusters of EPTs. Namely, we attempt here to further detail the physical processes governing the expansion of a MA plume, with particular attention on the interaction between the distinct plasma beams produced by each EPT, and the transport of plasma downstream across the closed magnetic lines. We then assess the influence of a variation in the magnetic field strength on the expansion properties, as well as facility effects linked to the vacuum chamber size and the collisional processes involving the neutral background population.

For such a parametric study, a physically accurate, but computationally undemanding model was required. The planar version of the in-house, hybrid code EP2PLUS was therefore employed, allowing through the reduced dimensionality fast but meaningful simulations of a planar MA. The hybrid formulation presents three advantages for the present problem. First, the PIC formulation for heavy species constitutes a more adequate approach for ions with respect to the single, cold ion fluid model. Second, the hybrid formulation allows the imposition of quasi-neutrality directly, keeping the Debye length as the smallest length of the plasma and limiting non-neutral effects to the Debye sheaths around surfaces. Third, the electron fluid model offers a computationally-efficient and low-noise way of obtaining electron currents and maps of the electric potential in a weakly collisional regime. Still, a polytropic law is used here for the closure of the fluid equations, meaning that the electron thermodynamics can only be captured through an empirical and approximate relationship with the plasma density. Nevertheless, this simplified description of the electron thermodynamics and the use of a planar study case are well within the scope of this work, that aims to enrich the fundamental understanding of the physical processes and qualitative relationships that govern the plasma properties in a MA.

The 3D version of EP2PLUS has been presented, described, verified and validated in numerous previous publications. Amongst these we point to: Ref. [29] for a general overview of the code and a detailed description of the particle-wise algorithms and collisional operators; to Refs. [121] and [122], respectively, for the derivation and numerical solution of the fluid equations for magnetized electrons; and to Refs. [123] and [124] for examples of the verification and validation of the code. The planar version of EP2PLUS is a trivial mathematical and numerical simplification of the 3D version.

The remainder of this article is structured as follows. The main characteristics of EP2PLUS and the modeling strategy are first explained in Section 3.2. Then the settings of the simulations presented in this work are detailed in Section 3.3, and Section 3.4 describes the results of a reference simulation, employed to showcase the general plasma response when expanding through a MA and the resulting propulsive properties. An analysis of the effect of the magnetic field strength on the plume expansion is then presented in Section 3.5, focusing on how its influence on the electron population translates into variations in the observed propulsive performance. Next, in Section 3.6 we discuss the implications of the choice of boundary conditions (BCs) and domain size on the plume characteristics, examining also the effectiveness of the BCs introduced in Ref. [64] in this more complex simulation scenario. Finally, a simulation case with a more complete description of the neutral population in the plume, and of the collisional processes that it entails, is described and analysed in Section 3.7. A summary of the main conclusions of this work is carried out in Section 3.8.

3.2. Model

EP2PLUS simulates the electrons by means of a weakly-collisional drift-diffusion fluid model, and heavy species through a PIC description. At each time-step of the code, the heavy species and electron modules are solved sequentially, with the former providing fundamental inputs to the latter through the hypotheses of quasi-neutrality and of a current-free plume. The computational loop is then restarted by advancing the heavy particles in the newly obtained electric field. Each module can be configured with several options and alternative models. An overview of their main features are described in the following subsections, while Section 3.3 states which modelling options are used in each of the simulations presented in this work.

3.2.1. Heavy Species Module

At each time-step the heavy species macro-particles are advanced employing a standard series of PIC algorithms. First, macro-particles are injected into the domain from appropriate injection surfaces (see Section 3.3.1.2). Second, a Boris-Cylrad Leapfrog scheme[125] is employed to integrate the particle's equation of motion according to the local electric and magnetic fields, linearly interpolated to the particle's position. Third, boundary effects are evaluated for those particles that have crossed important surfaces (*i.e.* domain boundaries, or material walls). Finally, the macro-particles are weighed to the nodes of the structured mesh, through a linear weighing scheme[126], yielding the densities, fluxes and temperatures of each population. These are then passed as inputs to the Electron Module. The heavy species module can be used to simulate only ions, but may also include neutrals either as a prescribed background map or as PIC macro-particles. Another optional feature of this module is the inclusion of collisional effects on heavy species such as ionization and CEX collisions, evaluated after the particle motion and before their weighting to the mesh nodes. As this option is only used in Section 3.7, the details of the collisional models used are deferred to that point.

3.2.2. Electron Module

For a quasi-neutral plasma, and a quasi-stationary ($\partial/\partial t = 0$), inertialess electron fluid characterised by a diagonal and isotropic pressure tensor, the electric current continuity and the electron momentum equations respectively read

$$\nabla \cdot \mathbf{j} = 0, \tag{3.1}$$

and

$$-\nabla(nT_e) + en\nabla\phi + \mathbf{j}_e \times \mathbf{B} - \mathbf{R}_e = \mathbf{0}. \tag{3.2}$$

Here most of the notation is standard, so that $n = n_i = n_e$ represents the quasi-neutral plasma density, $\mathbf{j} = \mathbf{j}_i + \mathbf{j}_e$ indicates the total electric current density obtained as the sum of the ion and electron currents, and T_e the scalar electron temperature in energy units. Moreover, e is the elementary charge, ϕ the electric potential, $\mathbf{B}$ the applied magnetic field vector and $\mathbf{R}_e$ the collisional force acting on the electron fluid.

For all the simulation cases presented here, the electron fluid equations are closed at the level of the momentum through the polytropic law

$$T_e = T_{e0}\left(\frac{n}{n_0}\right)^{\gamma-1}, \tag{3.3}$$

where both the polytropic coefficient γ and the constants T_{e0} and n_0 are calibrated empirically. Although such an empirical closure represents an important simplification of the electron thermodynamics, multiple experimental[127], [128], [129] and kinetic[63], [130], [131] studies have shown polytropic parameters in the range $\gamma = 1.1 - 1.24$ to qualitatively capture the electron cooling that takes place in the bulk of MNs sufficiently well for the purposes of this work. Indeed, the detailed study of the electron thermodynamics in a MA is out of the scope of this paper, and we simply employ a constant polytropic index $\gamma = 1.2$ in all the simulations presented here. The polytropic law allows the definition of a thermalized potential[132]

$$\Phi = \phi + \frac{\gamma T_{e0}}{e(\gamma-1)}\left[1 - \left(\frac{n}{n_0}\right)^{\gamma-1}\right], \tag{3.4}$$

such that the 'generalized electric force' $en\nabla\Phi$ groups the pressure and electric forces on electrons. Numerically, expressing the momentum equation in terms of the thermalized potential,

$$en\nabla\Phi + \mathbf{j}_e \times \mathbf{B} - \mathbf{R}_e = \mathbf{0}. \tag{3.5}$$

is advantageous as it allows the reduction of numerical cancellation errors[133] between these two counter-acting forces. Incidentally, in the case of a collisionless plasma ($\mathbf{R}_e = 0$), Eq. (3.5) would yield a balance between the magnetic force $\mathbf{j}_e \times \mathbf{B}$ and the generalized electric force $en\nabla\Phi$, so that Φ would be constant along the magnetic lines.[64] Typically, the plasma expansions in MNs and MAs are weakly collisional (*e.g.* in the collisional simulations of Section 3.7 the collisional force is two orders of magnitude smaller than the magnetic and generalized electric forces), so that we here retain the collisional term in Eq. (3.5), although we only expect mild deviations from the collisionless limit just described.

The general model for $\mathbf{R}_e$ implemented in EP2PLUS is

$$\mathbf{R}_e = \sum_{s=1}^{S} \nu_{es} m_e n (\mathbf{u}_e - \mathbf{u}_s) = \frac{B}{\chi}(\mathbf{j}_e + \mathbf{j}_c), \tag{3.6}$$

where m_e is the electron mass, $\mathbf{u}_e = -\mathbf{j}_e/en$ the bulk velocity of the electron fluid, the suffix s is used to discern between quantities relative to the different heavy species present in the simulation (be they modeled as macro-particles or as a fixed background), and ν_{es} is the momentum collision frequency between electrons and the heavy species s. In the second equality of Eq. (3.6) we have also introduced the dimensionless Hall parameter $\chi = eB/(m_e\nu_e)$, with $\nu_e = \sum_s \nu_{es}$ the effective electron momentum collision frequency, and an equivalent current density $\mathbf{j}_c = (en/\nu_e)\sum_s \nu_{es}\mathbf{u}_s$ that groups the collisional effects from the heavy species.

With the definition of these variables, the electron momentum equation can be solved for the total electric current density yielding the generalized Ohm's law[121]

$$\mathbf{j} = -\mathcal{K} \cdot \left(\frac{n}{eB} \nabla \Phi + \frac{\mathbf{j}_c}{\chi} \right) + \mathbf{j}_i. \tag{3.7}$$

Where, if written in a magnetically aligned reference frame $\{\mathbf{1}_\perp, \mathbf{1}_y, \mathbf{1}_\parallel\}$ (with $\mathbf{1}_\parallel = \mathbf{B}/B$, $\mathbf{1}_y$ the versor pointing out of the simulation plane, and $\mathbf{1}_\perp = \mathbf{1}_y \times \mathbf{1}_\parallel$),

$$\mathcal{K} = \frac{\chi}{1+\chi^2} \begin{bmatrix} 1 & -\chi & 0 \\ \chi & 1 & 0 \\ 0 & 0 & 1+\chi^2 \end{bmatrix} \tag{3.8}$$

is the normalized conductivity tensor. Of course, in the practical implementation of the code, this conductivity tensor is appropriately rotated to the employed Cartesian frame $\{\mathbf{1}_x, \mathbf{1}_y, \mathbf{1}_z\}$.

A first option in the electron module is to simplify equations (3.6) and (3.7) by prescribing a map of the Hall parameter χ in the domain, and dropping the negligible effect of $\mathbf{j}_c$ (in the more complete simulation of Section 3.7 we obtain $eBj_c/(\chi n|\nabla\Phi|) = O(10^{-3})$ throughout the domain)[29]. This effectively decouples the collisional effects on the electron fluid from the solution of the heavy species, and affords for cleaner parametric analyses. This option is indeed followed in most of the simulations presented in this work, as described in the next section. Alternatively, one can retain the full collisional model for electrons, and provide the necessary momentum collision frequencies for electron-neutral and electron-ion collisions. This is the approach employed in Section 3.7, using a set of collision frequencies reported there.

Once the appropriate boundary conditions are provided (see Section 3.3.1) the system of Eqs. (3.1) and (3.7) is solved for $\mathbf{j}_e$ and Φ with the staggered Finite Volume scheme presented in Ref. [122]. The new potential map, required to further advance the ion macro-particles, is then retrieved through Eq. (3.4).

3.3. Simulation Setup

As mentioned, the simulations presented in this work are structured so as to reproduce and expand on the problem analyzed in Ref. [64]. A total of seven different simulations have been run, with the following modeling choices and settings:

1. **Reference Simulation (H30):** employed to showcase the general characteristics of the plasma expansion in a MA. It makes use of the simpler version of the model described: neutrals populations and collisional effects on ions are omitted, and the collisional force on electrons is modeled by dropping $\mathbf{j}_c$ and assuming a fixed and uniform map of $\chi = 30$. In fact, we find that it aids the discussion to first analyze the plasma response in this simplified physical scenario, where the complexity of the numerous collisional processes that take place in a plasma plume is reduced.

2. **H3, H10, H150:** These three simulations are used to evaluate the effects of the magnetic field strength on the plasma plume. They employ increasing magnitudes of the magnetic field and the simpler version of the model. From one simulation to the other the fixed and uniform maps of χ are varied proportionally with the variation of the magnetic field.

3. **Big Domain:** used to elucidate the effects of the downstream BCs on the simulation results. It uses exactly the same simulation settings as the case H150, but with a doubled domain size (and cell count) in both dimensions.

4. **In Space:** proposes and alternative set of BCs more suitable for infinite in-space expansions in the case of high electron magnetization. It uses settings identical to the H150 simulation, except for the downstream BCs for electron currents, which are detailed in Section 3.6.

5. **Background Pressure (BGP):** proposes a more accurate study of the collisional effects on the plume structure. This is done by employing the more complex version of the model described: two neutral populations (a prescribed background one and a PIC one) and their collisions with ions are included, and the more general expression of the electron collisional force of Eq. (3.6) is used. The details of the settings for neutrals and collisional events considered in this simulation are provided in Section 3.7.

Table 3.1 summarizes the general simulation settings assumed for each case, along with the uniform values of χ employed in the simulations making use of the simpler version of the model.

The domain investigated in our simulations is defined by a right-handed reference frame with the Cartesian vector basis oriented so that the Oxz plane coincides with the 2D expansion plane, and the Oz axis points downstream. As a result, the Oy axis lies on the out-of-plane direction of the 2D expansion, along which the plasma properties are assumed infinitely uniform. Two plasma sources, emitting along $\mathbf{1}_z$, are located on the Oxy plane and span respectively from $x = -6\,\text{cm}$ to $x = -4\,\text{cm}$ and from $x = 4\,\text{cm}$ to $x = 6\,\text{cm}$, so that Oyz represents the simulations' symmetry plane. The applied magnetic field $\mathbf{B}$ is generated by four infinite electric wires positioned respectively in x = -7, -3, 3, 7 cm, and $z = 0$, each carrying the same electric current I along $\mathbf{1}_y$. The signs of the electric currents flowing along the wires are anti-symmetric about the Oyz plane, so that the total magnetic moment of the system is null, and the magnetic field at the center of each source is B_0. Figure 3.1 shows a sketch of the considered magnetic topology, computed by the analytical superposition of the Biot-Savart laws for each wire, and the simulation domain in the reference simulation H30, which corresponds to half of the physical domain described thanks to symmetry conditions. Note that the strength of the magnetic field, which is varied for some of the simulations of Table 3.1, scales linearly with the current passing through the wires (*e.g.* for $B_0 = 100\,\text{G}$ $I = 500\,\text{A}$, while for $B_0 = 300\,\text{G}$ $I = 1500\,\text{A}$).

Case	B_0 [G]	χ [-]	Domain Size [cm^2]	N. Cells [-]	t_{ss} [μs]	BCs
H3	30	3	25×15	180×300	500	EF[1]
H10	100	10	25×15	180×300	500	EF
H30 (Ref.)	**300**	**30**	**25×15**	**180×300**	**500**	**EF**
H150	1500	150	25×15	180×300	500	EF
Big Domain	1500	150	50×30	360×600	1000	EF
In Space	1500	150	25×15	180×300	500	Sp[2]
BGP	300	Comp[3]	25×15	180×300	900	EF

[1] BCs modeling the expansion in an experimental facility.
[2] BCs modeling the expansion in space.
[3] The hall parameter is computed from the local values of ν_{es}.

Table 3.1: Summary of the simulation cases presented in this work and of their defining characteristics. The t_{ss} column provides the simulation times. Note that for the majority of the simulations collisional effects are modelled in a simplified way by imposing a fixed value of the Hall parameter χ, while in the BGP case χ is self-consistently obtained through collisional algorithms.

Finally, the reference point for the polytropic closure is fixed at the center of the injection surface ($x_0 = 5$ cm, $z_0 = 0$), where we also impose $\Phi = \phi = 0$. The reference plasma density and electron temperature are $n_0 = 10^{18}\text{m}^{-3}$ and $T_{e0} = 5$ eV.

3.3.1. Domain Boundaries

As mentioned, the solution of the electron fluid Eqs. (3.1) and (3.7) requires the imposition of boundary conditions on all of the domain edges. The unknowns of these Eqs. are the thermalized potential (which replaces the more physical but numerically less stable electric potential) and the electron currents. The BCs can therefore be applied either on the value of Φ (Dirichlet conditions) or, more commonly, on the local normal electric current density $j_n = \mathbf{j} \cdot \mathbf{1}_n$ (Neumann conditions), with $\mathbf{1}_n$ the outward versor normal to the boundary.

Additionally, particles crossing any domain boundary must also be correctly treated depending on the boundary type. Figure 3.1 details the type of boundaries employed in this work, and the consequent BCs imposed on the electron fluid and on the the particle populations for the simulation cases H3, H10, H30, H150 and Big Domain are described in the following subsections. The minor deviations that the In Space and BGP simulations undergo with respect to these settings are detailed in their corresponding Sections (respectively 3.6 and 3.7).

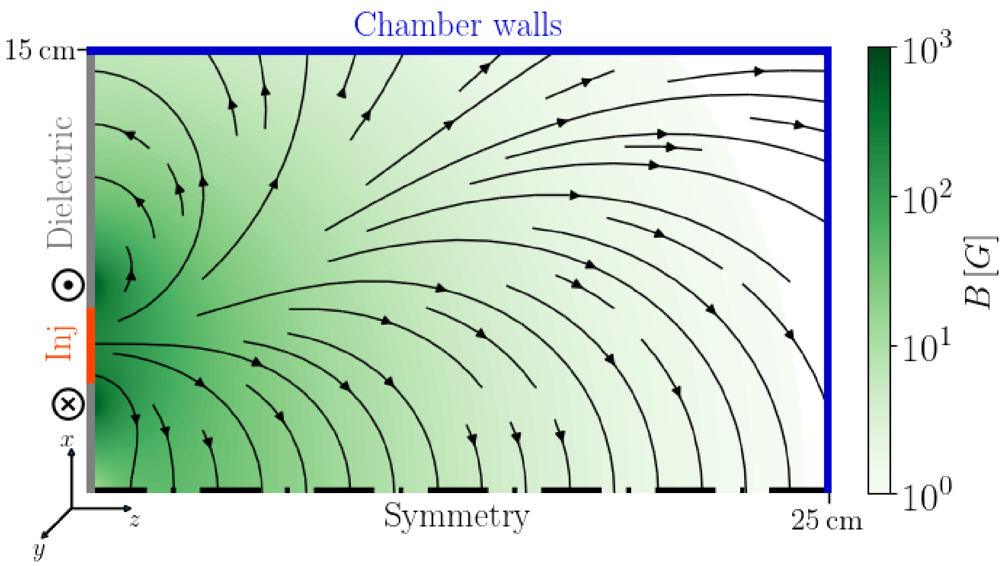

Figure 3.1: Sketch of the reference simulation domain and of the boundary conditions applied for a planar MA. The two counter-streaming current wires and the plasma source are infinite in the y direction. The green color-map and the streamlines display the intensity and direction of the magnetic field for the reference case.

3.3.1.1 Symmetry Boundary

In order to impose symmetry conditions, a null perpendicular current ($j_n = 0$) is imposed as BC for the fluid equations, while all particles crossing such boundaries are specularly reflected. Note that under these conditions $j_{ni} = j_{ne} = 0$, so that Eq. (3.7) yields $\mathbf{1}_n \cdot \nabla\Phi = 0$ as expected on a symmetry plane.

3.3.1.2 Injection Boundary

The plasma injected into the domain by the EPT source is composed of singly charged Xenon ions and electrons. The ion particles are injected by sampling through an acceptance-rejection algorithm[134] the forward portion of a Maxwellian distribution function[29]. The ion Maxwellian VDF is characterized by a Gaussian density profile centered in $x_0 = 5\,\text{cm}$, a uniform temperature profile, and a sonic velocity $c_s = \sqrt{(\gamma T_e + T_i)/m_i}$:

$$n_i(x,0) = n_0\, 10^{-3[(x-x_0)/R]^2}, \tag{3.9}$$

$$\mathbf{u}_i(x,0) = c_s(x,0)\mathbf{1}_z, \tag{3.10}$$

$$T_i(x,0) = 0.1\, eV. \tag{3.11}$$

Note that, with these injection conditions, ions at the center of the injection surface have an average sonic Larmor radius $r_{li} = m_i c_s(x_0,0)/(eB_0) = 1.5\,\text{cm}$, which is expected to rapidly decrease as they accelerate downstream and the magnitude of the magnetic field drops. Taking the half-width of the injection surface ($R = 1\,\text{cm}$) as a characteristic dimension of our problem, ions are only marginally magnetized near the source and rapidly demagnetize as they expand downstream. Finally, any particle returning to the injection surface from inside of the domain is simply removed from the simulation.

Regarding the electron fluid, instead, it is assumed that in the quasi-neutral bulk of the EPT source an equilibrium between the lateral electron pressure and magnetic forces exists (*i.e.* $\partial\phi/\partial x = 0$).[135], [136] This, from Eqs. (3.2) and (3.9), results in a Dirichelet condition to be imposed on the thermalized potential,

$$\Phi(x,0) = \frac{\gamma T_{e0}}{e(\gamma-1)}\left[1 - 10^{-3(\gamma-1)[(x-x_0)/R]^2}\right]. \tag{3.12}$$

Note that, from Eq. (3.4) and in absence of numerical noise, this condition indeed recovers a flat electric potential profile across the injection surface,

$$\phi(x,0) = 0. \tag{3.13}$$

3.3.1.3 Dielectric Boundary

A dielectric condition is imposed along all of the upstream boundary, with the exception of the injection region. Since a neutral particle population is omitted in all simulations except the BGP case, and therefore ion recombination at material walls is not simulated, all particles crossing this surface are removed from the simulation. From the point of view of the electron fluid, a Neumann condition is imposed on Φ by locally requiring that $j_{ne} = -j_{ni}$, with the latter value of the normal ion current obtained from the heavy species module. Incidentally, note that to assure the consistency of our simulations a case in which this upstream boundary was modelled as a floating metallic object was also run, and the simulation results were found to be essentially insensitive to the BCs imposed at this surface.

3.3.1.4 Chamber walls

In the commonly adopted experimental scenario in which the vacuum chamber and the thruster body are electrically decoupled (*i.e.* a floating thruster configuration) a zero net current flowing to the facility walls should be obtained at steady-state. In order to enforce this condition, let ϕ_W be the potential of the metallic chamber, and let us call Q the edge of the Debye sheath that develops between the quasi-neutral boundary of the domain and the chamber walls. The sheath is assumed electron-confining, planar, collisionless, and characterized by an undrifting Maxwellian electron distribution. Then, according to classical sheath theory, the electron current density crossing the sheath is [137]

$$j_{neQ}(\phi_W) = -e\left[n\exp\left(\frac{e(\phi_W-\phi)}{T_e}\right)\sqrt{\frac{T_e}{2\pi m_e}}\right]_Q, \tag{3.14}$$

and imposing that the total electric current collected by the chamber walls is zero one has

$$I_{iW} + \int_{A_{out}} j_{neQ}(\phi_W)dA = 0, \tag{3.15}$$

with I_{iW} the total ion current flowing towards the wall, computed from the heavy species module. Eq. (3.15) is implicit for the wall potential ϕ_W, and is therefore solved with an iterative Newton-Raphson scheme at each time-step. Once ϕ_W is known, Eq. (3.14) provides the electron current density to be imposed as BC in the electron module.

Regarding the heavy species, all particles crossing these boundaries are removed from the simulation, analogously to what is done in the case of the dielectric boundaries.

3.3.2. Numerical settings

The domain of the reference simulation is shown in Figure 3.1. This domain is discretized by means of a uniform mesh composed of cells of dimensions $\Delta x = \Delta z = 0.8\overline{3}$ mm. To guarantee the stability of the model the simulation time-step is required to respect a CFL-like condition $\Delta t < \Delta z/(5c_s(x_0, 0))$.[126] Where a safety factor 5 has been considered to ensure the global compliance to the constraint. Regarding the weight of the ion macro-particles, a population control algorithm[29] was used to guarantee the presence of at least $N_{mp,min} = 10$ ion macro-particles per cell in the less dense regions of the domain (meaning that more that 100 macro-particles per cell are present in the denser parts of the plume), leading at the end of the reference simulation to more than 2×10^6 ion macro-particles in the simulation domain. The steady-state condition of all simulations was confirmed by verifying that both the number of macro-particles in the domain, and the value of the vacuum chamber potential ϕ_W varied by less than 1% over the last 700 steps. A convergence analysis was performed on all numerical parameters discussed here (*e.g.* cell size, particle number, time-step, and simulation length), and no appreciable changes were observed in the simulations by refining them beyond these values. The most relevant simulation settings, shared among all simulations in this work, are summarized in Table 3.2. For specific settings, refer to Table 3.1.

Parameter	Value	Parameter	Value
Δx	$0.8\overline{3}$ mm	Δz	$0.8\overline{3}$ mm
Δt	7×10^{-2} μs	$N_{mp,min}$	10
T_{e0}	5 eV	γ	1.2

Table 3.2: Summary of the most relevant numerical settings shared by all simulation cases.

3.4. Reference Simulation

The panels of Figure 3.2 show the steady-state maps for the reference simulation case (H30) of the thermalized potential Φ, electric potential ϕ, plasma density n and in-plane

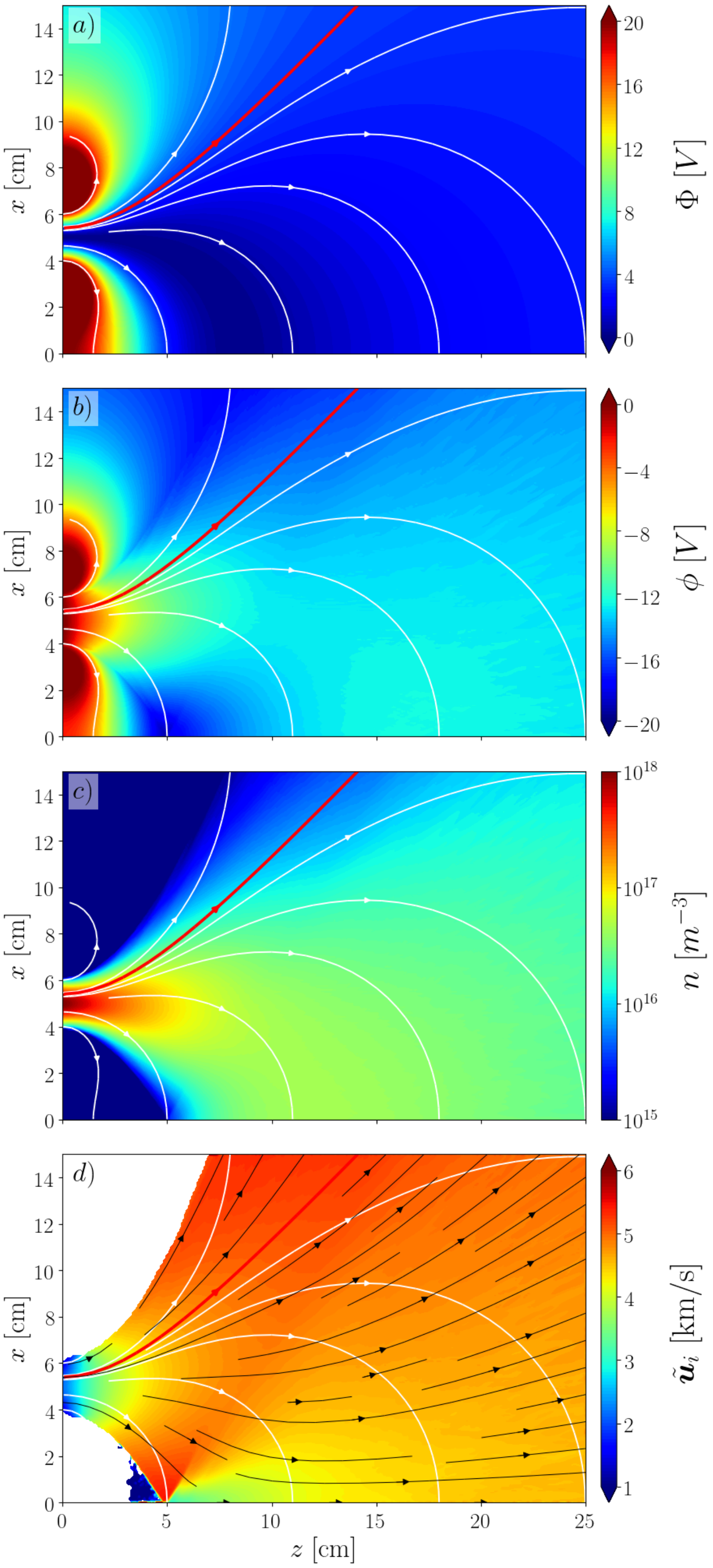

Figure 3.2: Plasma properties for the reference case ($\chi = 30$). The magnetic field lines are shown in white, with the outermost ones corresponding to the lines intersecting the extremities of the injection surface, while the magnetic separatrix is highlighted in red. Note that, for visualization purposes, all plots are saturated at the extremities of their color-maps.

ion velocity $\tilde{\mathbf{u}}_i = \mathbf{u}_i - u_{yi}\mathbf{1}_y$ (with $u_{yi} = \mathbf{u}_i \cdot \mathbf{1}_y$, note that hereafter we will employ a tilde to indicate vectors thus projected on the simulation plane). To aid with the ensuing discussion, Figure 3.3 also displays the profiles of Φ, ϕ and n along the symmetry boundary of the simulation ($x = 0$) and the axis $x = 5$ cm of one of the injection surfaces. Figure 3.4, instead, presents the same plasma properties at axial sections $z = 0$, 10, and 20 cm. The curves corresponding to the reference simulation analyzed here are shown in green in the two latter plots. Incidentally, through the polytropic closure, the electron temperature is simply proportional to the plasma density and is therefore not shown in these figures; for completeness, however, we note that it ranges approximately from 5 eV at injection to 2.5 eV at the downstream boundary. The analysis of the steady-state properties of a strongly magnetized plasma expansion ($\chi \gtrsim 10$) is most easily tackled by starting from the map of the thermalized potential. As mentioned, in fact, Eq. (3.5) shows that for weakly collisional plasmas the thermalized potential Φ remains roughly constant along the magnetic lines. This can be ascertained by observing the magnetic lines overlain in white in Figure 3.2(a). As a consequence, in this regime, the value of Φ in the domain is mostly dependent on the chosen boundary conditions, and is decoupled from the remaining plasma properties. The inverted Gaussian profile of Φ imposed at the injection surface through Eq.(3.12) [see Figure 3.4(a)] is in fact mapped over the whole simulation domain by following the magnetic field lines, forming the curved valley observed in the 2D profile of Φ. A given profile of the thermalised potential imposes a strict relationship between the electric potential and the ion density through Eq. (3.4), which together with the ions' equation of motion determines the maps of ϕ, n and $\tilde{\mathbf{u}}_i$.

The two lobes of high electric potential at the edges of the injection surface in Figure 3.2(b), together with the sharp axial decrease immediately in front of it [see also Figure 3.3(d)] force ions to initially accelerate axially, following the magnetized electron fluid. As the magnetic lines begin to diverge, however, so does the plasma beam, although the large inertia of ions allows a slight diffusion of the plasma density across the field lines [see Figure 3.2(c)]. This is evidenced by the relative angles between the velocity streamlines and the magnetic lines in Figure 3.2(d). The strong initial axial acceleration combined with the outward curving of the magnetic lines, in fact, causes ions to detach inwards as they advance downstream.[101] This portion of the domain is the *near-plume*, in which the two ion beams proceeding from the distinct plasma sources are yet to interact, and the expansion in front of each EPT is independent of the other. As a consequence, the plume's behaviour here is analogous to the one observed for a traditional MN, which is typically characterized by an inward ion detachment and a strong axial drop in the plasma density and electric potential[71] (see Figure 3.3, second column).

Starting from $z \approx 6$ cm, however, the ion beam begins to merge at the symmetry plane with the one emitted from the specular source (here represented by macro particles reflected at $x = 0$). As a result the ion density, along with the thermalized and electric potential, rises when moving downstream along the symmetry axis (see Figure 3.3, first column). In the lateral direction, on the other hand, these quantities still display two

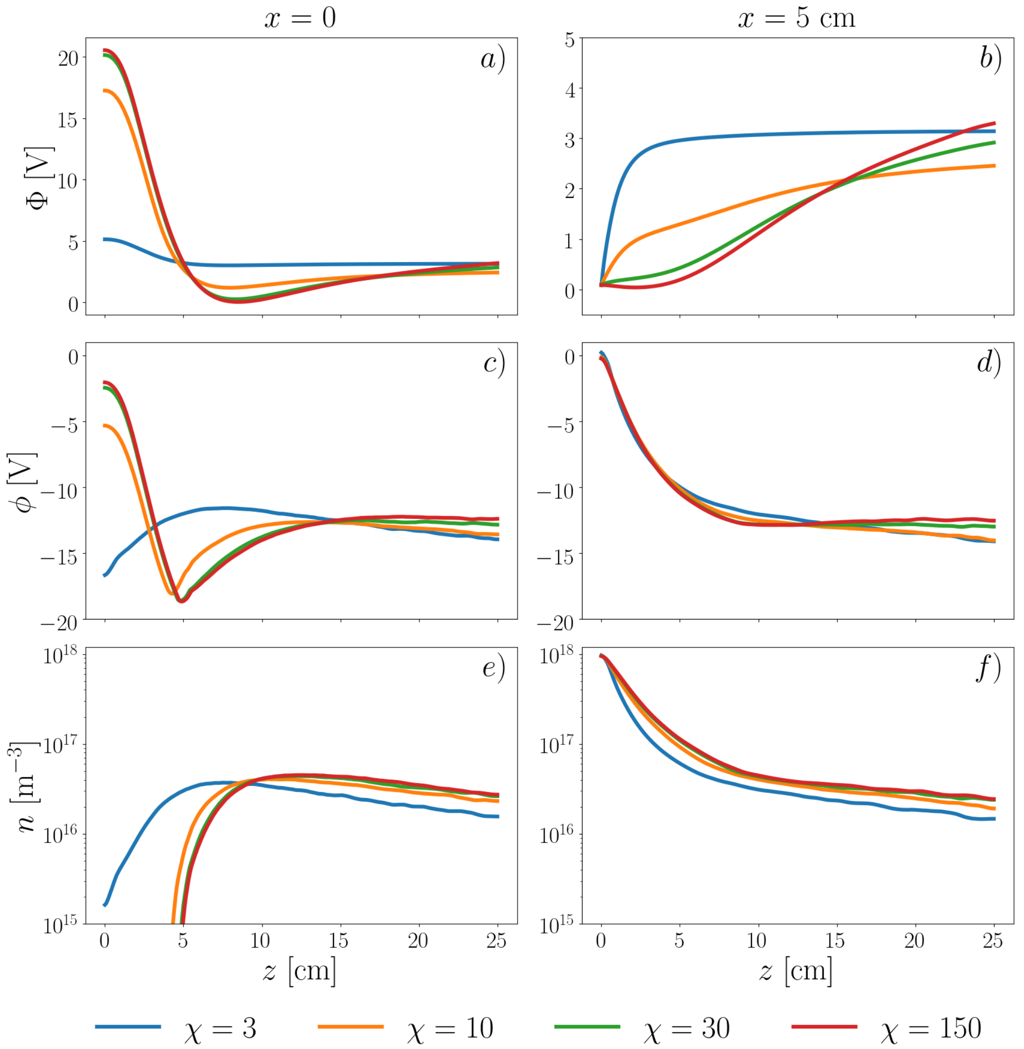

Figure 3.3: Comparison of the axial profiles of Φ, ϕ, and n for all simulation cases. The first column shows the plasma properties along the symmetry plane, the second along the axis of the plasma source. Note the changes in scales in the vertical axes of the plots of the thermalized potential.

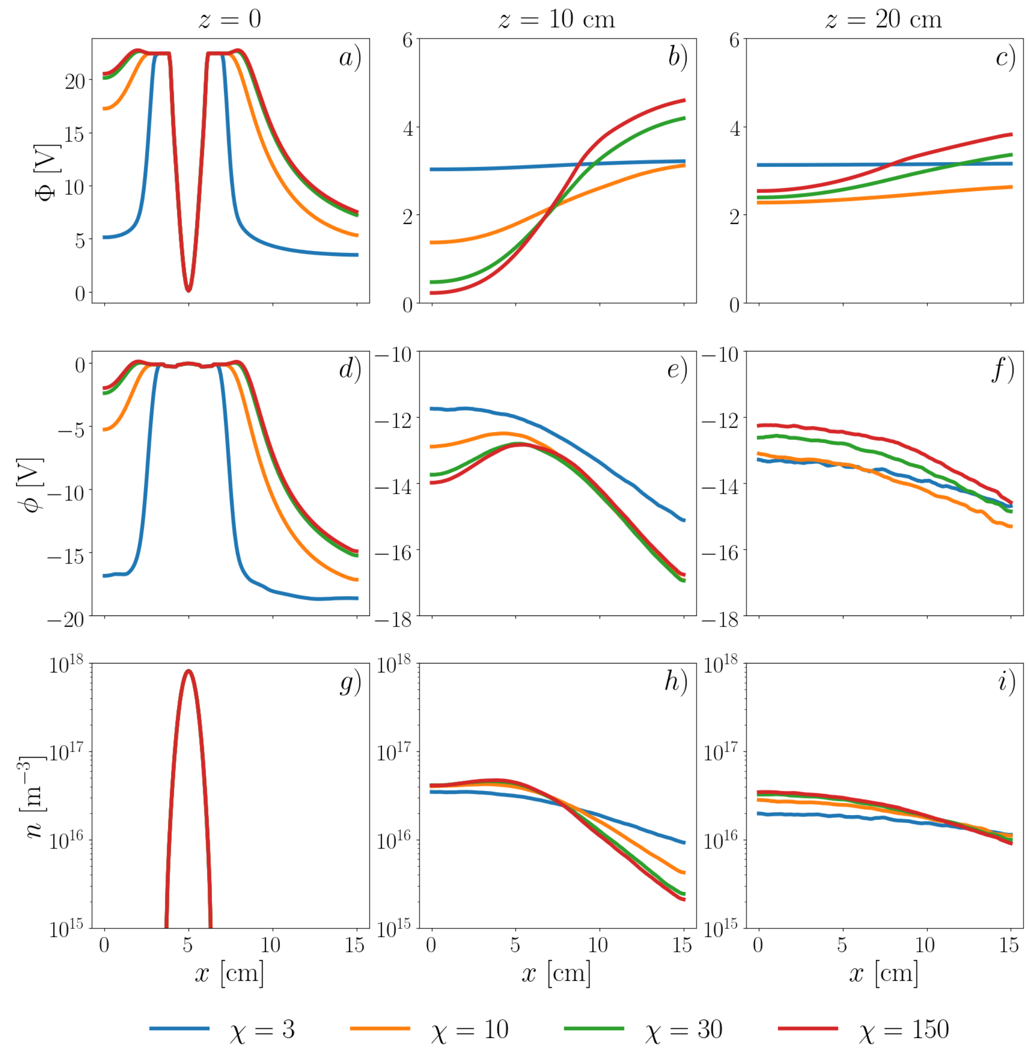

Figure 3.4: Comparison of the lateral profiles of Φ, ϕ, and n for all simulation cases at $z = 0$, 10, and 20 cm. Note the changes in the scales of the vertical axes between the first column of plots and the other two.

local maxima (see Figure 3.4, second column, and consider the presence of a symmetry plane in $x = 0$), indicating that the coalescence of the beams is yet under way. The plume's behaviour thus drifts away from the one of a MN, signaling the entrance into the *transition-region*. Here, the magnetic lines begin to curve back towards the symmetry plane to close into the specular EPT source, and Figure 3.2(d) shows that the majority of ion streamlines are now forced to cross the magnetic lines with a negative detachment angle $\alpha = \angle(\tilde{\mathbf{u}}_i, \tilde{\mathbf{B}})$ (*i.e.* the angle between the ion velocity and the magnetic field vector) in order to continue their axial motion downstream. Nevertheless, a region with positive detachment angles persists beyond the magnetic separatrix [shown in red in Figure 3.2(d)], which divides open and closed field lines in the top left portion of the domain.

As the ion beams begin to merge at $z \approx 6$ cm, the lateral velocity of the total ion population reduces to zero near the lower edge of the simulation domain. This results in the sharp drop observed in Figure 3.2(d) in the magnitude of the ion velocity and the swift axial swerve of their streamlines around $x = 0$, $z \approx 6$ cm. Note that, conversely to what is observed in traditional MN geometries or unmagnetized plumes, the axial potential profile from this point downstream increases rather than dropping, as highlighted by Figure 3.3(c). Consequently, the ions moving downstream along the symmetry axis experience a slight deceleration. This is caused by two concurring effects. The first is the closed magnetic topology of the MA, characterized by magnetic lines orthogonal to the axial direction in the proximity of the symmetry plane, which have the effect of reducing the axial mobility of electrons. To maintain quasi-neutrality, therefore, the axial force acting on ions must also decrease. The second is the symmetrical geometry, which causes a rise in the plasma density where the ion beams meet [see Figure 3.3(e)]. Under the polytropic assumption this also implies an additional confining contribution of the pressure forces acting on the electron fluid, which must again be balanced by the electric field. Mathematically this effect is obtained by the inversion and axial derivation of Eq. (3.4) to yield the axial electric field

$$E_z = -\frac{\partial \Phi}{\partial z} - \gamma \frac{T_{e0}}{e n_0} \left(\frac{n}{n_0} \right)^{\gamma - 2} \frac{\partial n}{\partial z}. \tag{3.16}$$

While in most conventional plumes the second term in this equation provides a positive contribution as the plasma expands, in this case it can have a negative effect due to the increase in density observed along the symmetry plane. Likewise, the axial profile of the thermalized potential displays an initial sharp drop followed by a gradual axial increase due to the mapping of the injection BCs to the points of the symmetry plane [refer to Figure 3.3(a)]. It is this later, gradual rise in Φ that, together with the corresponding increase in the plasma density, causes negative values of E_z and a deceleration of the ion population. It is interesting that, although at the outer edges of the plume the ions continue to accelerate downstream, the effect just described acts on the denser portion of the plasma bulk and on the axial component of the ion momentum, and therefore has, as will be seen later, a negative impact on the provided thrust.

Starting from the local maximum in the plasma density along the symmetry plane (at $x = 0$, $z \approx 12.5\,cm$) the two plasma beams can be considered fully merged into a unique *far-plume*, and all properties present a single maximum in the profiles along x (see the right-most panels of Figure 3.4). At the outer edges of the plume the ion streamlines continue to diffuse with a positive detachment angle across the field lines, similarly to what happens in a MN. At the center, instead, the magnetic lines become roughly parallel to the x axis, forcing the ions to cross them orthogonally in order to expand downstream. Soon, however, the electric forces acting on the ions become small enough to be neglected, and their streamlines gradually straighten.

The general plasma response in a planar MA detailed here provides results in qualitative accordance with the study of a 3D MA carried out in Ref. [107]: in both works one may identify the local minimum at the symmetry plane of the electric potential in the *near-plume*, the plateau in the ion velocity in the *transition-region*, and the complete merging of the plasma beams in the *far-plume*. Nevertheless the different dimensionality of the problem (together with the other distinctions in the models employed) causes some quantitative discrepancies between the two configurations. At an axial distance $z/R \approx 25$, in fact, the plasma density has dropped roughly by a factor 10^2 in the present planar case and 10^3 in the 3D case. Similarly, the potential drop from the injection surface at $z/R \approx 25$ is $e\Delta\phi/T_{e0} \approx 2.5$ for the planar MA and $e\Delta\phi/T_{e0} \approx 4$ in the 3D one. Interestingly, though, the total potential difference between the thruster and the vacuum chamber walls does not display marked differences between the two cases, with the planar case yielding $e\phi_W/T_{e0} = -4.56$ while the 3D simulations give $e\phi_W/T_{e0} = -5.1$. The total potential drop that develops in the plume, in fact, does not depend on the dimensionality of the expansion, but rather on the confining energy required to control the outflow of electrons and impose a current-free plume. As a consequence, ϕ_W depends strongly on the gradual cooling of electrons, here modeled with a polytropic parameter $\gamma = 1.2$ in good accordance with the electron thermodynamics observed in Ref. [107].

The differentiation of the thermalized potential map allows, through Eq. (3.7), the retrieval of the out-of-plane and in-plane electron current densities ($j_{ye} = \mathbf{j}_e \cdot \mathbf{1}_y$ and $\tilde{\jmath}_e = \mathbf{j}_e - j_{ye}\mathbf{1}_y$ respectively). These are displayed in Figure 3.5, together with the in-plane total current density $\tilde{\jmath} = \tilde{\jmath}_i + \tilde{\jmath}_e$. Note that, considering the conductivity matrix written in a magnetically aligned reference frame in Eq. (3.8), and keeping in mind that all out-of-plane gradients are null, the out-of-plane currents are a factor χ larger than the in-plane ones. This is confirmed when comparing the scales of panels (a) and (b). Indeed, the first panel displays a large diamagnetic loop of electron currents (exiting the simulation plane in the bottom, red part of the plot, and entering it in the upper, blue portion), which, because of the negligible ion velocities in the out-of-plane direction, can be considered equal to the total out-of-plane current density $j_y \simeq j_{ye}$. Note that the curvature of the axis of the diamagnetic current loop (*i.e.* the line $j_{ye} = 0$), turns towards the symmetry plane so that it is always aligned with the externally imposed magnetic field. This generates the in-plane magnetic forces which are fundamental for the lateral confinement of the plasma plume and, as will be discussed shortly, for the propulsive performance of a MA.

Figure 3.5(b), on the other hand, shows clearly that the value of the Hall parameter

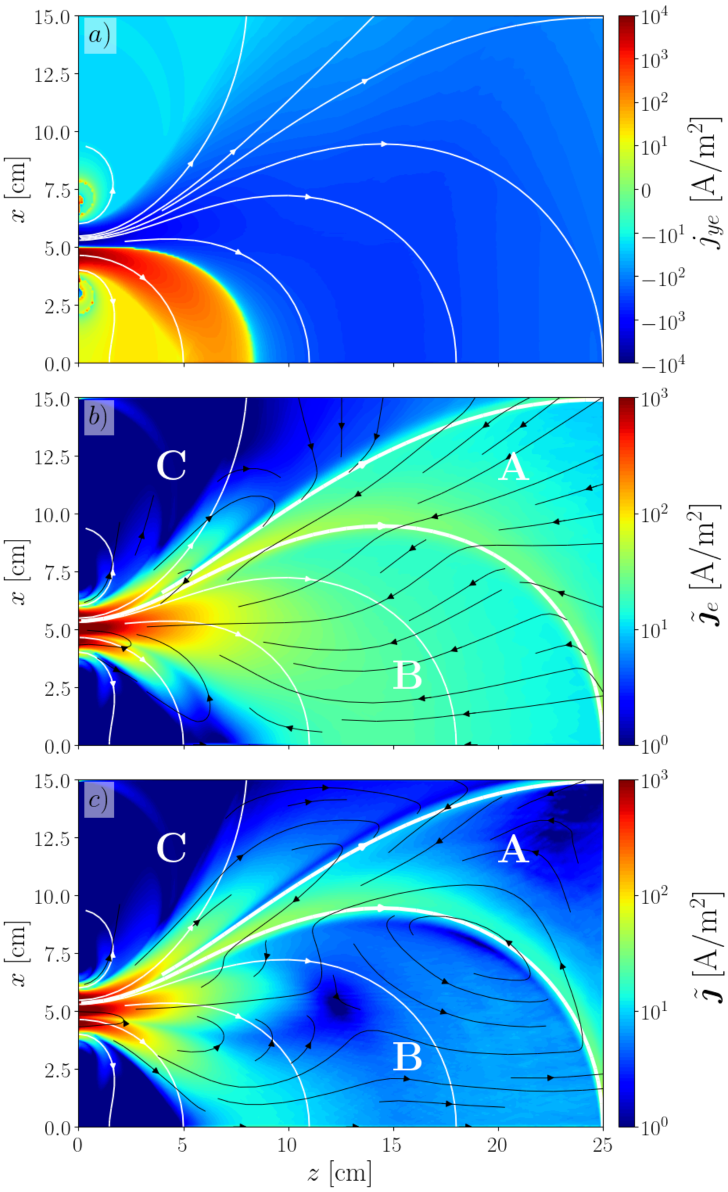

Figure 3.5: The out-of-plane electron currents (panel (a)), and the in-plane electron and total currents (panels (b) and (c)) for the reference case (χ = 30).

$\chi = 30$ considered here is insufficient to force the electron current to precisely follow the magnetic lines. Indeed, numerous electron streamlines form large angles with the magnetic field in order to reach the downstream domain boundary. Nevertheless, the effects of magnetization may be appreciated by noting that the magnetic lines that lead to the domain corners (highlighted in the plots by the thicker white lines) carry larger current values with respect to the ones found in their surroundings (*e.g.* consider the higher current intensity surrounding the magnetic line to the bottom-right domain corner). This is due to the larger mobility of electrons moving along magnetic lines rather than across them, and to the presence of the symmetry plane, that imposes a null outflow of currents through the bottom domain boundary. As a consequence, slightly reduced values of the electron currents are observed in the inner region of the MA, between the magnetic line to the bottom corner and the symmetry plane (labeled Region B in the plot), where electrons must diffuse across the magnetic field to leave the domain through the downstream boundary. The flow of electron currents is instead freer in the portion of the domain found between the two field lines to the domain corners (Region A), where electrons can run along the magnetic lines to reach the downstream boundary. This effect is even more prominent in the plot of the total current density. The total currents in Region A, in fact, flow mostly upstream, while in the rest of the simulation domain (Regions B and C) the total currents tend to flow downstream. Indeed, the increased mobility of electrons flowing parallel to the magnetic lines in Region A has the effect of imperceptibly increasing the electron flux inside it, and causes the upstreaming total currents observed there. In Regions B and C, on the other hand, the electron mobility along z is reduced by the magnetic field mainly directed along x, so that the electron current drops below the magnitude of the ion current –unaffected by the magnetic field and therefore flowing straight in the axial direction– and forms a region of downstreaming total current.

As mentioned, the out-of-plane diamagnetic currents ultimately provide the magnetic force crucial for the propulsive performance of magnetic nozzles. Indeed, the accumulated axial magnetic thrust (per unit of y-length) generated in a control area Ω by a planar MA is

$$F_m(z) = -\int_{\Omega} j_y B_x \, d\Omega. \tag{3.17}$$

Taking advantage of the domain symmetry to consider also the plume in front of the second EPT (*i.e.* located at $x < 0$ and not represented in the plots), $\Omega(z)$ is defined as the rectangular region spanning from $x = -15\,\text{cm}$ to $x = 15\,\text{cm}$ and from $z = 0$ to a given z coordinate. Figure 3.6(a) plots the accumulated magnetic thrust thus computed, expressed as a fraction of the total plasma momentum flux across the injection surfaces ($F_0 = 2\int_{x_0-R}^{x_0+R} n(x,0)\left[T_e(x,0) + m_i u_{zi}^2(x,0)\right] dx = 12.5\,\text{mN/m}$). Once again the results obtained for the reference case described here are shown in green. The magnetic propulsive force displays an initial sharp rise, corresponding to the first portion of the plume where the intensity of j_{ye} is largest. As the field lines bend towards the symmetry plane, however, the total magnetic thrust provided drops slightly, showcasing a region of negative axial magnetic force $j_y B_x$ (*i.e.* magnetic drag), and the resistance of the magnetic field to the axial expansion of the plasma plume. This is a natural consequence of the closed topology of a MA, and is also highlighted by the deceleration of the ion population close to the symmetry axis discussed above. Indeed the axial coordinate at which we observed the decrease in the ion velocity corresponds roughly to the one of the maximum cumulative magnetic thrust. These observations highlight the necessity of plasma detachment in the far plume of a MA, to avoid the null total magnetic thrust that would ensue from a perfect plasma magnetization and the continuous decrease of the accumulated thrust beyond $z = 6\,\text{cm}$. Finally, note that the computed magnetic thrust displays small gradients a the downstream domain boundary ($z = 25\,\text{cm}$), indicating that the domain dimension is adequate for the discussion of the propulsive properties of this MA, and that the regions beyond the domain boundaries only provide marginal contributions to the total value of F_m.

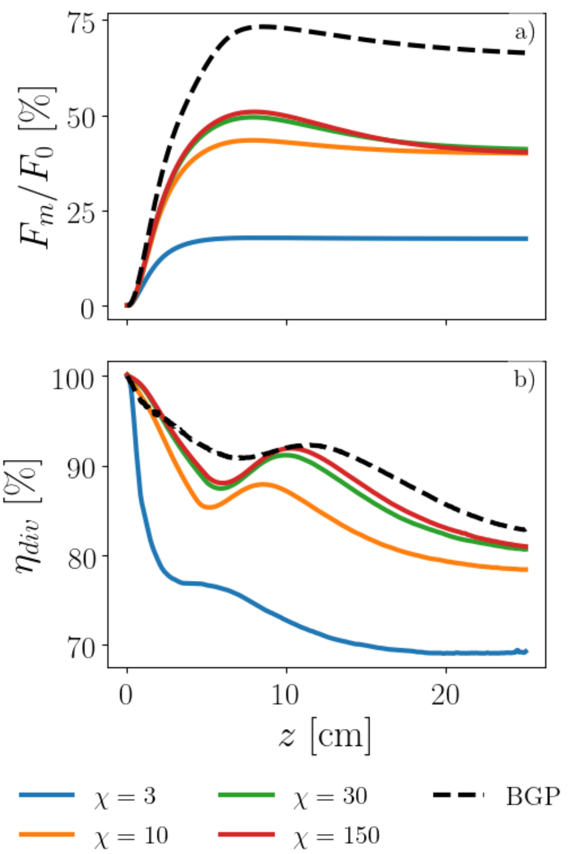

Figure 3.6: Comparison of the accumulated axial magnetic thrust and divergence efficiency for all simulation cases. The magnetic thrust is expressed as a percentage of the total plasma momentum flux through the exhaust of the two EPT sources. For all simulations except the BGP case $F_0 = 12.5\,\text{mN/m}$. For this latter one $F_0 = 5.26\,\text{mN/m}$.

Figure 3.6(b), instead, displays the divergence efficiency,

$$\eta_{div}(z) = \frac{\dot{E}_{kin,z}(z)}{\dot{E}_{kin}(z)}, \tag{3.18}$$

computed as the ratio between the flux of axial ($\dot{E}_{kin,z}$) and total ($\dot{E}_{kin}$) kinetic energy through the lateral and downstream boundaries of the control area $\Omega(z)$. Here the subdivision in *near-plume*, *transition region* and *far-plume* is evident once again. The divergence efficiency in fact decreases in the *near-plume*, analogously to what happens in a MN because of the portion of lateral acceleration that ions are subjected to. However, in the *transition region*, η_{div} rises again because of the symmetry conditions that cause an increase of the ion density close to the symmetry plane, where their bulk velocity becomes essentially axial. Finally, once in the *far-plume*, the merging of the ion beams has fully taken place, and their lateral expansion causes once more a decrease of η_{div}.

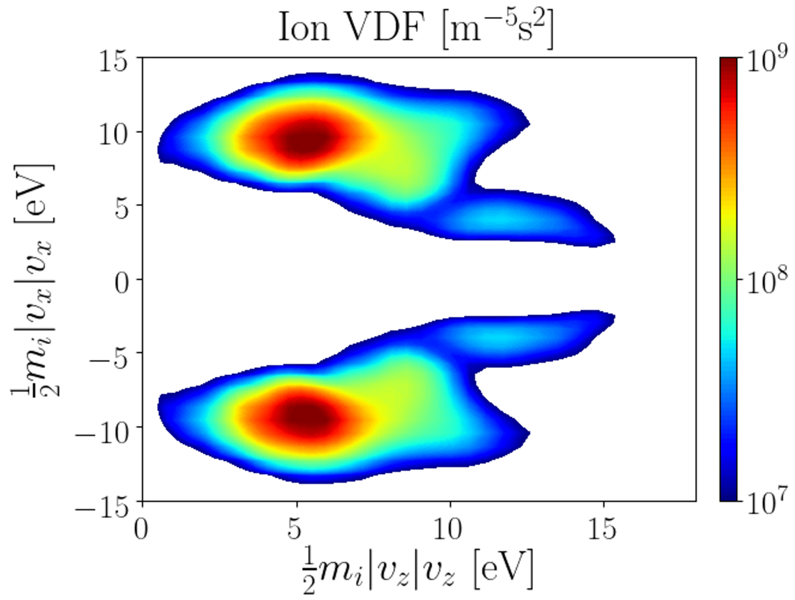

Figure 3.7: Histogram of the ion VDF at $x = 0$ and $z = 6$ cm for the reference simulation, obtained by discretizing the in-plane phase-space in 60×60 velocity bins, and averaging the ion macro-particle count in these bins over 600 simulation time-steps.

It is important to mention that the results obtained in Ref. [64] for a simulation case analogous to the one presented here displayed in all ion properties a shock-like structure that propagated from the symmetry plane. The main difference between that work and the present one is, indeed, the model adopted for the ion population, which is here described through the PIC approach as opposed to the single fluid formulation employed there. By simulating the ions with a kinetic approach, the formation of a double-peaked ion VDF is observed in the region close to the symmetry plane, where the two ion beamlets deriving from the distinct plasma sources merge. Each peak of the VDF represents the ions pertaining to one of the two sources. Indeed, Figure 3.7 displays the histogram of the ion VDF (*i.e.* the number of particles per unit volume and area of phase-space) measured at $x = 0$, $z = 6$ cm, which presents two marked and symmetrical peaks at energies corresponding roughly to the potential drop that develops between the injection surface and the considered location $\Delta\phi \approx 20$ V. Although, taken individually, each ion beam only has a temperature of 0.25 eV and can be roughly considered to be monoenergetic, their coalescence results in a VDF with a spread in velocities corresponding to a temperature $T_i \approx 5\,\mathrm{eV}$. Such a distribution cannot be represented with a single and cold ion fluid as done in Ref. [64], causing the shock-like artifact observed in that work.

3.5. Effect of the Magnetic Field Strength

Having presented and analysed the general properties of a plasma expanding through the magnetic topology of a MA, we now investigate how this response is influenced by the strength of the applied magnetic field. We therefore consider three additional cases (H3, H10, and H150), identical to the reference one except for the intensity of the magnetic field map, which is modulated to yield $B_0 = 30, 100$, and $1500\,G$ at the center of the injection surface. Under the assumption that the electron collisionality remains unvaried between simulations, the uniform map of the Hall parameter is also proportionally scaled to $\chi = 3, 10$, and 150. Figures 3.3 and 3.4, along with Figure 3.6, already displayed the axial and lateral profiles of the plasma properties and magnetic thrust obtained for these new values of χ. It becomes immediately evident that the cases with $\chi = 10, 30$ and $\chi = 150$ yield very similar results, and the Hall parameter has to be decreased to $\chi = 3$ for relevant changes to develop. In fact, the value of χ affects the employed electron model only through the conductivity tensor introduced in Eq. (3.7). As the Hall parameter increases, the conductivity tensor has the effect of decoupling the electron currents perpendicular to the magnetic field from the gradients of Φ through a factor $1/(\chi^2+1)$. This essentially inhibits the diffusion of electrons perpendicular to the magnetic field, and confines their motion along the magnetic lines, impeding the lateral expansion of the plume under the effect of the electron pressure gradients. The magnitudes of $\tilde{j}_e$, however, are delimited throughout the domain by the BCs employed and the continuity equation. As a consequence, because of the large values of the parallel conductivity $\sigma_e = \chi n/(eB)$ that characterize the weakly collisional plasma typical of a MA, the parallel gradients of Φ must be negligible in order to produce finite electron currents along the magnetic lines. As we approach the case of perfect magnetization and an infinite Hall parameter, then, the thermalized potential must remain constant along the magnetic lines, so that its map in the domain will only depend on the values imposed at the injection surface and on the magnetic topology[71]. As a consequence, when $\chi > 10$ changes in the Hall parameter will only cause small variations in the map of Φ, and in the general plasma response. Keeping this in mind, and for the sake of conciseness, the present section employs mainly the comparison between the cases with $\chi = 3$ and $\chi = 150$ to showcase the effects linked to variations in the electron magnetization.

Figure 3.8 compares the general plasma properties obtained for these two cases. The first thing that jumps to the eye is the noticeable differences between the maps of the thermalized potential. As for the reference case, in the case $\chi = 150$ the profile of Φ imposed at the injection surface remains practically constant along the magnetic field lines, and is mapped over the domain by following them. On the other hand, when $\chi = 3$ the electron currents may move more freely across the magnetic lines (allowing larger

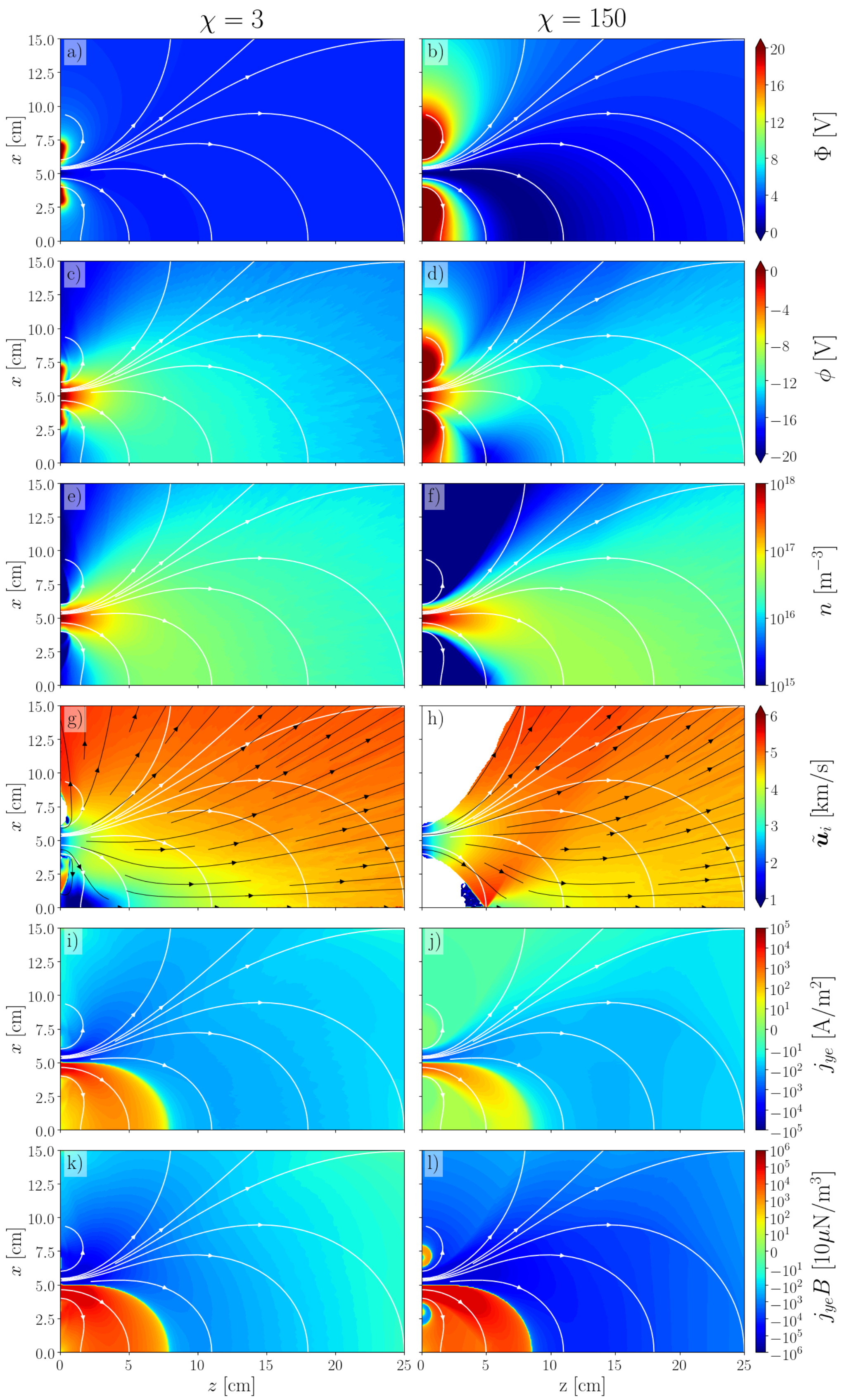

Figure 3.8: Comparison of the main plasma properties for χ = 3 and χ = 150.

currents to form in the domain) and close at domain boundaries which are instead shielded by the magnetic field for $\chi = 150$. Steeper gradients of Φ can therefore form along the magnetic lines, and the inverted Gaussian profile of Φ imposed at injection through Eq. (3.12) gradually dissipates along the domain [see Figures 3.3(b) and 3.4(b)]. This parallel smoothing of the gradients of Φ also allows a reduction of the cross field gradients of the thermalized potential, so that the map of Φ in the far plume is nearly uniform and flat.

The first effect that the larger cross-field mobility of electrons obtained for $\chi = 3$ has on the map of ϕ is the relevant reduction of the two lobes of high electric potential at the edges of the injection boundary, caused by the decay of the lateral gradients of Φ. These lobes, as already commented in Section 3.4, had the effect of laterally confining the ion beam in order to follow the magnetized electron fluid. As a result, both the maps of the plasma density and ion velocity depict a less dense and more divergent plume for the case with $\chi = 3$ than with $\chi = 150$. The potential rise that was observed in the reference case after the merging of the ion beams is also present and enhanced for $\chi = 150$, but is instead shifted upstream and flattened out when lowering the Hall parameter to 3 (see Figure 3.3, first column). In fact, although the axial increase in density along the symmetry plane is still present in both simulations, it moves upstream for the less magnetized and focused plume. Moreover, the axial rise in the thermalized potential observed in the more magnetized cases from $z = 8$ cm downstream, and which contributed to the negative axial electric field in this region of the domain, is absent for the case with $\chi = 3$ because of the smoothing of the map of Φ obtained at low magnetic fields. Observing the map of the ion velocity, this results in a monotonic axial acceleration of ions along the symmetry axis of the domain for $\chi = 3$, and a more complex profile for $\chi = 150$. In this latter case, in fact, ions are strongly accelerated by the sharp potential drop present just in front of the plasma injection, but are then mildly slowed down close to the symmetry plane [note the axial potential rise after $z = 6$ cm in Figure 3.3(c)]. The result is that at the downstream boundary of the domain ions have roughly reached the same outflow velocity for both cases, and noticeable variations in the ion velocity are only observed at the upper simulation boundary.

The last panels of Figure 3.8 show the out-of-plane electron currents, and the corresponding magnetic force density $j_{ye}B$ directed perpendicularly to the magnetic field (here positive or negative respectively if aligned or opposed to $\mathbf{1}_\perp$) and responsible for the magnetic thrust and the lateral confinement of the plume. It is interesting to note here that the magnitude of j_{ye} displays a non-monotonic variation as the strength of the magnetic field increases. Between $\chi = 3$ and $\chi \approx 10$, in fact, the plume undergoes a noticeable magnetic focusing under the effect of the rising magnetic force, reducing the lateral expansion and increasing the density in the plume bulk. This larger density and the smaller divergence of the plume [compare the $\chi = 3$ and $\chi = 10$ lines in Figure 3.3(f) and 3.4(h)] are responsible for the increase in the magnitude of j_{ye} observed between Figure 3.8(i) and Figure 3.5(a). As the strength of the magnetic field further increases (*i.e.* $\chi > 10$), however, the plume does not display further relevant focusing, as shown by the density plots in the last rows of Figures (3.3) and (3.4). The confining magnetic force $j_{ye}B$ necessary to balance the expanding action of the electron pressure [shown in Figure 3.8(k) and (l)] is therefore roughly constant for $\chi > 10$, and can be obtained with smaller out-of-plane currents as B increases. The magnitude of j_{ye} is therefore observed to decrease as χ moves from 30 to 150 [see Figures 3.5(a) and 3.8(j)].

Nevertheless, because of the higher plasma densities found at the symmetry plane for larger values of χ, the propulsive performance of the MA is expected to increase as the strength of the magnetic field rises. Figure 3.6(a), in fact, shows a noticeable improvement in the magnetic thrust when moving from the mildly magnetized case ($\chi = 3$) to higher magnetizations. Note however, that the imparted magnetic force does not scale proportionately with the strength of the magnetic field, and that it appears that already at $\chi = 10$ the maximum magnetic thrust of this MA has almost been reached. A similar scaling of the magnetic thrust with the magnetic field was obtained by Andrews *et al.* in the PIC simulations of a traditional MN[63]. The trade off between the strength of the magnetic field forming the MA, and the thrust obtained from the thruster under design should therefore take into account the non-linear dependence between these two values.

Interestingly, the initial slope of all the thrust curves in Figure 3.6(a) is identical. This is caused by the BCs applied at the injection surface, as demonstrated by retrieving the axial derivative of F_m by inserting the expression for j_y obtained from Eq. (3.7) into Eq. (3.17):

$$\left.\frac{dF_m}{dz}\right|_{z=0} \approx -\int_0^{L_x} \frac{B_x}{B}\frac{\chi^2}{(1+\chi^2)} en_0 \frac{d\Phi(x,0)}{dx}\, dx, \tag{3.19}$$

which yields approximately the same value for $\chi >> 1$.

The trends of the magnetic thrust with χ are further confirmed by taking into account the plot of the divergence efficiency. Figure 3.6(b), in fact, shows how η_{div} increases under the effect of a stronger magnetic confinement. In the case of a higher χ, in fact, the plasma density is higher close to the symmetry plane, where most of the ion kinetic energy flows axially; n instead drops steeply at higher values of x, where the ion kinetic energy has a more relevant x component [see panels (h) and (i) of Figure 3.4]. As a consequence the energy flux becomes mostly axial, yielding the large values of η_{div}. Conversely, for lower values of χ, we observe in Figure 3.4 smaller densities close to the symmetry plane and a less pronounced drop in n as one moves along x, justifying the decrease of the divergence efficiency.

Finally, the first two plots in Figure 3.9 show the electron in-plane current densities obtained for $\chi = 3$ and $\chi = 150$. In the former case, the map of $\tilde{j}_e$ exhibits two current loops leaving the plasma source near its edges, and returning back to the source along its center. The existence of these loops raises the overall value of $\tilde{j}_e$ in this region, but does not contribute to the net electron current delivered by the source into the plume. This structure, which was already present in the case $\chi = 30$ of Figure 3.5 (albeit much smaller in importance and extent), is explained as follows. First, we remark again that, for sufficiently high values of χ, the strong perpendicular gradients of Φ imposed at the source

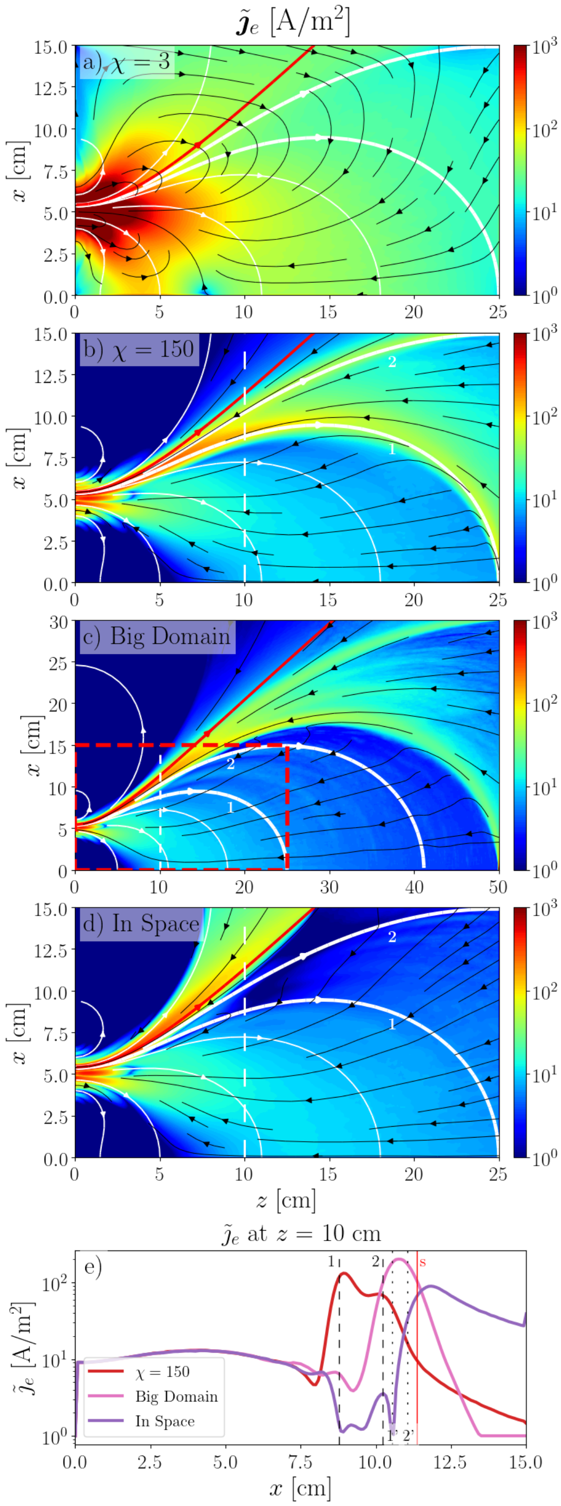

Figure 3.9: Comparison of the in-plane electron currents for different simulation cases. The magnetic separatrix is highlighted with a red line, the magnetic lines to the reference domain corners (lines 1 and 2) are shown with thicker white lines, and the dashed red rectangle in panel (c) indicates the reference domain size. Panel (e) shows a lateral section of the in-plane currents. Here the lines to the corners of the reference domain (1 and 2) and big domain (1' and 2') are shown with dashed and dotted lines. The separatrix is marked with a vertical red line.

are successfully propagated downstream along the magnetic lines, with little diffusion or smoothing. However, as B is lowered and χ becomes sufficiently small, the damping of the perpendicular gradients of Φ as we progress from the source and into the domain becomes more marked. Eventually, this mechanism leads to a near-homogeneous value of Φ early in the expansion. Second, this smoothing of the map of Φ means that a non-negligible variation of this quantity takes place along the magnetic lines for small values of χ. We observe that, in the central part of the source exit, the parallel component of $\nabla\Phi$ points upstream, while in the periphery of the source exit it points downstream. Third, since the parallel electron conductivity σ_e is large, the existence of these parallel gradients drives the strong electron currents into and out of the source, respectively. Our numerical experiments prove that this is a robust mechanism whenever σ_e is sufficiently large, as in this regime Φ is essentially governed by χ alone and is unaffected by σ_e, whereas the parallel electron currents are proportional to the parallel gradient of Φ and σ_e.

Analysing now the rest of the domain in Figure 3.9, it is apparent that for the low magnetization case $\chi = 3$, the electron fluid is well capable of crossing the magnetic lines freely, reaching the outer boundaries without being noticeably influenced by the magnetic lines. In the $\chi = 150$ case, instead, the largest portion of the electrons is forced to follow the magnetic tube that reaches the downstream boundary. The guiding effect of the magnetic lines, already commented in Section 3.4, is in fact further enhanced in Figure 3.9(b), causing the streams of high electron current density running along the magnetic lines to the domain corners, highlighted once again by the thicker white lines. These streams of high current density are also clearly visible in the lateral section of the in-plane currents presented in Figure 3.9(e), where it is evident that they coincide with the streamlines to the domain corners, located on the vertical dashed lines labelled 1 and 2. As will be shown in the next section this is an effect liked to the domain size and geometry, which however only influences the map of $\tilde{j}_e$. The strong magnetization obtained with $\chi = 150$ also causes the reduced current densities found in the inner region of the MA, between the symmetry plane and the magnetic line to the bottom domain corner, where electrons attempting to move downstream experience a mobility across the magnetic lines decreased by a factor $(\chi^2 + 1)$.

3.6. Boundary Effects

It is clear from the plots of the in-plane electron currents described above that, at high values of the Hall parameter, the domain corners and in general the shape and size of the domain affect the solution for $\tilde{j}_e$ (which is only weakly coupled to the rest of the plasma solution). If the simulation domain is dictated by the dimensions of a vacuum chamber then the influence of the domain boundaries on the simulation results is physical: electron currents will preferentially follow those magnetic lines that intersect with the downstream walls, which may vary for differently shaped and sized facilities. However, if the simulation aims to reproduce the infinite expansion that takes place in space, the BCs imposed at the domain edges should not represent the plasma sheath that develops between the quasi-neutral bulk of the domain and the facility walls, but a global downstream matching layer[138] that expresses through a reduced model the plasma expansion between the domain boundaries and infinity. In this case, therefore, the applied (numerical) BCs should not influence electron currents. For this reason we dedicate the present section to the analysis of the effects that the domain boundaries have on the simulation results.

Firstly, we note that for lower values of the Hall parameter ($\chi = 3$) the chamber boundary conditions employed up to here hold also for an infinite expansion. Indeed, because electrons in this case can freely cross the magnetic lines when expanding to infinity the expression for a global matching layer is analogous to the expansion in a Debye sheath. On the other hand, at higher χ, when the magnetic field has a larger influence in the electrons' motion towards infinity, the choice of appropriate BCs becomes more challenging. In order to assess the effects of the domain boundaries in this case, we repeat the case $\chi = 150$ but with the domain size doubled in both directions in the 'Big Domain' simulation case. The resulting electron currents are shown in Figure 3.9(c), where the dashed red box indicates the original domain size. It is clear that once again the electron currents follow the magnetic tube that intersects the downstream boundary, highlighting a dependency of the currents on the domain size and shape. Indeed, marked differences are evident when comparing the electron currents inside of the dashed red rectangle with those of Figure 3.9(b). In the case of the larger simulation domain, in fact, the extended symmetry plane imposes a null current over a bigger portion of the magnetic lines connected with the injection surface, pushing the electron flux tube to those outer magnetic lines that arch beyond the bottom boundary. As stated, this is to be expected when simulating vacuum chambers of different dimensions, but represents a numerical artifact when attempting to reproduce an expansion to infinity.

The outflow BCs introduced in Ref. [64] for the electron fluid represent a possible solution to this problem for the specific case of a MA with large values of χ. As already mentioned, in fact, two categories of field lines may be identified in this magnetic topology: closed lines connecting the two plasma sources through the symmetry plane, and open lines circling back towards their original source in the opposite direction. For perfectly magnetized electrons ($\chi \to \infty$), the zero outflow of current imposed at the symmetry plane causes all closed field lines to carry null electron currents. As a consequence, a condition on the normal electron current $j_{ne} = 0$ can be applied on all boundary faces lying on closed filed lines, even those that do not cross the symmetry plane inside of the simulation domain. In order to obtain a current free plume, therefore, all electron current must flow through the boundary crossed by the open field lines. As before, Eq. (3.15) is therefore used to recover the value of ϕ_W (now representing the potential at infinity) that grants the current free condition, and Eq. (3.14) yields the Neumann BCs to be applied at the cell faces composing this surface. Note for clarity that the treatment of particles remains unvaried with respect to the previous simulation cases.

The currents obtained with the BCs described above are plotted in Figure 3.9(d), where we have also highlighted in red the magnetic separatrix, that divides open and closed field lines. To aid comparison, this same magnetic line has also been traced in red in all other panels. Notice how, as we increase the domain size from panel (b) to panel (c), the beam of electron current shifts closer to the separatrix. This is even more clearly observable in panel (e), where we have plotted the magnitude of $\tilde{j}_e$ along a lateral section with $z = 10\,\mathrm{cm}$, and where it is evident that the peak in the current density is located above streamline 1, which as we move from the smaller domain (red line) to the bigger one (pink line) shifts towards the magnetic separatrix, marked here with a vertical red line. It stands therefore to reason that, if we were to simulate an infinite domain, the electron currents would follow the magnetic lines surrounding the separatrix to reach infinity. Indeed, already with a doubled domain size, it is clear that the electron current density map within the red dashed rectangle in panel (c) approaches the one obtained with the modified BCs [see also panel (e)].

	Big Domain	In Space
$\Delta n/n_0$ [%]	0.4	0.4
$\Delta j_{ye}/j_{y0}$ [%]	4.82	4.80
$\Delta F_m(15\mathrm{cm})/F_0$ [%]	0.8	2.2

Table 3.3: Maximum relative variation of n, j_{ye}, and F_m computed for the Big Domain and In Space cases with respect to the H150 case. The variations have been normalized with the reference density n_0, the total injected plasma momentum F_0, and a reference out-of-plane current $j_{y0} = \Delta\Phi e n_0/(B_0 R)$, with $\Delta\Phi = 22\,\mathrm{V}$ the variation of thermalized potential across the injection boundary.

We remark that, although the domain size or BCs have an effect on $\tilde{j}_e$, they cause extremely marginal variations in all other plasma properties, including the out-of-plane currents. The maximum relative variations in n, j_{ye} and total magnetic thrust $F_m(15\,\mathrm{cm})$ between the Big Domain and In Space cases with respect to the H150 case are reported in Table 3.3. For all these quantities the maximum variations are negligible, never exceeding 5%. These small variations when changing or moving the domain boundaries are due to the large values of the electron conductivity parallel to the magnetic lines. Any small variation of the thermalized potential parallel to B will in fact cause relevant changes in the electron in-plane currents (see Eq. (3.7)). As a consequence, the solution to the system of fluid equations is capable of complying to any BC imposed on $\tilde{j}_e$ with negligible changes in the map of Φ, and therefore negligible influence on the other plasma properties. In general, in fact, as one approaches the collisionless plasma limit, one has $\sigma_e \to \infty$, forcing the gradients of Φ along the magnetic lines to be identically zero in Eq. (3.7). Therefore the map of Φ in the domain becomes solely dependant on the upstream BCs imposed at the injection surface, and $j_{ye} = (en/B)\,\partial\Phi/\partial\mathbf{1}_\perp$ is also insensitive to the downstream BCs. On the other hand, because of perfect electron magnetization, the in-plane electron currents are forced to flow parallel to the magnetic field and are completely decoupled from the rest of the plasma properties in our drift-diffusion model, since with an infinite parallel conductivity their value becomes inconsequential for the determination of Φ. Although this decoupling between the electron currents and the general plasma response may cause numerical challenges in the accurate determination of $\tilde{j}_e$ when σ_e assumes very large values, it also ensures that any inaccuracies in its computation will not relevantly affect the plume's response. Finally, note that the small variation in the rest of the plasma and propulsive properties when comparing the different sized domains in Table 3.3 is an indication of the fact that the domain sizes and BCs employed in this work are large enough to confidently allow an extrapolation of the simulation results to larger domains and to more realistic dimensions of experimental facilities. This should not entail, in fact, any changes in the plasma properties and propulsive performance, if not for the map of $\tilde{j}_e$.

3.7. Background pressure effects

With the knowledge provided by the previous sections on the plasma response to the magnetic field strength and the applied BCs, we now set up and analyze a more complex simulation scenario (termed BGP case), that aims to reproduce a MA expansion inside the environment of a vacuum chamber, and thus subject to facility effects. To this end, the simplified formulation for the electron collisionality has been dropped, and two neutral populations have been added to the heavy species module. The first population of neutral particles is characterized by a prescribed density $n_{n1} = 2 \times 10^{17}\mathrm{m}^{-3}$, a zero bulk velocity and a temperature $T_{n1} = 0.05\,\mathrm{eV} \approx 500\,\mathrm{K}$. It represents the background neutral population present in an experimental facility, and corresponds to a background pressure of 8×10^{-9}bar[114], [115]. In order to avoid simulating the long transient times linked to the generation of this population of background neutrals, we provide it as a constant and uniform background, postulating that it represents the steady-state equilibrium solution between collisional events, plasma and neutral interaction with the chamber walls, recombination, and extraction from the chamber pumps. This allows us to maintain the simple outflow BCs for macro-particles crossing the domain edges presented in Section 3.3.1, since the physical scattering and recombination processes that would take place at material walls are already included in the hypothesized equilibrium of this background population. The second neutral population (this time modeled as particles) represents the neutrals injected by the EPT sources. For its description we assume a propellant utilization efficiency in the source $\eta_{u0} = 0.43$ and a uniform injection of neutrals across the injection surface.[139] Keeping the total mass flow rate constant with respect to the previous simulation cases, we therefore inject neutrals with a density $n_{n2} = 4.1 \times 10^{18}\,m^{-3}$, an axial velocity $u_{zn2} = 300\,m/s$, and a temperature $T_{n2} = 0.05\,eV$. The ion flux also has to be accordingly adjusted, so that the reference density in Eq. (3.9) now becomes $n_0 = 4.3 \times 10^{17}\,m^{-3}$. The simulation settings for these new populations of neutral particles essentially mimic the ones for ions: outflow BCs at the various simulation surfaces as described in Section 3.3.1; a controlled macro-particle weight for a minimum of 20 macro-particles per cell (corresponding to a total of 1 million macro-particles at steady-state); and the same time-step as the one employed to advance the ion macro-particles and the electron fluid. The magnetic field for this collisional case is identical to the one of the reference simulation, with a magnetic induction $B_0 = 300\,G$ at the center of each source.

The collisional processes that affect the electron fluid are now evaluated explicitly, rather than fixing a uniform Hall parameter χ in the domain as in the simulation cases H3, H10, H30, H150, In Space and Big Domain. In particular, in the BGP case we include the effect of electron-neutral elastic, excitation and ionization collisions, and electron-ion Coulomb collisions, on the electron fluid. These collisional processes influence the model through the collision frequencies ν_{es} of Eq. (3.2). In the case of electron-neutral collisions these frequencies $\nu_{es}(T_e)$ are obtained as a function of the electron temperature by integrating the collision cross-sections $\sigma_{es}(v_e)$ over a non-drifted Maxwellian VDF with temperature T_e.[29] The collision cross-sections as a function of the electron velocity for elastic, excitation and ionization collisions are taken respectively from the Hayashi[140], NIFS[141], and Biagi[142] databases available on the LXCat website[143]. The electron-ion Coulomb collision frequency is instead obtained as[29], [144]

$$\nu_{ei} = \frac{2^{1/2} n_i e^4 \ln\Lambda}{12\pi^{3/2}\varepsilon_0^2 m_e^{1/2} T_e^{3/2}}, \tag{3.20}$$

with the Coulomb logarithm taken to be $\ln\Lambda \approx 10$. Note here that, although the inclusion of inelastic collisions would in principle affect the cooling of the electron fluid, we maintain the polytropic parameter $\gamma = 1.2$ to aid the comparison with the previous cases.

Regarding the effect of collisions on the heavy species, we consider two collisional phenomena: ionization and charge exchange. These two are evaluated respectively by means of MCC[29], [145] and DSMC[134], [146] algorithms. For CEX collisions, the collision cross-sections as a function of the relative collision velocity are taken from the Miller[147] database, while the ionization frequency is taken locally equal to the one employed in the electron fluid. Reference [29] provides a more detailed description of the collisional algorithms implemented in EP2PLUS.

Figure 3.10 presents the plasma properties for this new simulation case. Panel (a) shows that the Hall parameter in the bulk of the plume decreases from the initial values of 150 at injection to roughly 20 at the downstream boundary of the domain. In light of this, the previously employed assumption of a uniform value of χ throughout the domain is inaccurate. Nevertheless, the magnetization of the electron fluid falls within the parametric range previously analyzed, and for which the plasma and propulsive properties displayed a reduced sensitivity to the value of χ. As a consequence, the thermalized potential map for this case, shown in panel (b), is nearly identical to the one obtained for the previous cases where a constant $\chi > 10$ was assumed. Once again, in fact, the value of Φ remains practically constant along the magnetic lines because of the large scalar conductivity obtained for this weakly collisional plasma and the low cross-field transport of electrons.

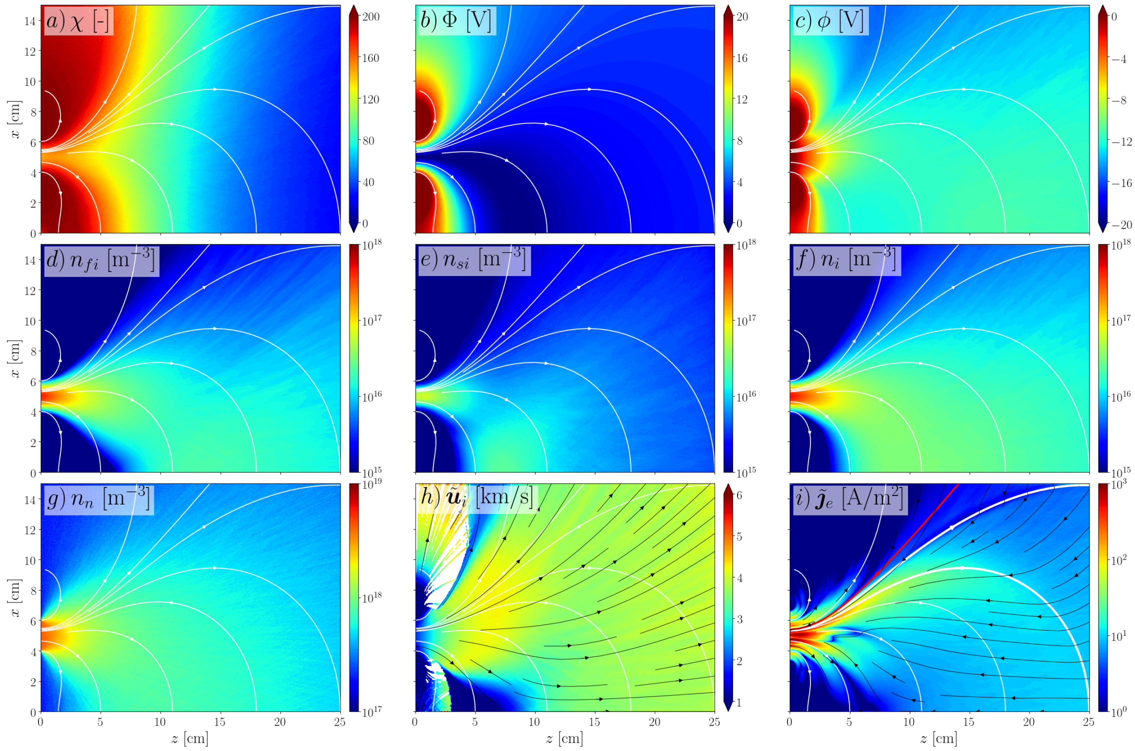

Figure 3.10: The plasma response in the BGP case. Note that the suffices *fi* and *si* indicate respectively the properties of fast and slow ions. Likewise, *i* and *n* mark the quantities of the total ion and neutral populations.

The plasma density for this case, on the other hand, is expected to display variations with respect to the previous simulations because of two distinct effects. The first is the moderate propellant utilization efficiency, which implies a decrease in the injected ion flux (and therefore in the plasma density) by a factor η_{u0}. The second is the inclusion of collisional processes (ionisation and CEX) that cause the generation of low energy ion particles downstream of the injection surface. To better distinguish these two effects we divide ions into two separate particle lists: the first comprised only of ions produced in the EPT source and injected sonically into the simulation domain (*i.e.* fast ions), the second generated by CEX and ionization collisions in the plume (*i.e.* slow ions). The densities of these two populations are respectively shown in panels (d) and (e) of Figure 3.10, while panel (f) shows the total plasma density that results from their combination (and the assumption of quasi-neutrality). Interestingly, in the *near plume* and *transition region* the slow ion density is a significant fraction of the total ion density, an observation in accordance with experimental studies of MNs, which have measured double-peaked total ion VDFs (one peak for the slow ions and one for the fast ones) in the main bulk of the plume.[35] The generation of slow ions only decays in the *far plume*, where the decrease in electron temperature and neutral density (see panel (g)) cause a strong reduction of the ionization and CEX collision frequencies. More specifically, this population is particularly present in two locations. The first is just in front of the injection surface, where the neutral density and the electron density and temperature are highest, resulting in the maximum collision frequency found in the domain. The second is at the symmetry plane where the two ion beams first meet, because of the combined effect of the higher densities found here, and the merging of the slow ion populations that are generated in front of each source. As a consequence of the relevant presence of slow ions, the total plasma density in this case does not display the reduction by a factor η_{u0} that would be expected with respect to the previous cases, and indeed it remains of a similar magnitude throughout the domain. This observation is representative of the neutral entrainment detected in multiple experimental studies[35], [117], which can cause an overestimation of the thrust when measured in on-ground facilities. Finally, note that the majority of the total ion density remains concentrated close to the symmetry axis even for large z coordinates, likely because of the generation of ions close to the symmetry plane through ionization collisions.

The differences in the plasma density described above are also responsible for the variations in the map of the electric potential shown in panel (c), with respect to what was obtained for the previous simulation cases for large values of χ. While the lobes of high potential at the edges of the injection surface, responsible for the axial confinement of ions in the *near-plume*, and the sharp axial potential drop in charge of their acceleration are still present, in fact, the potential well previously observed in the *transition region* close to the symmetry axis is here strongly reduced. This is likely due to the relevant presence of slow ions slightly upstream of where the fast ion beams emitted by the sources merge, causing a reduction of the axial pressure gradient along the symmetry axis, and a smaller contribution of the second term of Eq. (3.16), linked to the plasma density. As a consequence of collisions, therefore, the potential and plasma density maps displays monotonic profiles along x shortly after the *near-plume*, effectively shortening the length of the *transition region*.

The potential map just described is responsible for the acceleration of both the high and slow ions downstream, whose cumulative in-plane velocity is plotted in panel (h). It is immediately evident that the total ion velocity is much lower than the ones depicted for the previous simulation cases. This is due to the large fraction of slow ions, which are generated in the plume from neutrals with a low velocity, and accelerated downstream only by the potential drop that develops from their generation point to infinity. As a consequence these ions possess a much lower velocity, and heavily reduce the average speed of the total ion population.[119] Note, however, that the fast ions produced by the source maintain a velocity map very similar to the one shown for the reference simulation, omitted here for the sake of conciseness. In general, the net axial acceleration of both these ion populations, as well as the one of neutrals through CEX and momentum exchange collisions, is representative of the magnetic thrust provided by the MA. Another notable feature of panel (h) are the two regions of increasing lateral velocity that develop at the edges of the injection surface (the first in the region $x = 6 - 15$cm, $z = 0 - 4$cm, and the second in the region $x = 0 - 3$cm, $z = 0 - 4$cm) and move mostly along x. These are once again caused by the slow ions generated just in front of the injection, and accelerated laterally by the electric field. Note however, by observing panel (e), that the number density of these ions is largely negligible.

Finally, panel (i) shows the in-plane electron currents for this simulation scenario. As may be expected by observing the axially decreasing values of the Hall parameter throughout the domain, the behaviour of the electron current gradually transitions from the one observed for $\chi = 150$ to the one of $\chi = 10 - 30$. The electrons near the source, in fact, initially move mostly along the magnetic tube encompassing the downstream domain boundary (once again delimited by the thicker white magnetic field lines). As the Hall parameter decreases as they proceed downstream, however, electrons begin diffusing across the field lines, and the confined current arc that was observed for $\chi = 150$ breaks down into a more homogeneously spread out electron flux. Finally, at the downstream boundary, the electron current streamlines turn upwards in order to comply with the fluxes there imposed as BCs.

Regarding the propulsive performance for the BGP case, the obtained accumulated magnetic thrust and divergence efficiency have been included in Figure 3.6 with a black dashed line. Note, when considering the plotted thrust, that the force provided without a MA and used to normalize the plotted values reduces to $F_0 = 5.11mN/m$ in this case, because of the effect of the non-unitary utilization efficiency. Relatively speaking, the MA in these conditions is much more effective, as it provides a total magnetic thrust $F_m = 0.6F_0$ (see Figure 3.6), although in absolute terms the net magnetic thrust provided is actually slightly lower than the one obtained in the cases with $\chi \geq 10$. This increase in the propulsive effectiveness in spite of the moderate value of η_{u0} employed, is due to the plasma production that takes place in the plume. Indeed, the plasma densities of the current simulation are only slightly lower than the ones of the reference case, pointing to an effective propellant utilization efficiency (when considering also the plasma production in the plume) which is considerably larger than 0.43. When taking the ratio between the total ion mass flow at the downstream domain boundaries and the total mass flow of ions and neutrals injected by the thruster, we obtain a utilization efficiency $\eta_u = 0.53$. It is important to state, however, that the production of plasma in the plume is, from a propulsive viewpoint, not as efficient as its generation and confinement in the source, since it shifts the plasma production downstream of the more intense acceleration region. Note also that, for the values of background pressure and utilization efficiency employed here, the majority of the electron-neutral collisions involve neutral atoms emitted by the thruster, rather than the ones composing the chamber background population, and their effects would therefore be present also in space conditions. Finally, Figure 3.6(b) shows that the divergence efficiency for this BGP case ultimately results the highest out of all of the considered scenarios. This confirms the improved confinement of the plasma density close to the symmetry plane already observed in the density plots.

3.8. Conclusions

The in-house, hybrid code EP2PLUS has been employed to simulate the expansion of the plasma produced by two EPTs in a planar magnetic arch, and to further study the effects linked to variations in the magnetic field strength and to facility conditions. The analysis has allowed the identification of three distinct regions: (i) a *near plume*, where the plasma in front of each thruster displays a behaviour analogous to that of a traditional MN topology, (ii) a *transition region*, where the merging of the two distinct plasma beams takes place, and (iii) a *far plume*, in which the lateral profiles of the plume's properties become single peaked, and the distinct plasma beams have fully merged. In particular, a detailed study of the *transition region* unveils the complex kinetics of ions, characterized in this area by a double peaked VDF, and the presence of a region of magnetic drag due to the closed magnetic lines that arch between the two EPTs, that mildly reduces the total provided magnetic thrust.

A parametric sweep on the strength of the applied magnetic field shows that only small changes are visible for values of the Hall parameter $\chi \geq 10$ both in the general plasma properties and in the propulsive performance of the MA. The only quantities that show a relevant sensitivity to χ in this magnetized regime are the in-plane electron currents. These are found to be only weakly coupled to the other plasma properties for the weakly collisional plasma analyzed, and progressively become constrained to the magnetic lines that intersect the domain's outflow boundaries as the magnetization level rises. At lower values of χ, instead, the confining effect of the magnetic field begins to break down, and the plasma is capable of diffusing across the magnetic lines, increasing the plume's divergence and reducing the magnetic thrust provided by the MA.

A further study on the influence of the boundary conditions demonstrates that different domain sizes (corresponding to different dimensions of the vacuum chamber) impose different electron current paths in a strongly magnetized plasma, although this does not appreciably alter the other plasma properties of the plume. In light of this dependency of the in-plane electron currents on the domain size, an alternative set of boundary conditions[64] was also employed and tested, and was found to be more suitable for the simulation of the infinite expansion that takes place in space.

Then, an analysis of background pressure effects has been carried out by including in our simulations the neutral atoms emitted by the EPTs, as well as a uniform population of neutrals representing the background density found even far from the thruster exhaust in vacuum chambers. The collisional processes involving these neutral populations, and which modify the response of ions and electrons, were also included. Although a propellant utilization efficiency $\eta_{u0} = 0.43$ was prescribed for the plasma source in this case, the thrust provided is only slightly lower than the one obtained in the previous simulations (in which $\eta_{u0} = 1$), because of the entrainment of the neutral atoms caused by ionization and CEX collisions, which implies an increase in the effective value of the utilization efficiency. Interestingly, a majority of these collisions involved neutrals emitted by the thrusters, and not those populating the chamber background, so that a similar behaviour is to be expected also in space conditions under low utilization conditions.

While the present work has offered an extensive analysis of the main physics in a planar MA and the sensitivity to central aspects such as the Hall parameter and the boundary conditions, the implementation of the electron energy equation instead of the polytropic law, will provide a more consistent response of electron thermodynamics, mainly when collisional and facility effects are important[132]. Finally, we acknowledge that a big step forward would be to simulate a 3D MA, as done in Ref. [107], but with finite values of the Hall parameter, and focusing on the 3D details of the plasma detachment, the topology of the electron current lines, and the induced magnetic field.

Acknowledgements

The authors would like to thank Celian Boyé for his contributions in the initial definition of the simulation setup. This project has received funding from the European Research Council (ERC) under the European Union's Horizon 2020 research and innovation program (grant agreement No 950466)

CHAPTER 4

Electron Populations and Neutralization Process in the Plume of a Gridded Ion Thruster

This chapter reproduces the contents of Ref. [49], published in the peer-reviewed journal Plasma Sources Science and Technology. The typography has been adapted to the style of this thesis.

Abstract

In order to assess the importance of collisional processes in the neutralization of a gridded ion thruster plume this study presents a series of simulations carried out with a planar, full-PIC code provided of a library of electron, ion and neutral collisions. In particular, we find that the inclusion of electron inelastic collisions, such as ionization and excitation, is fundamental in the generation of a population of electrons trapped in the plume's potential well, which play a major role in the neutralization of the plume and in the formation of the electric potential map. A further investigation is therefore carried out on the properties of the electron populations present in the plume, suggesting that the trapped population is mostly insensitive to the emission properties of the cathode, but displays a strong dependence on the inclusion of inelastic collisions and a slow approach to stationary conditions dictated by the timescales of these collisions. Given the symmetry of the plume bulk even in presence of an externally mounted cathode, we further extend the study to an axisymmetric simulation case with an annular cathode, that allows the evaluation of a three-dimensional expansion process. The build up of the trapped electron population in this case is even slower, because of the smaller neutral density observed when expanding the plume in three dimensions, and an acceleration strategy that speeds-up

the approach to steady state without altering it is therefore proposed. Nevertheless, the main governing physical processes observed in the planar case remain prominent also in this latter case.

4.1. Introduction

Gridded Ion Thrusters (GITs) are a commonly employed form of electric propulsion, principally because of their high specific impulse ($I_{sp} > 3000\,$s) and large flight heritage[16]. These kind of thrusters extract and accelerate an ion beam from a plasma source through a system of electrically biased grids, which is neutralized downstream by means of an electron current emitted by a cathode. This allows the closure of the electric circuit, producing a current-free plume and avoiding the charging of the thruster and spacecraft.[148] Although GITs are a mature technology and the final neutralization of the thruster plume is readily obtained in practice, the theoretical understanding of the coupling between the positive ion beam and the negative electron cloud that allows it is still a matter of research[32]. Moreover, the experimental quantification of their lifespan, and the characterization of their plume and of its possible interaction with the hosting spacecraft, is still hindered by the uncertainties linked to the extrapolation of testing conditions in on-ground vacuum chambers to the in-space environment, commonly termed as 'facility effects'[26]. Of these, the most prominent are (i) the presence of a background population of neutral particles in vacuum chamber experiments, that may alter the plume characteristics through collisional processes, and (ii) the chamber walls, that interact with the plume and provide additional conductive paths for the closure of the electric currents.

Model	Authors	Ref.	Year	Ions	State	Conditions	Collisions	Cathode
Hybrid	Korkut	[149], [150]	2014-2017	Xenon	Steady	Both	CEX, MEX	Both
	Cichocki	[29]	2017	Xenon	Steady	In-Space	CEX,MEX,el	External
PIC	Usui	[151]	2013	Hydrogen	Transient	In-Space	None	External
	Hu, Wang	[152], [153], [31], [154]	2014-2017	Hydrogen	Transient	Both	None	Co-located
	Nuwal	[155]	2020	Xenon	Steady	Chamber	CEX,MEX	External
	Jambunathan	[84], [156], [82], [157]	2017-2020	Xenon	Steady	Both	CEX,MEX	Both
	Nishii	[158]	2023	Xenon	Steady	Chamber	CEX,MEX	Co-located
	Nishii	[32]	2023	Xenon	Steady	Both	CEX,MEX	External
Particle-Particle	Zhao	[159]	2018	Xenon	Transient	In-Space	None	Both

Table 4.1: Summary of recent numerical works on GIT plumes.

Numerous numerical investigations have tackled these topics in the last decade, preciously increasing our understanding of the GIT plume, its dynamics and its response to facility conditions. A non-extensive summary of the most recent of these works, specifying the type of numerical model that was employed and the main characteristics of the physics that were simulated, is presented in Table 4.1. The first studies to investigate the steady-state properties of GIT plumes employed hybrid codes[29], [30], [149], [150], [160], that through a particle in cell (PIC) description of the heavy species and a fluid model for electrons, together with the assumption of quasi-neutrality, allowed a reduction of the computational costs and the achievement of steady-state. This approach was useful for a first qualitative study of the effects of ion-neutral resonant charge exchange (CEX) collisions, that generate the characteristic high-density lateral wings around GIT plumes. Additionally, these studies allowed a preliminary investigation of the effect of the electrostatic field, responsible for determining the ion backflow to the thruster and the gradual divergence of the plume. However, the body of work by Wang and Hu[31], [152], [153], [154] on co-located plasma sources (i.e. ions and electrons were emitted by the same injection surface), together with the later studies of Nuwal and Jambunathan [84], [155], [156], demonstrated the importance of electron kinetics in the retrieval of the electric potential map and the accurate evaluation of the electric forces acting on ions. Simultaneously, the problem of the ion beam neutralization by means of electrons emitted by an externally located cathode was tackled by Usui and Zhao [151], [159] with fully kinetic and non-neutral codes, highlighting the strong non-neutrality of the problem and the presence during the initial transient of axial and radial electron density waves, caused by the bouncing motion of electrons trapped in the potential well generated by the positive ion beam. However, these studies only concentrated on the initial transient, as steady-state conditions for fully kinetic simulations of GIT plumes have only recently become achievable, thanks to the heavy parallelization of modern PIC codes and the introduction of energy-based boundary conditions for electrons[63], [157], [161], [162].

With the aid of PIC simulations, the recent works by Jambunathan, Nishii and Levin [32], [82], [157], [158] have explored the dependence of the steady-state conditions of a GIT plume on facility effects and cathode properties. This allowed a precise determination of the energy of backstreaming ions, and the alteration of the densities in the facility, caused by the neutralization of the plasma beam at the chamber walls and their sputtering by high-energy ions. Interestingly, all simulation cases with an externally located cathode (thus simulating the neutralization process of the plasma plume) displayed values of the electric potential and electron temperature in front of the thruster grids that were several times higher than what is observed in experimental measurements[163], [164], [165]. As we propose to show in this work, this was likely caused by the exclusion of inelastic electron collisions in the simulated physics, that would provide an energy sink for the electron population and, in the case of ionization, also introduce a new source of low energy electrons capable of decreasing the positive space charge of the ion plume.

Past kinetic studies of magnetized[46], [47], [89], [166], [167] and unmagnetized[130], [131] plumes have highlighted the presence, in electric propulsion plasmas, of different populations of electrons, termed ‘free’, ‘reflected’ and ‘trapped’ depending on their total energy and their capacity to escape to the downstream or upstream boundaries of the plume. These studies also suggested that one of the most prominent mechanisms in the generation of the trapped electron population may indeed be the collisional processes that take place in the plume, hinting at the possible underestimation of such a population when neglecting collisions in simulations. However, to the authors' knowledge no fully kinetic, steady-state study of a GIT plume that includes an extensive library of electron and ion collisions has been carried out yet. Additionally, we also note that a scarce number of kinetic simulations of GIT plumes exist in the literature that employ parameters corresponding to real thrusters and their operating points. These observations form the main motivations for this work, in which we present the steady-state, kinetic and collisional simulations of the plume of Ariane's RIT10-EVO thruster, carried out with the in-house, 2D3V explicit PIC code PICASO[68]. In these simulations we categorize the electron particles into distinct 'primary' and 'trapped' populations, allowing the independent study of their macroscopic properties, their generation mechanisms, and their influence on the plume's neutralization and on the general plasma properties.

The remainder of this article is structured as follows. Section 4.2 describes the methodology followed for the presented simulations, detailing the properties of PICASO and the assumptions and numerical choices involved. Section 4.3 then presents a reference planar simulation and the general plasma response that it provides, which is further analysed in Section 4.4 by detailing the properties of the distinct electron populations. A sensitivity analysis on the free parameters of the model and on the effects of electron collisionality is next presented in Section 4.5, while the study of an axisymmetric simulation and the proposal of an acceleration strategy to speed up the simulation's approach to steady state may be found in Section 4.6. Finally, Section 4.7 summarizes the main contributions and results of this work.

4.2. Methodology

Two distinct codes were employed to obtain the simulations presented and discussed in this work. As mentioned, in fact, the PIC code PICASO was used for the kinetic simulation of the ion-electron expansion of the plume, which represents the main focus of this study. However, in order to consider collisions with neutrals in this kinetic framework, these would have to be included as particles in the simulations, pushing the physical time to reach steady-state from $t_{ss} = 0.3$ ms to $t_{ss} = 6$ ms due to the much slower dynamics of neutrals. To avoid the prohibitive computational costs linked to this increased simulation duration, the hybrid in-house code EP2PLUS[29], [122] was first used to provide the steady-state properties of the neutral atoms populating the simulation domain, that were then loaded into the PIC code and kept frozen during the subsequent simulations.

We present here both planar and axisymmetric simulations of the plume. The former, in fact, have the advantage of capturing the asymmetry of the problem caused by the externally located cathode, and are therefore employed to assess the limitations linked to the subsequent axisymmetric assumption. The latter, on the other hand, lose this capability but provide a description of the plasma expansion in 3D geometry. As a consequence two different versions of both the hybrid and the PIC code were used: EP2PLUS was run in its

2D and 3D versions, while PICASO, was employed in its planar and axisymmetric forms. The following subsections present the setup of these different simulations, starting from the general and physical properties of the problem and then detailing the specific choices made in each case.

4.2.1. The Simulation Domain

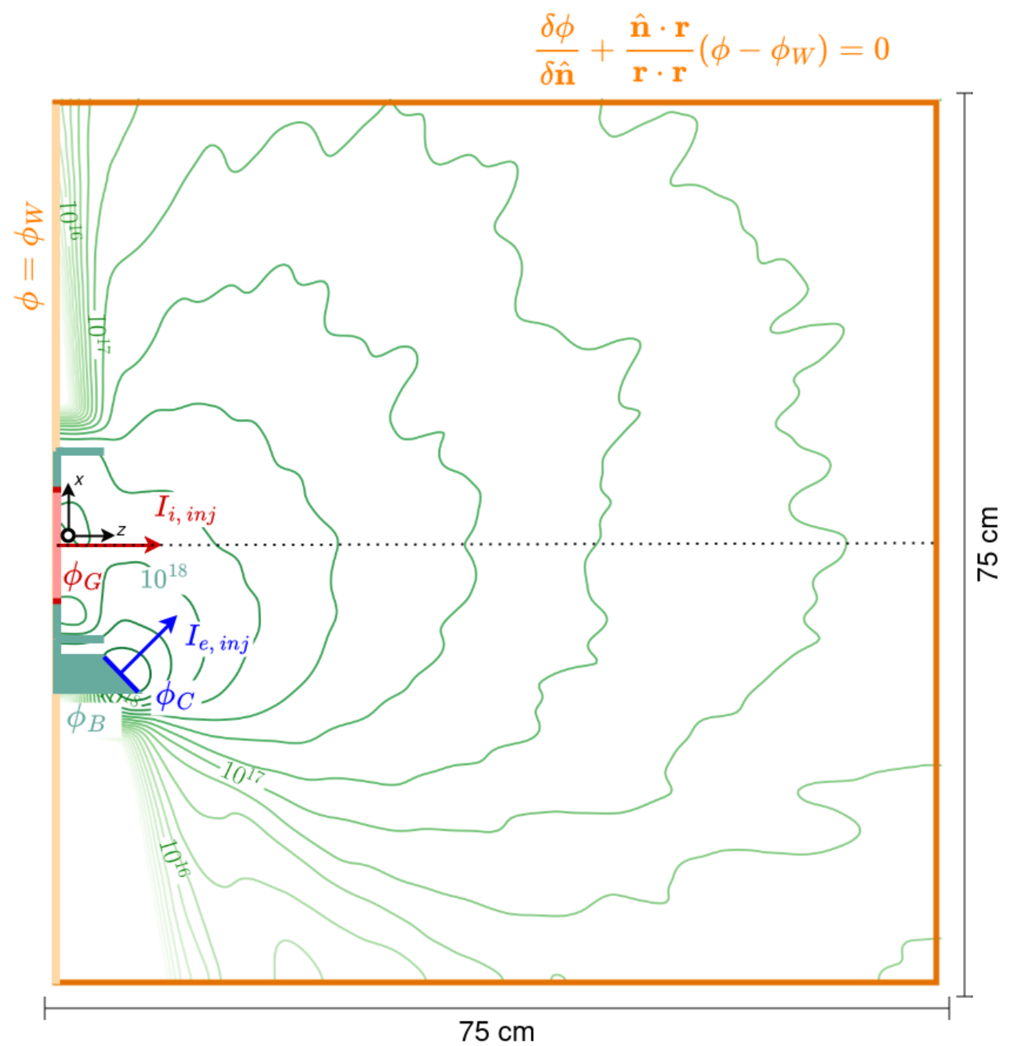

Figure 4.1: Sketch of the problem geometry. The ion and electron injections are depicted respectively in red and blue, while the green isolines display in m^{-3} the neutral density map obtained with the hybrid code EP2PLUS for the planar case. All potentials are defined with respect to the thruster body potential. In particular, note that in all simulations the cathode is considered to be at the same potential as the thruster body $\phi_C = \phi_B = 0$.

Figure 4.1 presents the geometry considered for this study. This domain reproduces, within the possibility of the spatial discretization employed in our simulations, the physical geometry of Ariane's RIT10-EVO[168]. In particular, we show here the plane passing through the center of the cathode and the axis normal to the grids of the GIT. The body of the thruster has a total diameter of 16 cm, at the center of which an acceleration grid with a diameter of 10 cm is located. Ions are only injected from a circle of 9 cm in diameter at the center of this grid, since the outer 1 cm is composed of solid metal devoid of extraction holes. The outer edge of the thruster is encircled by a cylindrical wall which protrudes 4 cm into the simulation domain. The thruster body and cylindrical walls can be observed in green in Figure 4.1, while the punctured and solid portions of the grid are shown respectively in light and dark red. The neutralization of the plume was here assumed to be guaranteed by a radio-frequency cathode, oriented towards the plume by an angle of roughly 45°, with a diameter of 7.8 cm, and an extraction plate of 2 cm in radius.[169] The center of the cathode's extraction plate was positioned 5.5 cm downstream of the acceleration grid and at a distance of 11 cm along x from the center of the thruster.

In all our simulations we take the thruster body potential as the reference one (i.e. $\phi_B = 0$) and define the other potentials in the simulation with respect to it. As a consequence, in order to impose an electrically floating thruster configuration (i.e. no net current is emitted by the ensemble of thruster and cathode), the chamber walls must collect a globally zero net current ($I_W = I_{iW} + I_{eW} = 0$) at steady-state, with the currents considered positive when flowing to the chamber walls. This is obtained by varying, at each time-step k, the potential of the facility walls ϕ_W

$$\phi_W^{(k+1)} = \phi_W^{(k)} + \frac{1}{C} I_W^{(k)} \Delta t, \tag{4.1}$$

so as to converge at steady-state to a current-free plume, and to a value of the vacuum chamber potential with respect to the thruster body. Note that here C is a numerical capacitance used to evolve the facility potential in time, and its value should be appropriately chosen for the stability of the simulations. With regard to the thruster components, we consider an acceleration grid potential of $\phi_G = -150$ V, and a cathode extraction plate potential $\phi_C = 0$ V.

The plasma plume is assumed to be composed of (i) Xenon neutral atoms, injected by the external grid of the thruster and the cathode, or present in the facility background; (ii) singly charged Xenon ions, injected through the thruster grid with a current $I_{i,inj}$ or produced in the plume; and (iii) electrons introduced from the cathode with a current $I_{e,inj}$ or generated by ionization inside of the domain. The injection of all of these species is carried out by assuming a Maxwellian distribution in their respective source, and introducing in the simulation domain only the forward-marching portion of this VDF. The backward-marching portion of the VDF, instead, is an output of the model which in general depends on the global response of the plasma, and cannot be known *a priori*. We therefore underline here that (as we will see later) $I_{e,inj}$ is not the net current emitted by the cathode, which would instead be obtained as $I_e = |I_{e,inj}| - |I_{e,out}|$ (with $I_{e,out}$ the electron current returning to the cathode because of the electric forces in the domain). Note that the use of this constant injection condition for the cathode is a necessary simplification of the complex coupling between cathode and plume, that ignores the internal dynamics of the cathode, the consequent modulation of the emitted electron current, and the possible instabilities and oscillations that it entails.[170] The macroscopic properties defining the injected Maxwellians of ions and electrons depend on the geometrical nature of the simulation considered, as discussed below.

4.2.1.1 Planar Simulations

The planar simulation domain corresponds to the sketch of Figure 4.1, and has the advantage of preserving the asymmetry linked to the externally located cathode. In these simulations we assume that the plasma properties in the out-of-plane direction are infinitely uniform, and therefore extensive quantities such as the injected net current or flux are measured per unit of y-length. To maintain the plasma properties in these simulations close to the ones of the physical thruster the intensive injection parameters (e.g. velocity, specific flux, etc.) have been chosen in accordance with the typical operating point of the RIT10-EVO, as summarized in Table 4.2. Reasonable assumptions were made where no data was available (e.g. sonic neutral velocity, ion temperature, etc.). Note in particular that the ions' axial velocity at injection was chosen to respect the potential drop of 1150 V imposed between the thruster's grids, and the ion specific flux would correspond to the nominal beam current of 0.1 A under the assumption of singly charged ions, when considering the real 3D geometry of the acceleration grid.

As a marginal note on the notation used in this work, when considering planar simulations we will refer to vectorial quantities projected onto the simulation plane with a tilde. For example, $\tilde{\boldsymbol{u}}_i = \boldsymbol{u}_i - (\boldsymbol{u}_i \cdot \mathbf{1}_y)\mathbf{1}_y$ and $\tilde{\boldsymbol{j}}_e = \boldsymbol{j}_e - (\boldsymbol{j}_e \cdot \mathbf{1}_y)\mathbf{1}_y$ represent respectively the ion bulk velocity and the electron current projected onto the simulation plane.

4.2.1.2 Axisymmetric Simulations

In the case of the axisymmetric simulations the domain corresponds to the lower half of Figure 4.1, and the grid axis displayed with a black dotted line becomes the axis of symmetry of the problem. Clearly, from a geometrical stand point, this yields a physically accurate geometry of the ion injection surface, but implies the assumption of an annular cathode that revolves around the thruster. We therefore lose the ability of simulating asymmetrical domains, but gain the possibility of a fully three-dimensional plume expansion. Once again the injection properties at the ion grids are chosen to match with the thruster operating point (as shown in Table 4.2), while the specific fluxes at the cathode are scaled in accordance with the large annular injection surface, so as to maintain the same total fluxes and currents as the ones expected from the real cathode.

4.2.2. Description of the Neutral Population

A fully self-consistent modeling of neutral particles is a particularly challenging aspect in full-PIC simulations of plasma plumes. The characteristic time of the neutral dynamics,

Species	Property	Planar	Axisymmetic	Unit
Ions	Specific flux	9.82×10^{19}	9.82×10^{19}	$m^{-2}s^{-1}$
	Axial velocity	41137	41137	m/s
	Temperature	0.1	0.1	eV
	Current	1.41	0.1	A/m or A
Thruster Neutrals	Specific flux	4.39×10^{19}	4.39×10^{19}	$m^{-2}s^{-1}$
	Axial velocity	300	300	m/s
	Temperature	0.0345	0.0345	eV
Electrons	Specific flux	1.5×10^{21}	6.95×10^{19}	$m^{-2}s^{-1}$
	Axial velocity	0	0	m/s
	Temperature	3	3	eV
	Injected current	4.23	0.3	A/m or A
Cathode Neutrals	Specific flux	1.13×10^{21}	5.23×10^{19}	$m^{-2}s^{-1}$
	Axial velocity	300	300	m/s
	Temperature	0.0345	0.0345	eV
Background Neutrals	Density	10^{16}	10^{16}	m^{-3}
	Temperature	0.0345	0.0345	eV

Table 4.2: Injection properties of the species composing the plasma plume.

in fact, is orders of magnitude larger than the simulation time-step imposed by stability considerations on the characteristic electron frequencies. Worse still, the time required to consistently simulate the build-up of the facility background pressure, through the modeling of collisions, ion neutralization at the chamber walls, and the action of the facility pumps, pushes the time to steady-state to prohibitively large values for a PIC code. To avoid this large computational burden, the PIC simulations presented in this work do not evolve the neutral population in time, but employ constant density, velocity and temperature maps for its description. Specifically, two distinct sets of maps are used. The first consists of uniform and constant maps of density, velocity and temperature with the values shown in Table 4.2. These represent the facility background population of neutrals that forms as an equilibrium between the plasma recombination at the chamber walls and the extraction of gas by the facility pumps. The density and temperature of these neutrals was therefore chosen to correspond to a background pressure of 5×10^{-7} mbar[171], while their velocity map was set to zero. The second instead represents the neutrals injected by thruster and cathode, and is obtained by simulating the problem described in Sections 4.2.1.1 or 4.2.1.2 with the hybrid code EP2PLUS. Thanks to a simplified quasi-neutral fluid description of electrons, closed at the momentum equation by means of a polytropic law, steady-state maps of the injected neutral population can be obtained with a reduced computational cost. The neutral properties employed in the full-PIC simulations thus represent the steady-state equilibrium between the expansion of neutrals injected from the cathode and through the thruster grids, and the effects of depletion through collisional processes such as ionization or resonant charge exchange. The neutral density map obtained with EP2PLUS for the planar scenario is displayed with density isolines in Figure 4.1, and the interested reader may refer to Appendix 4.A for further details on the most relevant plasma properties obtained with the hybrid code, which should agree sufficiently well with the steady-state PIC results to ensure the correct coupling between the two simulations. Finally, we note here that previous works, that modeled in a fully consistent manner the build-up of the neutral population responsible for a facility's background pressure, have indeed obtained neutral density maps that, when sufficiently far from the chamber walls, agree well with the present approach of overlapping an injected neutral population and a uniform background density[32], [150]. The approach employed here should therefore offer a sufficiently accurate description of the steady-state properties of neutrals, although since it ignores the neutral dynamics it cannot provide a fully consistent characterization of the initial transient that takes place when the thruster is first ignited.

4.2.3. The PIC/MCC Formulation

PICASO[68] is a 2D3V, time-explicit, momentum-preserving PIC code that makes use of a uniform, rectangular mesh. The classical Boris leapfrog algorithm[125] is used to advance particles in two spatial and three velocity space dimensions, a first order cloud-in-cell shape function is employed for the particle weighing and the reconstruction of the species' macro-properties at the mesh nodes[126], and a linear interpolation scheme allows the retrieval of the electromagnetic fields acting on each particle. The electric potential values at all domain nodes are obtained through the solution of Poisson's equation,

$$\varepsilon \nabla^2 \phi = -\rho_{el}, \tag{4.2}$$

which is discretized through second order finite difference schemes, and solved with Intel's MKL Pardiso solver[172]. Here $\rho_{el} = e(n_i - n_e)$ is the local space charge, and ε the electric permittivity.

The solution of Eq. (4.2) requires the imposition of boundary conditions at all simulation boundaries. In the case of the thruster components, their potentials ϕ_B, ϕ_C, and ϕ_G are imposed as Dirichelet conditions at the corresponding nodes. The vacuum chambers typically used for plume investigations, however, are too big to be entirely simulated in PICASO with reasonable computational expenses. As a consequence, the condition to be imposed at the domain edges is of more complex determination, as the domain must be inevitably cut short of the chamber walls, where it would be most natural to impose ϕ_W as BC. In order to truncate the domain before the facility walls, the Robin boundary conditions

$$\frac{\partial \phi}{\partial \mathbf{n}} + \frac{\mathbf{n} \cdot \mathbf{r}}{\mathbf{r} \cdot \mathbf{r}}(\phi - \phi_W) = 0 \tag{4.3}$$

proposed by Andrews et al.[63], and based on the approximation of a monopole decay of the electric potential far from the plume's bulk, are employed at all downstream boundaries (in dark orange in Figure 4.1). Here ϕ is the potential at the boundary node, $\mathbf{n}$ is the outward versor normal to the boundary, and $\mathbf{r}$ is the distance between the boundary node and a reference position, which is taken at the center of the acceleration grid ($x = 0$, $z = 0$). While these conditions were shown to hold at boundaries that do not contain the reference node, we argue that their imposition on the upstream boundary may be inaccurate. At this surface, in fact, the monopole term in the multipole expansion employed in the derivation of Eq. (4.3) is multiplied by $\mathbf{r} \cdot \mathbf{n} = 0$, so that the higher order terms of the expansion may not be neglected. We prefer therefore to directly impose the facility wall potential as a Dirichlet condition at this upstream boundary (highlighted in light orange in Figure 4.1).

The BCs proposed by Andrews et al. also require an energy based evaluation of all particles crossing the downstream boundaries. It is in fact possible that, in reality, the direction of motion of charged particles is inverted back towards the plasma source downstream of the domain boundaries, so that they ultimately return back into the domain. These returning particles are fundamental to obtain quasi-neutrality in the plume bulk, and should not be eliminated from the simulation domain to avoid incurring in the electron pump instability[162]. The normal kinetic energy of all particles crossing the downstream boundaries is therefore evaluated, and compared with the potential energy required to reach the facility walls

$$\frac{1}{2}m(\mathbf{v} \cdot \mathbf{n})^2 \geq Ze(\phi_W - \phi), \tag{4.4}$$

where m represents the mass of the single physical particle, Z its charge number, e the elementary charge, and $\mathbf{v}$ the velocity vector of the macro-particle. If Eq.(4.4) is respected and the kinetic energy of the particle is sufficient to reach the chamber walls, it is removed from the simulation. If, on the other hand, Eq. (4.4) is not satisfied , and the particle is trapped in the plume's potential well, then it is specularly reflected back into the domain. For completeness, note that all particles that cross any other domain boundary are simply removed from the simulation.

Finally, Table 4.3 summarizes the collisional operators considered in this work, detailing also the modeling strategy employed and the source of the data for the collision cross-sections. In order to spare computational power, the multiple possible excited states of Xenon have been lumped in a single operator, characterized by an average cross-section and energy threshold. Moreover, all collisions with neutrals have been modelled with the Monte Carlo Collision (MCC) approach, neglecting any form of depletion of the neutral density that some of these collisions would entail (e.g. CEX or ionization collisions) as the neutral maps employed already consider these effects in their steady-state equilibrium. The electron-ion Coulomb collisions, on the other hand, are modelled with a Direct Simulation Monte Carlo (DSMC) operator that employs an isotropic scattering of electrons and an analytical determination of the collision cross-section based on the classical Coulomb collision theory[144]. This approach allows the reproduction of the cumulative drag effect on electrons caused by several small angle interactions, without resorting to the more kinetically faithful but computationally heavy models proposed by Takizuka[173], Nanbu[174], and Chap[175]. We note here that although Coulomb collisions are within the capabilities of the model and are therefore included in the simulations of this work, their effect on the present study is negligible.

Collision	Species	Model	Data	Ref.
Elastic	e - n	MCC	E	[142]
Ionization	e - n	MCC	E	[142]
Excitation	e - n	MCC	E	[142]
Coulomb	e - i	DSMC	A	[144]
CEX	i - n	DSMC	E	[147]
Elastic	i - n	MCC	E	[176]

Table 4.3: Description of the models used for the collisional events considered in the simulation. Data 'E' points to the use of cross-section data measured experimentally, while Data 'A' refers to the use of an analytical model for the determination of the collision frequency. All experimental data is taken from LXCat[143], but references to the specific databases are also provided.

4.2.4. Electron and Ion Populations

Previous kinetic studies have highlighted the possible presence of primary and trapped electrons[32], [42] in the plumes of GITs. This categorization subdivides electrons based on their total planar energy $\mathcal{E} = 1/2 m_e \tilde{v}^2 - e\phi$ (or $\mathcal{E} = 1/2 m_e v^2 - e\phi$ for the axisymmetric case) with respect to the minimum energy required to exit the domain through one of its boundaries $\mathcal{E}_{ex} = -e \max(\phi_W, \phi_B, \phi_C, \phi_G)$. If $\mathcal{E} < \mathcal{E}_{ex}$, the considered electron does not have sufficient energy to reach one of the domain boundaries, and is trapped inside of the plume's potential well. On the other hand, electrons with sufficient total energy to leave the domain (either through the upstream or downstream boundaries) are termed 'primary electrons', and group together the 'free' and 'reflected' electron populations identified in other kinetic studies[46], [130]. In order to study in detail the properties of these two electron populations we sort them in separate particle lists in the code, so as to compute the macroscopic magnitudes of both populations independently. All electrons are therefore initially injected in the primary electron list (note, in fact, that electrons born at the cathode with a non-zero velocity always have $\mathcal{E} > -e\phi_C$). Every 100 simulation time-steps, however, the code loops over the primary electron list, and sorts those electrons with $\mathcal{E} < \mathcal{E}_{ex}$ into the list of trapped electrons.

Similarly, ions have also been subdivided into two separate lists: 'fast ions' and 'slow ions'. The former are all ions injected at high velocities through the thruster grids, while the latter are all of those ions produced inside of the plume either by ionization or CEX collisions. The 'slow ions', therefore, are generated with energies similar to those of their parent neutral, and are consequently more prone to a trajectory inversion back towards the thruster under the effects of the electric field. It is then convenient to sort them in a separate list in order to allow a more precise study of their interaction with the thruster and spacecraft. Finally, note that ions undergoing elastic or Coulomb collisions with neutrals or electrons are left in their original list, since in this case their energy is not altered as significantly as for ionization and CEX events.

4.2.5. Considerations on Numerical Parameters

Stability criteria for explicit momentum-conserving PIC codes impose limitations on the cell size Δl and time-step Δt.[53] In particular, for the unmagnetized plasma at hand, the most restrictive conditions require that the cell size is smaller than the Debye length λ_D throughout the domain, and that the time-step is sufficiently small to accurately discretize the electron plasma frequency ω_{pe}. Imposing a minimum of 10 time-steps for each electron plasma frequency oscillation, and considering the most restrictive value of the Debye length, this gives

$$\Delta l < \min\left(\lambda_D\right), \qquad \Delta t < 0.1 \times \min\left(2\pi/\omega_{pe}\right). \tag{4.5}$$

These constraints can be computationally excessive for the considered plasma properties, and as a consequence we resort to the artificial increase of the characteristic length and time scales of our problem through an augmentation factor f_D. This is carried out by employing an augmented electric permittivity $\varepsilon = f_D^2 \varepsilon_0$ in Eq. (4.2), that substitutes the vacuum permittivity physically present in Poisson's equation and relaxes the numerical constraints of our problem. In the present work we employ an augmentation factor $f_D = 20$, which falls well within the range $f_D = 10 - 40$ used in other studies[63], [68], [177], and which is expected to only increase the characteristic size of the Debye sheaths in the domain, without affecting significantly the physics of the plasma expansion. A confirmation of this has been obtained by running a planar simulation with $f_D = 10$, which yields results in very good agreement with the ones presented in the following sections, as shown in Appendix 4.B.

Considering a characteristic plasma density $n_* = 2.4 \times 10^{15}$ m^{-3} and temperature $T_* = 3$ eV, corresponding to the injection properties in Table 4.2, we obtain an augmented Debye length $\lambda_D = 5.3$ mm, and an increased electron plasma period $2\pi/\omega_{pe} = 7.2 \times 10^{-9}$ s at the thruster exit. The physical values, in absence of the acceleration factor f_D, would respectively be $\lambda_D = 0.265$ mm and $2\pi/\omega_{pe} = 3.6 \times 10^{-10}$ s. In order to satisfy the numerical conditions in Eq. (4.5), the simulations use a cell size $\Delta l = 3$ mm (leading to a mesh of 251×251 nodes) and a time-step $\Delta t = 2 \times 10^{-10}$ s. This leads to a ratio between the augmented Debye length and the cell size at the thruster exit of $\lambda_D/\Delta l = 1.7\overline{6}$, and of $\lambda_D/\Delta l = 1.462$ at the cathode exit (these values would be respectively $\lambda_D/\Delta l = 0.088\overline{3}$ and $\lambda_D/\Delta l = 0.073$ with the non-augmented Debye length). The total simulated time in planar simulations is $t_{ss} = 3 \times 10^{-4}$ s (i.e. 1.5×10^6 simulation steps), corresponding to 15 times the average ion transit time. Finally, a constant weight $w_p = 1.5 \times 10^8$ of physical particles per computational ion or electron macro-particle was employed, leading in the planar case to a total of respectively $1.9{\times}10^6$ and $1.8{\times}10^6$ ion and electron macro-particles at steady-state. These values correspond to a maximum of 300 macro-particles per cell in the denser regions of the plume bulk (in front of the grids), and around 100 macro-particles per cell in the portion of the plume bulk close to the downstream boundary of the domain. With these numerical settings, running on the 40 physical cores of an Intel Xeon Silver 4316 processor, the planar simulations require 59 hours to complete.

4.3. The General Plasma Response

The panels of Figure 4.2 show the plasma properties averaged over the final 70000 time-steps of the planar simulation of the GIT plume. As expected, the most prominent features of the plume are defined by the highly inertial population of fast ions, which form the axial plasma beam visible in all panels. Because of their large initial velocity, in fact, these ions traverse the domain displaying a mild sensitivity to the lateral electric forces, that only cause the small plume divergence observed at high axial coordinates in panels (a) and (g). Note here that the lateral streaks external to the main ion beam visible in panel (g) are due to those few fast ions that undergo elastic collisions. Axially, fast ions only suffer a relevant variation in velocities in the first few centimeters of the plume, in front of the acceleration grid (note the transition from a darker to a lighter red in panel (g)). In fact, because the acceleration grid is directly exposed to the plasma plume, its very negative voltage causes the formation of a Debye sheath in front of it, visible both in the local absence of electrons shown in panel (c), and in the strongly positive space charge displayed in panel (f). The plasma potential consequently rises across the sheath by roughly 156V, decelerating the axial motion of fast ions.

Observing the electric charge density (here divided by the elementary charge to allow a direct comparison with the density values) of panel (f) it is clear that the bulk of the ion beam, downstream of the Debye sheath in front of the grids, is mainly quasi-neutral. Space charge is in fact principally present at its edges, with electrons charging negatively the outer part of the plume boundary, and ions predominant at the inner edge. This lateral profile of the electric charge density causes, through Eq. (4.2), the lateral drop observed in the electric potential map of panel (i) when moving from the center of the plasma beam to the outer edges of the domain. On the other hand, at the center of the plume and downstream of the initial potential rise, a negligible electric charge is found, leading to a mild axial drop in the potential. As will be discussed later, this potential profile, characterized by a maximum value some centimeters downstream of the thruster grids, is responsible for the trapping of electrons inside of the plasma plume, and for the acceleration of slow ions laterally and backwards.

The map of the electric charge in panel (f) also highlights the presence of a strong

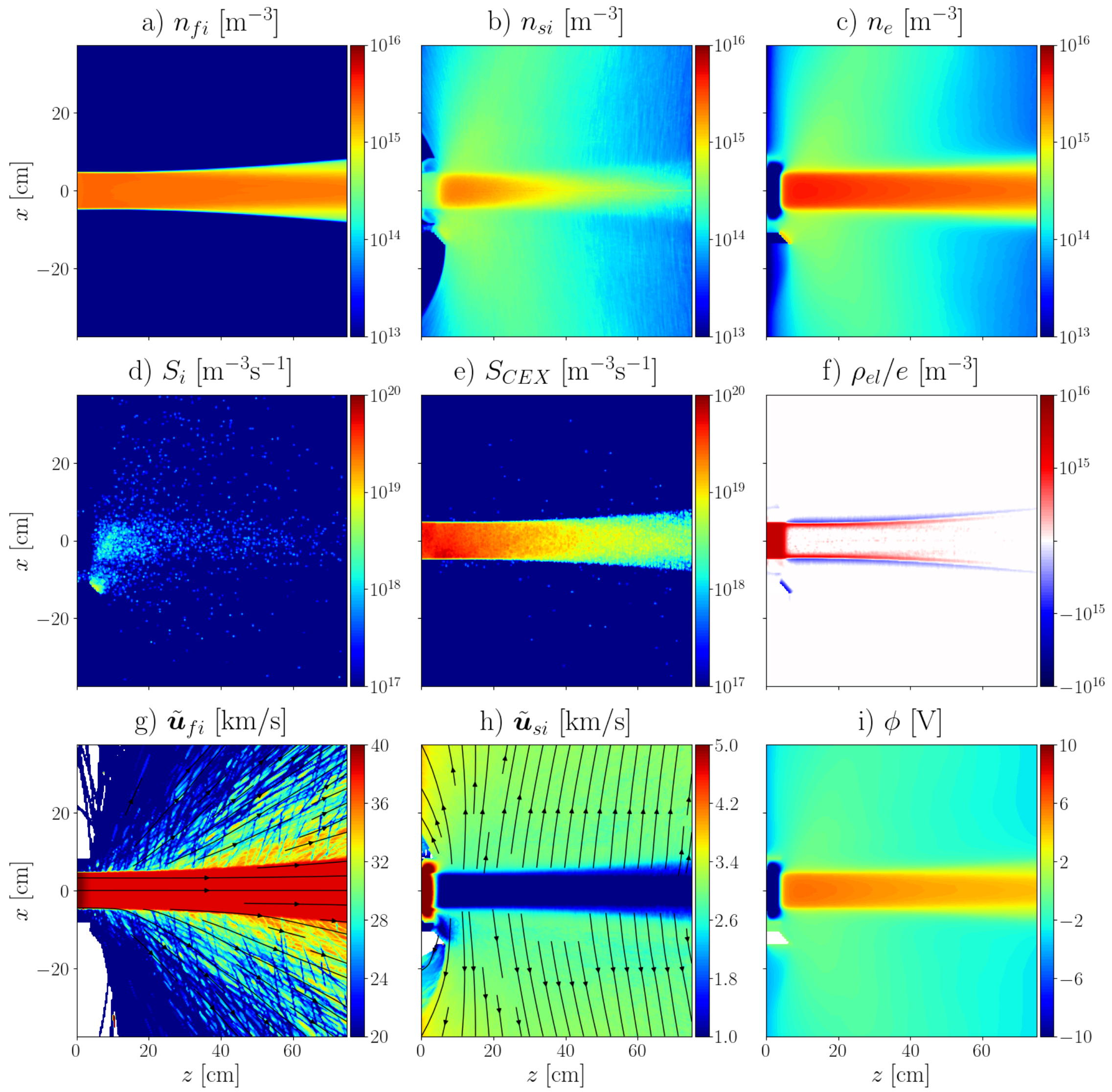

Figure 4.2: The plasma properties at the end of the reference simulation. From left to right and from top to bottom the panels show the fast ion, the slow ion and the total electron densities; the ionization and charge exchange production terms, and the electric charge density divided by the elementary charge; and the in-plane fast and slow ion velocities along with the electric potential. In panels (g) and (h) the black arrows represent the velocity streamlines. The color-maps saturate above and below the extremes of the color-bars.

negative charge in front of the cathode. This is due to the fact that the forward-marching electron current injected from the cathode in this simulation is three times larger than the ion current emitted through the acceleration grid. As a consequence, because we impose a current-free plume at the downstream boundaries, a reverse sheath and a potential drop develops just in front of the cathode that allows a current $|I_e| = |I_{e,inj} - I_{e,out}| = |I_{i,inj}|$ composed of the most energetic electrons to proceed from the cathode into the plume, and reflects the less energetic ones back towards the cathode or the thruster body. This energetic mechanism for the selection of the electron current capable of entering the plume makes the choice of the electron flux injected by the cathode, which is an input parameter of the model, particularly challenging. In fact, any electron current $|I_{e,inj}| > |I_{i,inj}|$ inserted in the domain will yield a current-free plume, since any electrons injected in excess will be deflected back to the cathode or thruster walls. Additionally, experimental measurements of the cathode currents do not provide valuable data in this sense, since what is typically measured is the net electron current emitted from the cathode (which is therefore very similar to the ion current flowing through the grids), rather than the separate values of the injected and returning electron currents which would be needed by the model. For this reason Section 4.5 presents the sensitivity of the simulation results to, amongst other input parameters, the injected electron current.

Figure 4.2(b) highlights how the population of slow ions represents a relevant portion of the total ion density in the domain, and even constitutes about half of the total ion density a few centimeters downstream of the acceleration grid. By considering the ionization and CEX production rates S_i and S_{CEX} for this population of ions (respectively in panels (d) and (e)) it is clear that the vast majority of these ions are produced through CEX collisions, and that ionization could be freely neglected in the description of this population. Nevertheless, panel (h) shows how both CEX and newly ionized ions produced downstream of the grid's Debye sheath undergo a relevant lateral acceleration caused by the potential drop at the edges of the fast ion beam. This process forms the characteristic CEX wings at the edges of the plume, populated by slow ions and electrons. More importantly, from the point of view of the lifetime of the acceleration grid, slow ions produced inside of the grid's Debye sheath are accelerated back towards it by the strong potential slope present here, and can impinge on the grid with energies of up to 156 eV.

Although slow ions are principally produced by CEX collisions, the presence of ionization in the region just in front of the cathode (see Figure 4.2(d)) is essential for the formation of the 'plasma bridge', a quasi-neutral region that develops between the cathode exhaust and the ion beam and that allows an efficient conduction of a net electron current $I_e \approx I_{i,inj}$ from the cathode to the ion beam. A zoom of the electric potential, electron currents, and electron and ion densities in this region is provided in Figure 4.3 for the case analyzed here ($I_{e,inj} = 3 \times I_{i,inj}$) and for a case with an increased cathode emission current $I_{e,inj} = 6 \times I_{i,inj}$ (which will be discussed in further detail in Section 4.5). The potential maps in panels (a) and (b) show how the potential drop that develops in front of the cathode to select the neutralizing electron current steepens when increas-

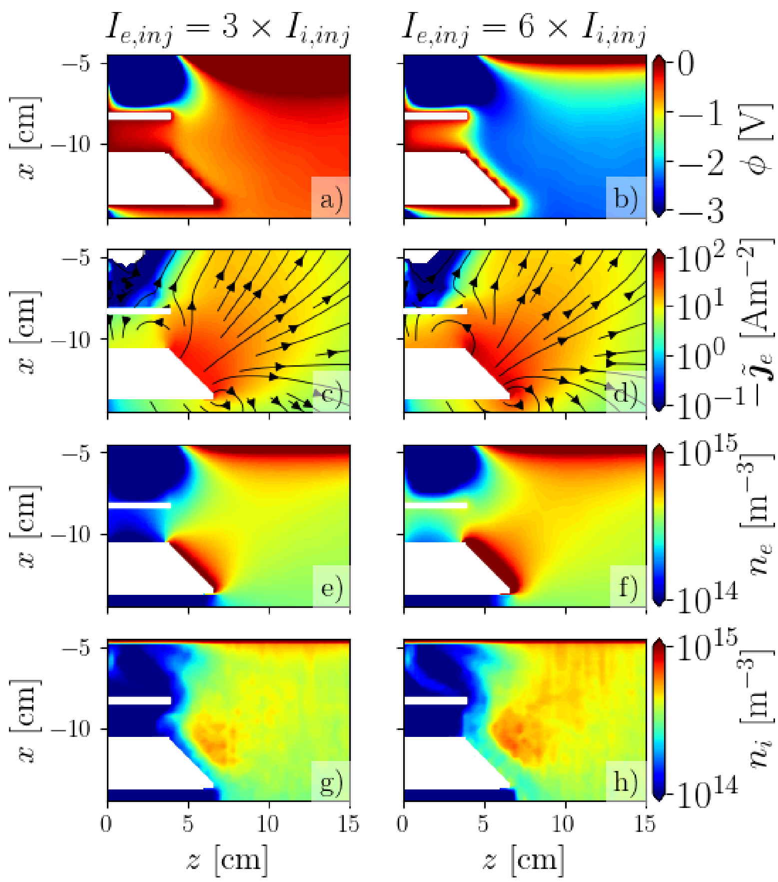

Figure 4.3: A zoom of the electric potential, total electron density and total ion density in the region between the cathode and the bulk of the GIT plume.

ing $I_{e,inj}$, so as to reflect the excess current back to the cathode. Indeed, the maps of the electron currents, in panels (c) and (d), show very similar currents reaching the ion beam at the upper boundary of the plots for the two simulations. Beyond this initial reversed sheath the potential rises once more, accelerating electrons towards the ion beam. As a consequence panels (e) and (f) show a gradual drop in the density of the electron beam, required to maintain a constant total current as electrons expand and accelerate towards the upper right corner of the plot. This electrostatic acceleration of electrons also provides them with the energy necessary to ionize the neutral particles injected from the cathode into this portion of the domain, as shown by the large ionization source term present in front of the cathode in Figure 4.2(d). In turn, these collisions generate the ion population shown in Figures 4.3(e) and 4.3(f), that slowly moves towards the cathode (see Figure 4.2(h)) and compensates the local negative electron charge, leading to the formation of a quasi-neutral plasma beam between the cathode and the bulk of the GIT plume.

The general plasma properties discussed so far are in good agreement with the ones of previous kinetic studies of GIT plumes with an externally located cathode[32], [82]. The one exception is that the maximum values of the electric potential found in front of the thruster grids (just downstream of the Debye sheath that develops there) are relevantly smaller than what was obtained in previous numerical works. This observation results in much better agreement with the values of the plasma potential typically obtained experimentally[164], [165], and as discussed in the next section, can be attributed to an increased generation of trapped electrons and a more effective neutralization of the ion beam that takes place when considering electron inelastic collisions in the simulations.

4.4. Primary and Trapped Electrons

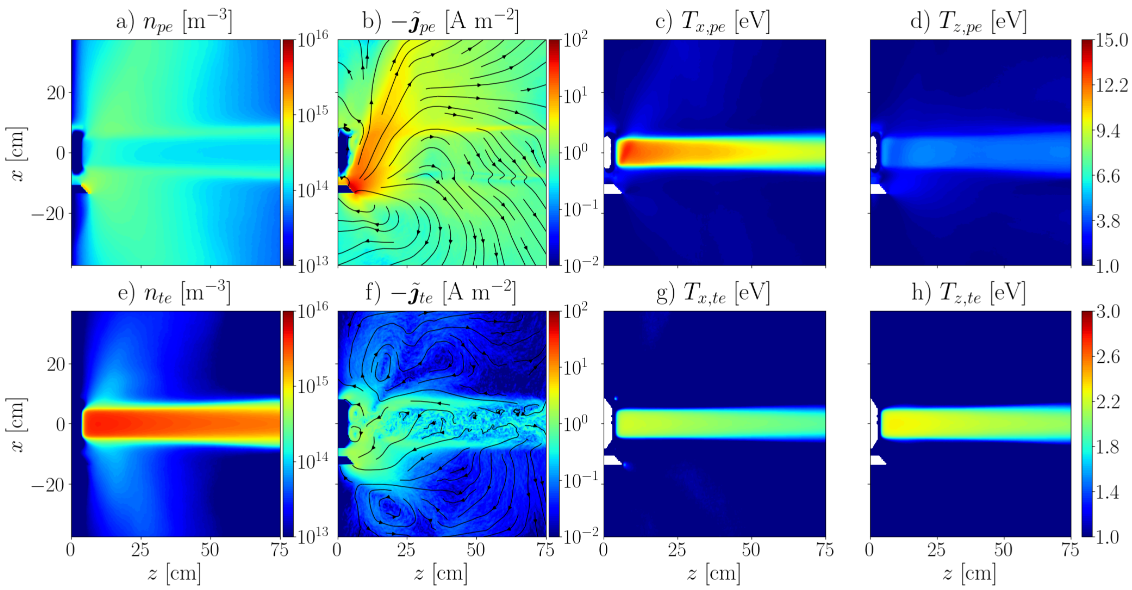

Figure 4.4: Properties of the primary electron (upper row) and trapped electron (bottom row) populations for the reference simulation. From left to right the columns show respectively the electron densities, specific currents, and the temperature tensor diagonal components along x and z. The black arrows in panels (b) and (f) are the streamlines along $-\tilde{\boldsymbol{j}}$, so that they point in the direction of the electron motion. Note the change of scales between the colour-maps of the primary and trapped electron temperatures.

The first and second rows of Figure 4.4 display respectively the macroscopic properties of the primary and trapped electron populations. The comparison between the two density plots (panels (a) and (e)) immediately shows that the bulk of the ion beam is predominantly neutralized by trapped electrons, which represent more than 90% of the total electron population along the plume axis. Considering that all electrons injected at the cathode are initially primary, since they have at least the energy necessary to return to the cathode or to the thruster body, an energy loss mechanism must exist that causes the progressive trapping of these electrons. Indeed, two mechanisms in our simulations are capable of reducing an electron's energy, causing it to be listed as trapped: ionization and excitation collisions, and the temporal variation of the electric potential during the initial transient. In the former case of inelastic collisions, colliding electrons provide part of their kinetic energy to excite or extract the electrons in the orbitals of the target neutral atoms, effectively decreasing their total energy and possibly causing them to be trapped in the plume. In the specific case of ionization collisions, not only is the energy of the parent electron reduced when providing a portion of the ionization energy, but a second electron may be produced inside of the plume's potential well, resulting in its immediate trapping. On the other hand, the total energy of electrons is only conserved under the hypothesis of a time-invariant electric potential, so that it is possible that primary electrons undergo a decrease in their total energy during the initial transient, essentially trapping them in the developing potential well.[167]

Once the total in-plane energy of an electron becomes low enough for it to become trapped, very few escape mechanisms are available for it to exit the simulation domain. This is confirmed by the in-plane specific currents of trapped electrons shown in Figure 4.4(f), which displays negligible flows to any of the domain boundaries, and by Table 4.4, which reports the net currents of trapped and primary electrons flowing to each domain boundary (positive when electrons are absorbed by the surface, negative when emitted) as a fraction of the injected ion current. Additionally, no coherent structure can be identified in the streamlines at the center of the plasma beam when observing the plot of the trapped electron specific currents. The dense column of trapped electrons at the center of the plume is therefore essentially static, and is agitated only by a slight chaotic motion. Note that, although collisional events between these electrons and the ions and neutrals in the plume are infrequent, the trapped electron population turns out to be thermalized, because of their large residence time. This is evidenced by panels (a) and (b) of Figure 4.5, in which we plot the primary and trapped electron velocity distribution functions (VDFs) measured at two points along the axis of the plasma plume ($x = 0$, $z = 10.2$ and $37.5\,\text{cm}$). The trapped electron VDF, in fact, appears to follow a Maxwellian distribution (overlain with a dash-dotted black line) at low energies, but shows a depletion of the high energy tails, that would contain electrons sufficiently energetic to escape the simulation domain, and which can therefore be observed in the primary electron VDF. The similarity between the trapped electron distributions in v_x, v_y, and v_z also explains the isotropy of the temperature tensor, whose in-plane, diagonal components are shown in panels (g) and (h). It is also interesting that the population of trapped electrons is roughly isothermal at the center of the plume, with $T_{te} \approx 2\,\text{eV}$, and relevantly colder than the population of primary electrons (consider also the change in the scale of the colour-maps between the plots of primary and trapped electron temperatures). This rather low value of T_{te} is likely set by a combination of the energy threshold for ionization or excitation collisions, and the potential drop between the plume bulk and the domain boundaries. On one hand, trapped electrons with sufficiently high kinetic energies will sooner or later undergo an inelastic collision, lowering their energy and consequently removing any high energy particle from the trapped electrons VDF. On the other hand, the smallest potential difference between the plume bulk and the domain boundaries will define the maximum energy range that trapped electrons may have, as any electron with an energy outside of this range would not be considered trapped.

Although the residence time of trapped electrons in the plume is largely increased with respect to that of primary electrons, the former do possess a few escape mechanisms. The

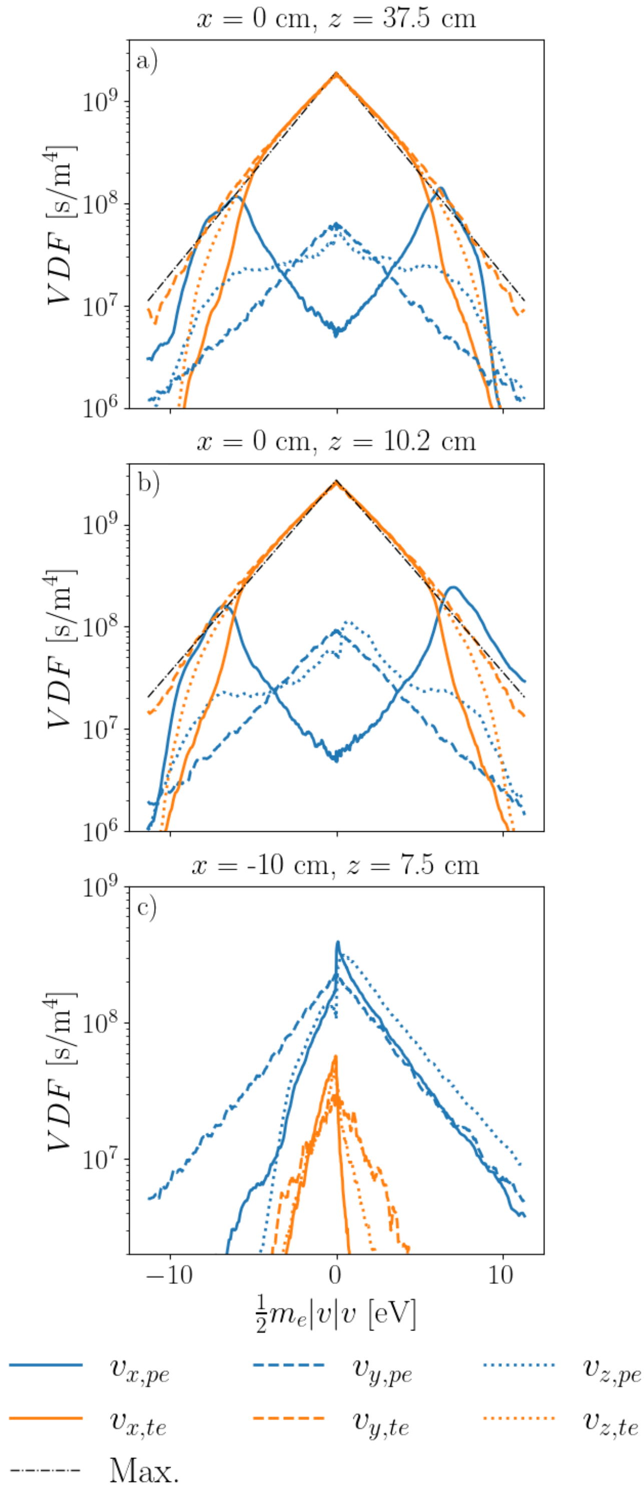

Figure 4.5: The primary and trapped electron VDFs at the center of the simulation domain ($x = 0$, $z = 37.5$ cm), just downstream of the acceleration grid sheath ($x = 0$, $z = 10.2$ cm), and in front of the cathode ($x = -10$ cm, $z = 7.5$ cm). Each curve represents a mono-dimensional distribution, obtained by integrating the 3D VDF in the remaining two dimensions. The data has been smoothed with a sliding window filter to remove noise and increase readability. In panels (a) and (b) the dashed-dotted black line shows a Maxwellian VDF with the macroscopic parameters of trapped electrons.

	$I_{pe}/I_{i\,inj}$	$I_{te}/I_{i\,inj}$
Thruster Body	0.003	0.034
Grid	0.0	0.0
Cathode	-1.11	0.086
Chamber walls	0.96	0.013

Table 4.4: Primary and trapped electron currents to the different domain boundaries expressed as a fraction of the ion current injected through the thruster grids. Positive values indicate a net collection of electrons; negative values indicate a net electron emission from the boundary.

first is linked to the fact that the present simulation is bi-dimensional in space, but three-dimensional in velocity. As a consequence, electrons that undergo a collisional event that scatters the direction of their velocity vector may trade part of their out-of-plane kinetic energy for an increase of the in-plane kinetic energy, which could now be sufficient to escape the plume's potential well. It is worth noting that the inverse process may also lead to the trapping of primary electrons, by tilting their in-plane velocity in the out-of-plane direction. However this latter case is statistically less probable, as there are two useful directions for electron escape (x and z) and only one for electron trapping (y). The second mechanism for the escape of trapped electrons is once again the time-variation of the electric potential[178]. As we will later discuss with the use of Figure 4.7, the potential values in the plume bulk (and in particular the maximum potential value ϕ_{max}, found ~9 cm downstream of the acceleration grid) gradually decrease over the course of the simulation. As a result the trapping potential drop also decreases, allowing an outflow of what were previously the most energetic trapped electrons. These escape mechanisms are likely the explanation for the moderate electron flux observed to reach the cathode in Figure 4.4(f) and Table 4.4. Indeed the cathode is the domain boundary surrounded by the largest plasma density and with the highest electric potential, and represents as a result the easiest escape route for any trapped electron that has undergone an increase in its total in-plane energy.

Primary electrons, on the other hand, consist of those particles that are injected by the cathode and never undergo a sufficient energy loss to cause their trapping inside of the plume. A portion of these electrons, indeed, never reach the ion plume, as their downstream motion is halted by the potential drop located in front of the cathode and inverted back upstream, where they neutralize on the cathode or thruster walls (these are the electrons that in other works are termed 'reflected'[46], [130]). This causes the density peak just in front of the cathode observed in Figure 4.3(e), and the presence of electrons with negative velocities along x and z in front of the cathode, as shown if Figure 4.5(c). The majority of the electrons with sufficient energy to overcome this initial potential drop are instead accelerated into the plume by the positive electric charge of the ion beam. Here, because of the large local neutral density and the recent gain in kinetic energy, a portion of these electrons undergo those inelastic collisions responsible for the production of trapped electrons. The others, instead, either cross the potential drop at the top of the plume and reach the upper domain boundary, or are reflected back into the plume (Figure 4.7(b)). This latter portion of primary electrons remain inside of the ion beam, bouncing against its lateral edges until they reach the downstream boundary or return to the cathode and exit the simulation. This can be noticed in panels (a) and (b) of Figure 4.5, that show that at the center of the domain the primary electron population is characterized by a double peaked VDF along v_x, caused by the bouncing motion of these electrons between the upper and lower edges of the plume. This motion causes both the local maxima in the primary electron density at the lateral edges of the plasma beam in Figure 4.7(a), and the large component of the primary electron temperature tensor along x, symptom of the large spread of electron velocities in v_x. Note that $T_{z,pe}$ is about half of the magnitude of $T_{x,pe}$, pointing to a strong anisotropy in the primary electron population, which is confirmed by the plots of their VDF. Finally, it is important to consider that the potential of the chamber walls ϕ_W is mostly influenced by the properties of this electron population, and is largely insensitive to the characteristics of trapped electrons. Indeed the total electron current to the facility walls I_{eW} in Eq. (4.1) is mostly comprised of primary electrons, as clearly demonstrated by Table 4.4. Except for the few escape mechanisms described, in fact, trapped electrons do not have by definition the energy necessary to reach the chamber walls, and are therefore reflected by the downstream simulation boundaries.

The presence of these distinct electron populations in the plume prompts the question on their description by reduced models. With this objective it is important to first observe that, since trapped electrons represent the vast majority of electrons in the plume bulk, the even moments of the VDF of the total electron population (e.g. density, temperature, etc.) will essentially coincide with those of the sole trapped electron population. On the other hand, since the trapped electron VDF is symmetric in all direction of phase-space, the odd moments of the total electron VDF (e.g. velocities, heat-flux, etc.) will be dominated by the properties of primary electrons. Figure 4.6 is used to investigate the compliance of the total electron population to the polytropic and Boltzmann relations often used in numerical and experimental investigations of a GIT plume. In particular, panel (a) shows the relationship between the densities and temperatures of the primary and trapped electron populations along the axis of the ion beam ($x = 0$). It appears evident that a polytropic law with a parameter $\gamma = 1.1475$ (overlaid in the plot with a dashed black line) is capable of precisely capturing the thermodynamics of trapped electrons in the plume bulk. On the other hand, primary electrons follow a more complex thermodynamic behaviour, which cannot be modeled with a polytropic relation. As mentioned, however, in the main plume bulk a relationship that correctly captures the temperature of trapped electrons will also give a very good estimation of that of the total electron population. It instead represents a less accurate approximation when considering the regions outside of the main ion beam, where primary electrons are the dominant population.

Panel (b), on the other hand, shows the relative error committed when employing the

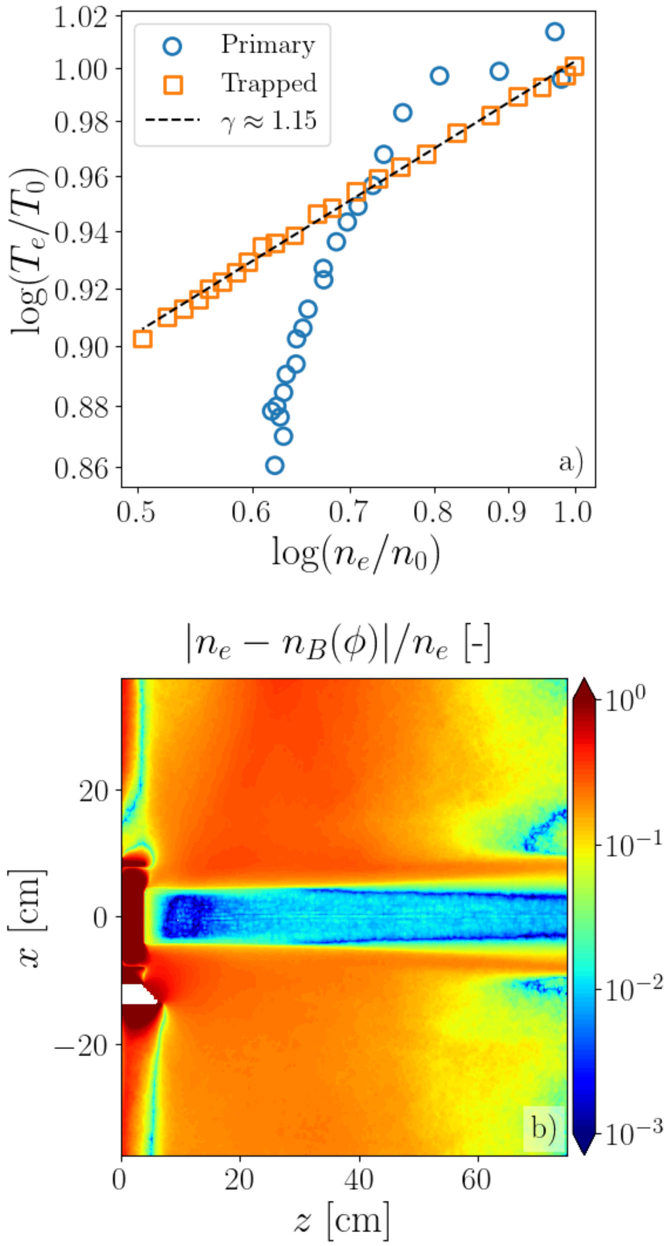

Figure 4.6: Panel (a) shows the relationship between the density and total temperature of primary (in blue) and trapped (in orange) electrons along the axis of the ion beam. The region of the initial plasma sheath was excluded from the plot, and the densities and temperatures were normalized to be 1 in the first point. Panel (b) shows the relative error obtained with the polytropic Boltzmann relation for the total electron density.

polytropic Boltzmann relation to obtain the density of the total electron population as a function of the local potential:

$$n_B(\phi) = n_0 \left[1 + \frac{\gamma - 1}{\gamma} \frac{\phi - \phi_0}{T_0} \right]^{\frac{1}{\gamma - 1}}, \tag{4.6}$$

where the reference density, potential, and temperature (n_0, ϕ_0 and T_0) were taken at the point of maximum density (roughly located at $x = 0$ and $z = 10.5\,\mathrm{cm}$) and $\gamma = 1.1475$ was used. As expected, such a Boltzmann relation appears to be mostly acceptable in the plume bulk, where trapped electrons (characterized by a near-Maxwellian VDF, and well-described by the polytropic law) are dominant, and instead provides larger errors in the outer regions of the plume where primary electrons prevail.

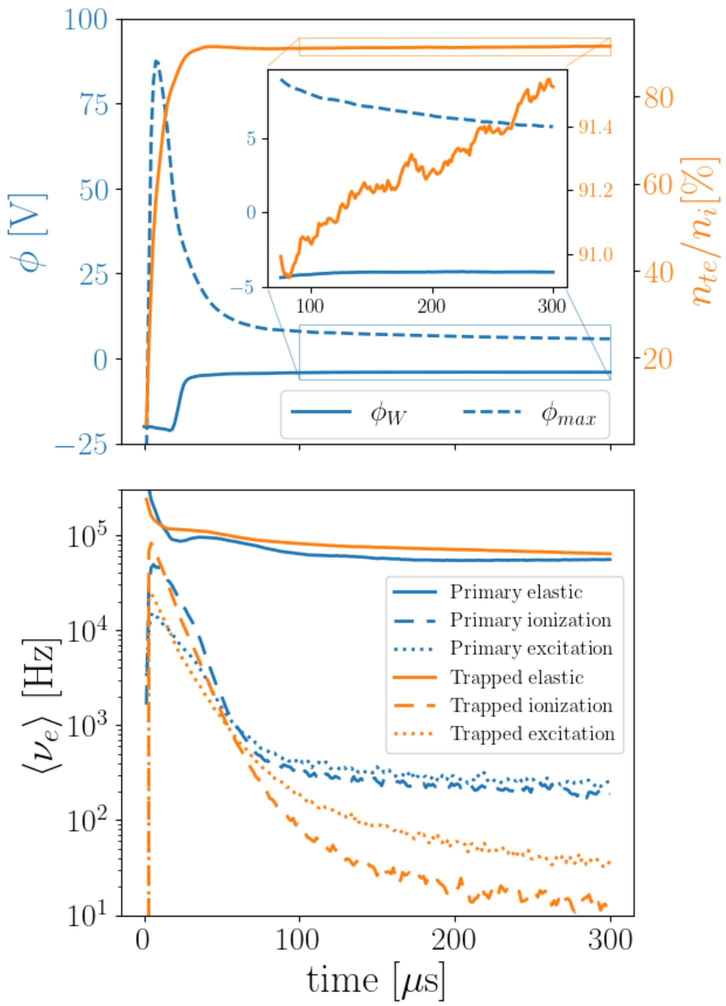

Figure 4.7: Panel (a) shows the convergence in time of the facility wall potential (dashed blue line), maximum potential value in the plume bulk (continuous blue line), and fraction of trapped electrons (orange line) for the reference simulation. Panel (b) shows the temporal trend of electron-neutral elastic (continuous lines) ionization (dashed) and excitation (dotted) collision frequencies for primary (in blue) and trapped (in orange) electrons, averaged over the whole simulation domain.

The steady-state of the simulation requires that an equilibrium is reached between the trapping and escape mechanisms described above, that determine the properties of the trapped electron population. This is a non-trivial process that may be better understood with the use of Figure 4.7. Here in panel (a) we show the temporal variation of the potential at the chamber walls with a continuous blue line, and the maximum of the potential along the plume axis (which is roughly located at $x = 0$, $z = 9\,\text{cm}$) with a dashed blue line. In orange, instead, we plot the ratio between the density of trapped electrons and the total density of ions around the point of maximum potential. The inlaid plot shows a zoom of the behaviour of these values in the last two thirds of the simulation, when the results are close to steady-state. Panel (b), on the other hand shows the profile in time of the average collision frequencies in the domain for primary (in blue) and trapped (in orange) electrons. It is apparent from this Figure that the value of ϕ_{max}, the fraction of trapped electrons present in the plume bulk, and the inelastic collision frequencies are intimately linked. During the initial transient, in fact, as the ion beam creates a region of high positive electric charge in front of the thruster grids, the plume potential rises to values close to $\phi_{max} = 90\,\text{V}$. This produces a strong potential ramp that accelerates primary electrons, injected at the cathode, towards the center of the ion beam with very high energies, leading to a profuse ionization and excitation of the neutral atoms emitted by the thruster and the decrease of the primary electron energy, which can thus become trapped in the plume. As the ratio of trapped electrons increases, they contribute to the neutralization of the ion beam, reducing the electric charge and consequently the value of the electric potential in the plume. This in turn diminishes the energy of the primary electrons arriving into the plume and the inelastic collision rate, slowing down the trapped electron production. As the simulation advances, the inelastic collision rate of primary electrons settles at a moderate value, dependent on the slight acceleration provided by the few volts of potential increase between the cathode and the ion beam, while the trapped electrons progressively cool down due to the sparse inelastic collisions (and the decrease of the potential barrier that traps them), causing their excitation and ionization frequencies to asymptotically approach zero. By the end of the simulation, the described trapping and escape mechanisms for trapped electrons almost balance each other out as steady-state is approached asymptotically. Indeed, the inlaid panel shows that the variation in the amount of trapped electrons n_{te} and maximum potential ϕ_{max} in the second half of the simulation is minor. It is important to consider that this asymptotic approach to equilibrium is characterized by a timescale linked to the inelastic collision frequencies, which at low electron energies are very low. We will in fact see in Section 4.6 that for the axisymmetric case, where the neutral densities and collision frequencies are even lower, this slow approach to steady-state will be further accentuated, to the point that an artificial acceleration mechanism will be proposed. For now, however, the considered simulation gets sufficiently close to steady-state in reasonable simulation times, so that no acceleration is needed, and we simply employ this case to stress that the slower dynamics of the problem should not be overlooked in the attempt to reduce the simulation's computational times. Finally note that the potential of the facility walls does converge to a constant value within the simulation time. As mentioned, in fact, ϕ_W is mainly determined by the primary electrons, and is therefore less affected by the slow build up of the trapped electron population.

These considerations highlight the importance of the correct inclusion of trapping mechanisms in simulations of the neutralization of GIT ion beams. Indeed, the underestimation of the trapped electron population leads to an overestimation of the potential rise in front of the grids of the thruster, which through Joule heating has led in previous works to excessively large electron temperatures, and to an increase in the beam divergence caused by the deceleration of ions at the thruster exhaust[32], [157]. The temperatures obtained here for trapped electrons (which as mentioned coincide with the total electron temperatures in the plume bulk) instead appear much closer to the typical values of around 2 eV obtained experimentally[164], [179]. We note, moreover, that Kozakov et al.[42] have recently shown that the trapped electron population may pose challenges also for experimental investigations. Intrusive probing of the plume, in fact, may provide an additional escape mechanism for electrons, which may now neutralize at the probe's surfaces. If the generation of trapped electrons is sufficiently slow this may strongly alter their equilibrium, depleting their population in the plume and causing an increase in the potential values in front of the thruster. This in turn can vary the general plume properties measured.

4.5. Sensitivity Analysis

The previous section has highlighted the importance of inelastic collisions in the plasma response. In order to confirm the physical mechanisms identified previously we present here two additional simulations: in the first we artificially decrease excitation and ionization cross-sections by a factor $f_{col} = 0.5$, and in the second we fully omit these collisions from the model. Moreover, the present section aims to study the sensitivity of the simulation results to some critically unknown input parameters of the model, such as the emitted current $I_{e,inj}$ and the temperature of the electrons injected by the cathode into the domain. As a result, two further simulations have been considered, in which the emitted cathode current and the electron temperature have been respectively doubled to $I_{e\,inj} = 8.46\,\mathrm{A/m}$ and $T_e = 6\,\mathrm{eV}$. Figure 4.8 compares the results of these four additional simulations with the reference one by plotting the densities and scalar temperatures of primary and trapped electrons, together with the electric potential and the electric charge density. These quantities are shown along the plume axis in the first column of plots, and in the lateral direction, 37.5 cm downstream of the thruster grids, in the second column. The results relative to the reference simulation are plotted in blue, while the cases with double electron temperature, double electron injection current, decreased inelastic collisions, and no inelastic collisions are respectively shown in green, red, purple and orange. To provide further information useful for the discussion of these results, Figure 4.9 shows a direct, bidimensional comparison between the reference simulation and the one without inelastic collisions, while Table 4.5 displays the steady-state values of the chamber potential for

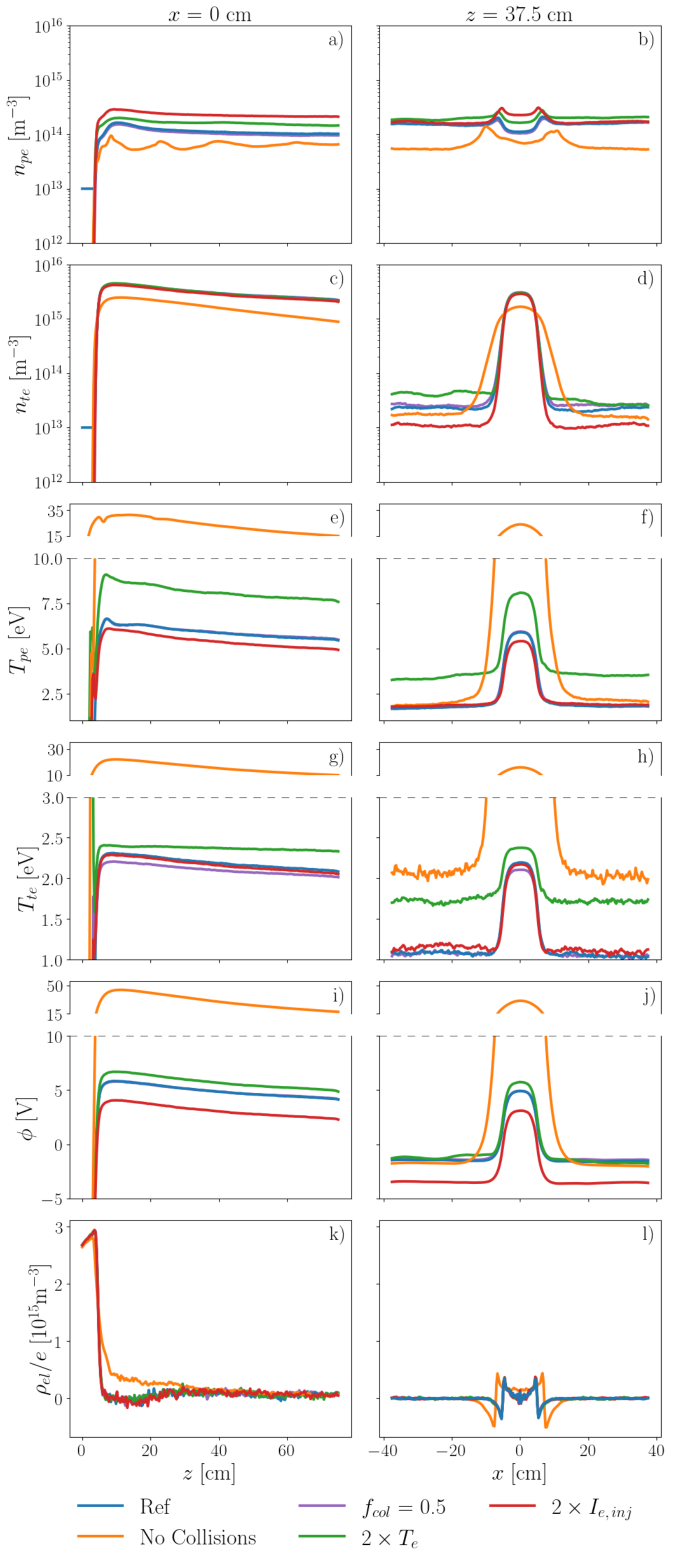

Figure 4.8: Comparison of the most relevant plasma properties obtained for the simulation scenarios considered. The first column of plots displays, in order, the primary and trapped electron densities, their temperatures, the electric potential, and the electric charge density along the ion beam axis. The second column shows these same quantities in the lateral direction, at the axial mid-line of the domain. Note that the results of the reference and mildly collisional (f_{col} = 0.5) simulations often perfectly overlap in the plots.

each case.

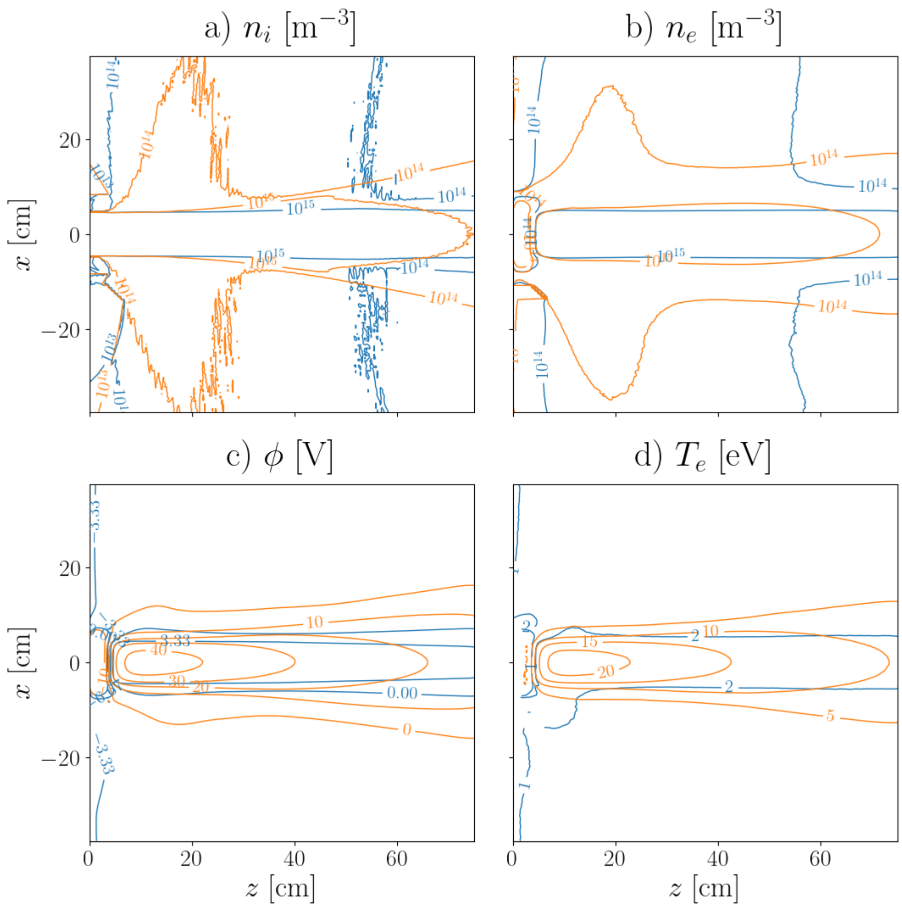

Figure 4.9: Comparison between the maps of total ion density, total electron density, electric potential and total electron temperature obtained for the reference simulation (in blue) and the simulation with no inelastic collisions involving electrons (in orange).

It is clear from Figures 4.8 that there is a strong discrepancy in all the plotted values between the simulation with no inelastic collisions and the other cases, to the extent that a break in the abscissas of the temperature and potential plots was required for visualization purposes. The cause of this variation has already been introduced in the previous sections: the absence of inelastic collisions removes one of the most prominent electron trapping mechanisms, strongly reducing the trapped population as shown by panels (c) and (d). This in turn leads to a reduced neutralization of the ion beam (note the positive electric charge present downstream of the acceleration grid in panel (k)) and a hefty increase in the plume's electric potential (see panel (i) and Figure 4.9(c)). The result is that fast ions undergo a stronger deceleration in front of the thruster grids, leading to the larger plume divergence observable in all plots of the second column. Moreover, the primary electrons accelerated into the plume gain a large amount of kinetic energy from the strong potential rise between the cathode and the plume bulk, which translates into the considerable values of the primary electron temperature observed in panels (e) and (f), and in the total electron temperature of Figure 4.9 (d). Once accelerated into the plume, a portion of the primary electrons may bounce on the plume edges, moving with a zig-zag motion downstream.

Case	ϕ_W [V]
Ref	-4.02
$2 \times T_e$	-7.49
$2 \times I_{e,inj}$	-6.30
$f_{col} = 0.5$	-4.01
No Collisions	-4.03

Table 4.5: Values of the facility wall potential for the simulation scenarios considered.

This kind of bouncing trajectory is present also in the collisional cases, but is damped by the inelastic collisions and by the gradual energy loss of these electrons that eventually fall into the trapped population. As a consequence, the density peaks, that are observed only for the collisionless case in the primary electron density of panel (a), indicate the positions where the beam of bouncing primary electrons crosses the plume axis. Similarly to primary electrons, trapped electrons for the collisionless case also display a substantial scalar temperature, which can be attributed to the large trapping potential drop found at the edges of the plume, capable of trapping electrons with a wide spread of velocities.

On the other hand, the simulation with reduced but still present inelastic collisions provides at steady-state results in excellent agreement with the reference scenario, to the point that the blue and purple lines often perfectly overlap in Figure 4.8. This steady-state is reached, however, in double the simulation time t_{ss}, indicating that it is the simple presence of a collisional trapping mechanism for electrons that relevantly modifies the simulation results, not its strength. More collisional or less collisional simulations will in fact require shorter or longer transients, but will eventually approach the same steady-state. Finally, note that the facility wall potential shown in Table 4.5 for the collisionless case is nearly identical to the one obtained with the reference and mildly collisional simulations. As already mentioned, in fact, the value of ϕ_W is strongly insensitive to the trapped electron properties, which is the electron population most affected by the exclusion of inelastic electron collisions. In fact, while the maps of the primary electron properties vary due to the changes in the potential profiles in the domain, the total energy of each primary electron, which is what determines whether it reaches the chamber walls or not, is essentially unaffected due to the conservative nature of the electric forces.

Conversely to the case with no inelastic collisions, the cases with a doubled injection electron temperature or current appear to influence mostly the properties linked to the primary electron population, while leaving the characteristics of trapped electrons mostly unvaried. Figures 4.8(c) and 4.8(d), in fact, display a negligible variation within the main ion beam both in the axial and lateral profiles of the trapped electron density for these two cases. Similarly, also the trapped electron temperature shown in Figures 4.8(g) and 4.8(h) appears to be mostly insensitive to the injected electron current, and only mildly dependent on the injected electron temperature. Interestingly in this latter case the trapped electron population is essentially isothermal along the plasma plume, causing it to become progressively warmer than in the reference case as one moves downstream. These negligible variations in the trapped electron population cause an identical neutralization of the ion beam throughout all three simulations, as demonstrated by panels (k) and (l), which leads to the very similar profiles of the electric potential observed in panels (i) and (j). The upward or downward shifts of these profiles with respect to the reference simulation are instead linked to the primary electron population. Note, in fact, that the primary electron properties are directly connected with the injection parameters at the cathode: doubling the injection temperature causes the temperature values of primary electrons to be roughly doubled (see panels (e) and (f)), while increasing the injected current causes an increase in the primary electron densities (panels (a) and (b)). Because this electron population groups the more energetic electrons present in the domain, which are therefore capable of further penetrating inside the Debye sheaths found at the edges of the plasma plume (i.e. in front of the thruster grids and at the chamber walls), it is the one mostly responsible for the determination of the sheaths' potential drop. According to classical sheath theory, in fact, the potential drop in a Debye sheath is known to be proportional to the electron temperature, causing the larger potential rise in front of the acceleration grid for the simulation with the increased electron temperature, and as a consequence the upward shift of its potential profile with respect to the reference simulation. The larger electron temperature in this simulation also accentuates the average energy of the primary electrons at the domain edge, explaining the low value of the chamber potential of Table 4.5 which is necessary to maintain the electron current to the walls equal to the ion one. A similar mechanism takes place for the case of the increased electron current, where more electrons must be reflected back into the domain at the outer boundaries to maintain $I_{eW} = -I_{iW}$. This causes the decrease of the facility potential with respect to the reference case shown in Table 4.5, which in turn drags down the entire potential map decreasing the potential values in comparison to the reference scenario.

4.6. Axisymmetric Simulation

In order to obtain a more faithful description of a real GIT plume, the simulation of a three-dimensional expansion is necessary. Nevertheless, the employed PIC code PICASO is bi-dimensional in space, and we therefore make use of axisymmetric simulations to achieve a 3D description of the plume. While this implies the simulation of an annular cathode that surrounds the ion source, and the consequent symmetrization of the real system, we believe this to be an acceptable approximation for our purpose. Indeed, all of the previous planar and asymmetric simulation results show that all asymmetry is lost immediately downstream of the cathode, and that the main bulk of the ion beam is symmetric. Analogously to the previous planar case, we therefore first ran a three-dimensional plume simulation in the hybrid code EP2PLUS to retrieve the neutral density map, which was then imported into PICASO. Note that, because of the additional dimension of the expansion, the density map obtained for this 3D case is relevantly more sparse with respect to the one shown in Figure 4.1 (see Appendix 4.A).

4.6.1. Approach to steady-state and simulation acceleration

Because of the lower values of neutral density obtained, and considering that the characteristic time of the formation of the trapped electron population is strongly linked to the frequency of inelastic collisions with neutrals (as discussed in Section 4.4 and 4.5), relevantly longer simulation times will be necessary for this axisymmetric case to approach steady-state. Nevertheless, the residence time t_{res} of trapped electrons in the domain is theoretically infinite, so that the number of inelastic collisions that they undergo is not delimited by $t_{res}/t_{col} \rightarrow \infty$ (with t_{col} the mean period between collisions), but by the ratio between the electron energy and the collision energy. It therefore stands to reason that the simulation times may be importantly reduced, without changing the underlying physical mechanisms and the final steady-state solution, by increasing by a factor f_{col} the inelastic collision cross-sections, and therefore the collision frequency, of trapped electrons. Indeed, the sensitivity analysis of the previous section already showed negligible variations in the simulation results when altering the inelastic collision frequencies (although in that case we were varying the collisionality of all electrons, not only of the trapped electron population).

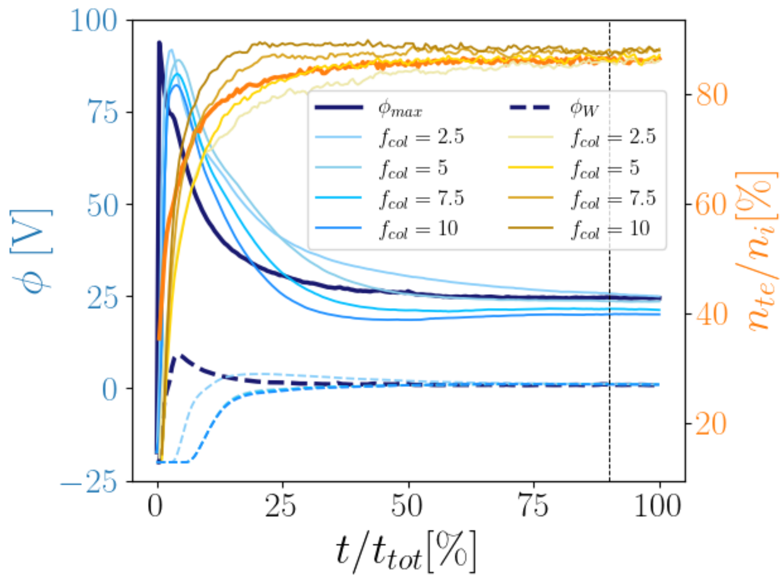

Figure 4.10: Temporal trend of the facility wall potential (dashed blue lines), maximum potential in the plume bulk (continuous blue lines), and fraction of trapped electrons (orange lines) for the unaccelerated and accelerated cases. Because of the different simulation lengths the x-axis shows the fraction of the total simulation time. The dashed vertical black line shows where the collision cross-sections were reset to their physical values.

To further confirm this we have run a total of five axisymmetric simulations: the first one with no acceleration factor on the collision cross-sections and a relatively large total simulation time $t_{ss} = 3\,\mathrm{ms}$, and the others with progressively increasing acceleration factors of $f_{col} = 2.5, 5, 7.5$, and 10, and proportionally decreasing simulation times. The cross-sections of all the accelerated simulations were reset to their physical values in the last tenth of each simulation, in order to avoid a non-physical ionization production at steady-state and to confirm that no relevant variations of the plume properties could be attributed to f_{col}. It must however be mentioned that similar simulations were run in which f_{col} was kept constant throughout the whole duration, and no visible changes were observed in the simulation results. Figure 4.10 displays once more the convergence of the maximum potential ϕ_{max}, facility wall potential ϕ_W and trapped electron fraction n_{te}/n_i for the simulations considered. Note that the non-accelerated simulation is shown with thicker dark blue and orange lines, while progressively darker thin lines are used for simulations with incrementing acceleration factors. It is immediately clear that the acceleration factor has only a minor effect on the plotted values for all of the considered cases. However, for values of $f_{col} > 5$ a slight overshoot of the fraction of trapped electrons, and a consequent undershoot of ϕ_{max} may be observed, which eventually leads to slightly lower values of the steady-state maximum potential. This is likely due to excessive inelastic collisions during the initial simulation transient, where the energy of trapped electrons is still very high and their residence time is not truly infinite because of the variation in time of the potential map. However, for $f_{col} \leq 5$ the steady-state values of the accelerated and non-accelerated simulations are indistinguishable. We therefore infer that, for this specific scenario, a simulation speed-up of roughly a factor 5 is possible with this technique without sensibly altering the steady-state results. This is confirmed by Figure 4.11, where the comparison between the axisymmetric simulation results for the non-accelerated case (in the upper portion of each plot) and the case with $f_{col} = 5$ (below), shows that negligible effects may be attributed to the acceleration technique introduced.

4.6.2. Simulation results

Regarding the plume response a few differences with respect to the planar case may be noticed in Figure 4.11. The first observation, and the more relevant from the point of view of the general plasma response, consists of the higher potential values shown in the bottom right plot when compared to those of the planar case. This is a consequence of the lower trapped electron density obtained here, which causes a worse neutralization of the ion beam, as shown by the charge density plot. The physical causes that lead to a lower trapped electron density in this case are not fully clear to the authors, as they likely depend on the complex equilibrium between the trapping and escape mechanisms that govern this electron population. The result, however, is the formation of a slightly more divergent plume, due to the the potential rise in front of the grids that reduces the axial velocity of the injected fast ions.

The second thing immediately noticeable in Figure 4.11, is the very low density of the primary electrons displayed in panel (b). Similarly to the case of the neutral density, this is simply explained by considering the additional direction of expansion that is now

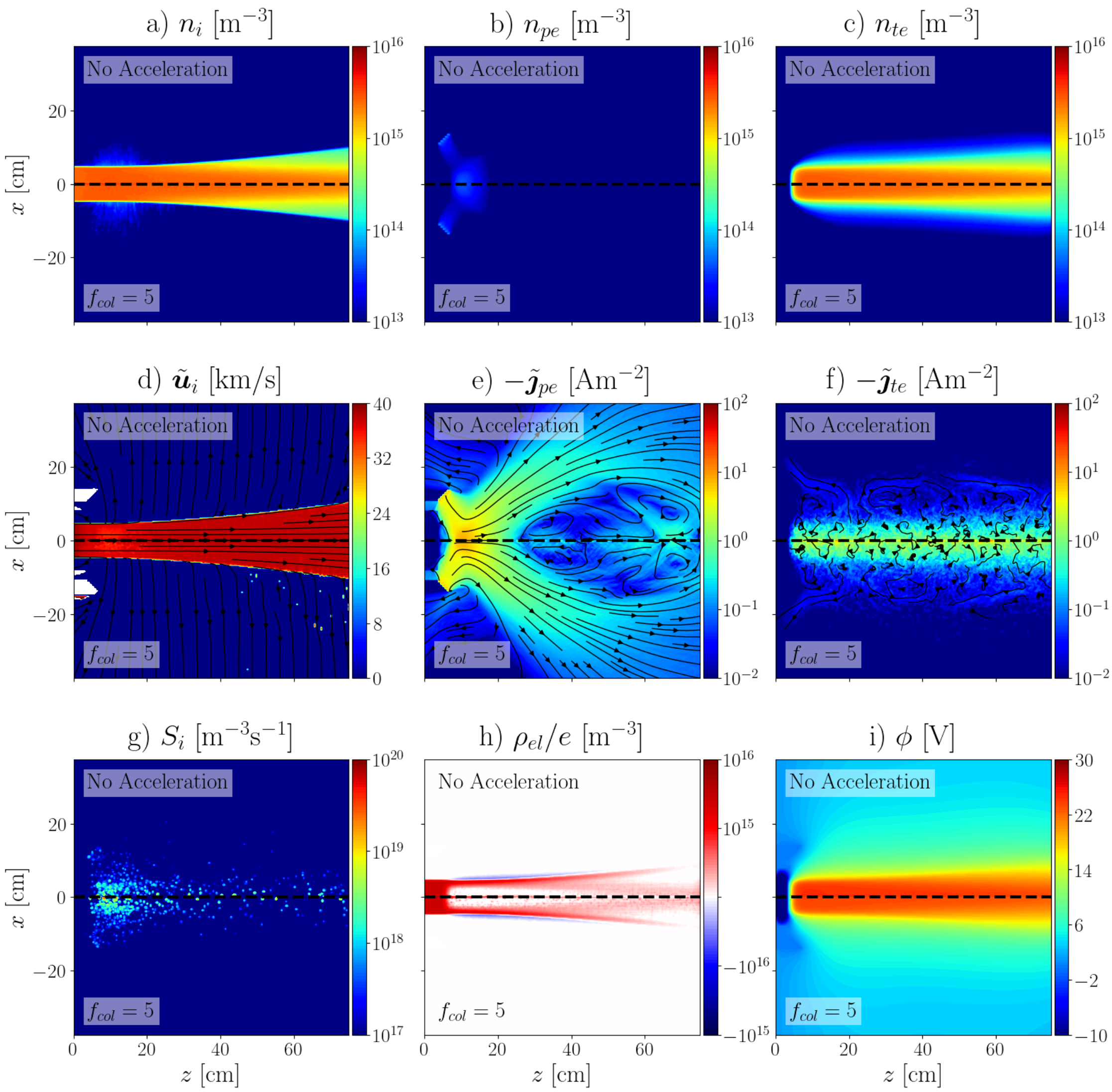

Figure 4.11: Comparison of the steady-state plasma properties obtained for the non-accelerated (upper portion of each plot) and accelerated (below) axisymmetric cases. From left to right and from top to bottom the panels show the total ion density, and the primary and trapped electron densities; the total ion velocity and the primary and trapped electron currents; and the ionization production term, the charge density and the electric potential. In panels (d), (e) and (f) the black arrows represent the velocity and current streamlines.

available to these electrons. In fact, while fast ions and trapped electrons essentially form a mono-dimensional beam, neutrals, slow ions and primary electrons are free to expand in all directions, causing a relevant decrease in their density when moving from a 2D to a 3D expansion. Note also that the motion of primary electrons described by panel (e) is slightly different in this axisymmetric case with respect to the planar one. These electrons, in fact, emitted by an annular cathode, cross radially the ion beam and are then re-attracted towards it by its positive space charge, causing the curvature of the current streamlines back towards the axis of symmetry. At the downstream boundary a portion of these primary electrons are reflected by the BCs imposing a current-free plume and return upstream, forming the current 'vortex' observed in the second half of the domain close the the plume's center-line.

Except for these variations, the axisymmetric simulation qualitatively behaves analogously to what has already been discussed for the planar cases. Fast ions are slightly decelerated in the Debye sheath in front of the grids, and then continue their axial motion, while slow ions are accelerated laterally (see the total ion velocities of panel (d)). Primary electrons accelerate through the ion beam and then reach the chamber walls on the opposite side (panel (e)), and the trapped ones only display a chaotic motion inside of the plume's bulk (panel (f)).

4.7. Conclusions

In this work we have employed our in-house 2D PIC code PICASO to simulate and study the expansion and neutralization process of a gridded ion thruster plume both in planar and axisymmetric geometries. Importantly, these simulations consider a library of collisional processes, including inelastic electron collisions such as ionization and excitation of the neutral background. These latter collisions were observed to be one of the primary mechanisms responsible for the generation in the plume of two distinct electron populations termed 'primary electrons' and 'trapped electrons' depending on their ability to escape the plume's potential well.

By using an energy-based criterion it was possible to sort the primary and trapped electrons in the simulations into separate lists, enabling the study of the generation mechanisms and properties of each population. Those electrons trapped in the potential well formed by the ion beam were found to represent the vast majority of the total electron population at steady-state, thus essentially determining the total electron density and temperature in the plume bulk. Because these electrons have a large residence time in the plume they undergo numerous collisions, and are thus characterized by an undrifted Maxwellian VDF (depleted at the high energy tails) and by moderate and isotropic values of the temperature tensor. As a consequence, the even moments of the tapped electron VDF (i.e. density and temperature) can be well approximated both by a polytropic law and by the Boltzmann relation, while all odd moments (e.g. particle flux and heat flux) are negligible. The formation of this electron population via inelastic collisions was found to be fundamental for the neutralization of the plume and the lowering of the maximum potential and electron temperature values observed downstream of the thruster grids. Indeed, our collisional simulations gave results in good agreement with the typical values for these experimental measurements in GIT plumes, while simulations that forego the inclusion of inelastic collisions were observed to underestimate the size of this population, and as a consequence to importantly overestimate the electron temperature and potential in the plume. Importantly, because of the small inelastic collision frequencies in a typical GIT plume, the collisional generation of trapped electrons is slow, meaning that this population will be sensitive to any perturbation (e.g. plasma probes) that may extract even small currents of trapped electrons from the plume. Finally, the properties of trapped electrons were found to be largely independent on the cathode injection conditions, and appeared mostly affected by the collisional processes considered in the simulations.

On the other hand, primary electrons, injected from the cathode and predominant at the outer edges of the plume, were observed to have a low residence time in the simulation domain, and as a consequence undergo a limited number of collisions and display large and anisotropic values of the temperature tensor. Because the odd moments of the trapped electron VDF are negligible, this electron population provides the total currents and heat fluxes of electrons in the plume, and as a consequence is also fundamental in determining the thruster's floating potential. A sensitivity analysis also showed that the steady-state equilibrium of this electron population is strongly dependent on the cathode injection properties, but that in any case the net primary electron current emitted by the cathode adjusts to provide a current free plume by means of the formation of a sheath in front of the cathode and the evolution of the thruster's floating potential. Finally, a study of the simulation transient revealed that these are the electrons that, accelerated into the ion beam, generate through inelastic collisions the trapped electron population.

The characteristic time for the formation of the trapped electron population was found to depend on the timescales of the inelastic collisions that generate them, extending noticeably the required simulation times to approach steady-state. As a consequence an acceleration strategy employed to speed-up the the simulations was presented for the case of an axisymmetric domain. This strategy, which consists in the artificial increase of the cross-section of inelastic collisions involving the trapped electron population, was shown to allow a reduction in simulation times of up to a factor 5 without influencing the steady-state results. The axisymmetric simulations thus obtained, which allow a three dimensional description of the plume expansion, displayed many of the characteristics of the planar case analyzed previously, but also showed a smaller fraction of trapped electrons, responsible for a larger potential increase in front of the thruster grids, and an increased divergence of the plasma plume. Because of the additional dimension in the simulated expansion the density of neutrals and of primary electrons also sharply decreased.

As a final remark, we would like to acknowledge the necessity of an experimental validation of the theoretical findings presented in this work. One approach to investigate the presence and effects of a trapped electron population could be to insert differently sized and biased electrodes in a GIT's plume. Because of the slow generation mechanism of trapped electrons, in fact, these electrodes would collect them and possibly lead to the depletion of their population, allowing a first experimental determination of their energy, production rate, and effect on the plume structure.

Acknowledgements

The authors would like to thank Konstantin Keil, Kristof Holste and Peter J. Klar from the Justus-Liebig Universität of Gießen for their invaluable help in the definition of the geometrical, electrical and operative properties of the RIT10-EVO, employed for the setup of the simulations presented. This work has been supported by the ECOMODIS project, funded by the European Space Agency, under contract 4000137869/22/NL/RA

Appendices

4.A. Hybrid Simulation

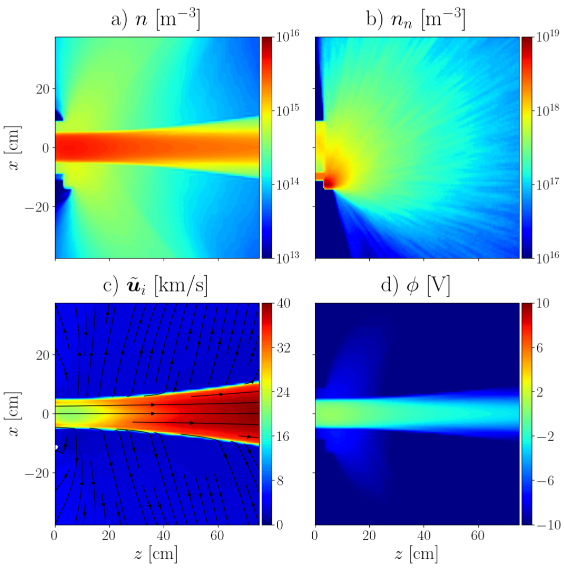

Figure 4.A.1: The plasma density, neutral density, ion velocity and electric potential for the planar case obtained with the quasi-neutral hybrid code EP2PLUS

Figures 4.A.1 and 4.A.2 show respectively the plasma properties obtained for the planar and axisymmetric cases with the quasi-neutral, hybrid code EP2PLUS. Notice that, while qualitatively the plume shape and the plasma densities match the ones obtained with PICASO, the values of electric potential and the behavior of the ion velocity display some marginal differences. Interestingly, the main variations observed in the PIC simulations when passing from the planar to the axisymmetric case are also seen here (e.g. the decrease of the density in the CEX wings and the increased plume divergence). Finally, note that, because the code is quasi-neutral, the Debye sheath in front on the thruster grids is here assumed infinitesimal, and described by means of an analytical model.[29]

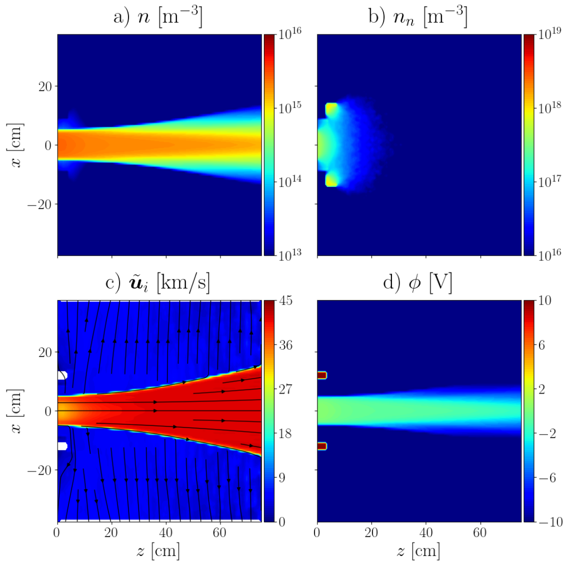

Figure 4.A.2: The plasma density, neutral density, ion velocity and electric potential for the axisymmetric case obtained with the quasi-neutral hybrid code EP2PLUS

4.B. Effects of the Artificial Vacuum Permittivity

The reference simulation presented and discussed in Sections 4.3 and 4.4 has also been run with an augmentation factor $f_D = 10$ in order to evaluate the effects of artificially increasing the vacuum permittivity. This decrease of the augmentation factor implies a doubling of the number of cells in each dimension and a decrease of the simulation time-step by a factor 2, ultimately increasing the computational burden by a factor 8. Figure 4.B.1 compares the quantities most sensitive to a variation in the vacuum permittivity (i.e. the electron properties and the electric potential) along the axis of the ion beam and at a lateral section with $z = 37.5$ cm. The most evident variation is the reduction of the size of the Debye sheath in front of the acceleration grid as f_D decreases, which also implies the presence of electrons at a shorter distance from the grids. Downstream of this sheath the electric potential reaches slightly lower values for the case with a smaller augmentation factor, and this minor shift between the two potential values is then kept constant throughout the domain. Indeed, the electric fields in the two simulations are essentially the same beyond the initial sheath. These lower potential values for the case of $f_D = 10$ are also responsible for a decrease in the electron temperatures shown in panels (g) and (h). Finally, all lateral profiles do not seem to suffer particular changes when varying the vacuum permittivity, except for the one of the trapped electron density. In any case this latter quantity remains between 2 and 5 times smaller than the primary electron density in the plume periphery, and therefore represents only a marginal fraction of the total electron density in this region of the domain. These small discrepancies between the two simulations are likely due to the different size of the Debye sheath in front of the acceleration grid, where the finite discretization of the electron VDF by means of macro-particles means that the electron density decreases identically to zero in some cells. A different dimension of this region with a null electron density leads to slightly different potentials, and to the differences observed between these two simulations.

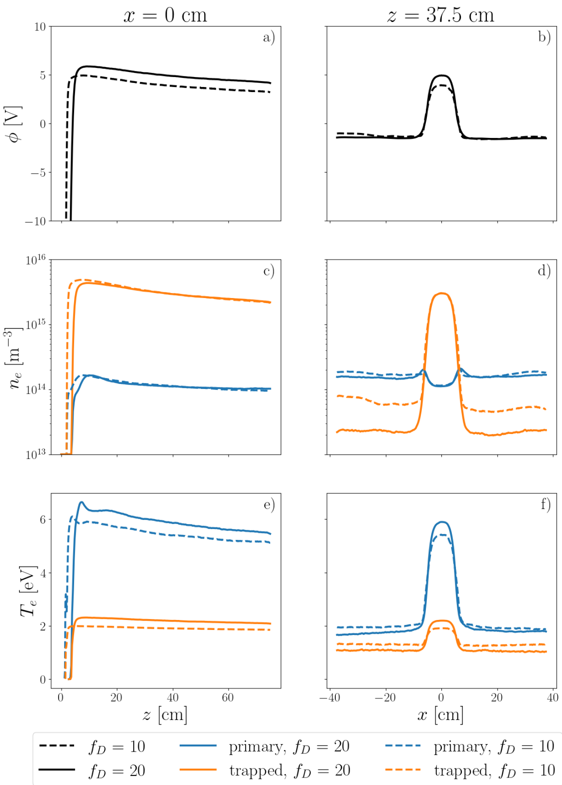

Figure 4.B.1: Comparison between the plasma properties obtained with acceleration factors $f_D = 20$ (continuous lines) and $f_D = 10$ (dashed lines).

CHAPTER 5

Numerical and Experimental Study of Facility Effects on a Gridded Ion Engine's Plasma Plume

This chapter reproduces the contents of Ref. [50], published in a special issue dedicated to facility effects in the peer-reviewed Journal of Applied Physics. The typography has been adapted to the style of this thesis.

Abstract

Combined numerical and experimental investigations of facility effects on gridded ion engines and their plumes are necessary to improve the extrapolation of experimental data to in-space conditions. This work presents —for different operating points, background pressures, and thruster potentials— the comparison between the experimental characterization of the RIT10-EVO's plasma plume and its simulations by means of an axisymmetric particle-in-cell code. The axial and radial profiles of the ion densities, energies and axial currents in the thruster's plume, as well as the electron temperature in the far plume computed by the code fall within experimental error bars. The electron temperature closer to the thruster, and the radial energies of backstreaming ions outside of the plasma beam, are instead underestimated by respectively about 4 eV and 20 eV. Simulations that include an immersed probe in the modeled plume do not fully explain this mismatch, but showcase an important dependence of the plume's potential on the probe's biasing voltage, hinting at a possible deformation of the measured IV curve. A closer inspection of the effects of the facility background pressure reveals that both experiments and the numerical model observe an increase in plasma density, a drop in electron temperature and a decrease in the backstreaming ion energy as the neutral density rises. Similarly, both simulations and experiments show an increase of the energy of backstreaming ions, and

the formation of a negative net current flowing from the thruster to the facility walls, when the thruster potential with respect to ground is decreased.

5.1. Introduction

The performance of gridded ion engines (GIE), the behavior of the plasma plume that they produce, and its interaction with the surfaces of the hosting satellite are principally studied through experiments carried out in ground facilities. These analyses make the assumption that the thruster's behavior will not be altered by the differences between the experimental and in-space conditions. However, numerous studies suggest that this is not the case, and that an ensemble of mechanisms, generally collected under the term "facility effects", may cause relevant variations in the properties of the thruster and its plume when operated in an experimental facility rather than in space.[26], [180], [181] The most evident and well documented among these are: (i) the larger density and different distribution of background neutral atoms found in an experimental facility[182], that increment the plume's collisionality and lead to the formation of low energy ions[29], [183] and electrons[49]; (ii) the presence of facility walls, that truncate the plasma expansion at a finite distance from the thruster[31], [39], introduce in the plume additional neutral particles and electrons through recombination, sputtering and secondary electron emission[42], [184], and set artificial boundary conditions for the electric potential[31]; and (iii) the use of immersed probes (or in general any immersed electrode) employed to measure the plasma properties and that may offer current paths to ground that are not present in space.[42], [49]

The presence of these facility effects means that an exact extrapolation of experimental data to in-space operating conditions is not trivial, especially for high power density applications that impose even more challenging requirements on the facility size and pumping rate.[184], [185] Important modeling efforts are therefore required in close collaboration with experimental studies to understand and isolate these effects, allowing a more accurate prediction of the thruster's operation in space. Recently, relevant contributions have been made in this direction by Nishii *et al.*. Their work first investigated, through a 3D full PIC code, the effect of facility background pressure and the sputtering of the chamber walls caused by high energy ions[158], and later concentrated on the analysis of the neutraliser's coupling with the thruster's ion beam.[32] Similarly, our previous work[49] —of which the present document is a natural continuation— developed a 2D full PIC model and applied it to study the fundamental physical mechanisms that lead to the neutralisation of a GIE plume. A major conclusion of that work is that inelastic electron collisions play a prominent role in the efficient neutralisation of the positive space-charge of the GIE's ion beam, and in the mitigation of the electric potential values in the plume. These collisional processes, in fact, cause the reduction of the total energy of electrons coming from the neutraliser (termed primary electrons as long as they have enough energy to escape from the plume), allowing their trapping within the plume's potential well and restraining the electron cloud within the ion beam (*i.e.* forming a trapped electron population)[47], [130]. As a consequence, the plume's neutralisation process takes place with time-scales dictated by the relatively slow inelastic collision frequencies of electrons, and may be perturbed by any mechanism that provides an efficient escape path to the trapped electrons.

While many different GIE plume models are present in the literature [29], [32], [150], [153], [159], only a few have been compared with existing experimental data [30], [32], [42], [186], and to the authors' knowledge none have undergone a dedicated and extensive validation campaign. In this work we attempt to validate the 2D axisymmetric, full PIC model presented in Ref. [49] —and the physical insights and conclusions discussed therein— by means of a thorough comparison with experimental data. To this end, measurements of the plasma plume of Ariane's RIT10-EVO were carried out at the Justus-Liebig-Universität (JLU) in Gießen for different background pressures and electrical configurations of the thruster with respect to ground [187], and are here compared with the model's results[188].

The remainder of this paper is structured as follows. Section 5.2 gives a general overview of the RIT10-EVO, its neutraliser, and the different operating conditions in which their plume was studied, before descending into the details of the experimental (Sec. 5.2.1) and numerical methodologies (Sec. 5.2.2). Section 5.3 then employs one of the operating conditions as a representative example of the comparison between the numerical and experimental results. This comparison is extended to the other operating conditions in Section 5.4, where the experimental and numerical response of the plume to variations in the background pressure and thruster potential are analyzed. Next, Section 5.5 provides a qualitative evaluation of the disturbances caused by the immersion of a probe in the plume, while Section 5.6 discusses the main sources of uncertainties in the model, and their relation to the discrepancies between numerical and experimental results. Finally, Section 5.7 summarizes the main conclusions and remaining open-points of this work.

5.2. Methodology

The RIT10-EVO is a medium-power radio-frequency ion thruster[16], [168], [189] provided by ArianeGroup, with a thrust range of 5–25 mN and a corresponding power range of 145–760 W. Its body has a total diameter of 16 cm at the center of which is located a grid system —composed of a screen grid and an acceleration grid— of 10 cm in diameter. During the test campaign the neutralisation of the ion beam was guaranteed by a radio-frequency neutraliser developed by ArianeGroup[190], with a total diameter of 7.8 cm and a 2 mm aperture in the extraction plate, positioned above the thruster and inclined towards the ion beam with an angle of roughly 45°. The neutraliser was operated with a fixed Xenon mass flow of 0.8 sccm and in electrical contact with the thruster, so that all its external surfaces were at the same potential as the thruster body. For this work the thruster was studied experimentally and numerically in the 12 distinct operating conditions detailed in Table 5.1, obtained as a combination of two operating points of the thruster (O1 and O2), three background pressures BP (P1, P2 and P3), and up to five values of the thruster potential with respect to ground V_t (an electrically floating thruster, and the prescribed potential differences of -15, -20, -25, and $-30\,\mathrm{V}$). Note that, in the case of O2, the thruster floated at $V_t \approx -20\,\mathrm{V}$ making the values of -15 and $-20\,\mathrm{V}$ impossible to impose with the voltage supply used during experiments. The corresponding operating points therefore were not investigated and are not present in Table 5.1.

Table 5.1: Operating conditions in which the plume of the RIT10-EVO was studied. Here I_i, ΔV, and $\dot{m}$ represent respectively the ion current, the potential difference between the thruster grids, and the Xenon mass flow at which the thruster is operated.

	Operating Point				
	I_i [mA]	ΔV [V]	$\dot{m}$ [sccm]	BP [mbar]	V_t [V]
O1 P1 F	100	1150	2.0	$4{\times}10^{-6}$	float[a]
O1 P2 F	100	1150	2.0	$4{\times}10^{-5}$	float[a]
O1 P3 F	100	1150	2.0	$8{\times}10^{-5}$	float[a]
O1 P1 V2	100	1150	2.0	$4{\times}10^{-6}$	-15
O1 P1 V3	100	1150	2.0	$4{\times}10^{-6}$	-20
O1 P1 V4	100	1150	2.0	$4{\times}10^{-6}$	-25
O1 P1 V5	100	1150	2.0	$4{\times}10^{-6}$	-30
O2 P1 F	200	1350	4.0	$4{\times}10^{-6}$	float[a]
O2 P2 F	200	1350	4.0	$4{\times}10^{-5}$	float[a]
O2 P3 F	200	1350	4.0	$8{\times}10^{-5}$	float[a]
O2 P1 V4	200	1350	4.0	$4{\times}10^{-6}$	-25
O2 P1 V5	200	1350	4.0	$4{\times}10^{-6}$	-30

[a] Thruster is electrically floating with respect to ground

5.2.1. Experimental Setup

The experimental data presented in this work was collected in the JUMBO vacuum test facility at JLU: a cylindrical vacuum chamber of 2.6 m in diameter and approximately 6 m in length. The chamber is equipped with four turbopumps with a combined Xenon pumping speed of $4000\,\mathrm{L\,s^{-1}}$ and eight cryogenic panels with a total pumping speed of approximately $150\,000\,\mathrm{L\,s^{-1}}$, that allow a baseline facility background pressure of $2{\times}10^{-7}$mbar. The chamber pressure is constantly measured by two Pfeiffer PKR251 cold cathode vacuum gauges (located at the front and center of the facility) and a Pfeiffer PBR260 Bayard-Alpert vacuum gauge (behind the thruster). At the opposite end of the facility with respect to the thruster a water-cooled carbon beam dump is installed. The background pressures P2 and P3 reported in Table 5.1 were obtained by operating only with the turbopumps and, for the higher pressure values, by feeding additional neutral Xenon gas into the center of the chamber, about 1.5 m downstream of the thruster exit plane. Finally, the control of the potential of the thruster-neutraliser combination was ensured by mounting it on an isolating Teflon plate, and when necessary biasing it with respect to ground using a CPX200DP power supply from Aim-TTi. The resulting thruster potential was continuously measured during operation using a digital multimeter.

An image of the RIT10-EVO and RF-neutraliser, mounted in the JUMBO facility is presented in Figure 5.1, while Figure 5.2 shows a sketch of the thruster inside of the vacuum vessel, and displays the locations and types of measurements carried out for each operating condition considered. These are further detailed below.

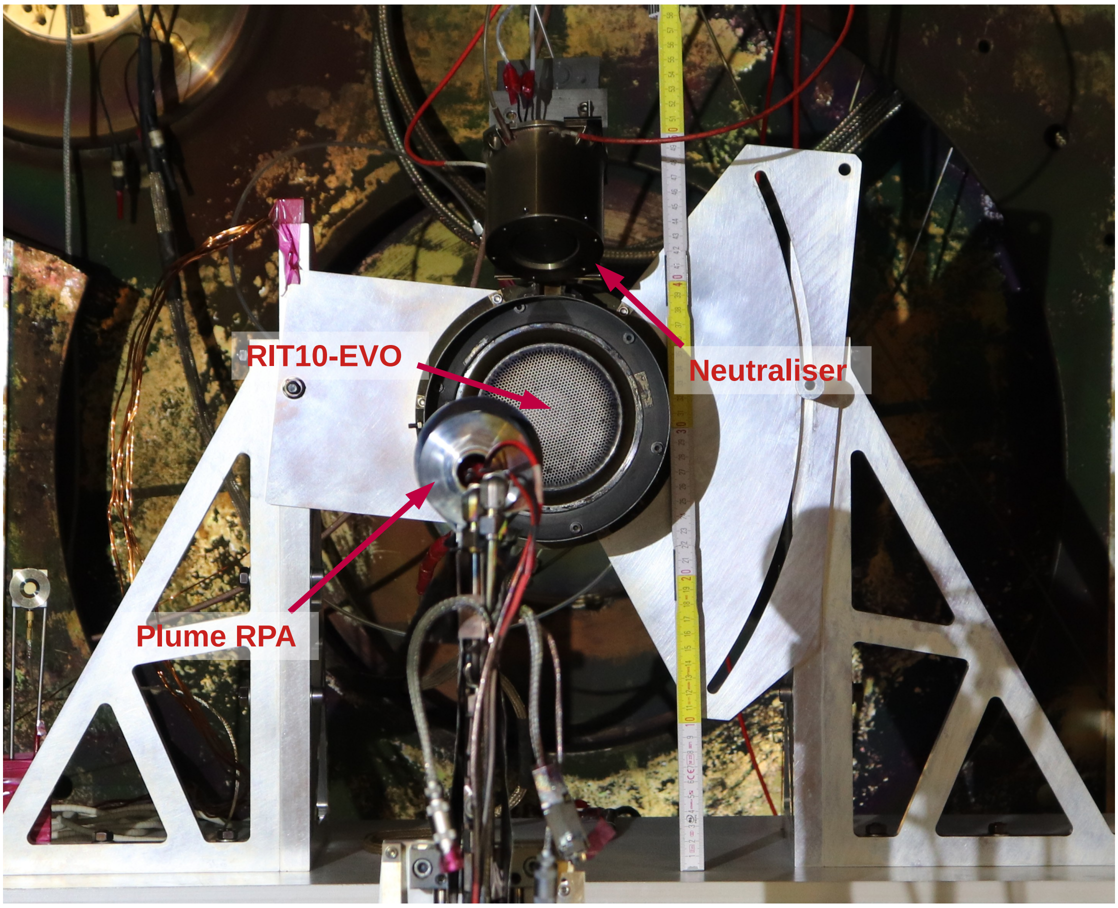

Figure 5.1: The RIT10-EVO mounted in the JUMBO facility at JLU with the RF-neutraliser positioned above it, and the plume RPA in front of it at $z = 30$ cm.

5.2.1.1 Double Langmuir Probe

A double Langmuir probe (DLP) was employed for the determination of the plasma density and temperature. The probe, manufactured in house, is composed of two 6 mm long and 0.3 mm thick tungsten wires connected to a Keysight B2901A Precision Source Meter via shielded cables in a four-wire configuration. Measurements were taken by biasing one wire with respect to the other at three axial distances from the thruster: $z = 10$, 30, and

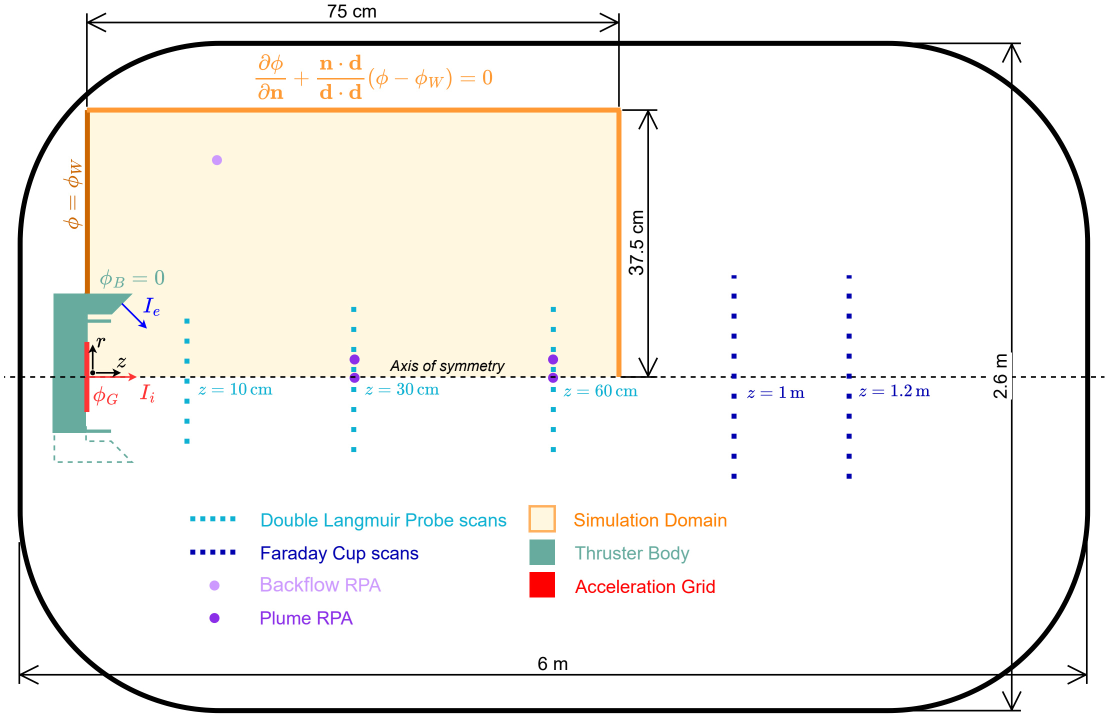

Figure 5.2: Sketch of the experimental and numerical (in yellow) domains. The dashed blue lines and purple circular markers show the probing locations of the DLP, FC and RPAs during the experimental campaign. The solid green shape at the left of the diagram represents the physical geometry of the thruster, while the dashed green lines contiguous to it indicate the annular neutraliser geometry considered in simulations due to the assumption of axisymmetry. For purposes of clear representation the elements of the diagram are not scaled equally.

60 cm. At each axial location a Cartesian translation stage was used to move the probe within a measurement area on the xy plane of respectively 30×30 cm^2, 60×35 cm^2, and 60×35 cm^2, each with a step size in the x and y directions of 2, 4, and 5 cm. At each measurement location the potential between the two probes was swept between −60 V and 60 V with steps of 0.5 V, each held for an averaging time of 40 ms. From the resulting current-voltage curve the electron temperature T_e and ion density n_i were obtained as

$$\left.\frac{dI}{dU}\right|_{U=0} = I_{i,sat}\frac{e}{2T_e}, \tag{5.1}$$

$$n_i = \frac{I_{i,sat}}{Ae\sqrt{T_e/m_i}}, \tag{5.2}$$

following the procedure detailed in Ref. [191]. Here e is the elementary charge, m_i the mass of ions, A the probe area, and $I_{i,sat}$ the ion saturation current, determined as the intercept on the y axis of a linear fit of the saturation region. The covariance of this fit was then used, in combination with an error propagation calculation, to determine an estimate of the measurement's standard error, displayed as error bars in the relevant figures of this work. We note here that, because the floating potential of the double probe was not measured during its operation, no estimation of the plasma potential could be retrieved from the measured IV curves.

5.2.1.2 Plume Retarding Potential Analyzer

A four aperture, in-house manufactured retarding potential analyzer (RPA) [192] was employed to evaluate the ion energy distribution function at four locations in the plume bulk: two points at an axial distance $z = 30$ cm from the thruster and at $r = 0$, and 5 cm; and two points at $z = 60$ cm and $r = 0$, and 5 cm. The voltage of the ion repelling grid with respect to the thruster body was swept between 850 V and 1150 V for O1, and between 1050 V and 1350 V for O2, in both cases in steps of 1.5 V; and the ion velocity distribution function (VDF) was obtained by fitting a Gaussian to the derivative of the resulting current-voltage curve. The standard error of the computed (VDF) was obtained from the covariance matrix of the fitting parameters.[193] Since the transparency of the apertures of the employed RPA is unknown, the obtained distributions (and the standard error) are normalized before comparing them with those given by the numerical model.

5.2.1.3 Backflow Retarding Potential Analyzer

The radial energy of ions flowing laterally, outside of the plume bulk, was measured in the point $z = 15$ cm, $r = 30$ cm with the use of a Semion RPA by Impedans[124]. Due to the small current densities of low energy ions passing through this point, the measurement was repeated up to 26 separate times for each operating condition, and the resulting curves were averaged to improve the signal-to-noise ratio. The derivative of the current-voltage curves was then fitted with a Gaussian (or for some operating conditions a double Gaussian) and the normalized fitting curve was used for the comparison with the numerical results. Note that the standard measurement errors were retrieved from the covariance matrix of the fitting parameters.[193]

5.2.1.4 Faraday Cup Array

The ion current density profiles were measured with the use of a Faraday cup (FC) array[194] at axial distances from the thruster of $z = 1$ m and $z = 1.2$ m. The array, permanently mounted within the JUMBO facility at JLU, is one meter tall and is composed of 53 FCs placed at mutual vertical distances ranging from 12.5 mm at the center of the array to 25 mm at its edges. Each FC has a circular aperture of area $A_{fc} = 3.14\,\text{mm}^2$, an acceptance angle of 60°, and is equipped with a repeller biased to −50 V with respect to ground to suppress perturbations due to secondary electron emission. At both axial distances the array was swept across the ion beam from $x = -40$ cm to $x = 40$ cm in steps of 1 cm, resulting in a measurement area of $80 \times 100\,\text{cm}^2$. The net current measured by each

FC at position i was then converted to an ion current density by dividing it by an effective aperture area A_i that takes into account the non-normal incidence of ions on the detection surface of the probe:

$$A_i = \begin{cases} A_{fc} & \text{, for } r_i \leq r_{grid}, \\ A_{fc} \cos\left[\arctan\left(\dfrac{r_i - r_{grid}}{z}\right)\right] & \text{, for } r_i > r_{grid}; \end{cases} \tag{5.3}$$

where r_i is the radial distance of the considered FC from the beam axis, r_{grid} is the radius of the thruster's grid system, and z is the axial distance between thruster and measurement plane.

As depicted in Figure 5.2, the axial distances at which the FC measurements were taken lie outside of the domain employed in the simulations, due to the large computational costs associated with an increase in domain size. In order to compare experimental and numerical data, it was therefore necessary to extrapolate the FC measurements to a location within the simulation domain. This was done by assuming a conical expansion of ions, which accelerated through the thruster grids possess a sufficiently large inertia to follow essentially straight trajectories over the distances considered here, and that their scattering due to ion-neutral collisions could be neglected. Under these assumptions, and passing to spherical coordinates ($\rho = \sqrt{z^2 + r^2}$ and $\alpha = tan^{-1}(r/z)$), one has that $j_i(\rho, \alpha)\rho^2$ does not vary with ρ, allowing the extrapolation of the ion current density from one axial location to another. This was first confirmed by extrapolating the measurements taken at $z = 1.2$ m to $z = 1$ m, and comparing the results with the measurements available there, yielding in all cases a maximum relative error below 7% . Then, the measurements taken at $z = 1$ m were extrapolated to an axial distance of $z = 0.6$ m, allowing the comparison with simulations.

5.2.2. Simulation Setup

The modeling approach and the specific description of the model employed have already been thoroughly discussed in Ref. [49]. We therefore limit our description here to a general outline of the methodology employed. Each operating condition of Table 5.1 was simulated in two phases. First, the quasi-neutral hybrid code EP2PLUS[29] was used to reach a steady-state solution of the expansion of the charged and neutral particles emitted by the thruster and neutraliser. This was complemented with a second stationary neutral population, with uniform densities and temperatures ($T_{n,bg} = 400$ K), representing the facility background density. The resulting maps of neutral densities, velocities and temperatures were then passed as an invariant background to the axisymmetric 2D3V, time-explicit, momentum-preserving PIC code PICASO[68], [195]. Charge-exchange (CEX), momentum exchange and elastic, excitation and ionization collisions were considered for ions and electrons through Montecarlo collision algorithms with these neutral maps[49]. The simulation domain employed in PICASO is shown in Figure 5.2, while Sections 5.2.2.1 and 5.2.2.2 will provide further details on the employed boundary conditions and injection properties of particles. Importantly, the use of an axisymmetric code causes a distortion of the real geometry of the thruster-neutraliser ensemble, since it implies the presence of an annular neutraliser that encircles the thruster (as depicted by the green dashed lines in the lower half of Figure 5.2), rather than the actual neutraliser, which breaks axisymmetry. However, planar simulations of this same setup[49] showed that, even in presence of an asymmetrically mounted neutraliser, plume symmetry was recovered just a few centimeters downstream of the thruster, justifying the simplification employed here. In any case, this issue and the one linked to the importantly larger exhaust area that an annular neutraliser implies with respect to the real problem geometry will be further addressed throughout this work.

5.2.2.1 Boundary Conditions

Regarding the boundary conditions applied to Poisson's equation for the electric potential ϕ, Dirichlet conditions with $\phi_B = 0$ are imposed at all thruster surfaces (including those pertaining to the neutraliser), except for the acceleration grid where $\phi_G = -150\,\mathrm{V}$. At the symmetry axis, Neumann conditions $\partial\phi/\partial\mathbf{n} = 0$ are applied, with $\mathbf{n}$ the versor normal to the surface. Finally, the Robin boundary condition detailed in Ref. [49] and introduced by Andrews *et al.*[63]

$$\frac{\partial\phi}{\partial\mathbf{n}} + \frac{\mathbf{n}\cdot\mathbf{d}}{\mathbf{d}\cdot\mathbf{d}}(\phi - \phi_W) = 0 \tag{5.4}$$

are used for the downstream boundaries. Here $\mathbf{d}$ is the distance between the boundary node and the center of the acceleration grid ($r = 0$, $z = 0$), and ϕ_W is the potential of the facility walls with respect to the thruster body, which is evolved in time so as to converge to a current free plume (note that at steady-state, and placing the reference potential at facility ground, $V_t = -\phi_W$). Simple Neumann conditions ($\partial\phi/\partial\mathbf{n} = 0$) were also tested for these downstream boundaries, and yielded negligible variations in the simulation results. The Robin boundary conditions are however used here to maintain continuity with our previous work.

As for the boundary conditions applied to macro-particles intersecting domain boundaries, all particles crossing material surfaces (*i.e.* the thruster body or acceleration grid) are removed from the simulation. Similarly, any ions intersecting the downstream boundary are removed, while an electron with velocity v is deleted only if $mv^2 \geq -2e(\phi_W - \phi)$, and is otherwise specularly reflected back into the domain. Finally, no special treatment of particles is required at the symmetry axis in axisymmetric simulations, since their trajectories are first integrated in three-dimensional Cartesian coordinates and then converted to cylindrical ones, so that their radial coordinate $r = \sqrt{x^2 + y^2}$ remains always positive.

5.2.2.2 Injection parameters

Table 5.2 summarizes, for each operating point, the macroscopic properties defining the Maxwellian distribution of ions and electrons (and neutrals in the hybrid simulations) injected from thruster and neutraliser into the simulation domain.

		O1		O2	
		GIE	neutraliser	GIE	neutraliser
Ions	n_{i0} [m^{-3}]	2.6×10^{15}	-	4.8×10^{15}	-
	u_i [km/s]	41.67	-	45.06	-
	T_{ri} [eV]	35	-	15	-
	T_{zi} [eV]	0.1	-	0.1	-
	I_i [mA]	100	-	200	-
Electrons	n_e [m^{-3}]	-	3.8×10^{14}	-	7.6×10^{14}
	u_e [m/s]	-	0	-	0
	T_e [eV]	-	4	-	4
	I_e^+ [mA]	-	160	-	320
Neutrals	n_n [m^{-3}]	2.34×10^{17}	10^{18}	6.27×10^{17}	10^{18}
	u_n [m/s]	180	0	180	0
	T_n [K]	400	400	400	400
	Γ_n $[g/s]$	5.8×10^{-5}	7.8×10^{-5}	1.6×10^{-4}	7.8×10^{-5}

Table 5.2: Thruster and neutraliser injection properties for each operating point. n, u and T refer to the density, normal bulk velocity, and temperature (isotropic for electrons and neutrals, anisotropic for ions) of each species at the relative exhaust surface. For ions and electrons I represents the emitted current, while for neutrals Γ refers to the total mass flux injected through the surface.

As evident from Table 5.2 no electrons are assumed to feed through the thruster's grid system, while the ion total current I_i and bulk velocity $u_i = \sqrt{2e(\Delta V + V_c)/m_i}$ (where $V_c = 30\,\text{V}$ is included to consider the potential drop between the source's ionization region and the screen grid[196]) are given from the thruster's operating point. The ion density distribution across the acceleration grid was instead assumed to depend on the distance from the thruster axis r following a heuristic law employed in global models of RIT discharge chambers[196], [197]

$$n_i(r) = n_{i0}\sqrt{1-(1-h_R^2)\left(\frac{r}{R}\right)^2}, \tag{5.5}$$

where $h_R = 0.36$ is the radial bulk to sheath density ratio, which depends on the ionization cross-section and on the assumed neutral density in the thruster source, and $R = 7\,\text{cm}$ is the internal radius of the ionization chamber. The ion density at the center of the acceleration grid n_{i0} may then be determined by imposing that $I_i = 2\pi e \int n_i(r)u_i r\,dr$. Finally, the temperature of the injected ion population formed by the merging of the ion beamlets emitted by each hole of the acceleration grid, is considered anisotropic. The dependence of the ion temperature on the divergence half-angle β detailed in Appendix 5.A, in fact, yields a relatively large radial temperature $T_{ri} \propto e(\Delta V + V_c)\sin^2\beta$, responsible for the overall plume divergence, and a much smaller axial one $T_{zi} \propto e(\Delta V + V_c)(1-\cos\beta)^2$. Here, also taking advantage of the RPA measurements taken in the bulk of the plume, we set $T_{zi} = 0.1$ eV.

Conversely, no ions were injected from the neutraliser, under the assumption that they would all neutralise on its extraction plate. However, ions will be generated outside of it, due to the ionization of the relatively large neutral density there. Regarding the electrons, a uniform injection of a non-drifted Maxwellian with an isotropic temperature[198] $T_e = 4$ eV was prescribed across a surface of 4.2 mm in length at the center of the neutraliser. The choice of the electron current I_e^+ was of more complex determination since, as explained in Ref. [49], it does not correspond to the net electron current emitted by the neutraliser (a relevant portion I_e^- of the injected current, unknown *a priori*, is in fact expected to return to the neutraliser), and one cannot simply impose $I_e = I_e^+ + I_e^- = -I_i$. However, our previous simulation efforts showed that I_e^+ has only a modest influence on the general plasma response and plume properties as long as $I_e^+ > I_e$, since any excess will be returned back to the neutraliser in I_e^-, and mostly has the effect of varying by a few volts the floating potential of the thruster[49]. The comparison with the experimental values of V_t at the lower background pressure was therefore employed to set $I_e^+ \approx 1.6 I_i$ for O1 and O2, which was then left unvaried for the other conditions at the same operating point. Finally, we note here that the neutral injection properties employed in the hybrid simulations were simply defined from the knowledge of the net mass flux injected into the thruster and neutraliser.

5.2.2.3 Numerical Considerations

For all simulations presented in this work the vacuum permittivity was artificially increased by a factor $f_D^2 = 400$, thus increasing the minimum Debye length in the domain to $\lambda_D^* = f_D \lambda_D \approx 4$ mm and allowing the stable use of a cell size $\Delta l = 3$ mm (leading to a domain of 250×125 cells) and of a time-step $\Delta t = 2 \times 10^{-10}$s (the simulations reached steady-state after $t_{ss} = 1.1$ ms, or 5.5×10^6 time-steps). A weight of $w_p = 1.6\times10^7$ physical particles per computational macro-particle was employed, leading to at least 2×10^6 ion or electron macro-particles at steady-state in the cases with the globally lower plasma densities (*i.e.* all O1 P1 cases). These values correspond to a maximum of 200 macro-particles per cell in the denser regions of the plume bulk (in front of the grids), and around 20 macro-particles per cell in the portion of the plume bulk close to the downstream boundary of the domain. With these numerical settings, running on the 40 physical cores of an Intel Xeon Silver 4316 processor, the simulations required on average a wall-time of 120 hours to complete. The robustness of simulation results to the number of particles and to the simulation time-step was verified, and is presented in Appendix 5.B. We also note here that the sensitivity of analogous simulations to the vacuum permittivity augmentation factor f_D^2, and to uncertainties on the cross-sections of inelastic collisions was investigated in our previous work (Ref. [49]), and found to be negligible.

5.3. Reference case: O1 P2 F

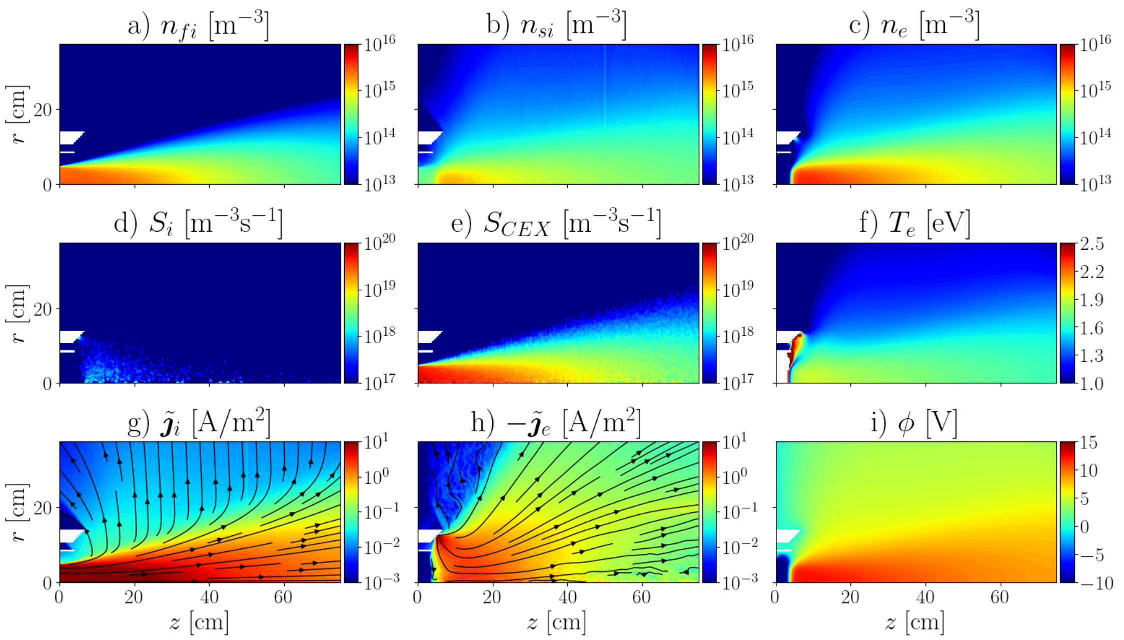

Figure 5.3: Steady-state simulation results for the case O1 P2 F. The bottom boundary coincides with the axis of symmetry that passes through the center of the thruster grids.

This section uses the case O1 P2 F (in which the thruster is operated in O1, electrically floating, and with a background pressure of $4{\times}10^{-5}$mbar) to showcase those elements of the comparison between numerical and experimental data that are common to all operating conditions. Figure 5.3 shows, from left to right and from top to bottom, the steady-state simulation results for the density of fast ions n_{fi}(those emitted by the thruster), of slow ions n_{si} (those produced by CEX and ionization collisions in the plume), and the electron density n_e; the ionization and CEX source terms of slow ions (S_i and S_{CEX}), and the electron temperature T_e; and finally the total ion and electron in-plane current densities ($\tilde{\jmath}_i$ and $\tilde{\jmath}_e$), and the plasma potential ϕ. These panels display many of the plume features already identified in previous numerical studies[32], [49], among which we highlight: (i) the relevant population of slow ions, mainly produced by CEX collisions, that forms in front of the thruster and then flows laterally guided by $-\nabla\phi$, (ii) the nearly isothermal electron population that neutralises the ion beam and the regions of lower ion density around it, and (iii) the electric potential map characterized by a global maximum a few centimeters downstream of the acceleration grid, a topology that causes the electrostatic trapping of electrons within the main ion beam and the efficient neutralisation of the plume. These characteristics are common to all the operating conditions studied in this work, although some quantitative variations in the plasma properties of the plume were observed from one case to the other, as further discussed in Section 5.4.

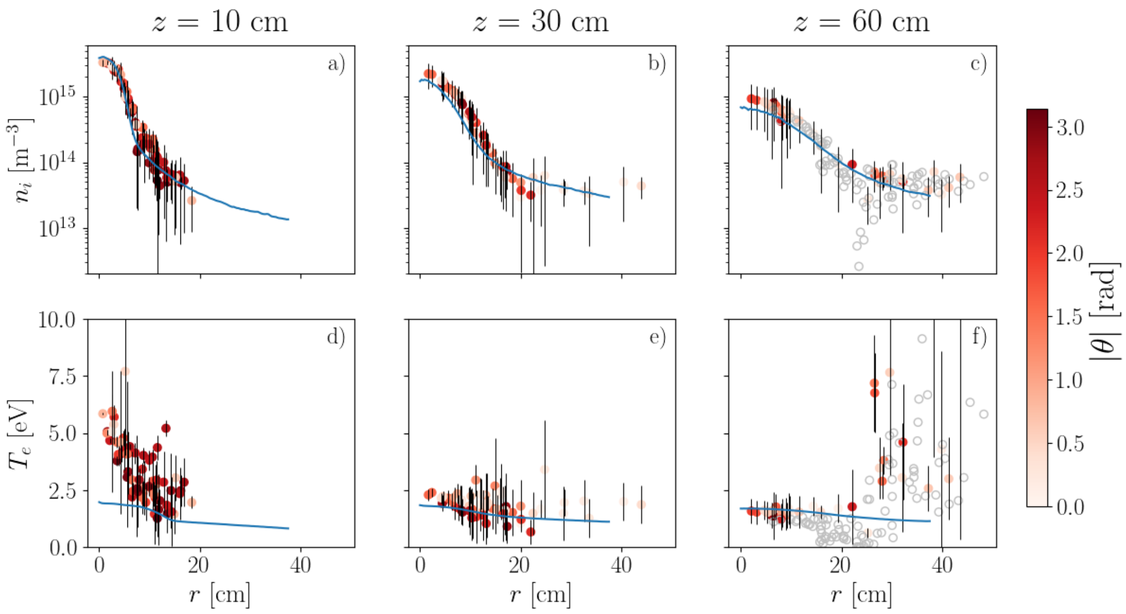

Figure 5.4: Comparison between the experimental and numerical radial profiles of the ion density [panels (a), (b), and (c)] and electron temperature [panels (d), (e), and (f)] at z = 10, 30, 60 cm. The experimental data-points are shown in shades of red depending on their azimuthal angle with respect to the thruster-neutraliser axis, or in gray if their standard error is larger than the measurement itself. The steady-state results of the simulation are shown with blue lines.

Figures 5.4 and 5.5 compare the simulation results (in blue) with the experimental data retrieved with the DLP (in red for data-points with small standard errors, in gray when the standard error is larger than the measurement value). In particular, Figure 5.4 displays the radial profiles of the ion density and electron temperature at three axial distances from the thruster exhaust z = 10, 30, and 60 cm. Note that the experimental data points in these plots have been marked with different shades of red depending on their azimuthal coordinate $\theta = \arctan(y/x)$. Importantly, there is no observable dependence of either density or temperature on the azimuthal coordinate, meaning that at z = 10 cm the plume already appears to be essentially axisymmetric, and the influence of an asymmetrically located neutraliser seems to be limited to a very reduced region just downstream of it. This observation supports our use of an axisymmetric model for the simulation of the plume bulk.

The first row of plots in Figure 5.4 shows a very good agreement between the experimental and numerical values of the ion density, with the simulation results consistently falling within the measurement error bars. However, a slight tendency of simulations to underestimate the ion density on the plume axis at larger values of z may be observed here and for other operating conditions (Section 5.4 will show that it tends to be more evident at low background pressures). The comparison between the experimental and numerical values of the electron temperature in the second row of Figure 5.4 shows instead some more evident disagreements between the simulation and experiments. Here, in fact, as

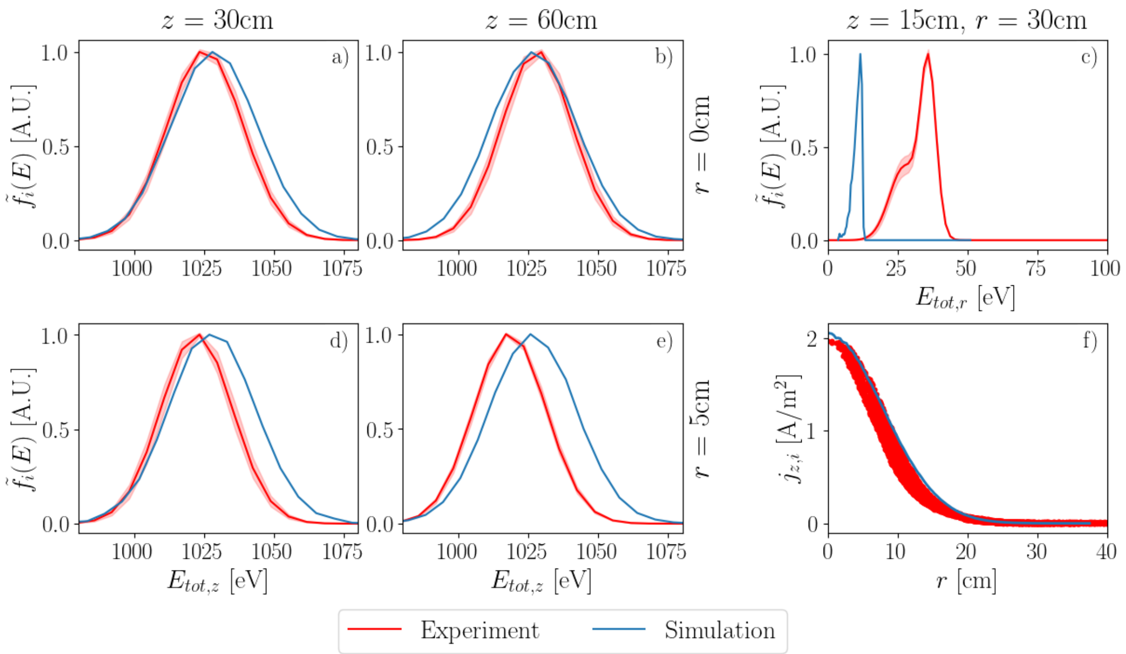

Figure 5.5: Comparison between the experimental and numerical data for the ion energies and currents for the case O1 P2 F. Panels (a),(b),(d), and (e) display the ion axial VDF in the bulk of the thruster plume. Panel (e) shows the ion radial VDF at the position of the lateral RPA, and panel (f) shows the radial profile of the axial ion current density at $z = 60$ cm.

for most of the other operating conditions analyzed, the model tends to underestimate the electron temperature closer to the thruster (at $z = 10$ cm) by about 3 eV. While this likely represents a physical mismatch between simulations and experiments, which will be further analysed in the course of this paper, it must be remarked for completeness that in presence of multiple electron populations the use of DLPs may cause the overestimation of the electron temperature[199]. Nevertheless, as the plume expands, the experimental data displays a more marked electron cooling with respect to what is foreseen by the model, so that from $z = 30$ cm a good agreement is reached between simulations and experiments. Finally, we note here that the experimental data-points at $z = 60$ cm and $r > 20$ cm that seem to indicate a radial increase in temperature should likely be discarded. The signal-to-noise ratio in the IV curve of the DLP in this region of low plasma density is, in fact, high, as evidenced by the large error bars associated with these points, and the reliability of this data should therefore be called into question.

The four panels to the left of Figure 5.5 compare the normalized axial energy distribution function of ions in the plume bulk according to simulations and experiments. We stress here that these plots refer to the total mechanical energy per charge of the collected ions

$$E_{tot,z} = \frac{1}{Ze}\left[\frac{1}{2}m_i v_{z,i}^2 + Ze(\phi - \phi_B)\right], \quad (5.6)$$

with Z the charge number and ϕ the plasma potential at the location of the probe. This energy includes also the potential energy that ions possess with respect to the collection plate of the RPA, which was biased to the potential of the thruster body ϕ_B. Once again, there is a good agreement between the model and the experimental data: both the value of the most probable energy and the spread of the distribution function display maximum deviations below 3%. Such a good agreement is to be expected, since the axial energy distribution of the ion beam is essentially imposed by the configuration of the thruster's grid system, and will suffer only small alterations due to the electric fields and collisional processes that take place in the plume bulk. Therefore, the agreement between experiments and simulations mostly depends on the injection conditions detailed in Section 5.2.2.2.

Figure 5.5(c), on the other hand, shows the comparison between the simulated mechanical radial energy distribution of ions at $z = 15\,\text{cm}$, $r = 30\,\text{cm}$ and the one measured by the backflow RPA. Although the qualitative shape of the distribution is similar (with an elongated low energy tail and a more abrupt cut-off at high energies), the model yields a most probable energy about 24 eV lower than the one measured experimentally. Since the radial energy of ions reaching the measurement location is provided by the potential drop that develops between it and the plume axis, this reduced ion energy is a symptom of an underestimation by the model of the plume potential. Our previous publications[49], [200] suggest that the plume potential is governed by the density of electrons trapped in the ion beam, which are created by the infrequent inelastic collisions. A higher density of trapped electrons results in a lower plume potential. The fact that the source term of this electron population is small means that their density may suffer wide changes if an artificial sink term is introduced in the plume, making their exact determination fragile, and consequently, that of the plume potential. The difference in ion energies seen in 5.5(c) could be the consequence of a difference of trapped electron density, due to an imbalance between their source and sink terms in the model and the experiments. This may be due to numerous effects, such as uncertainties in the employed neutral densities (either due to inaccuracies in the injection conditions, or to their simplified steady-state modelling), or to the exclusion of electron-electron Coulomb collisions that may act as an escape mechanism. Recent studies have also shown that the immersion of a probe and its holding apparatus in the plasma could have this effect.[42] To investigate this latter hypothesis, Section 5.5 will provide a qualitative assessment of the effect that an immersed probe may have on the plume equilibrium by providing an additional current path to ground for electrons. A discussion on other possible causes for the observed discrepancies between experimental and numerical results is instead deferred to Section 5.6.

Finally, Figure 5.5(f) compares the ion axial current density at $z = 60\,\text{cm}$ computed by the model with the one extrapolated from the FC array measurements taken at $z = 1\,\text{m}$. Because the FC scans provide 2D measurements of the plume cross-section in Cartesian coordinates, multiple data-points are available for the same radial coordinate $r = \sqrt{x^2 + y^2}$. Uncertainties in these measurements are responsible for the broadening of the experimental curve observed in the figure. Again, we obtain an excellent match between the numerical and experimental data for this case and for all the operating conditions considered in this work.

5.4. Trends with pressure and potential

In an effort to concisely present the comparison between the experimental and numerical results obtained for the many operating conditions considered, Figures 5.6 and 5.7 show the trends followed by some significant plume properties when altering the background pressure (P_{bg}) or thruster potential with respect to ground (V_t). In particular, Figure 5.6 shows in the first two columns the behavior of the ion density and electron temperature at the beam axis, and in the latter two the most probable radial energy with which ions reach the lateral RPA (E_{mp}), and the floating potential of the thruster. The rows instead refer respectively to O1 and O2, and as for all figures in this work, the experimental data is represented in red and the numerical data in blue. Panels 5.6(a) and 5.6(e) show how, in all cases, the densities obtained by simulations fall within the experimental error bars, although as already mentioned in Section 5.3, there is a tendency by the model to overestimate the beam divergence and yield smaller densities as z increases. As in other studies on the effects of background pressure[30], [150], both the numerical and experimental data show a clear increase in the plume's density as the chamber pressure rises due to the additional collisional processes that enlarge the slow ion population.

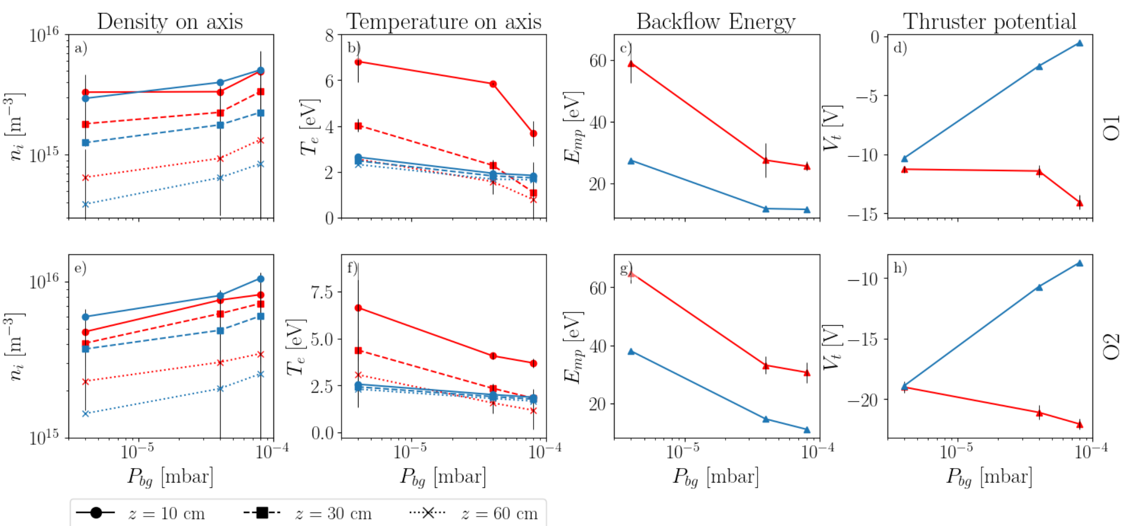

Figure 5.6: Behaviour of the ion density [panels (a), and (e)], electron temperature [(b), and (f)], ion energy to the backflow RPA [(c), and (g)], and floating thruster potential [(d), and (h)] with the background pressure P_{bg}. Simulation results are shown in blue and experimental data is shown in red. The first row of plots refers to O1 and the second to O2. Triangular markers are used for measurements that are not referred to a position along the plume axis.

Similarly, panels (b) and (f) confirm for all cases the comparison in electron temperature values already detailed in Section 5.3: the model predicts a smaller electron temperature than measured close to the thruster, but this difference decreases as one moves downstream. Interestingly, both the model and experiments show a global decrease in the values of the electron temperature as the background pressure increases. This is caused by the increase in inelastic electron collision frequency as the background neutral density rises, accelerating the production of trapped electrons. In turn, this will reduce the values of the plasma potential maxima in front of the thruster and the potential barrier trapping electrons within the plume, lowering the energy range for which an electron will be trapped, and causing the cooling of this electron population (which prevails in the plume bulk). Note that in simulations the decrease of the trapping potential barrier is mitigated by a simultaneous increase in the thruster's floating potential [see Fig. 5.6(d) and (h)], causing a milder electron cooling compared to experiments.

This physical mechanism is also responsible for the trends in the radial energies of backflowing ions observed in panels (c) and (g). Both simulations and experiments, in fact, observe a decrease in the ion energies reaching the lateral RPA as the background pressure increases. This may be associated to an improved neutralisation of the positive space-charge in front of the thruster and the subsequent decrease of the potential drop that accelerates ions radially. Nevertheless, as discussed in Section 5.3, the code appears to consistently underestimate the energies of these ions with respect to the experimental data, further suggesting (as for the case of the electron temperature) an exceedingly efficient trapping of electrons in the plume. A further analysis and a possible explanation for this disagreement between model and experiments are proposed in Sections 5.5 and 5.6.

Finally, panels (d) and (h) display the markedly different effects of the background pressure on the floating thruster potential within simulations and experiments. Although at P1 the two values of the floating potential coincide (we remind here that the current I_e^+ injected through the neutraliser in simulations was determined so as to match the floating thruster potential at P1), the experimental and numerical values drift away from each other as the background density is increased. In the case of simulations, the floating potential of the thruster increases due to the more numerous CEX collisions that take place in the plume and that deflect ions back towards the thruster body, charging it positively. Experimental measurements, instead, show a slight decrease of V_t with the background density, possibly caused by two concurring effects. First, we note that the ion current prescribed by the thruster's operating point was experimentally controlled by considering the difference between the currents flowing to the screen and acceleration grids. As a result, if more ions were to backflow to the acceleration grid by effect of the CEX collisions in the plume, the screen grid current would be increased to maintain the nominal net current required by the operating point. This methodology mitigates the mechanism through which V_t increases in simulations. Indeed, setting up the simulation for the case O1 P3 F so that ions collected by the acceleration grid are re-injected into the ion beam (*i.e.* imposing a net ion current of 100 mA as in experiments) the computed V_t decreases to −3 V, reducing the difference with respect to experiments. Second, we observe that the cooling of the electron temperature that takes place in experiments as P_{bg} rises is more pronounced with respect to the one seen in simulations. At high pressures, this would result in a milder potential drop developing from the potential maximum downstream of the acceleration grid to the chamber walls, possibly leading to smaller values of V_t.

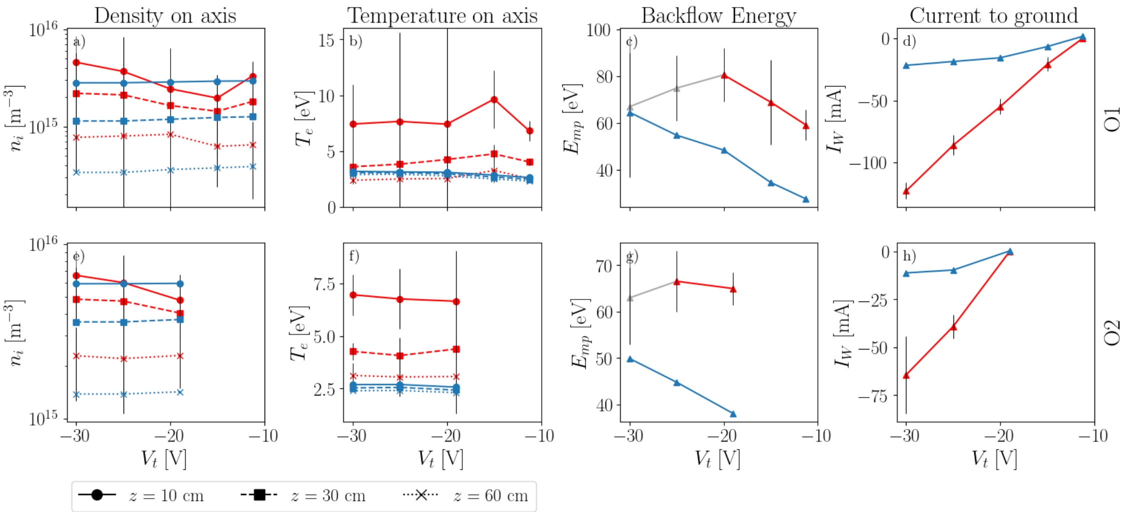

Figure 5.7: Behavior of the ion density [panels (a), and (e)], electron temperature [(b), and (f)], backflow ion energy [(c), and (g)], and current to ground [(d), and (h)] with the thruster potential V_t. Simulation results are shown in blue and experimental data is shown in red. Triangular markers are used for measurements that are not referred to a position along the plume axis. In panels (c) and (g) data-points in which the Gaussian fit of the ion VDF yielded a coefficient of determination $R^2 < 0.7$ are colored in gray.

Figure 5.7 shows the effects of the thruster potential V_t on the ion density, electron temperature, most probable ion energy to the backflow RPA, and total current to ground (I_W). Both the numerical and experimental curves of the ion density [panels (a) and (e)] and electron temperature [panels (b) and (f)] on the plume axis do not show distinctive trends as one varies V_t. On the other hand, the most probable ion energies to the backflow RPA display a more complex behavior. In simulations a clear monotonic trend links V_t to E_{mp}: as the thruster potential is decreased below its floating value more electrons are capable of reaching the vacuum chamber walls (which are now at a larger potential with respect to thruster and neutraliser), decreasing the density of trapped electrons in the plume and the efficiency with which the ion beam is neutralised. As a consequence, the potential values in the plume and the energies of ions flowing laterally increase as V_t decreases. Experimentally this trend is observed up to values of V_t mildly smaller than the floating potential ($V_t = -20$ V for O1, and $V_t = -25$ V for O2), but inverts (*i.e.* the most probable ion energy decreases) once the thruster potential is pushed to even smaller values. However, the signal-to-noise ratio in the IV curve measured by the RPA decreases noticeably (from around 40 to just below 2) for the lower values of V_t, disrupting the employed Gaussian fit to the point that it calls into question the reliability of the results. In order to visually highlight this we have colored in gray the experimental data-points in Figures 5.7(c) and (g) in which the Gaussian fit of the ion VDF yielded a coefficient of determination R^2 lower than 0.7.[201]

Finally, panels (d) and (h) show the total current flowing from the thruster-neutraliser ensemble to ground, which obviously starts at 0 when the thruster is floating and progressively becomes more negative as V_t decreases. The larger the potential slope between the thruster and electric ground, in fact, the more electrons will be able to reach the facility walls, producing the negative net current observed. The fact that I_W reaches much smaller values in the experiments compared to simulations is likely attributable to the larger exhaust surface of the annular neutraliser employed in the model compared to its real geometry. As further discussed in Section 5.6, this larger exhaust area implies smaller electron densities in front of the neutraliser, and thus a more efficient coupling between neutraliser and ion beam. In a more realistic geometry, in fact, the large negative space charge that develops in this region causes the development of a potential valley (sometimes referred to as a *virtual cathode*) which reflects the less energetic electrons back towards the neutraliser before they can reach the ion beam[32], [49]. In presence of a larger neutraliser exhaust this potential valley is much smaller, and only slight changes in V_t will therefore be necessary to eliminate the virtual cathode from the potential map, and saturate the total electron current flowing to ground.

5.5. Immersed Probe Effects

In order to evaluate the effects that an immersed probe may have on the plume's equilibrium, the trapped electron population, and the electrostatic potential, the simulation of the reference case O1 P2 F was repeated, this time with an additional object placed inside the plume to represent the DLP. In particular three distinct simulations were run, each with a cylindrical object of radius $R_P = 0.6\,\text{cm}$ and length $L_P = 1.2\,\text{cm}$, placed on the plume's axis at axial distances of $z = 10$, 30, and 60 cm. From an electrical point of view, the object's potential ϕ_P was evolved at each time-step k so as to reach a floating condition (*i.e.* a zero net current I_P collected from the plasma):

$$\phi_P^{(k+1)} = \phi_P^{(k)} + \frac{I_P^{(k)}}{C_P}\Delta t, \tag{5.7}$$

with $C_P = 3\,\text{nF}$ the object's capacitance, chosen for the numerical stability of ϕ_P but (if large enough) uninfluential on the simulation's steady-state. The resulting potential was imposed as a Dirichlet condition for the Poisson equation at the nodes belonging to the object's external boundary. As for all other material boundaries, particles intersecting the object's surface were removed from the simulation. The electrical and geometrical properties of this object are far from representing the real characteristics of the DLP and its holder (which have a much more complex geometry and electrical properties, which can span from dielectric surfaces to biased electrodes), but this arrangement allows a first qualitative estimation of the probe's effect.

Figure 5.8 shows in each of its columns the resulting radial profiles in ion density and electron temperature when the probe is placed at $z = 10$, 30, and 60 cm, compared with the corresponding experimental measurements. The results relative to the reference

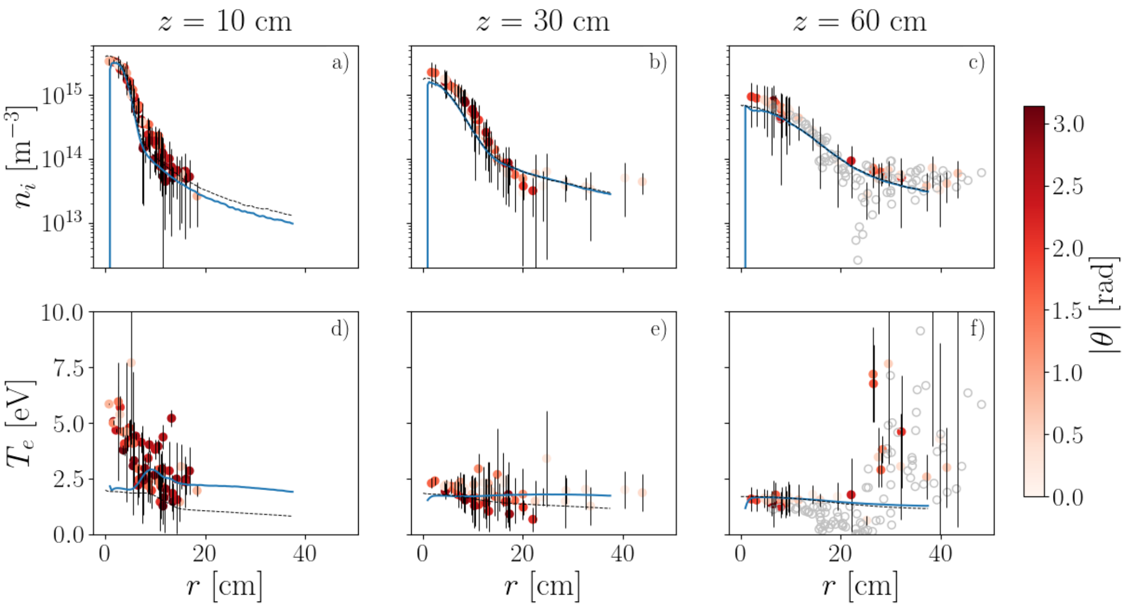

Figure 5.8: Comparison between the experimental (red markers) and numerical (blue line) radial profiles of the ion density [panels (a), (b), and (c)] and electron temperature [panels (d), (e), and (f)] at z = 10, 30, 60 cm when including the probe in simulations. Experimental points with standard errors larger than the measurement itself are colored in gray, while black dashed lines show the results of the simulation without a probe.

simulation (presented in Section 5.3) have also been traced with a dashed black line for easier reference. The upper row of plots, depicting the ion density, shows essentially no deviations with respect to the simulation that did not include the immersed probe, except for the foreseeable drop in density at the probe's location. As a result, the ion densities continue to match very well with what was measured experimentally. On the other hand, the second row of plots, illustrating the radial profiles of electron temperature, shows a slight heating of electrons with respect to the nominal simulation, especially at the radial edges of the plume bulk. Interestingly, this increase of T_e is more marked when the probe is inserted closer to the thruster, where the plume's plasma is denser, and instead fades away when the probe is in less dense regions and generates a smaller perturbation. Given this observation, it is also logical to assume that, as the probe moves radially away from the plume axis (which we cannot model with an axisymmetric code), a similar decrease in the perturbation occurs.

The physical cause of the observed increase in electron temperature is best explained with the use of Figure 5.9. Here we show in panel (a) the steady-state potential profiles along the plume axis for the nominal case without immersed probes (in blue), and for the cases with the probe located at z = 10, 30, and 60 cm. For these latter three simulations a clear Debye sheath develops around the probe, bridging the potential difference from the local plasma potential to the floating potential of the object. This floating potential tends to increase as the probe is moved closer to the thruster exhaust, where the ion current densities are larger and more electrons are thus pulled into the probe to balance the total

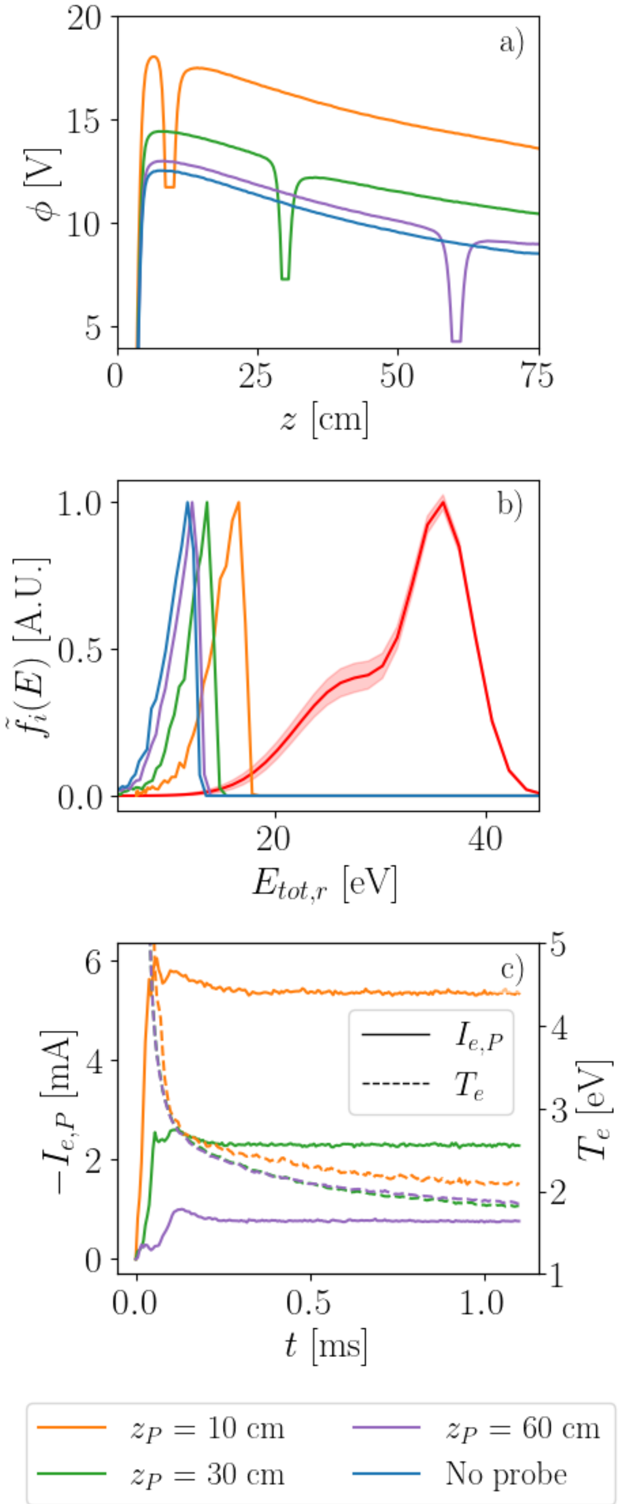

Figure 5.9: Plume properties for simulations without an immersed probe (in blue) and with a floating probe on the plume axis at z_P = 10, 30, and 60 cm (in orange, green, and purple). Panel (a) shows the axial plasma potential profile, while panel (b) displays the ion VDF at the location of the backflow RPA (the corresponding experimental data is reported in red). Panel (c) shows the evolution in time of the electron currents to the probe (in continuous lines), and the maximum electron temperature in the plume (in dashed lines).

absorbed current. As the probe floats to potentials larger than that of the facility walls (for all simulations here $\phi_W \approx -1$ V) electrons that were previously trapped now find an escape pathway, depleting their population and increasing the total space-charge in the plume. As a result the plume's potential also rises, forming a new potential "pocket", at values larger than ϕ_P, in which new electrons can be trapped. Importantly, the potential difference that forms this "pocket" is always of a similar magnitude ($\Delta\phi \approx 6.5$ V), so that the plume's potential is ultimately governed by the probes floating potential, and settles to values that peak at $\phi_P + \Delta\phi$ and decrease axially.

The increase in the plume's potential will act on the trapped and primary electron populations in two distinct ways. Primary electrons will experience a sharper acceleration from the neutraliser into the ion beam, increasing their kinetic and internal energies, and causing the noticeable rise in temperature at the edges of the plume bulk (where this population dominates the total electron density). On the other hand, since the potential barrier that separates trapped electrons from the lowest resistance neutralisation pathway remains roughly unchanged, the range of energies available to trapped electrons will not vary, and thus their macroscopic temperature will also remain the same. The result is that only marginal variations are observed in the electron temperature in the plume's bulk in Figure 5.8. The direct effect of the probe on the electron temperature is thus not sufficient to explain the mismatch between simulations and experiments in the very near-plume. Nevertheless, the relevant influence that the probe has on the plume potential may have a more subtle effect on experiments, since the models used to reconstruct the plasma properties from a probe's IV curve assume a negligible change in the plasma's state during the measurement.[199] If a new equilibrium is instead reached for each voltage point of the probe's scan, the resulting IV curve may not be interpretable with classical Langmuir probe theory.

Similarly, the increase of the plume's potential values has a relevant effect on the ion energies observed at the location of the backflow RPA, as shown in Figure 5.9(b). Here we observe that the ion energies outside of the plume gradually increase from the case without an immersed probe to those with a probe moving closer to the thruster, although the energy values never reach those measured experimentally (shown in red).

Finally, Figure 5.9(c) shows, over the simulation time span, the total electron current flowing to the immersed probe, along with the maximum electron temperature along the plume axis (for all cases that is at $z \approx 8.4$ cm). As expected, the plot shows larger electron currents flowing to the immersed probe the closer it gets to the thruster, justifying the increase in the perturbation that it causes. As commented before, this is also mildly mirrored in the values of the maximum electron temperature, which displays a slight increase from $z_P = 60$ cm to $z_P = 10$ cm. More critically, however, the settling time of the electron temperature displayed here is in the order of milliseconds, due to its dependence on the inelastic collision frequencies that trap electrons in the plume (incidentally, at lower background pressures, this settling time is expected to rise). Such a time scale is in the order of the voltage stepping time of typical Langmuir probe scans, meaning that —if peculiar care is not taken— the instrument may be measuring during its scan a plasma which is not in equilibrium, thus altering experimental results.

5.6. Discussion

The previous sections have identified discrepancies between experimental measurements and numerical results that can be attributed to a number of different and sometimes concurrent effects. In this section we therefore attempt to clarify and delimit the influence that these effects (be it a shortcoming of the numerical model, or systematic experimental errors) may have on the observed discharge properties. First, it is useful to distinguish between two categories of measured quantities: those principally dominated by the ion dynamics, and those that display a larger dependency on the electron population. Due to the large inertia of ions emitted by the thruster, the former, which include the plasma density, the ion current densities, and the ion mechanical energy within the plume bulk, are very robust and exhibit only a minor sensitivity to changes in the numerical model or in the experimental approach. These properties are also the ones that display the better agreement between numerical and experimental results. A second group of quantities, that depend on the delicate electron dynamics and include the radial ion energy in the plume periphery, the correlated bulk potential, the electron temperature, the currents to ground, and the floating thruster potential, is instead more sensitive to uncertainties or limitations in the model and to perturbations induced by invasive probing. As shown in the previous sections these are also the quantities that display a worse correlation when comparing simulations to experiments.

We now tackle the issue of possible systematic experimental errors due to invasive probing, especially for the case of the DLP measurements in the very near plume (z = 10 cm). Although Section 5.5 showed that the immersion of probes in the near plume may alter the global discharge equilibrium and the plasma potential of the plume, it did not detect sufficient variations in the bulk electron temperatures to explain the discrepancies in the numerical and experimental values of T_e. Moreover, the DLP scan time used during the experimental campaign was much larger than the settling time of the discharge predicted by simulations, so that each point of the IV curve should be representative of a quiescent plasma. In support of this we note that, consistently throughout our study, the independent measurements from both the backflow RPA and the DLP pointed to a systematic underestimation by simulations of the plume potential and the near-plume electron temperature by a similar factor. As a result, although acknowledging the need for a further refinement of DLP theory for these types of plasmas, we consider the experimental measurements presented here as a sufficiently reliable benchmark for simulations. The remainder of this section will therefore concentrate on identifying the model limitations that may be cause of discrepancies between numerical and experimental data.

We move on now to the evaluation of a major assumption of the numerical methodology: the axisymmetry of the plume. While planar asymmetric simulations of a GIE

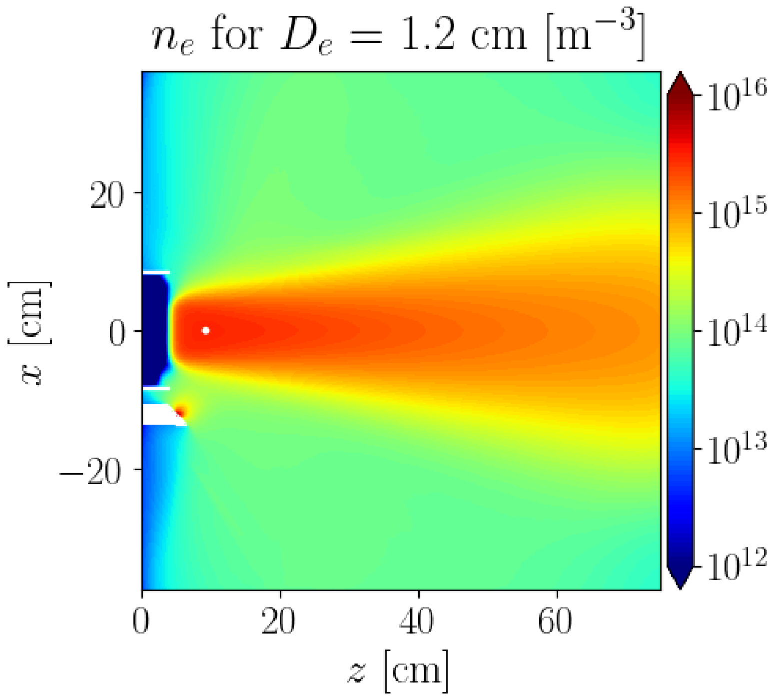

Figure 5.10: Electron density map for a planar asymmetric simulation with $D_e = 1.2$ cm. The white dot in the center of the plume marks the point of global maximum in the plasma potential.

plume[49] and the DLP and FC data presented here point to the formation of an axisymmetric plume bulk, the assumption of rotational symmetry may not be as accurate when considering the plasma bridge surrounding the neutraliser. The annular neutraliser geometry used in the model, in fact, is inevitably characterised by a much larger exhaust area than the actual one, leading to smaller electron densities in the plasma bridge for the same electron current I_e^+. This in turn will modify the potential profiles found in this area, altering the local plasma conductivity and possibly influencing the currents to ground, the thruster floating potential, and the potential and electron temperature values in the plume. A conclusive and quantitative study on the effects of the neutraliser exhaust area requires 3D simulations that are currently beyond our capabilities. Nevertheless, we propose here a first qualitative evaluation based on three planar simulations (with trivial variations in the numerical methodology, but with a full domain to account for the asymmetry of the geometry) in which the neutraliser exhaust diameter is respectively $D_e = 6$ cm, 2.4 cm, and 1.2 cm. Figure 5.10 shows the electron density map in this asymmetric scenario (with $D_e = 1.2$ cm), highlighting once more the symmetry immediately retrieved in the plume bulk. The comparison between this density map and its axisymmetric equivalent in Figure 5.3(c) also showcases the evident differences between a 2D and a 3D expansion, and reinforces the importance of the latter when comparing with experiments. Table 5.3 instead reports the variation of the potential, electron temperature and electron density measured at the point M of maximum ϕ in the domain [indicated by the white point in panel (a)], along with the thruster floating potential and the electron density in front of the neutraliser, as the exhaust diameter is varied. The table shows that, while the electron density in the plume bulk remains essentially unvaried, the plasma potential and electron temperature both show a slight increase as D_e decreases. Considering that the real electron densities in front of the neutraliser (n_{e0}) are still orders of magnitude larger than the ones considered here (going to real neutraliser densities is computationally unfeasible), this suggests that the discrepancies between the experimental and numerical data reported in the previous sections may be in part attributed to an increased neutraliser exhaust area. We additionally note here that a similar numerical experiment was carried out for the axisymmetric case, but yielded negligible differences between simulations. This is likely because, even for exhaust widths corresponding to a single cell, n_{e0} in this case remains too small to relevantly modify the local potential map.

Table 5.3: Variation of relevant discharge properties with the neutraliser exhaust area D_e. Densities, temperatures and the potential are reported at point M, location of the global plasma potential maximum (marked with a white circle in Figure 5.10). The electron density at the neutraliser exhaust n_{e0} is also shown.

	n_{e0} [m^{-3}]	$n_{e,M}$ [m^{-3}]	$T_{e,M}$ [eV]	ϕ_M [V]	V_t [V]
$D_e = 6$ cm	1.3×10^{15}	3×10^{15}	2.24	6.7	2.48
$D_e = 2.4$ cm	3×10^{15}	3×10^{15}	2.3	7.2	2.37
$D_e = 1.2$ cm	6×10^{15}	2.99×10^{15}	2.39	7.88	2.26

Finally, it is worth commenting on the influence of uncertainties in collisional algorithms on the simulation results. As mentioned throughout this work, the inclusion of inelastic electron collisions in the model is paramount for a proper charge neutralisation of the plume. However, as was demonstrated in Ref. [49], it is the mere presence of these collisions, no matter how small the collisionality, what is important to enable the electron trapping mechanism (*i.e.* the strictly collisionless case is a singular limit of the problem). There, it was shown that reasonable variations in inelastic collision cross-sections have negligible effects on the steady-state equilibrium reached by the discharge, affecting only the time to relaxation. We do not expect, therefore, the uncertainties on the experimentally determined cross-sections to relevantly influence the simulation results. Conversely, the absence in the literature of a computationally affordable model for electron-electron Coulomb collisions[175] hinders their inclusion in the code, and the precise evaluation of their effect on the plume equilibrium. Nevertheless, given the relatively low plasma densities of GIE plumes, the momentum transfer Coulomb collision frequency is estimated to be about an order of magnitude smaller than that of electron neutral elastic collisions[49], [144], so that until further investigation their effect is assumed to be of secondary importance.

5.7. Conclusions

This work presents the first methodical comparison between full PIC simulations of the plume of the RIT10-EVO, and its experimental characterization by means of double Langmuir probe, RPA, and FC measurements. The comparison was carried out for 12 different operating conditions (involving two operating points of the thruster, three different background pressures, and up to five different thruster potentials with respect to electrical ground). When compared with experimental data, the developed axisymmetric, explicit full PIC code was found to adequately predict the ion densities, current densities and energies in the plume. A good agreement was also obtained between the simulated and measured electron temperature in the far plume, although the code was shown to underestimate it closer to the thruster grids by about 4 eV. Moreover, when considering the radial energies of ions streaming to the sides of the plasma plume, the qualitative shapes of the experimental and numerical VDFs compared well, but the RPA measurements observed substantially larger energies (in the order of 20 eV) with respect to simulations. This observation, coupled with the underestimation of the electron temperature, points towards an excessively efficient neutralisation of the ion beam in the numerical model with respect to reality. The possibility that this may be caused by the presence of probes immersed in the plume during experiments was then qualitatively analysed by representing a probe and its holder as an electrically floating object in simulations. Although this study highlighted a noteworthy dependence of the plume potential on the voltage of the probe, it was unable to explain the measured electron temperatures and radial ion energies.

The analysis of the plume behavior when increasing the facility background pressure showed an increment in the plasma density and a drop in the electron temperature both in experiments and in the numerical model. Similarly, the simulations and the RPA measurements outside of the plume bulk displayed a decrease of the backflowing ion energies as the neutral background density rises, although the numerical model continued to underestimate these values with respect to experiments. On the other hand, when investigating the effects of the potential of the thruster body on the plume, the plasma densities and electron temperatures were observed to remain essentially unchanged in the model and in experiments, while the backflowing ion energies were found to increment as the thruster was pushed to smaller potentials with respect to facility ground.

While the general comparison between numerical and experimental data partially validates the developed PIC code for the simulation of GIE plumes, and corroborates the physical insights previously presented in Ref. [49], it also highlights some mismatches in the results which should be the subject of further research. First, it is clear from our limited planar study of the effects of the neutraliser exhaust surface, that an improvement in the modeling of the neutraliser is necessary. On one hand, an important advancement would be the use of a 3D model, allowing the correct simulation of the neutraliser geometry and of the plasma bridge region that develops in front of it. On the other hand, the introduction of a global model for the neutraliser would permit the self-consistent determination of an important free parameter of the model, the emitted electron current I_e^+, and allow its coupling with the thruster plume. This would also allow an important step forward in the self-consistent determination of the thruster floating potential and current to ground, which are inevitably tied to I_e^+. Second, the analysis carried out on the influence of immersed probes is only qualitative, and requires a more rigorous framework to yield relevant quantitative insight. In particular, a simulation that includes the temporal variation of the probe's potential and retrieves the resulting IV curve would allow an evaluation of the plume's response to a dynamic biasing of the probe, and an assessment of the deformation of the IV curve that this may entail. Third, the inclusion of an algorithm for electron-electron Coulomb collisions, that may provide an electron escape mechanism through energy transfer but are neglected in this work, is necessary to conclusively assess their influence on the plume equilibrium. Finally, the coupling into the plume of a residue of the RF wave generated by the thruster and neutraliser should be numerically and experimentally assessed, as it would provide energy to trapped electrons allowing their escape to the facility walls and contribute to the reduced neutralisation observed in experiments.

Acknowledgements

This work has been supported by the ECOMODIS project, funded by the European Space Agency, under contract 4000137869/22/NL/RA. The authors would also like to thank Alberto Marín-Cebrián for his invaluable contributions to the development of PICASO and to the physical interpretation of the simulation results, and Käthe Dannenmayer and Fabrice Cipriani for the invaluable support throughout the arc of the project.

Appendices

5.A. Ion Injection Temperature

The extraction of ions from the thruster's ionization chamber through the grid system produces a series of beamlets —one per grid hole— which expand and merge a small distance downstream of the acceleration grid into a homogeneous and single-peaked ion beam. In first approximation, these beamlets may be assumed as composed of mono-energetic ions with velocity $v_0 = \sqrt{2e(\Delta V + V_c)/m_i}$ that can form up to a maximum angle β (the beamblet's divergence half-angle) with the normal to the grid's surface. Their eventual merging produces an ion fluid with an essentially axial bulk velocity, and a distribution function populated limited in the axial velocity range $\mathcal{V}_z = [v_i - \Delta v_z; v_i]$ and the radial velocity range $\mathcal{V}_r = [-\Delta v_r; \Delta v_r]$, with $\Delta v_z = v_0(1 - \cos\beta)$ and $\Delta v_r = v_0 \sin\beta$. These expressions are obtained considering the ion velocity vector has an angle $\leq \beta$ with respect to the axis.

What shape the distribution function takes within these limits depends on the details of the ion optics of the grid system, and on the collisional and electrostatic effects that take place during the beamlet merging, but is outside of the limited scope of this derivation. We therefore assume here a uniform (or "water-bag") VDF

$$f(v_z, v_r) = \begin{cases} \dfrac{n_{i0}}{\pi \Delta v_r^2 \Delta v_z}, & \text{for } v_z \in \mathcal{V}_z,\, v_r \in \mathcal{V}_r \\ 0, & \text{otherwise,} \end{cases} \tag{5.8}$$

which, given the absence of a decay of the distribution at its outer edges, will yield a reasonable upper-bound to the temperatures we wish to compute. Using cylindrical coordinates the radial and axial ion temperatures after the merging of the beamlets are then obtained as

$$\begin{aligned} T_{ri} &= \frac{1}{n_0} \frac{n_0}{\pi \Delta v_r^2 \Delta v_z} \int_0^{2\pi} \int_0^{\infty} \int_0^{\infty} f m_i v_r^2 \, dv_z dv_r d\theta \\ &= \frac{1}{2} m_i \Delta v_r^2 = e(\Delta V + V_c) sin^2\beta \end{aligned} \tag{5.9}$$

and

$$T_{zi} = \frac{1}{\pi \Delta v_r^2 \Delta v_z} \iiint f m_i (v_z - v_0 + \Delta v_z/2)^2 \, dv_z dv_r d\theta$$
$$= \frac{1}{12} m_i \Delta v_z^2 = \frac{1}{6} e(\Delta V + V_c)(1 - cos\beta)^2. \quad (5.10)$$

Using the parameters from operating point 1 in Table 5.1 and a beamlet divergence of $\beta = 10°$, we obtain $T_{ri} = 35\,\text{eV}$, and $T_{zi} = 0.05\,\text{eV}$.

5.B. Sensitivity of Simulations

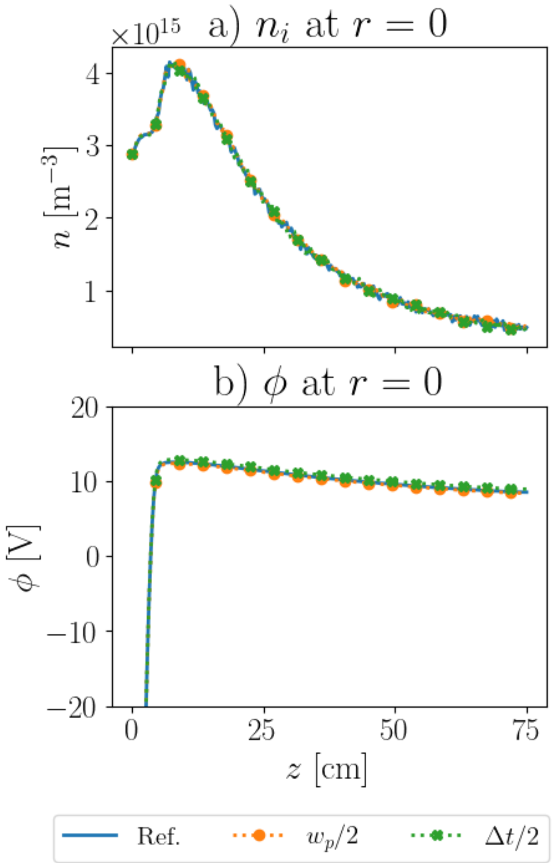

Figure 5.B.1: Comparison between the total ion density and electric potential profiles along the plume axis for the reference simulation (O1 P2 F) in blue, and simulations with halved time-step and particle weight respectively in green and orange.

The robustness of simulation results against numerical parameters such as the simulation time-step Δt and the particle weight w_p was verified by running two new simulations of the reference case (O1 P2 F), respectively with a halved time-step and particle weight. Figure 5.B.1 shows the resulting total ion density and electric potential along the plume axis compared with the one obtained in the reference simulation. As can be seen the differences on the plume axis (and in general in the whole simulation domain) when changing these numerical parameters are negligible, confirming the convergence of our simulations.

CHAPTER 6

PIC-Informed Reduced Electron Model for Gridded Ion Engine Plumes

This chapter reproduces the contents of Ref. [51], presented at the 10th Space Propulsion Conference in Bari, Italy in May 2026. The typography has been adapted to the style of this thesis.

6.1. Introduction

Many recent works on gridded ion engine (GIE) plumes have studied their properties by means of high-fidelity full PIC simulations. While these types of codes represent the state of the art for the detailed analysis of plasma thruster plumes in the academic EP community[42], [49], [50], [202], their computational burden hinders their use in an industrial design and integration pipeline. Even with dedicated codes, in fact, built for efficient parallelized computation and run on state of the art computing nodes, important simplifications of the problem are required (*e.g.* the assumptions of axisymmetry, increased vacuum permittivity, and frozen neutral dynamics made in Ref. [50]) to reduce simulation times to the order of days or even weeks. Industrial applications for the evaluation of plume-spacecraft interactions, on the other hand, require models with run-times that allow the execution of parametric analyses on design choices and operating conditions, while simultaneously permitting a fully dimensional description of the plume and its interaction with the complex spacecraft geometry. As a result, hybrid models —that describe the heavy species as particles and employ the fluid formalism for the characterization of electrons— are those of choice for this kind of application, since they allow one to overcome the constraints on time-step and cell size that burden PIC codes by assuming quasi-neutrality.

However, hybrid codes encounter their own set of challenges when applied to the simulation of GIE plumes. First, there is the issue of the closure to be employed for the set of fluid equations describing electrons. Indeed, a basic isothermal closure has been shown to provide inaccurate predictions of the electron thermodynamics outside of the plume bulk, ultimately leading to an imprecise determination of the potential map and of the radial acceleration that it imposes on CEX ions[156]. The use of a polytropic expression for the electron temperature, on the other hand, produces more accurate results but may not hold in regions of lower plasma density, and requires the empirical determination of the polytropic parameter γ[49], [79], [80]. Finally, higher order fluid models that include the electron energy equation represent a further step forward, but introduce the problem of the definition of a heat flux closure capable of outperforming the classically employed Fourier law, which has been generally shown not to hold in the plasma plumes of EP devices [81], [130].

Second, the implementation of a quasi-neutral model requires an externally imposed value of the reference plasma potential. In the specific case of a GIE plume, the most natural location in which to provide this reference potential would be the quasi-neutral point just downstream of the acceleration grid. However, as this work will show, the determination of the value of this potential with respect to that of the material walls of the thruster is not a trivial task. Stemming from these considerations, the present work attempts to overcome the mentioned limitations to the hybrid modelling of GIE plumes through the study of the detailed kinetic information provided by the numerous PIC simulations presented and discussed in our previous works (Refs [49] and [50]).

To this end, we propose to exploit the conceptual distinction between the trapped and primary electrons that populate and neutralise a GIE plume. Recent works have in fact highlighted how the neutralisation of the ions' electric charge and current depends on two distinct categories within the electron population[49], [130], [202]. Trapped electrons are those electrons that have an insufficient mechanical energy to overcome the electric forces confining them within the plume, and are thus characterized by an ideally infinite residence time (in reality, infrequent collisional processes offer a means to populate/depopulate the trapped electron region of phase space). These electrons represent the vast majority of the electrons in the plume, thus playing a major role in determining the values of the total electron density and temperature. Conversely, due to the symmetry of their distribution, they do not contribute to the electron currents and heat fluxes (or any other odd moment of the total electron distribution function). Primary electrons, on the other hand, are those electrons that possess sufficient energy to escape the plume's potential well, be it either by neutralising at one of the spacecraft's material surfaces or by reaching infinity. Although they represent a small percentage of the total electron population and barely contribute to density or other even moments of the distribution, these are the electrons responsible for the definition of the total currents and heat fluxes.

Given the enormous difference in particle densities between trapped and primary electrons, we postulate here that the latter population has a negligible authority on the determination of the plume's potential map. The formulation of a model capable of precisely capturing the density evolution of trapped electrons would therefore be sufficient for an accurate determination of the electric potential and consequently for the integration of the ion trajectories required to advance in time in the hybrid model. The derivation, implementation and verification of such a model for trapped electrons are thus the main objectives of the following sections.

6.2. Hybrid Model Formulation

As stated, the proposed model relies on the assumption (verified in Section 6.3) that trapped electrons vastly outnumber the primary ones, and that the contribution of this latter population to the even moments of the complete electron velocity distribution function (VDF) may be comfortably neglected. Under this assumption, the total electron density and temperature are approximated by those of trapped electrons (*i.e.* $n_e = n_{te}$ and $T_e = T_{te}$). In order to provide a description of this latter population we start by considering its VDF at the point of maximum potential in the plume (denoted here with the suffix 0), which is assumed to be representable through a truncated Maxwellian, with a truncation energy given by the potential at infinity, $\phi_0 - \phi_\infty$:

$$\begin{cases} f_0(v_0) = n^* \left(\frac{m}{2\pi T^*}\right)^{\frac{3}{2}} \exp\left(-\frac{mv_0^2}{2T^*}\right), & \text{if } \frac{1}{2}mv_0^2 < e(\phi_0 - \phi_\infty), \\ f_0(v_0) = 0, & \text{if } \frac{1}{2}mv_0^2 \geq e(\phi_0 - \phi_\infty) \end{cases} \tag{6.1}$$

where n^* and T^* are respectively the density and temperature of the untruncated Maxwellian, ϕ_0 and ϕ_∞ are the potentials at 0 and at an infinite distance from the thruster, and m and v_0 are the electron mass and the velocity norm. This expression for the trapped electron VDF derives from two properties of the population. The first is their large residence time, which implies that eventually the population reaches a state close to thermal equilibrium, and justifies the use of a quasi-Maxwellian distribution. The second is the absence of trapped electrons with a mechanical energy $(1/2)mv_0^2 - e\phi_0 \geq -e\phi_\infty$, since these would have a sufficient energy to escape the plume and would not be trapped by definition. Because in the collisionless limit the mechanical energy of electrons is conserved, the velocity v of an electron that at point 0 had a velocity v_0 can be computed at a general point of potential ϕ as

$$v = \sqrt{v_0^2 - \frac{2e(\phi_0 - \phi)}{m}}. \tag{6.2}$$

Additionally, the Boltzmann equation for the evolution of the particle distribution ensures the conservation of a VDF along particle orbits if the collisional source term on its right hand side is small enough, so that at the general point of potential ϕ one has $f(v) \approx f_0(v_0)$. Combining these two considerations, the following general expression for the trapped electron VDF is can be obtained

$$\begin{cases} f(v,\phi) = n^* \left(\frac{m}{2\pi T^*}\right)^{\frac{3}{2}} \exp\left(-\frac{mv^2 + 2e(\phi_0 - \phi)}{2T^*}\right), & \text{if } \frac{1}{2}mv^2 < e(\phi - \phi_\infty), \\ f(v,\phi) = 0, & \text{if } \frac{1}{2}mv^2 \geq e(\phi - \phi_\infty). \end{cases} \tag{6.3}$$

By integrating over three-dimensional velocity space, one finds the following expressions for the trapped electron density and temperature as a function of the local potential

$$n_{te}(\phi; n^*, T^*, \phi_0, \phi_\infty) = n^* \exp\left[-\frac{e(\phi_0 - \phi)}{T^*}\right] \mathrm{P}\left[\frac{3}{2}, \frac{e(\phi - \phi_\infty)}{T^*}\right], \tag{6.4}$$

$$T_{te}(\phi; T^*, \phi_\infty) = T^* \frac{\mathrm{P}\left[\frac{5}{2}, \frac{e(\phi - \phi_\infty)}{T^*}\right]}{\mathrm{P}\left[\frac{3}{2}, \frac{e(\phi - \phi_\infty)}{T^*}\right]}. \tag{6.5}$$

$\mathrm{P}(\alpha, x) = \int_0^x t^{\alpha-1} \exp(-t)\, dt / \int_0^\infty t^{\alpha-1} \exp(-t)\, dt$ is the lower regularized gamma function, that guarantees physically meaningful results only if $x \geq 0$. Nevertheless, by definition, no trapped electrons can be present in regions of the domain where $\phi < \phi_\infty$, and we can comfortably take $n_{te} = 0$ there. Note that the variables n^* and T^*, of rather obscure physical meaning, can be related to the electron density and temperature at point 0 by $n^* = n_0 / \mathrm{P}[3/2, e(\phi_0 - \phi_\infty)/T^*]$ and $T^* = T_0 \mathrm{P}[3/2, e(\phi_0 - \phi_\infty)/T^*] / \mathrm{P}[5/2, e(\phi_0 - \phi_\infty)/T^*]$. In particular, for cases in which $e(\phi_0 - \phi_\infty)/T^* \geq 4$ (a condition that we will show to be regularly fulfilled) the terms containing $\mathrm{P}(\cdot,\cdot)$ in Eqs. (6.4) and (6.5) approach unity, so that $n^* \approx n_0$ and $T^* \approx T_0$. In the interest of the numerical implementation proposed later, we also report here the partial derivative in ϕ of the trapped electron density:

$$\frac{\partial n_{te}}{\partial \phi} = \frac{en^*}{T^*} \exp\left[-\frac{e(\phi_0 - \phi)}{T^*}\right] \mathrm{erf}\left[\sqrt{\frac{e(\phi - \phi_\infty)}{T^*}}\right]. \tag{6.6}$$

Given this description of the trapped electron population, and assuming that ϕ_0, ϕ_∞ and T^* are known (Section 6.5 will discuss their determination), the following numerical algorithm for the implementation of a hybrid code is suggested.

1. Inject ion and neutral macro-particles into the simulation domain through the thruster grids and, in the case of neutrals, from the neutraliser's orifice.

2. Compute the ion density n_i at the mesh nodes.

3. Set n_0 equal to the current maximum ion density, and position the point 0 in this location. The electric potential at each point in the domain can now be computed in two ways:

   (a) Assume quasi-neutrality and solve for ϕ the implicit equation $n_{te}(\phi; n_0, T^*, \phi_0, \phi_\infty) = n_i$ with a Newton-Raphson scheme employing Eqs. (6.4) and (6.6).

(b) Retrieve ϕ from the non-linear Poisson equation $\nabla^2\phi = -e[n_i - n_{te}(\phi)]/\varepsilon_0$. This approach is numerically more cumbersome, since it requires a cell size of the order of the Debye length in the non-neutral regions of the domain, and the numerical implementation of a non-linear Poisson solver. However, it still permits a time-step that is unconstrained by the plasma frequency, since the model does not resolve the electron dynamics, and allows a consistent retrieval of the plasma sheaths in front of material surfaces.

4. Employ the computed electric fields to advance the ion (and neutral) macro-particles.

5. Execute any collisions between ions and neutrals.

6. Iterate over steps 1 through 5 until steady-state is reached.

7. If desired, the electron temperature may be obtained at the end of the simulation from Eq. (6.5). The electron currents and heat fluxes, on the other hand, can be retrieved by freezing the steady-state potential map and injecting primary electron test particles from the neutraliser (with the flux, velocity and temperature that most appropriately describe the its exhaust). If the quasi-neutral version of this algorithm is employed, care must be taken in correctly reflecting those test particles that do not posses sufficient energy to cross the infinitesimal sheaths present at the domain boundaries. Once this population of electron macro-particles has reached steady-state, their weighting to the mesh nodes provides an estimation of the macroscopic properties of primary electrons, which in the case of the odd moment of the VDF coincide with those of the entire electron fluid.

Incidentally, the proposed algorithm can be executed with any expression that, analogously to Eq. (6.4), provides the electron density as a function of the local plasma potential. By far the most employed expressions of this kind are the Boltzmann relation,

$$n_B(\phi; n^*, T^*, \phi_0) = n^* \exp\left[\frac{e(\phi - \phi_0)}{T^*}\right], \tag{6.7}$$

and the one that ensues from the use of a polytropic closure in the collisionless and unmagnetized limit

$$n_{poly}(\phi; n^*, T^*, \phi_0, \gamma) = n^* \left[1 + \frac{\gamma - 1}{\gamma}\frac{\phi - \phi_0}{T^*}\right]^{\frac{1}{\gamma - 1}}. \tag{6.8}$$

Note that Eq. (6.7) coincides with Eq. (6.4) when the incomplete gamma function is unity (*i.e.* when no truncation of the underlying VDF is carried out), and therefore provides a good evaluation of the electron density if primary electrons complete the Maxwellian distribution at energies larger than $e(\phi_0 - \phi_\infty)$. In other words, Eq. (6.7) is accurate when the primary electron density $n_{pe} \approx n_B(\phi) - n_{te}(\phi)$, while Eq. (6.4) provides a better description of the total electron population if $n_{pe} \ll n_B(\phi) - n_{te}(\phi)$. An evaluation of the precision of these two closures can therefore be locally obtained by considering the non-dimensional parameter $n_{pe}/|n_B(\phi)-n_{te}(\phi)|$, that assumes a value of 1 where the Boltzmann relation is the most accurate, and a value of 0 where $n_e \approx n_{te}$ and Eq. (6.4) provides a good description of the electron density. Regarding the polytropic relation, we point out that Eq. (6.8) employs the same set of parameters as Eq. (6.4), especially considering that the collisionless fluid equations yield a relationship between the polytropic coefficient and the total potential drop

$$\frac{\gamma}{\gamma-1} = \frac{e(\phi_0-\phi_\infty)}{T^*}. \tag{6.9}$$

6.3. Verification of Assumptions

The model proposed in the previous section relies on a series of assumptions that must be verified and discussed before proceeding. To this end we employ the full PIC simulations of a GIE plume presented and validated in Ref [50] to evaluate the accuracy of our hypotheses. The results presented hereafter refer to the specific operating conditions of case O1 P1 F, in which electron macro-particles were sorted into primary and trapped particle lists depending on their mechanical energy[49], but an analogous outcome is obtained when considering all other simulation cases. For this specific simulation the values of the characteristic electron temperature, the maximum plume potential, and the infinity potential obtained by the PIC code and employed hereafter were respectively $T^* = 2.58\,\text{eV}$, $\phi_0 = 28.56\,\text{V}$, and $\phi_\infty = 10.38\,\text{V}$.

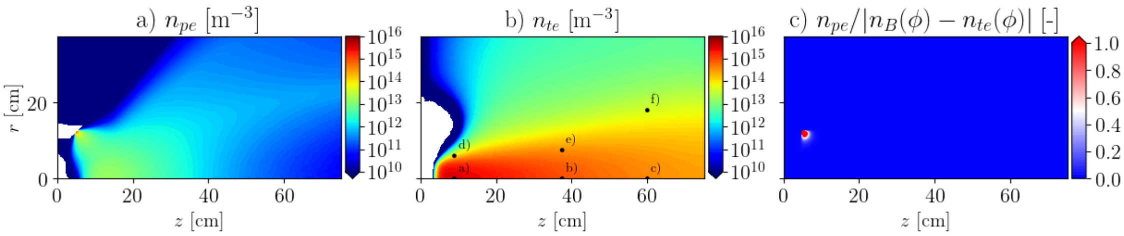

Figure 6.1: The steady-state primary and trapped electron densities (n_{pe} and n_{te} respectively), along with the non-dimensional parameter indicating the effectiveness of the assumption on the electron densities behind the proposed closure, for the case O1 P1 F of Ref [50]. The black dots and labels in panel (b) indicate the positions where the VDFs displayed in the corresponding panels of Figure 6.2 are measured.

First, Figure 6.1, displays the steady-state densities of primary and trapped electrons, along with the non-dimensional parameter employed to evaluate the applicability of the Boltzmann and trapped electron relations for the total electrons densities (respectively Eqs. (6.7) and (6.4)). The comparison of the first two panels confirms that —except in the immediate proximity of the neutraliser— the primary electrons provide a negligible contribution to the total electron density, and $n_e \approx n_{te}$ is an accurate assumption in most of the domain. Additionally, the value of $n_{pe}/|n_B(\phi)-n_{te}(\phi)|$ (which has been computed employing the values of T^*, ϕ_0, and ϕ_∞ retrieved by the PIC simulation) is close to zero everywhere in the domain, excluding the region right in front of the neutraliser, indicating that Eq. (6.4) provides a more accurate estimation of the total electron density with respect to the Boltzmann relation.

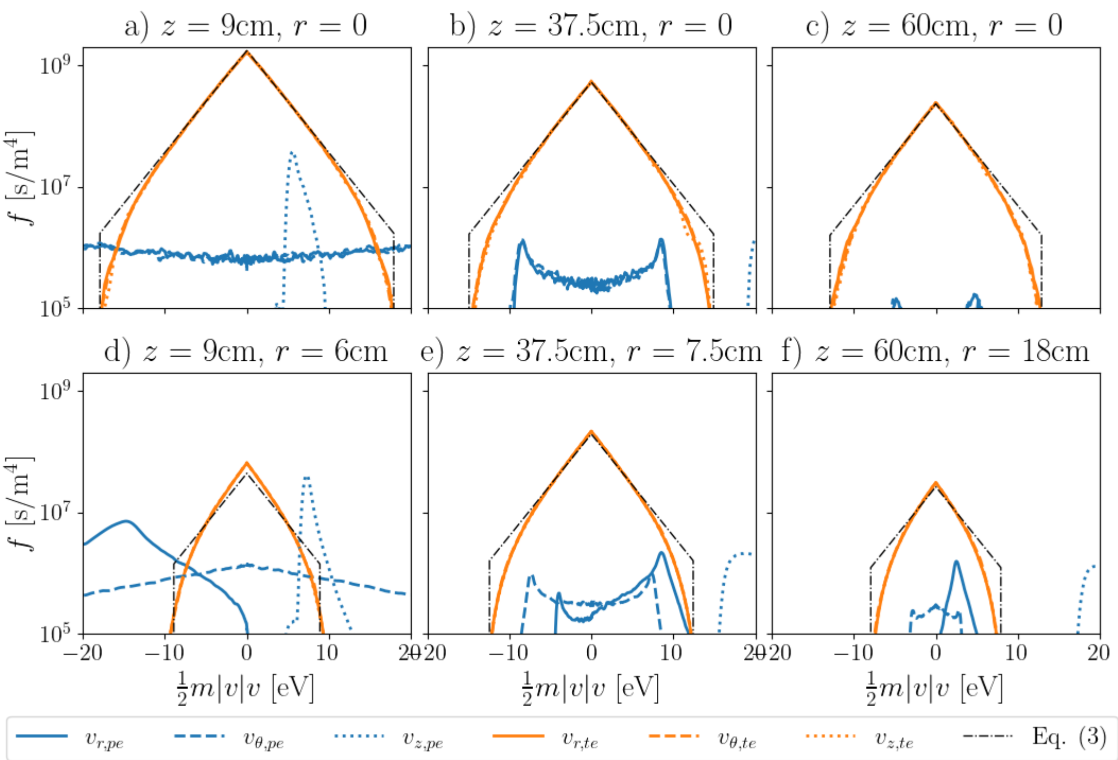

Figure 6.2: The primary and trapped electron VDFs at along the plume's centerline (in the upper row of plots) and at the plume periphery (in the lower row). Each curve represents a mono-dimensional distribution, obtained by integrating the 3D VDF in the remaining two dimensions. The data has been smoothed with a sliding window filter to remove noise and increase readability. In all panels the dashed-dotted black line represents the analytical formulation of Eq. (6.3). Note that in some cases the axial energy of primary electrons exceed the bounds of the x axis.

Second, Figure 6.2 displays the VDFs of primary (in blue) and trapped electrons (in orange) at six different points in the plume (on the plume axis in the upper row, and in the plume's periphery in the second). The location in the plume corresponding to each panel of Figure 6.2 has also been marked in Figure 6.1(b). The black dash-dotted line displays the analytical formulation for the trapped electron VDF of Equation (6.3), in which the values of n_0, ϕ_0, ϕ_∞, T^* and of ϕ at the considered point were taken from the PIC simulation itself. At all the considered points (possibly excluding the one of panel (d), located just in front of the neutraliser), Eq. (6.3) proves to be a good estimation of the trapped electron VDF, although a rounding of the high energy "corners" of the VDF obtained by the PIC code —which is not captured by our analytical formulation— can be observed. This is to be expected, since the corners of the trapped electron distribution are smoothed out by collisional processes that enable the escape of those electrons that already belong to the higher energy regions of the VDF. Consider, however, that this rounding only affects a minimal portion of the electron population (note that the y-axis in Figure 6.2 is in logarithmic scale) and that the slight overestimation of the trapped electron density (and temperature) that it causes partially balances out the omission of primary electrons.

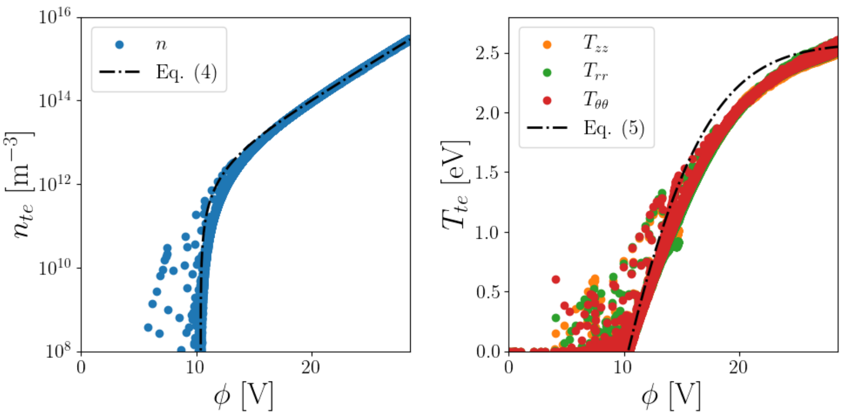

Figure 6.3: Comparison between the derived expressions for the trapped electron density and temperature as a function of the local potential (in dash-dotted black lines), and the corresponding data-points obtained from the full PIC simulation (shown with coloured markers).

Having confirmed that our approximation of the trapped electron VDF captures sufficiently well its profile, Figure 6.3 displays the comparison between the consequent expressions for their density and temperature as a function of the local potential (respectively Eqs. (6.4) and (6.5), where once again n^*, ϕ_0, ϕ_∞ and T^* are taken from the PIC simulation) and the results of the full PIC model. Focusing first on the profile of T_{te}, Figure 6.3(b) shows in differently coloured markers the three diagonal components of the temperature tensor obtained by the PIC simulation (the off-diagonal ones are negligible), confirming that the trapped electron population is perfectly isotropic and that the use of a single scalar temperature is appropriate. Additionally, because of the clear-cut corners of the underlying VDF observed in Figure 6.2, Eq. (6.5) is shown to provide a slight overestimation of the temperature at potential values between 13 V and 21 V. Nevertheless, both analytical expressions for the density and temperature of trapped electrons as a function of ϕ display a satisfactory correlation with the PIC simulation data.

Finally, Figure 6.4 evaluates the accuracy of the two approaches proposed above (quasi-neutral and non-neutral) for the computation of the electric potential. This is done by considering the ion density map retrieved by the PIC simulation at steady-state, computing the resulting electric potential map by either imposing quasi-neutrality or solving the non-linear Poisson problem, and comparing it with the potential values self-consistently obtained by the full PIC code. In order to provide a benchmark for the proposed model, the results obtained employing the Boltzmann and polytropic relations of Eqs. (6.7) and (6.8) are also shown in Figure 6.4. Both in the quasi-neutral and in the

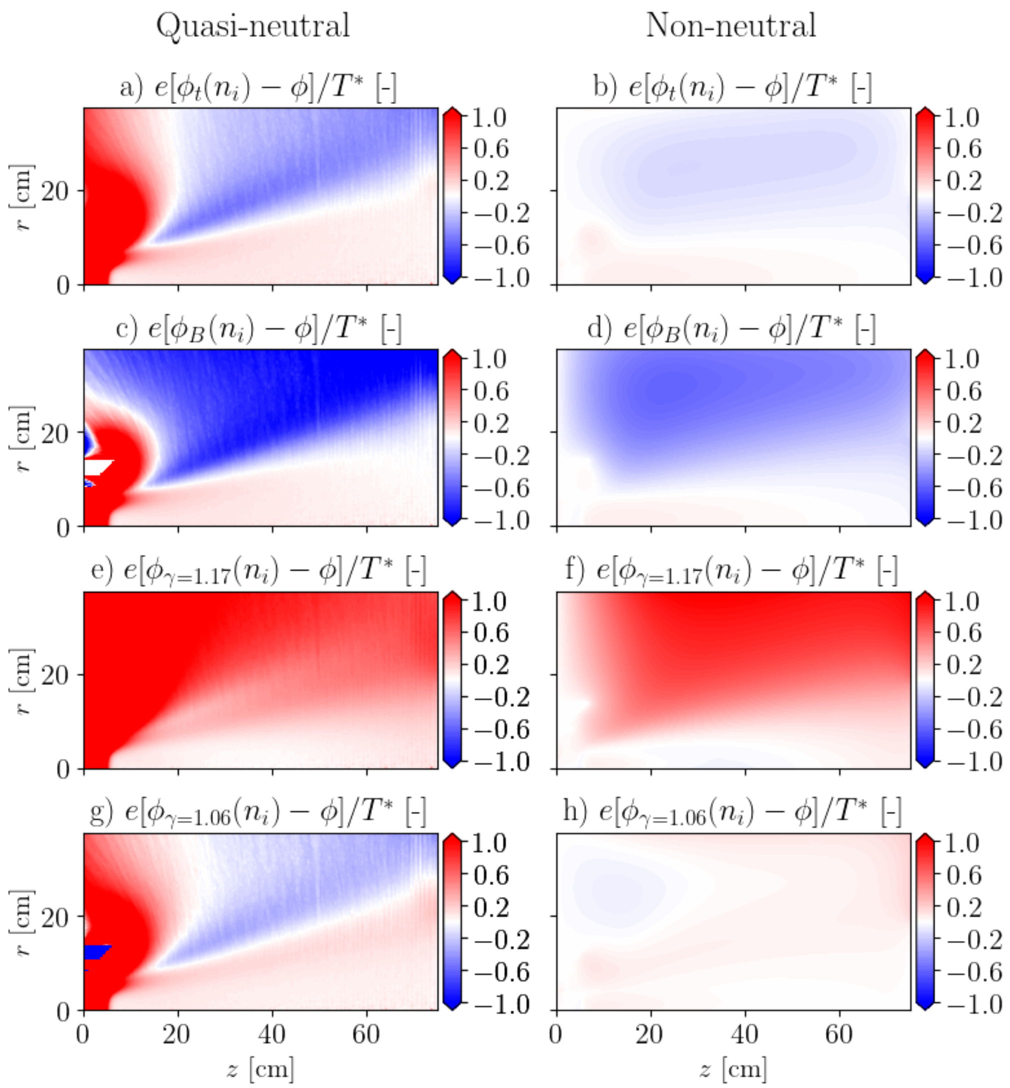

Figure 6.4: Errors between the PIC solution and the the potential maps computed with the proposed closure [panels (a) and (b)], with a Boltzmann relation [panels (c) and (d)], and with the polytropic relation [panels (e) to (h)]. All errors are normalised by the characteristic electron temperature T^*.

non-neutral case, the proposed approach provides smaller errors compared to the Boltzmann closure, which tends to amplify the potential drop outside of the plume due to its overestimation of the primary electron density. The evaluation of the precision of the polytropic relation, on the other hand, is not as straight forward. Indeed, if a polytropic parameter $\gamma = 1.166$ is used, as obtained by inserting the value of ϕ_∞ in Eq. (6.9), the resulting quasi-neutral and non-neutral potential maps tend to overestimate the values of ϕ at the plume periphery, as shown in panels (e) and (f). Nevertheless, panels (g) and (h) prove that, within the considered domain, potential errors equivalent to those obtained with the use of Eq. (6.4) can be obtained by decreasing arbitrarily the polytropic index to $\gamma = 1.06$. This value of γ, however, theoretically corresponds to a potential at infinity of $\phi_\infty = -17$ V (as opposed to the $\phi_\infty = 10.38$ V obtained by the PIC simulation), so that if one could enlarge the simulation domain, an eventual disagreement between the PIC and the polytropic solutions is to be expected.

Focusing now on the quasi-neutral cases, all closures display large errors close the the thruster grids and cathode due to the non-neutral sheaths that are present there, which can only be resolved by integrating Poisson's equation. It is important to remember, however, that in order to relax the computational burden of the PIC code, the vacuum permittivity in those simulations (and thus in the computation of the map of ϕ that is here used as reference) was artificially increased by a factor $f_D^2 = 400$, thus enlarging the non-neutral regions by approximately a factor f_D =20. Similarly, the errors in the potential outside of the main ion beam may be accentuated by the use of a larger vacuum permittivity in the PIC code, which leads to an overestimation of non-neutrality in these regions of lower plasma density. In the rightmost row of plots, on the other hand, in which the Poisson equation is solved for (also with $f_D^2 = 400$ to ensure a consistent comparison), the discrepancies due to the sheaths in front of cathode and grids disappear since they are now solved for. In particular, in the case of the closure proposed in this work [see panel (b)], the error in the whole domain never exceeds 0.4 V, confirming the validity of the hybrid approach proposed here.

6.4. Result Comparison

Up to this point the validation of the proposed model and its underlying assumptions has been carried out considering the steady-state equilibrium reached by the full PIC simulation. A more complete and consistent evaluation of the model's accuracy, however, must take into account the steady-state reached when employing the proposed hybrid approach, and compare its relevant plasma properties with those obtained by the full PIC model. To this end, the non-neutral version of the algorithm outlined in Section 6.2 was implemented in FORTRAN, and was used to simulate a scenario identical to the full PIC simulation case O1 P1 F of Ref. [50]. The problem geometry, the operating point of the thruster, the background neutral density and the numerical mesh were thus kept unvaried, while the simulation time-step could be incremented by a factor 100 thanks to the relaxation of its numerical constraints. The non-neutral approach was here preferred to the quasi-neutral one because of its ease of comparison with the non-neutral PIC code, especially in presence of an artificially augmented vacuum permittivity, which for consistency was also employed in the hybrid code. As a consequence, a numerical method for the resolution of the non-linear Poisson equation was developed. At each simulation time-step, the method starts from an initial guess of the potential map $\phi^{(0)}$ and iteratively corrects it until a convergence criterion is reached. In practice, at a generic iteration instance k, the potential map $\phi^{(k)}$ is used to compute the corresponding electron density and charge density, and the resulting linear Poisson equation is solved, yielding a potential map ϕ'.

This map is then used to update the guess of the potential as

$$\phi^{(k+1)} = \phi^{(k)} + C\frac{T^*}{e}\frac{\phi' - \phi^{(k)}}{\max(|\phi' - \phi^{(k)}|, 4T^*/e)}. \tag{6.10}$$

Where a value of the tuning parameter $C = 0.05$ was found to guarantee stable convergence. The iterations on the potential map were stopped when $\max(|\phi^{(k)} - \phi'|) < 0.1\,\mathrm{V}$, which for the scenario considered was reached in the vast majority of time-steps with less than 10 iterations. This approach proved to be simple and effective, especially for the demonstrative scope of the present work. However, the time employed in the inversion of the non-linear Poisson problem foreseeably constitutes a relevant fraction of the total simulation time (in the present scenario it accounted for 30% of the simulation), so that future optimized versions of the model should take into consideration alternative numerical schemes for its resolution.

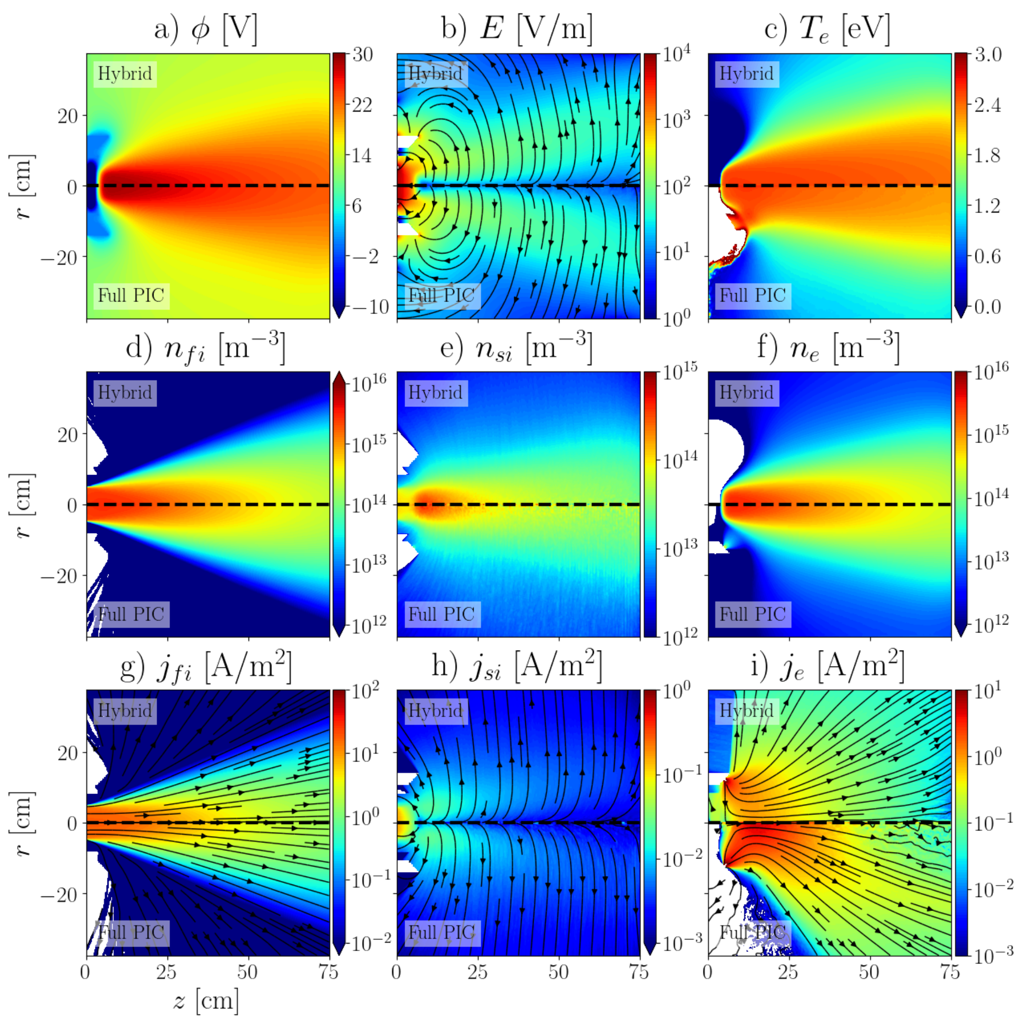

Figure 6.5: Comparison between the steady-state results for the simulation case O1 P1 F of the hybrid and full PIC simulations.

Figure 6.5 shows the comparison between the steady-state results of the proposed hybrid methodology, and those of the PIC simulation. In particular, from left to right the panels of each row show the maps of the electric potential, the electric field and the electron temperature; the densities of fast ions (those emitted by the thruster), slow ions (those generated in the plume), and electrons; and their respective electric currents. The upper half of each panel shows the results of the hybrid simulation, while the bottom half displays the steady-state reached by the PIC model. Both codes provide very similar results, especially when considering the fast and slow ion properties In line with this general agreement, the hybrid and PIC potential maps shown in panel (a) display only minimal differences, and as a consequence the profiles of the electric field, electron density, and temperature of panels (b), (c) and (f) are also very similar. In all three cases, in fact, the main differences can be observed in proximity of the neutraliser, where the assumption of a negligible primary electron density does not hold. These differences, however, remain confined to the region of the plasma bridge, while the comparison in the plume bulk for the electric field and electron densities remains excellent. Similarly, only a minimal overestimation by the hybrid model of the electron temperature in the plume can be observed in panel (c), in line with the observations already made for Figure 6.3(b).

Finally, panel (i) displays the comparison between the electron current maps, which we remind here are computed in the hybrid approach once the simulation has reached steady-state by freezing the potential map and integrating within it the trajectories of test particles injected from the neutraliser. Comparing the two solutions, the currents obtained by the full PIC code are more focused around the neutraliser axis, because of the electric forces that are present at the cathode orifice due to the high primary electron density. These have a lasting effect the electron trajectories even further downstream, which tend to fan out more in the case of the hybrid simulations, but remain slightly more focused in the case of the full PIC code. Nevertheless, even in presence of these minor differences, the comparison between the results of the two codes is satisfactory when considering the difference in computational costs. Indeed, while the full PIC model takes roughly 80 hours to reach steady-state running on the 40 physical cores of two Intel Xeon Silver 4316 processors, the hybrid code takes roughly 3 hours to run an analogous simulation on 16 physical cores of the same processor.

6.5. Determination of ϕ_0, ϕ_∞ and T^*

Sections 6.3 and 6.4 have proven that, if a sufficiently accurate estimation of the free parameters of the closure ϕ_0, ϕ_∞ and T^* is provided, the proposed model provides a satisfactory description of the plasma in GIE plumes. The problem now becomes, therefore, the precise determination of these three scalar values. On the one hand, this new query takes advantage of the fact that all three parameters represent clear and measurable physical values (unlike, for example, the γ parameter in a polytropic closure): ϕ_∞ is the floating thruster potential with changed sign, ϕ_0 the maximum plasma potential value in the plume bulk (which should be located just downstream of the thruster grids), and T^* approximately coincides with the electron temperature at that same point. On the other hand, all three values depend on the delicate global equilibrium reached by the column of trapped electrons, which even the higher-fidelity full PIC model struggles to precisely identify, as demonstrated in the comparison with experiments of Ref. [50]. This is partially due to the fact that ϕ_0, ϕ_∞ and T^* all represent energies which are orders of magnitude smaller than the energies externally applied to the system (ions are injected with around 1000 eV of energy into the plume, and a potential difference of 150 V is set between the acceleration grid and the neutraliser), making their precise determination challenging. To further complicate things, none of the three parameters appears to depend on a single physical process, but rather from the interaction between multiple interdependent mechanisms such as the equilibrium of collisional processes that trap and release trapped electrons, the requirement of a current free plume, the electron conductivity in the plasma bridge, and the development of plasma sheaths in front of material objects.

An illustrative example of the delicate and malleable equilibrium reached by the column of trapped electrons may be found in our attempts to establish a simple model for ϕ_0. At a naive first glance, in fact, the value of the maximum potential appears to depend on the characteristics of the plasma sheath that forms in front of the acceleration grid. A simple 1D axial model, that describes the variation of ion and electron densities along the plume axis coupled with Poisson's equation, should therefore be capable of providing a first estimation of ϕ_0. To this end we employ the expression derived in Reference [83] for the ion density along the axis of a GIE plume

$$n_i(\phi, z) = \frac{I_i}{eA_{ag}\left(1 + \dfrac{z}{R}\tan\alpha\right)^2 \sqrt{u_{i0}^2 - \dfrac{2e(\phi - \phi_{ag})}{m_i}}}, \tag{6.11}$$

where z is the axial coordinate, I_i is the ion current emitted by the thruster, A_{ag} is the emission area of the acceleration grid, R and ϕ_{ag} are its radius and potential, and α and u_{i0} are the initial divergence and velocity of the mono-energetic ion beam. This expression for the ion density is then coupled with the law for the trapped electron density of Eq. (6.4) (where ϕ_∞ and T^* are still assumed to be given, while ϕ_0 is now an additional unknown of the problem) and with the 1D Poisson equation and its boundary conditions:

$$\begin{cases} \dfrac{d^2\phi}{dz^2} & = -\frac{e}{\varepsilon_0}\left[n_i(\phi, z) - n_e(\phi, \phi_0)\right] \\ \phi(0) & = \phi_{ag} \\ \left.\dfrac{d\phi}{dz}\right|_{z=z_0} & = 0. \end{cases} \tag{6.12}$$

Although this may appear a closed system of equations, the last boundary condition implicitly introduces a new unknown: the position of the potential maximum z_0. Without an additional condition that either provides the value of ϕ_0 or of z_0, therefore, the system of equations is undetermined. This is shown in Figure 6.6, where we plot the axial potential profiles obtained by solving with a shooting method the described axial 1D model parametrized in function of z_0. As obvious from the plot, a different ϕ_0 is obtained for

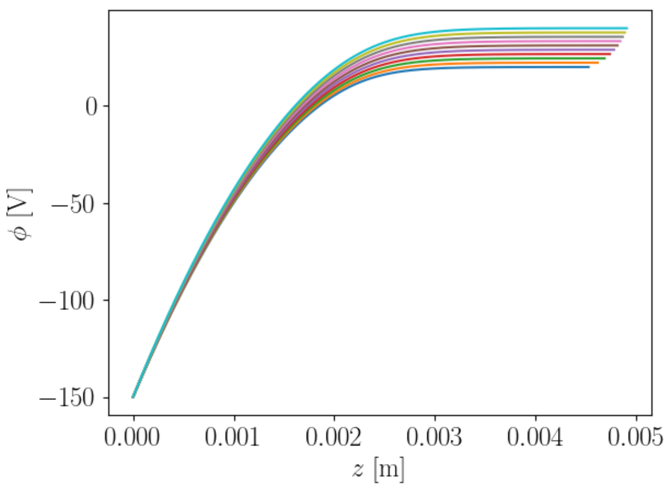

Figure 6.6: Potential profile within the plasma sheath that develops in front of the acceleration grid according to the 1D model. Each line corresponds to the solution with a different total sheath z_0.

each value of z_0 imposed; or, in other terms, any value of ϕ_0 required by the global equilibrium of the plasma plume can be obtained through a slight extension or contraction of the sheath in front of the acceleration grid.

Given this complexity, the dependence of ϕ_0, ϕ_∞ and T^* on parameters of the problem such as the operating point of the thruster, the neutral background pressure, and the relative position and orientation between thruster and neutraliser requires further, detailed research and should eventually lead to a theoretical, physics-based model for their determination. In the meantime, however, we propose here a heuristic approach for their approximation based on the numerical and experimental observations presented in Ref [50]. First, we note that from the experimental standpoint the value of ϕ_∞ is largely independent on the background pressure and is of relatively simple determination. An experimental measurement of the thruster's floating potential (and its variations with the operating point) would therefore be the most direct and dependable approach to its quantification. Second, we observe that in all of the cases considered there is, both numerically and experimentally, a direct dependence between the background pressure and T^*, which on the other hand does not depend on the thruster's operating point. To visualize this, Figure 6.7 displays, for the two operating points considered, the variation of T^* in function of the background pressure p_{bg} according to experimental and numerical data (respectively in red and blue markers), along with two linear fits which we provide below for completeness:

$$T^* = 7.233 - 43492 p_{bg} \tag{6.13}$$

for the experimental data, and

$$T^* = 2.508 - 9679 p_{bg} \tag{6.14}$$

for the simulation data, where T^* and P_{bg} are respectively given in eV and mbar.

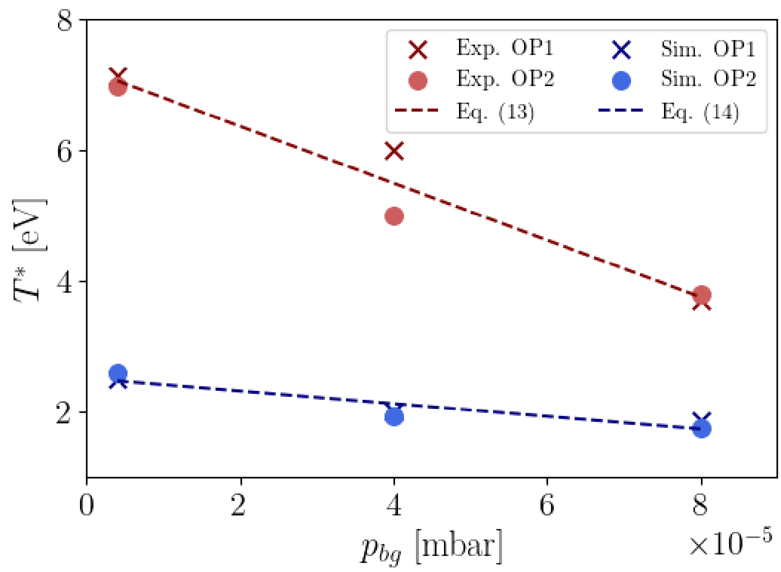

Figure 6.7: Behaviour of the trapped electron characteristic temperature as a function of the background pressure according to experimental and numerical data.

The final observation, that can be used to retrieve ϕ_0, is that the ratio $e(\phi_0 - \phi_\infty)/T^*$ is roughly constant both for simulations and experiments, as shown in Table 6.1. Numerically this ratio suffers only small fluctuations around the average value $\langle e(\phi_0 - \phi_\infty)/T^* \rangle_n$ = 6.82. Experimentally, on the other hand, the fluctuations around the average value $\langle e(\phi_0 - \phi_\infty)/T^* \rangle_e$ = 4.74 are larger, although it must also be stated that the determination of this ratio from the available experimental data is of much more complex and uncertain nature. This is because the experimental campaign of Reference [50] did not provide a map of the plume potential, so that the location of the reference point 0 had to be assumed just downstream of the thruster grids, and the value of ϕ_0 had to be roughly extrapolated from the energies of ions flowing radially outside of the plume. Even so, our experimental measurements also yields a ratio between T^* and the total potential drop in the plume that remains roughly constant throughout all of the operating conditions explored. As a result, with the value of ϕ_∞ obtained experimentally, and that of T^* given by Eq. (6.13) or (6.14), ϕ_0 can be trivially determined by assuming a reasonable value of $e(\phi_0 - \phi_\infty)/T^*$, and the hybrid methodology introduced in Section 6.2 can be employed without the need of a supporting model.

6.6. Conclusions

This paper develops and presents an approach for hybrid simulations of GIE plumes, that attempts to overcome the challenge of the identification of an accurate closure for the classical electron fluid formulation. The proposed methodology stems from the subdivision of plume electrons into primary and trapped populations, and from the observation that the former category provides a negligible contribution to the total electron density.

Case	Simulation	Experiment
O1 P1 F	6.97	7.46
O2 P1 F	6.99	6.58
O1 P2 F	6.71	4.17
O2 P2 F	6.65	4.85
O1 P3 F	6.65	4.17
O2 P3 F	6.53	4.17

Table 6.1: Numerical and experimental values of the ratio $e(\phi_0 - \phi_\infty)/T^*$ for the different operating conditions considered.

The latter electron population can instead be described through an approximation of their VDF, which allows the determination of analytical expressions for their density and temperature as a function of the local plasma potential. As a result, a quasi-neutral and a non-neutral version of the hybrid model are proposed, that guarantee a relevant reduction of computational times (upward of a factor 10) with respect to an equivalent full PIC formulation.

The assumptions on the negligible influence of primary electrons and on the VDF profile of trapped ones, that are at the base of the developed electron model, are then verified by means of previously developed and validated full PIC simulations of a GIE plume[49], [50]. Moreover, a practical implementation of the developed non-neutral hybrid model is proposed and its results are compared with those obtained with the full PIC code. The comparison demonstrates an excellent agreement between the results of the two codes if an accurate estimation of the three scalar free parameters of the developed hybrid model (the floating thruster potential ϕ_∞, a characteristic electron temperature T^*, and the maximum plume potential ϕ_0) can be provided.

Unfortunately, a theoretical and fully consistent approach to the determination of these parameters could not be identified in the present work, and will be the topic of future research. Nevertheless, a heuristic method for the determination of ϕ_∞, ϕ_0 and T^* was extrapolated from the available numerical[188] and experimental[187] data of the RIT10-EVO's plasma plume, permitting an independent utilization of the model.

Although the developed hybrid methodology displays enticing computational costs and a promising comparison with full PIC results, important additional research must be undertaken before it can be confidently and independently employed for the simulation of GIE plumes. Chief among the remaining open points is the issue of the accurate determination of ϕ_0, ϕ_∞ and T^*, and the sensitivity of the model to their values. The provided heuristic approach, in fact, relies on a limited set of experimental and numerical data of the sole plume of the RIT10-EVO, which must thus be expanded to other thrusters and other operating conditions before it can be assumed to have predictive capabilities. Moreover, the proposed approach does not and can not provide a theoretical and physics-based understanding of the behaviour of ϕ_0, ϕ_∞ and T^* as a function of the operating conditions and design parameters of the thruster and neutraliser. A deeper understanding of this dependency likely requires dedicated research on the influence of the neutraliser and plasma bridge properties on the plume equilibrium, and on the effects of collisional processes on the trapped electron population. Finally, the proposed hybrid model would benefit from an investigation of the accuracy of its quasi-neutral version, which was not extensively elaborated in this work, as well as from a study dedicated to the injection conditions for the primary electron test particles employed to obtain the electron currents in the domain, which may allow a better comparison with the full PIC results.

Acknowledgements

This work has been supported by the ECOMODIS project, funded by the European Space Agency, under contract 4000137869/22/NL/RA. The authors would also like to thank Alberto Marín-Cebrián for his invaluable contributions to the development of PICASO and to the physical interpretation of the simulation results, and Käthe Dannenmayer and Fabrice Cipriani for the invaluable support throughout the arc of the project.

CHAPTER 7

Conclusions

This chapter provides a summary of the main achievements accomplished throughout the thesis, and proposes future work to build upon the present results.

7.1. Summary and Main Results

This thesis consists of a collection of simulation efforts, employing different modelling approaches, of EPT and GIE plasma plumes. Each of these efforts strives to provide novel insight on the core physical mechanisms that govern the plume equilibrium, on the external factors that may influence it, and on the effectiveness of the chosen modelling approach. Their results are here covered separately based on the propulsive architecture investigated.

Simulation of Magnetic Arches: The 3D in-house hybrid code EP2PLUS was adapted, assuming a polytropic closure for electrons, to the simulation of a planar magnetic arch, the magnetic topology that arises when clustering a pair of EPTs with opposite magnetic polarities. The use of a planar hybrid code allowed, for the first time, a parametric analysis of the influence on the plume properties of electron magnetization, collisional processes, and boundary conditions. The plume of a magnetic arch was found to be divisible in (i) a near plume, where the plasma beams emitted by each EPT source are yet to interact; (ii) a transition region, where the weakly collisional merging of the two plasma beams gradually takes place, giving rise to non-Maxwellian ion VDFs and double-peaked plasma properties; and (iii) a far plume, where the merging of the two plasma beams has fully completed. The presence of a region of magnetic drag was observed where the expanding plasma is forced to cross closed magnetic field lines, but ultimately a saturation of the effects of the magnetic field on the propulsive and discharge properties was detected for values of the Hall parameter larger than 10. At high electron magnetization levels the in-plane electron currents were found to be sensitive to the magnetic topology and BCs (prompting the distinction between BCs to be applied in a vacuum vessel or in space), but were also shown to be strongly decoupled from other plasma properties. Finally, a study on the effects of ion-neutral collisions highlighted a relevant production of slower ions within the plume, and the consequent increase in propulsive performance due to neutral entrainment.

Simulation of GIE plumes: The ion beam of a gridded ion thruster, neutralised by an externally mounted cathode, was simulated by means of a full PIC code in its planar and axisymmetric versions. These simulations highlighted for the first time the importance of inelastic collisional processes between electrons and neutrals in the neutralisation of the thruster's ion beam, that provide the energy loss mechanism required to reduce the mechanical energy of electrons and confine them within the potential well of the plume. As a result, a relevant improvement with respect to previous works in the literature was observed in the values of the electric potential and electron temperature predicted by the model. The process of electron trapping allows a conceptual subdivision of electrons into primary ones, those yet to undergo an inelastic collision and sufficiently energetic to escape the ion beam, and the trapped ones, electrostatically confined within the plume. A parametric analysis of the model inputs also revealed that, at equilibrium, the characteristics of primary electrons are directly associated with the emission properties of the neutraliser, while the much more numerous trapped electron population reaches a delicate and complex equilibrium that interacts with the neutraliser and primary electrons through the mediation of scarce collisional events.

Later, these theoretical conclusions and the results of the full PIC code were thoroughly compared with the data from a dedicated experimental investigation of the RIT10-EVO's plasma plume. This analysis showed that the developed model accurately predicted the ion properties in the plume bulk, but was not as exact in the determination of the equilibrium reached by the confined electron cloud. Nevertheless, simulations were capable of qualitatively explaining the decrease of the plasma potential and electron temperature in the plume as the facility background pressure was raised, and their increase when negatively biasing the thruster body with respect to the chamber walls. Additionally, simulations were also employed to evaluate the effect of immersing a double Langmuir probe into the plume, indicating that it could lead to a change in the plume's equilibrium, causing non-negligible shifts in the plasma potential but leaving the electron temperature and density nearly unaffected.

Finally, a closure for the electron fluid equations, based on an approximation of the electron VDF, was proposed for the specific case of GIE plumes. The closure, employed in a non-neutral hybrid code, was shown to markedly reduce computational costs with respect to a full PIC code, while providing very similar results. However, the suggested algorithm relies on the knowledge *a priori* of the maximum potential value in the plume, of the floating potential of the thruster, and of a reference electron temperature. Although a heuristic approach has been proposed for the determination of these values, extensive further research is required for their theoretical determination as a function of the parameters of the problem, and for the confident extension of the algorithm to any GIE plume.

7.2. Future Research

As is often the case in research, the physical and numerical insight provided in this work opens the door to many further queries and open points. In an attempt to guide said research, the more relevant of these points are schematically summarized below.

Magnetic arch simulations:

1. Extend the analysis to the three-dimensional scenario, providing a more realistic overview of the full expansion, and allowing the study of the closure of the electron currents in the direction normal to the plane containing the arch.
2. Improve the description of the electron thermodynamics, either by including the energy equation in their fluid module or by considering the use of a kinetic methodology for the determination of their properties. This improvement would allow a more accurate description of the pressure forces and a study of the effects of inelastic collisions on the plasma equilibrium and on the propulsive properties of the magnetic arch.
3. Provide a first evaluation of the effect that the exchange of particles (principally electrons) along closed magnetic lines may have on the plasma discharge within the chambers of the two EPTs. The ionization region in EPTs, in fact, communicates directly with the plume, and the flow of electrons produced in one source into the other (and *vice versa*) may have a strong influence on the properties of the discharge. A first approach to this study consists in coupling a PIC model (a kinetic description of electrons is necessary to distinguish between the outgoing and incoming electron properties) with a global model for the discharge chamber of the EPT.
4. Study the applicability and effectiveness of controlling the direction of the thrust vector by modulating the intensities of the magnetic fields of the two EPTs.

GIE plumes:

1. Develop and couple the PIC simulations with a global model for the internal neutraliser dynamics, capable of self-consistently determining its exhaust properties as a function of the plume equilibrium. This development should allow to restrict the uncertainties linked to the currently externally imposed values of T_e and I_e^+.

2. Study the importance of the plasma bridge that develops between the neutraliser and the ion beam in the determination of the final plume equilibrium. The assumption of axisymmetry often employed in the thesis, in fact, importantly distorts the plasma properties in this region, possibly influencing the potential values ultimately obtained at equilibrium. Given the prohibitive computational costs associated with a full plume 3D simulation characterized by realistic plasma densities at the neutraliser exhaust, this research line should first consider the study of an isolated cathode and its plume, and then envision an approach to couple it with the ion beam.

3. Analyse in detail the effects of elastic and inelastic collisions on the final equilibrium reached by the column of trapped electrons. At steady-state and in absence of oscillations an exact equilibrium between collisional processes that allow the trapping and escape of electrons from the plume bulk must exist, and in some cases may be delicately dependent on the collisional algorithms employed. Central to this study would be the inclusion of an accurate description of Coulomb interactions, and a precise evaluation of the effects of numerical thermalisation.

4. Extend the research on the effects of an immersed probe by executing a virtual voltage scan of the simulated probe and recording the resulting IV curve. This would allow a more precise evaluation of the measurement distortions that the non-stationary plasma equilibrium may cause.

5. Improve the description of neutrals by periodically updating their properties to be in equilibrium with the current plasma characteristics.[203] This would ensure that the maps of neutral density, velocity and temperature are consistent with the final plume equilibrium, without extending the simulation length to the full neutral timescales.

6. Improve the code parallelization, possibly porting it to GPUs. In particular this latter development may help make 3D simulations, or ones with more realistic values of the vacuum permittivity, computationally affordable.

7. Finally, the closure to the electron fluid equations proposed in Chapter 6 requires extensive further research to (i) ensure that it provides an accurate and general description of the electron properties in most GIE architectures; and (ii) provide a theoretical framework for the determination of the floating thruster potential, maximum plume potential, and characteristic electron temperature.

Bibliography

[1] R. Cybulski et al., "Results from SERT I ion rocket flight test," in *Air Force Office of Scientific Research Proceedings*, vol. 1, 1965, p. 21. [Online]. Available: https://ntrs.nasa.gov/citations/19650009681.

[2] E. Y. Choueiri, "A critical history of electric propulsion: The first 50 years (1906-1956)," *Journal of Propulsion and Power*, vol. 20, no. 2, pp. 193–203, 2004. DOI: 10.2514/1.9245.

[3] E. Y. Choueiri, "A critical history of electric propulsion part II: 1957-1979," in 39th *International Electric Propulsion Conference*, London, United Kingdom, September 14-19: Electric Rocket Propulsion Society, Fairview Park, OH, Sep. 2025. [Online]. Available: https://www.electricrocket.org/IEPC_2025/London/submission_723.pdf.

[4] W. Kerslake, R. Goldman, and W. Nieberding, "SERT II - mission, thruster performance, and in-flight thrust measurements," *Journal of Spacecraft and Rockets*, vol. 8, no. 3, pp. 213–224, 1971. DOI: 10.2514/3.30250.

[5] C. Purvis, R. Bartlett, and S. DeForest, "Active control of spacecraft charging on ATS-5 and ATS-6," in *1st Spacecraft Charging Technology Conference*, Colorado Springs, Colorado, USA, 1977, pp. 108–120. [Online]. Available: https://ntrs.nasa.gov/citations/19780002193.

[6] R. A. Johnson, W. T. Morgan, and S. R. Rocklin, "Design, ground test and flight test of snap 10a, first reactor in space," *Nuclear engineering and design*, vol. 5, no. 1, pp. 7–21, 1967. DOI: https://doi.org/10.1016/0029-5493(67)90074-X.

[7] A. R. Frederickson, "Upsets related to spacecraft charging," *IEEE Transactions on Nuclear science*, vol. 43, no. 2, pp. 426–441, 1996. DOI: 10.1109/23.490891.

[8] J. I. Minow et al., "ISWAT spacecraft surface charging review," *Advances in Space Research*, 2024. DOI: https://doi.org/10.1016/j.asr.2024.08.058.

[9] H. C. Koons and D. J. Gorney, "Relationship between electrostatic discharges on spacecraft p78-2 and the electron environment," *Journal of Spacecraft and Rockets*, vol. 28, no. 6, pp. 683–688, 1991. DOI: 10.2514/3.26300.

[10] H. C. Koons and H. A. Cohen, "Plasma waves and electrical discharges stimulated by beam operations on a high altitude satellite," in *Artificial Particle Beams in Space Plasma Studies*, B. Grandal, Ed. Boston, MA: Springer US, 1982, pp. 111–120. DOI: 10.1007/978-1-4684-4223-6_7.

[11] J. Likar et al., "Spacecraft charging monitoring at GEO: Natural and electric propulsion environment measurements," in *47th AIAA Aerospace Sciences Meeting including The New Horizons Forum and Aerospace Exposition*, ser. AIAA 2009-121, Orlando, Florida, USA: American Institute of Aeronautics and Astronautics, Reston, VA, Jan. 2009, p. 121. DOI: 10.2514/6.2009-121.

[12] S. Bergman, G. Stenberg Wieser, M. Wieser, F. L. Johansson, and A. Eriksson, "The influence of spacecraft charging on low-energy ion measurements made by RPC-ICA on Rosetta," *Journal of Geophysical Research: Space Physics*, vol. 125, no. 1, e2019JA027478, 2020. DOI: 10.1029/2019JA027478.

[13] M. Rojo et al., "Electron moments derived from the Mercury Electron Analyzer during the cruise phase of BepiColombo," *Astronomy & Astrophysics*, vol. 683, A99, 2024. DOI: 10.1051/0004-6361/202347843.

[14] J. Geach, S. J. Schwartz, V. Génot, O. Moullard, A. Lahiff, and A. N. Fazakerley, "A corrector for spacecraft calculated electron moments," *Annales Geophysicae*, vol. 23, no. 3, pp. 931–943, 2005. DOI: 10.5194/angeo-23-931-2005.

[15] L. N. Ahmed and M. W. Crofton, "Surface modification measurements in the T5 ion thruster plume," *Journal of propulsion and power*, vol. 14, no. 3, pp. 336–347, 1998. DOI: 10.2514/2.5302.

[16] K. Holste et al., "Ion thrusters for electric propulsion: Scientific issues developing a niche technology into a game changer," *Review of Scientific Instruments*, vol. 91, no. 6, p. 061 101, 2020. DOI: 10.1063/5.0010134.

[17] D. Rafalskyi et al., "In-orbit demonstration of an iodine electric propulsion system," *Nature*, vol. 599, pp. 411–415, 2021. DOI: 10.1038/s41586-021-04015-y.

[18] D. Brinza, J. Wang, J. Polk, and M. Henry, "Deep Space 1 measurements of ion propulsion contamination," *Journal of Spacecraft and Rockets*, vol. 38, no. 3, pp. 426–432, 2001. DOI: 10.2514/2.3701.

[19] J. Wang et al., "Deep Space One investigations of ion propulsion plasma environment," *Journal of Spacecraft and Rockets*, vol. 37, no. 5, pp. 545–555, 2000. DOI: 10.2514/2.3608.

[20] M. Capacci, G. Matticari, G. Noci, A. Severi, and D. Borie, "An electric propulsion diagnostic package for the characterization of the plasma thruster/spacecraft interactions on STENTOR satellite," in *35th Joint Propulsion Conference and Exhibit*, ser. AIAA99-2277, Los Angeles, California, USA: American Institute of Aeronautics and Astronautics, Reston, VA, Jun. 1999. DOI: 10.2514/6.1999-2277.

[21] M. Tajmar, J. Gonzalez, and A. Hilgers, "Modeling of spacecraft-environment interactions on SMART-1," *Journal of Spacecraft and Rockets*, vol. 38, no. 3, pp. 393–399, 2001. DOI: 10.2514/2.3697.

[22] D. L. Estublier, "The SMART-1 spacecraft potential investigations," *IEEE transactions on plasma science*, vol. 36, no. 5, pp. 2262–2270, 2008. DOI: 10.1109/TPS.2008.2002032.

[23] I. G. Mikellides, G. A. Jongeward, I. Katz, and D. H. Manzella, "Plume modeling of stationary plasma thrusters and interactions with the Express-A spacecraft," *Journal of Spacecraft and Rockets*, vol. 39, no. 6, pp. 894–903, Nov. 2002. DOI: 10.2514/2.3896.

[24] R. L. Corey, J. S. Snyder, X. Price, S. P. Malone, and T. M. Randolph, "Hall thruster plume model for spacecraft impingement torque: Development and validation," *Journal of Spacecraft and Rockets*, vol. 45, no. 4, pp. 766–775, 2008. DOI: 10.2514/1.35905.

[25] T. Trottenberg et al., "An in-flight plasma diagnostic package for spacecraft with electric propulsion," *EPJ Techniques and Instrumentation*, vol. 8, no. 1, p. 16, 2021. DOI: 10.1140/epjti/s40485-021-00073-8.

[26] J. E. Foster and T. J. Topham, "A review of the impact of ground test-related facility effects on gridded ion thruster operation and performance," *Physics of Plasmas*, vol. 31, no. 3, p. 030 501, Mar. 2024. DOI: 10.1063/5.0173655.

[27] D. Byers and J. W. Dankanich, "A review of facility effects on hall effect thrusters," in *31st International Electric Propulsion Conference*, 2009, pp. 2009–076. [Online]. Available: http://electricrocket.org/IEPC/IEPC-2009-076.pdf.

[28] J. S. Sovey, R. H. Vetrone, S. P. Grisnik, R. M. Myers, and J. E. Parkes, "Test facilities for high-power electric propulsion," *Journal of Propulsion and Power*, vol. 10, no. 1, pp. 18–24, 1994. DOI: 10.2514/3.23706.

[29] F. Cichocki, A. Domínguez-Vázquez, M. Merino, and E. Ahedo, "Hybrid 3D model for the interaction of plasma thruster plumes with nearby objects," *Plasma Sources Science and Technology*, vol. 26, no. 12, p. 125 008, 2017. DOI: 10.1088/1361-6595/aa986e.

[30] R. Roy, D. Hastings, and N. Gastonis, "Ion-thruster plume modeling for backflow contamination," *Journal of Spacecraft and Rockets*, vol. 33, no. 4, pp. 525–534, 1996. DOI: 10.2514/3.26795.

[31] J. Wang, D. Han, and Y. Hu, "Kinetic simulations of plasma plume potential in a vacuum chamber," *IEEE Transactions on Plasma Science*, vol. 43, no. 9, pp. 3047–3053, 2015. DOI: 10.1109/TPS.2015.2457912.

[32] K. Nishii and D. A. Levin, "Kinetic simulation of ion thruster plume neutralization in a vacuum chamber," *Plasma Sources Science and Technology*, vol. 32, no. 11, p. 115 009, Nov. 2023. DOI: 10.1088/1361-6595/ad0836.

[33] E. Ahedo and M. Merino, "On plasma detachment in propulsive magnetic nozzles," *Physics of Plasmas*, vol. 18, no. 5, p. 053 504, 2011. DOI: 10.1063/1.3589268.

[34] J. D. Frieman, T. M. Liu, and M. L. Walker, "Background flow model of hall thruster neutral ingestion," *Journal of Propulsion and Power*, vol. 33, no. 5, pp. 1087–1101, 2017. DOI: 10.2514/1.B36269.

[35] B. Wachs and B. Jorns, "Background pressure effects on ion dynamics in a low-power magnetic nozzle thruster," *Plasma Sources Science and Technology*, vol. 29, no. 4, p. 045 002, 2020. DOI: 10.1088/1361-6595/ab74b6.

[36] K. Diamant, R. Spektor, E. Beiting, J. A. Young, and T. Curtiss, "The effects of background pressure on Hall thruster operation," in *48th AIAA/ASME/SAE/ASEE Joint Propulsion Conference & Exhibit, Atlanta, Georgia*, ser. AIAA 2012-3735, 2012. DOI: 10.2514/6.2012-3735.

[37] R. A. Filatov, A. E. Hramov, Y. P. Bliokh, A. A. Koronovskii, and J. Felsteiner, "Influence of background gas ionization on oscillations in a virtual cathode with a retarding potential," *Physics of Plasmas*, vol. 16, no. 3, p. 033 106, Mar. 2009. DOI: 10.1063/1.3080200.

[38] J. A. Walker, J. D. Frieman, M. L. Walker, V. Khayms, D. King, and P. Y. Peterson, "Electrical facility effects on hall-effect-thruster cathode coupling: Discharge oscillations and facility coupling," *Journal of Propulsion and Power*, vol. 32, no. 4, pp. 844–855, 2016. DOI: 10.2514/1.B35835.

[39] J. A. Walker, S. J. Langendorf, M. L. Walker, V. Khayms, D. King, and P. Pertson, "Electrical facility effects on Hall current thrusters: Electron termination pathway manipulation," *Journal of Propulsion and Power*, vol. 32, no. 6, pp. 1365–1377, 2016. DOI: 10.2514/1.B35904.

[40] F. Boni, V. Désangles, P.-Q. Elias, J. Jarrige, and D. Packan, "Investigation of facility effects on the performance of an electron cyclotron resonance magnetic nozzle thruster," in 38th *International Electric Propulsion Conference*, Toulouse, France, June 23-28: Electric Rocket Propulsion Society, Fairview Park, OH, 2024. [Online]. Available: https://electricrocket.org/IEPC_2024/792.pdf.

[41] V. Désangles et al., "ECRA thruster advances: 30w and 200w prototypes latest performances," *Journal of Electric Propulsion*, vol. 2, no. 1, p. 10, 2023. DOI: 10.1007/s44205-023-00046-x.

[42] R. Kozakov, M. Maigler, J. Schein, and N. Wallace, "Determination of self-neutralization phenomena of ion beams with Langmuir probe measurements and PIC-DSMC simulations," *Applied Sciences*, vol. 14, no. 8, p. 3470, 2024. DOI: 10.3390/app14083470.

[43] G. Lim, H. Tran, D. A. Levin, H. B. Chew, and K. Nishii, "Kinetic simulation of carbon sputtering by a gridded ion thruster with a molecular dynamics based model," in 38th *International Electric Propulsion Conference*, Toulouse, France: Electric Rocket Propulsion Society, Fairview Park, OH, 2024. [Online]. Available: https://electricrocket.org/IEPC_2024/186.pdf.

[44] L. Grimaud, A. Pétin, J. Vaudolon, and S. Mazouffre, "Perturbations induced by electrostatic probe in the discharge of hall thrusters," *Review of Scientific Instruments*, vol. 87, no. 4, 2016. DOI: 10.1063/1.4945563.

[45] K. Gasa, S. B. Gabriel, A. Daykin-Iliopoulos, and F. Guarducci, "Plasma potential measurements in a dry neutraliser coupled with a rf ion thruster," in 39th *International Electric Propulsion Conference*, London, United Kingdom, September 14-19: Electric Rocket Propulsion Society, Fairview Park, OH, Sep. 2025. [Online]. Available: https://www.electricrocket.org/IEPC_2025/London/submission_542.pdf.

[46] M. Martínez-Sánchez, J. Navarro-Cavallé, and E. Ahedo, "Electron cooling and finite potential drop in a magnetized plasma expansion," *Physics of Plasmas*, vol. 22, no. 5, p. 053 501, 2015. DOI: 10.1063/1.4919627.

[47] J. Zhou, G. Sánchez-Arriaga, and E. Ahedo, "Time-dependent expansion of a weakly-collisional plasma beam in a paraxial magnetic nozzle," *Plasma Sources Science and Technology*, vol. 30, no. 4, p. 045 009, 2021. DOI: 10.1088/1361-6595/abeff3.

[48] M. Guaita, E. Ahedo, and M. Merino, "Pic/fluid simulations of the plasma expansion in a planar magnetic arch," *Plasma Sources Science and Technology*, vol. 34, no. 1, p. 015 007, Jan. 2025. DOI: 10.1088/1361-6595/adab8e.

[49] M. Guaita, A. Marín-Cebrián, M. Merino, E. Ahedo, F. Cipriani, and K. Dannenmayer, "Electron populations and neutralization process in the plume of a gridded ion thruster," *Plasma Sources Science and Technology*, Mar. 2025. DOI: 10.1088/1361-6595/adc482.

[50] M. Guaita, K. Keil, K. Holste, P. J. Klar, E. Ahedo, and M. Merino, "Numerical and experimental study of facility effects on a gridded ion engine's plasma plume," *Journal of Applied Physics*, vol. 139, no. 9, p. 093 301, Feb. 2026. DOI: 10.1063/5.0315733.

[51] M. Guaita, E. Ahedo, and M. Merino, "PIC-informed reduced electron model for gridded ion engine plumes," in *Space Propulsion Conference 2026*, Bari, Italy: Association Aéronautique et Astronautique de France, May 2026.

[52] C. Cui and J. Wang, "Vlasov simulations of electric propulsion beam," *Plasma Sources Science and Technology*, vol. 33, no. 12, p. 125 005, 2024. DOI: 10.1088/1361-6595/ad98c0.

[53] C. Birdsall and A. Langdon, *Plasma Physics via Computer Simulation*. Bristol: Institute of Physics Publishing, 1991.

[54] L. Brieda, *Plasma simulations by example*. CRC Press, 2019. DOI: 10.1201/9780429439780.

[55] C. K. Birdsall, "Particle-in-cell charged-particle simulations, plus Monte Carlo collisions with neutral atoms, PIC-MCC," *IEEE Transactions on plasma science*, vol. 19, no. 2, pp. 65–85, 1991. DOI: 10.1109/27.106800.

[56] D. A. Brown, M. T. Bettencourt, S. A. Wright, S. Maheswaran, J. P. Jones, and S. A. Jarvis, "Higher-order particle representation for particle-in-cell simulations," *Journal of Computational Physics*, vol. 435, p. 110 255, 2021. DOI: https://doi.org/10.1016/j.jcp.2021.110255.

[57] V. Vahedi and M. Surendra, "A Monte Carlo collision model for the particle-in-cell method: Applications to argon and oxygen discharges," *Computer Physics Communications*, vol. 87, no. 1, pp. 179–198, 1995. DOI: https://doi.org/10.1016/0010-4655(94)00171-W.

[58] V. Serikov, S. Kawamoto, and K. Nanbu, "Particle-in-cell plus direct simulation Monte Carlo (PIC-DSMC) approach for self-consistent plasma-gas simulations," *IEEE Transactions on Plasma Science*, vol. 27, no. 5, pp. 1389–1398, 1999. DOI: 10.1109/27.799817.

[59] I. H. Hutchinson, *A Student's Guide to Numerical Methods*. Cambridge University Press, 2015. DOI: 10.1017/CBO9781316155516.

[60] S. Jubin et al., "Numerical thermalization in 2D PIC simulations: Practical estimates for low-temperature plasma simulations," *Physics of Plasmas*, vol. 31, no. 2, 2024. DOI: 10.1063/5.0180421.

[61] D. Poli, "Advanced fluid models of ExB discharges applied to Hall effect thrusters," Ph.D. dissertation, Universidad Carlos III de Madrid, Leganés, Spain, 2026. [Online]. Available: https://phd-aerospace.uc3m.es/wp-content/uploads/2021/12/phd_thesis_davide_poli.pdf.

[62] A. Domínguez-Vázquez, J. Zhou, A. Sevillano-González, and E. Ahedo, "Modelling of a Hall thruster plume: Influence of plume boundary conditions and size, and cathode location," *Plasma Sources Science and Technology*, vol. 34, no. 8, p. 085 004, 2025. DOI: 10.1088/1361-6595/adf576.

[63] S. Andrews, S. Di Fede, and M. Magarotto, "Fully kinetic model of plasma expansion in a magnetic nozzle," *Plasma Sources Science and Technology*, vol. 31, no. 3, p. 035 022, Apr. 2022. DOI: 10.1088/1361-6595/ac56ec. [Online]. Available: https://doi.org/10.1088/1361-6595/ac56ec.

[64] M. Merino, D. García-Lahuerta, and E. Ahedo, “Plasma acceleration in a magnetic arch,” *Plasma Sources Science and Technology*, vol. 32, no. 6, p. 065 005, Jun. 2023. DOI: 10.1088/1361-6595/acd476.

[65] M. Merino and E. Ahedo, “Effect of the plasma-induced magnetic field on a magnetic nozzle,” *Plasma Sources Science and Technology*, vol. 25, no. 4, p. 045 012, 2016. DOI: 10.1088/0963-0252/25/4/045012.

[66] D. Tskhakaya, K. Matyash, R. Schneider, and F. Taccogna, “The particle-in-cell method,” *Contributions to Plasma Physics*, vol. 47, no. 8-9, pp. 563–594, 2007. DOI: 10.1002/ctpp.200710072.

[67] P. Singh, A. Majumder, A. Pulhani, G. Sridhar, and N. Maiti, “Development of a 1-D electrostatic particle-in-cell code,” *IEEE Transactions on Plasma Science*, vol. 49, no. 10, pp. 3257–3267, 2021. DOI: 10.1109/TPS.2021.3114219.

[68] A. Marín-Cebrián, E. Bello-Benítez, A. Domínguez-Vázquez, and E. Ahedo, “Non-maxwellian electron effects on the macroscopic response of a Hall thruster discharge from an axial–radial kinetic model,” *Plasma Sources Science and Technology*, vol. 33, no. 2, p. 025 008, Feb. 2024. DOI: 10.1088/1361-6595/ad227c.

[69] F. Taccogna, S. Longo, M. Capitelli, and R. Schneider, “Self-similarity in Hall plasma discharges: Applications to particle models,” *Physics of Plasmas*, vol. 12, no. 5, 2005. DOI: 10.1063/1.1877517.

[70] E. Ahedo and D. Escobar, “Two-region model for positive and negative plasma sheaths and its application to Hall thruster metallic anodes,” *Physics of Plasmas*, vol. 15, p. 033 504, 2008. DOI: 10.1063/1.2888523.

[71] E. Ahedo and M. Merino, “Two-dimensional supersonic plasma acceleration in a magnetic nozzle,” *Physics of Plasmas*, vol. 17, no. 7, p. 073 501, 2010. DOI: 10.1063/1.3442736.

[72] A. L. Ortega, B. A. Jorns, and I. G. Mikellides, “Hollow cathode simulations with a first-principles model of ion-acoustic anomalous resistivity,” *Journal of Propulsion and Power*, vol. 34, no. 4, pp. 1026–1038, 2018. DOI: 10.2514/1.B36782.

[73] D. Poli and E. Ahedo, “Full-fluid modelling of rotating plasma instabilities in penning-like configurations,” *Plasma Sources Science and Technology*, vol. 35, no. 1, p. 015 007, Jan. 2026. DOI: 10.1088/1361-6595/ae33ef.

[74] R. Sahu, A. Mansour, and K. Hara, “Full fluid moment model for low temperature magnetized plasmas,” *Physics of Plasmas*, vol. 27, no. 11, p. 113 505, 2020. DOI: 10.1063/5.0021474.

[75] A. Alvarez Laguna and K. Hara, “High-order moment closure for nonmagnetized electrons in partially ionized plasmas,” *Physical Review E*, vol. 113, no. 2, p. 025 207, 2026. DOI: https://doi.org/10.1103/lm1z-bzt3.

[76] L. Reboul, M. Massot, and A. A. Laguna, "Numerical challenges in the simulation of 1D bounded low-temperature plasmas with charge separation in various collisional regimes," *AIP Conference Proceedings*, vol. 2996, no. 1, p. 190 004, Feb. 2024. DOI: 10.1063/5.0187483.

[77] I. G. Mikellides, B. Jorns, I. Katz, and A. Lopez Ortega, "Hall2De simulations with a first-principles electron transport model based on the electron cyclotron drift instability," in *52nd AIAA/SAE/ASEE Joint Propulsion Conference*, 2016, p. 4618. DOI: 10.2514/6.2016-4618.

[78] B. Korkut and D. A. Levin, "Three-dimensional simulations of backflows from ion thruster plumes using unstructured grid refinement," *Journal of Propulsion and Power*, vol. 33, no. 1, pp. 264–275, 2017. DOI: 10.2514/1.B35847.

[79] J. Wang and Y. Hu, "The breakdown of the fluid approximation for electrons in a plasma wake," *Journal of Geophysical Research: Space Physics*, vol. 123, no. 10, pp. 8797–8805, 2018. DOI: https://doi.org/10.1029/2018JA025743.

[80] Y. Hu and J. Wang, "Assessment of electron thermodynamic and fluid approximations for collisionless plasma expansion into a wake," *Physics of Plasmas*, vol. 26, no. 2, p. 023 515, 2019. DOI: 10.1063/1.5065395.

[81] E. Ahedo, S. Correyero, J. Navarro, and M. Merino, "Macroscopic and parametric study of a kinetic plasma expansion in a paraxial magnetic nozzle," *Plasma Sources Science and Technology*, vol. 29, no. 4, p. 045 017, 2020. DOI: 10.1088/1361-6595/ab7855.

[82] R. Jambunathan and D. A. Levin, "Kinetic, 3-D, PIC-DSMC simulations of ion thruster plumes and the backflow region," *IEEE Transactions on Plasma Science*, vol. 48, no. 6, pp. 2017–2034, 2020. DOI: 10.1109/TPS.2020.2988010.

[83] J. Perales-Díaz, F. Cichocki, M. Merino, and E. Ahedo, "Formation and neutralization of electric charge and current of an ion thruster plume," *Plasma Sources Science and Technology*, vol. 30, no. 10, p. 105 023, 2021. DOI: 10.1088/1361-6595/ac2a19.

[84] R. Jambunathan and D. Levin, "Kinetic modeling of plasma plumes using multi-GPU forest of octree approach," in *35th International Electric Propulsion Conference*, Atlanta, Georgia, 2017. [Online]. Available: http://electricrocket.org/IEPC/IEPC_2017_67.pdf.

[85] J.-L. Vay et al., "Warp-X: A new exascale computing platform for beam–plasma simulations," *Nuclear Instruments and Methods in Physics Research Section A: Accelerators, Spectrometers, Detectors and Associated Equipment*, vol. 909, pp. 476–479, 2018. DOI: https://doi.org/10.1016/j.nima.2018.01.035.

[86] S. S. Ganta et al., "Investigating instabilities in magnetized low-pressure capacitively coupled RF plasma using particle-in-cell (PIC) simulations," *Physics of Plasmas*, vol. 31, no. 10, 2024. DOI: https://doi.org/10.1063/5.0221111.

[87] H. Sun et al., “Direct implicit and explicit energy-conserving particle-in-cell methods for modeling of capacitively coupled plasma devices,” *Physics of Plasmas*, vol. 30, no. 10, 2023. DOI: https://doi.org/10.1063/5.0160853.

[88] A. T. Powis and I. D. Kaganovich, “Accuracy of the explicit energy-conserving particle-in-cell method for under-resolved simulations of capacitively coupled plasma discharges,” *Physics of Plasmas*, vol. 31, no. 2, 2024. DOI: 10.1063/5.0174168.

[89] P. Jiménez, L. Chacón, and M. Merino, “An implicit, conservative electrostatic particle-in-cell algorithm for paraxial magnetic nozzles,” *Journal of Computational Physics*, vol. 502, p. 112 826, 2024. DOI: https://doi.org/10.1016/j.jcp.2024.112826.

[90] G. Joyce, M. Lampe, S. Slinker, and W. Manheimer, “Electrostatic particle-in-cell simulation technique for quasineutral plasma,” *Journal of Computational Physics*, vol. 138, no. 2, pp. 540–562, 1997. DOI: 10.1006/jcph.1997.5833.

[91] M. Lampe, G. Joyce, W. Manheimer, and S. Slinker, “Quasi-neutral particle simulation of magnetized plasma discharges: General formalism and application to ecr discharges,” *IEEE Transactions on Plasma Science*, vol. 26, pp. 1592–1609, 1998. DOI: 10.1109/27.747877.

[92] M. Guaita, A. Modesti, M. Merino, and E. Ahedo, “A quasi-neutral full PIC model for the study of electron thermodynamics in a plasma thruster plume,” in 76^{th} *Gaseous Electronics Conference*, Ann Arbor, MI, October 9-13, 2023.

[93] E. Ahedo, “Plasmas for space propulsion,” *Plasma Physics and Controlled Fusion*, vol. 53, no. 12, p. 124 037, 2011. DOI: 10.1088/0741-3335/53/12/124037.

[94] S. Mazouffre, “Electric propulsion for satellites and spacecraft: Established technologies and novel approaches,” *Plasma Sources Science and Technology*, vol. 25, no. 3, p. 033 002, 2016. DOI: 10.1088/0963-0252/25/3/033002.

[95] M. Manente et al., “Regulus: A propulsion platform to boost small satellite missions,” *Acta Astronautica*, vol. 157, pp. 241–249, 2019. DOI: 10.1016/j.actaastro.2018.12.022.

[96] K. Takahashi, “Helicon–type radiofrequency plasma thrusters and magnetic plasma nozzles,” *Reviews of Modern Plasma Physics*, vol. 3, p. 3, 2019. DOI: 10.1007/s41614-019-0024-2.

[97] S. Pottinger, V. Lappas, C. Charles, and R. Boswell, “Performance characterization of a helicon double layer thruster using direct thrust measurements,” *Journal of Physics D: Applied Physics*, vol. 44, no. 23, p. 235 201, 2011. DOI: 10.1088/0022-3727/44/23/235201.

[98] J. Sercel, "Electron-cyclotron-resonance (ECR) plasma thruster research," in *24th Joint Propulsion Conference*, American Institute of Aeronautics and Astronautics, Reston, VA, 1988. DOI: 10.2514/6.1988-2916.

[99] F. Cannat, T. Lafleur, J. Jarrige, P. Chabert, P. Elias, and D. Packan, "Optimization of a coaxial electron cyclotron resonance plasma thruster with an analytical model," *Physics of Plasmas*, vol. 22, no. 5, p. 053 503, 2015. DOI: 10.1063/1.4920966.

[100] A. Sánchez-Villar, J. Zhou, M. Merino, and E. Ahedo, "Coupled plasma transport and electromagnetic wave simulation of an ECR thruster," *Plasma Sources Science and Technology*, vol. 30, no. 4, p. 045 005, 2021. DOI: 10.1088/1361-6595/abde20.

[101] M. Merino and E. Ahedo, "Plasma detachment in a propulsive magnetic nozzle via ion demagnetization," *Plasma Sources Science and Technology*, vol. 23, no. 3, p. 032 001, 2014. DOI: 10.1088/0963-0252/23/3/032001.

[102] A. Fruchtman, K. Takahashi, C. Charles, and R. Boswell, "A magnetic nozzle calculation of the force on a plasma," *Physics of Plasmas*, vol. 19, no. 3, p. 033 507, 2012. DOI: 10.1063/1.3691650.

[103] K. Takahashi, T. Lafleur, C. Charles, P. Alexander, and R. Boswell, "Electron diamagnetic effect on axial force in an expanding plasma: Experiments and theory," *Physical Review Letters*, vol. 107, no. 23, p. 235 001, 2011. DOI: 10.1103/PhysRevLett.107.235001.

[104] Y. Hu, Z. Huang, Y. Cao, and Q. Sun, "Kinetic insights into thrust generation and electron transport in a magnetic nozzle," *Plasma Sources Science and Technology*, vol. 30, no. 7, p. 075 006, 2021. DOI: 10.1088/1361-6595/ac0a48.

[105] B. Longmier et al., "Ambipolar ion acceleration in an expanding magnetic nozzle," *Plasma Sources Science and Technology*, vol. 20, p. 015 007, 2011. DOI: 10.1088/0963-0252/20/1/015007.

[106] M. Merino, D. García-Lahuerta, C. Boyé, J. Navarro-Cavallé, and E. Ahedo, "Preliminary model of the plasma expansion in a magnetic arch thruster (and overview of the first prototype)," in 37^{th} *International Electric Propulsion Conference*, Boston, MA, June 19-23: Electric Rocket Propulsion Society, 2022. [Online]. Available: https://www.jotform.com/uploads/electricrocket/220994246997171/5315340331311245602/magnetic_arch_model_IEPC2022.pdf.

[107] S. Di Fede, M. Manente, P. J. Comunian, and M. Magarotto, "Magnetic nozzle performance in a cluster of helicon plasma thrusters," *Plasma Sources Science and Technology*, vol. 32, no. 6, p. 065 013, 2023. DOI: 10.1088/1361-6595/acdaf2.

[108] C. Boyé, J. Navarro-Cavallé, and M. Merino-Martinez, "Preliminary analysis of the magnetic arch plasma expansion in a cluster of two ECR plasma thrusters," in *10th EUCASS Conference*, Lausanne, Switzerland, July 9–13, 2023. DOI: 10.13009/EUCASS2023-681.

[109] K. Vereen et al., "Recent advances in the clustering of high power helicon thrusters," in *AIAA Propulsion and Energy 2019 Forum*, 2019. DOI: 10.2514/6.2019-3902.

[110] M. Merino, *Motor espacial de plasma sin electrodos con geometría en U*, pat., PCT patent, Spanish Patent Office, Patent no. ES2733773, 2019.

[111] B. Breizman, M. Tushentsov, and A. Arefiev, "Magnetic nozzle and plasma detachment model for a steady-state flow," *Physics of Plasmas*, vol. 15, p. 057 103, 2008. DOI: 10.1063/1.2903844.

[112] M. Merino and E. Ahedo, "Plasma detachment mechanisms in a magnetic nozzle," in 47^{th} *AIAA/ASME/ SAE/ASEE Joint Propulsion Conference & Exhibit*, American Institute of Aeronautics and Astronautics, 2011. DOI: 10.2514/MJPC11.

[113] F. Cescon, S. D. Fede, M. Manente, and M. Magarotto, "Cluster of magnetic nozzles: A fully kinetic 3D PIC simulation study," in 38^{th} *International Electric Propulsion Conference*, Toulouse, France, June 23-28: Electric Rocket Propulsion Society, Fairview Park, OH, 2024. [Online]. Available: https://electricrocket.org/IEPC_2024/415.pdf.

[114] C. Boyé, J. Navarro-Cavallé, M. Merino, A. Lecervoisier, and S. Mazouffre, "Determining ion velocity in the interconnected plume of a cluster of two ecrts using 2d lif," in 38^{th} *International Electric Propulsion Conference*, Toulouse, France, June 23-28: Electric Rocket Propulsion Society, 2024. [Online]. Available: https://electricrocket.org/IEPC_2024/717.pdf.

[115] C. Boyé, J. Navarro-Cavallé, and M. Merino, "Ion current and energy in the magnetic arch of a cluster of two ECR plasma sources," *Journal of Electric Propulsion*, vol. 4, no. 1, p. 10, Feb. 2025. DOI: 10.1007/s44205-025-00100-w.

[116] M. Nakles, L. Brieda, G. Reed, W. Hargus, and R. Spicer, "Experimental and numerical examination of the BHT-200 Hall thruster plume," in *43rd AIAA/ASME/SAE/ASEE Joint Propulsion Conference & Exhibit*, Washington DC: American Institute of Aeronautics and Astronautics, Reston, VA, 2007. DOI: 10.2514/6.2007-5305.

[117] B. Wachs and B. Jorns, "Effect of background pressure on ion dynamics in an electron cyclotron resonance thruster," in *2018 Joint Propulsion Conference*, 2018. DOI: 10.2514/6.2018-4585.

[118] N. R. Caruso and M. L. Walker, "Neutral ingestion effects on plume properties of a radio-frequency plasma discharge," *Journal of Propulsion and Power*, vol. 34, no. 1, pp. 58–65, 2018. DOI: 10.2514/1.B36404.

[119] R. Andriulli, S. Andrews, N. Souhair, M. Magarotto, and F. Ponti, "Fully kinetic study of facility pressure effects on RF-source magnetic nozzles," *Acta Astronautica*, vol. 215, pp. 362–372, 2024. DOI: https://doi.org/10.1016/j.actaastro.2023.12.014.

[120] S. Baldinucci, S. Bergmann, J. A. Hondagneu, B. Wachs, and B. A. Jorns, "Impact of facility electrical boundary conditions on the performance of an electron cyclotron resonance magnetic nozzle thruster," in *37th International Electric Propulsion Conference*, Boston, MA, June 19-23, 2022. [Online]. Available: https://www.jotform.com/uploads/electricrocket/220994246997171/5314752600414590890/IEPC_2022_510.pdf.

[121] F. Cichocki, A. Domínguez-Vázquez, M. Merino, and E. Ahedo, "3D simulations of a magnetized Hall Effect thruster plume," in 36^{th} *International Electric Propulsion Conference*, Vienna, Austria: Electric Rocket Propulsion Society, 2019. [Online]. Available: http://electricrocket.org/2019/460.pdf.

[122] A. Modesti, F. Cichocki, and E. Ahedo, "Numerical treatment of a magnetized electron fluid model in a 3d simulator of plasma thruster plumes," *Frontiers in Physics*, vol. 11, p. 1 286 345, 2023. DOI: 10.3389/fphy.2023.1286345.

[123] F. Cichocki, A. Domínguez-Vázquez, M. Merino, P. Fajardo, and E. Ahedo, "Three-dimensional neutralizer effects on a Hall-effect thruster near plume," *Acta Astronautica*, vol. 187, pp. 498–510, 2021. DOI: 10.1016/j.actaastro.2021.06.042.

[124] F. Cichocki, J. Navarro-Cavallé, A. Modesti, and G. Ramírez Vázquez, "Magnetic nozzle and RPA simulations vs. experiments for a helicon plasma thruster plume," *Frontiers in Physics*, vol. 10, p. 876 684, 2022. DOI: 10.3389/fphy.2022.876684.

[125] R. Hockney and J. Eastwood, *Computer simulation using particles*. CRC Press, Boca Ratón, FL, 1988. DOI: 10.1201/9780367806934.

[126] C. Birdsall and D. Fuss, "Clouds-in-clouds, clouds-in-cells physics for many-body plasma simulation," *Journal of Computational Physics*, vol. 135, no. 2, pp. 141–148, 1997. DOI: https://doi.org/10.1006/jcph.1997.5723.

[127] J. Little and E. Choueiri, "Electron cooling in a magnetically expanding plasma," *Physical Review Letters*, vol. 117, no. 22, p. 225 003, 2016. DOI: 10.1103/PhysRevLett.117.225003.

[128] G. Giono et al., "Non-Maxwellian electron energy probability functions in the plume of a SPT-100 Hall thruster," *Plasma Sources Science and Technology*, vol. 27, no. 1, p. 015 006, 2018. DOI: 10.1088/1361-6595/aaa06b.

[129] S. Correyero, J. Jarrige, D. Packan, and E. Ahedo, "Plasma beam characterization along the magnetic nozzle of an ECR thruster," *Plasma Sources Science and Technology*, vol. 28, no. 9, p. 095 004, 2019. DOI: 10.1088/1361-6595/ab38e1.

[130] M. Merino, J. Mauriño, and E. Ahedo, "Kinetic electron model for plasma thruster plumes," *Plasma Sources Science and Technology*, vol. 27, no. 3, p. 035 013, 2018. DOI: 10.1088/1361-6595/aab3a1.

[131] M. Merino et al., "Collisionless electron cooling in a plasma thruster plume: Experimental validation of a kinetic model," *Plasma Sources Science and Technology*, vol. 29, no. 3, p. 035 029, 2020. DOI: 10.1088/1361-6595/ab7088.

[132] E. Ahedo, "Using electron fluid models to analyze plasma thruster discharges," *Journal of Electric Propulsion*, vol. 2, no. 1, p. 2, 2023. DOI: 10.1007/s44205-022-00035-6.

[133] J. Zhou, "Modeling and simulation of the plasma discharge in a radiofrequency thruster," Ph.D. dissertation, Universidad Carlos III de Madrid, Leganés, Spain, 2021. [Online]. Available: https://hdl.handle.net/10016/32945.

[134] G. Bird, *Molecular Gas Dynamics and the Direct Simulation of Gas Flows* (The Oxford Engineering Science Series). Oxford University Press, Oxford, UK, 1994.

[135] J. Zhou, A. Domínguez-Vázquez, P. Fajardo, and E. Ahedo, "Magnetized fluid electron model within a two-dimensional hybrid simulation code for electrodeless plasma thrusters," *Plasma Sources Science and Technology*, vol. 31, no. 4, p. 045 021, 2022. DOI: 10.1088/1361-6595/ac64bc.

[136] E. Ahedo, "Parametric analysis of a magnetized cylindrical plasma," *Physics of Plasmas*, vol. 16, no. 11, p. 113 503, 2009. DOI: 10.1063/1.3262529.

[137] K. Riemann, "The Bohm criterion and sheath formation," *Journal of Physics D: Applied Physics*, vol. 24, pp. 492–518, 1991. DOI: 10.1088/0022-3727/24/4/001.

[138] A. Domínguez-Vázquez, J. Zhou, A. Sevillano-González, P. Fajardo, and E. Ahedo, "Analysis of the electron downstream boundary conditions in a 2D hybrid code for Hall thrusters," in 37th *International Electric Propulsion Conference*, Boston, MA, USA, June 19-23: Electric Rocket Propulsion Society, 2022. [Online]. Available: https://www.jotform.com/uploads/electricrocket/220994246997171/5313916106906264056/IEPC-2022-338.pdf.

[139] M. R. Inchingolo, M. Merino, and J. Navarro-Cavallé, "Plume characterization of a waveguide ecr thruster," *Journal of Applied Physics*, vol. 133, no. 11, p. 113 304, 2023. DOI: 10.1063/5.0138780.

[140] *Hayashi database*, https://www.lxcat.net/Hayashi, Accessed: 2019-10-23.

[141] *NIFS database*, https://dbshino.nifs.ac.jp/, Accessed: 2025-03-23.

[142] *Biagi database*, https://www.lxcat.net/Biagi, Accessed: 2025-03-23.

[143] L. Pitchford et al., "LXCat: An open-access, web-based platform for data needed for modeling low temperature plasmas," *Plasma Process and Polymers*, vol. 14, p. 1 600 098, 2017. DOI: https://doi.org/10.1002/ppap.201600098.

[144] R. Goldston and P. Rutherford, *Introduction to Plasma Physics*. Institute of Physics Publishing, Bristol, 1995.

[145] F. I. Parra, E. Ahedo, J. M. Fife, and M. Martínez-Sánchez, "A two-dimensional hybrid model of the Hall thruster discharge," *Journal of Applied Physics*, vol. 100, no. 2, p. 023 304, 2006. DOI: 10.1063/1.2219165.

[146] F. Alexander and A. Garcia, "The direct simulation Monte Carlo method," *Computers in Physics*, vol. 11, no. 6, pp. 588–593, 1997. DOI: 10.1063/1.168619.

[147] J. Miller, S. Pullins, D. Levandier, Y. Chiu, and R. Dressler, "Xenon charge exchange cross sections for electrostatic thruster models," *Journal of Applied Physics*, vol. 91, no. 3, pp. 984–991, 2002. DOI: 10.1063/1.1426246.

[148] W. Kerslake and L. Ignaczak, "Development and flight history of the SERT II spacecraft," *J. Spacecr. Rockets*, vol. 30, pp. 258–290, 1993. DOI: 10.2514/6.1992-3516.

[149] B. Korkut, Z. Li, and D. Levin, "3-D simulation of ion thruster plumes using octree adaptive mesh refinement," *IEEE Transactions on Plasma Science*, vol. 43, no. 5, pp. 1706–1721, 2015. DOI: 10.1109/TPS.2015.2415458.

[150] B. Korkut, D. A. Levin, and O. Tumuklu, "Simulations of ion thruster plumes in ground facilities using adaptive mesh refinement," *Journal of Propulsion and Power*, vol. 33, no. 3, pp. 681–696, 2017. DOI: 10.2514/1.B35958.

[151] H. Usui, A. Hashimoto, and Y. Miyake, "Electron behavior in ion beam neutralization in electric propulsion: Full particle-in-cell simulation," in *Journal of Physics: Conference Series*, vol. 454, IOP Publishing, 2013, p. 012 017. DOI: 10.1088/1742-6596/454/1/012017.

[152] Y. Hu and J. Wang, "Electron properties in collisionless mesothermal plasma expansion: Fully kinetic simulations," *IEEE Transactions on Plasma Science*, vol. 43, no. 9, pp. 2832–2838, 2015.

[153] Y. Hu and J. Wang, "Fully kinetic simulations of collisionless, mesothermal plasma emission: Macroscopic plume structure and microscopic electron characteristics," *Physics of Plasmas*, vol. 24, no. 3, p. 033 510, 2017. DOI: 10.1109/TPS.2015.2433928.

[154] J. Wang, O. Chang, and Y. Cao, "Electron-ion coupling in mesothermal plasma beam emission: Full particle PIC simulations," *IEEE Transactions on Plasma Science*, vol. 40, no. 2, pp. 230–236, 2012. DOI: 10.1109/TPS.2011.2179066.

[155] N. Nuwal, R. Jambunathan, and D. Levin, "Kinetic modeling of spacecraft surfaces in a plume backflow region," *IEEE Transactions on Plasma Science*, vol. 48, no. 12, pp. 4305–4325, 2020. DOI: 10.1109/TPS.2020.3039110.

[156] R. Jambunathan and D. A. Levin, "CHAOS: An octree-based PIC-DSMC code for modeling of electron kinetic properties in a plasma plume using MPI-CUDA parallelization," *Journal of Computational Physics*, vol. 373, pp. 571–604, 2018. DOI: 10.1016/j.jcp.2018.07.005.

[157] R. Jambunathan and D. A. Levin, "A self-consistent open boundary condition for fully kinetic plasma thruster plume simulations," *IEEE Transactions on Plasma Science*, vol. 48, no. 3, pp. 610–630, 2020. DOI: 10.1109/TPS.2020.2968887.

[158] K. Nishii and D. A. Levin, "Three-dimensional kinetic simulations of carbon backsputtering in vacuum chambers from ion thruster plumes," *Journal of Propulsion and Power*, pp. 1–15, 2023. DOI: 10.2514/1.B39194.

[159] Y. Zhao, J. Wang, and H. Usui, "Simulations of ion thruster beam neutralization using a particle–particle model," *Journal of Propulsion and Power*, vol. 34, no. 5, pp. 1109–1115, 2018. DOI: 10.2514/1.B36770.

[160] D. VanGilder, I. G. Font, and I. D. Boyd, "Hybrid Monte Carlo particle-in-cell simulation of an ion thruster plume," *Journal of Propulsion and Power*, vol. 15, no. 4, p. 530, 1999. DOI: 10.2514/2.5475.

[161] M. Li, M. Merino, E. Ahedo, and H. Tang, "On electron boundary conditions in PIC plasma thruster plume simulations," *Plasma Sources Science and Technology*, vol. 28, no. 03, p. 034 004, 2019. DOI: 10.1088/1361-6595/ab0949.

[162] L. Brieda, "Model for steady-state fully kinetic ion beam neutralization studies," *IEEE Transactions on Plasma Science*, vol. 46, no. 3, pp. 556–562, 2018. DOI: 10.1109/TPS.2018.2801282.

[163] P. De Boer, "Electric probe measurements in the plume of an ion thruster," *Journal of Propulsion and Power*, vol. 12, no. 1, pp. 95–104, 1996. DOI: 10.2514/3.23996.

[164] Y. Yang, S. Zhou, K. Yan, Z. Wang, Z. Zhang, and W. Nie, "Measurement and diagnosis of miniaturized ion thruster plume," *AIP Advances*, vol. 13, no. 3, 2023. DOI: 10.1063/5.0143330.

[165] J. Foster, G. Soulas, and M. Patterson, "Plume and discharge plasma measurements of an NSTAR-type ion thruster," in *36th Joint Propulsion Conference and Exhibit*, Huntsville, Alabama, July 16-19: American Institute of Aeronautics and Astronautics, Reston, VA, 2000. DOI: 10.2514/6.2000-3812.

[166] M. Merino, J. Nuez, and E. Ahedo, "Fluid-kinetic model of a propulsive magnetic nozzle," *Plasma Sources Science and Technology*, vol. 30, no. 11, p. 115 006, 2021. DOI: 10.1088/1361-6595/ac2a0b.

[167] G. Sánchez-Arriaga, J. Zhou, E. Ahedo, M. Martínez-Sánchez, and J. J. Ramos, "Kinetic features and non-stationary electron trapping in paraxial magnetic nozzles," *Plasma Sources Science and Technology*, vol. 27, no. 3, p. 035 002, 2018. DOI: 10.1088/1361-6595/aaad7f.

[168] H. Leiter, R. Killinger, H. Bassner, R. Kukies, J. Mueller, and T. Froelich, "Evaluation of the performance of the advanced 200 mn radio frequency ion thruster rit-xt," in *38 th AIAA/ASME/SAE/ASEE Joint Propulsion Conference and Exhibit, Indianapolis, IN*, 2002. DOI: 10.2514/6.2002-3836.

[169] P. Dietz, F. Becker, K. Keil, K. Holste, and P. J. Klar, "Performance of a RF neutralizer operating with noble gases and iodine," *The European Physical Journal Applied Physics*, vol. 91, no. 1, p. 10 901, 2020. DOI: 10.1051/epjap/2020190213.

[170] D. M. Goebel, G. Becatti, I. G. Mikellides, and A. Lopez Ortega, "Plasma hollow cathodes," *Journal of Applied Physics*, vol. 130, no. 5, 2021. DOI: 10.1063/5.0051228.

[171] K. Keil, K. Holste, and P. J. Klar, "Multi-diagnostics system in the Jumbo space simulation test facility in Giessen, Germany," in *Proc. 38th Int. Electric Propulsion Conference*, 2024. [Online]. Available: https://electricrocket.org/IEPC_2024/308.pdf.

[172] *OneMKL PARDISO - Parallel Direct Sparse Solver Interface*, https://www.intel.com/content/www/us/en/docs/onemkl/developer-reference-c/2023-1/onemkl-pardiso-parallel-direct-sparse-solver-iface.html, Accessed: 2023.

[173] T. Takizuka and H. Abe, "A binary collision model for plasma simulation with a particle code," *Journal of computational physics*, vol. 25, no. 3, pp. 205–219, 1977. DOI: https://doi.org/10.1016/0021-9991(77)90099-7.

[174] K. Nanbu and S. Yonemura, "Weighted particles in Coulomb collision simulations based on the theory of a cumulative scattering angle," *J. Comput. Phys.*, vol. 145, no. 2, pp. 639–654, Sep. 1998. DOI: https://doi.org/10.1006/jcph.1998.6049.

[175] A. M. Chap and R. J. Sedwick, "Coulomb collision model for use in nonthermal plasma simulation," *Physical Review E*, vol. 95, no. 6, p. 063 209, 2017. DOI: 10.1103/PhysRevE.95.063209.

[176] A. Phelps, "Technical report 28," *JILA Information Center Report, University of Colorado, Boulder, Colorado, US*, 1985. [Online]. Available: http://jilawww.colorado.edu/~avp/.

[177] T. Yuan, J. Ren, J. Zhou, Z. Zhang, Y. Wang, and H. Tang, "The effects of numerical acceleration techniques on PIC-MCC simulations of ion thrusters," *AIP Advances*, vol. 10, no. 4, p. 045 115, 2020. DOI: 10.1063/1.5113561.

[178] J. Zhou, G. Sánchez-Arriaga, E. Ahedo, M. Martínez-Sánchez, and J. Ramos, "Collisional effects in non-stationary plasmas expansions along convergent-divergent magnetic nozzles," in *Space Propulsion Conference 2018*, ser. 00332, Seville, Spain: Association Aéronautique et Astronautique de France, 2018. [Online]. Available: http://hdl.handle.net/10016/27853.

[179] E. Roibás, S. Tierno, E. Criado, J. Doménech-Garret, J. Donoso, and L. Conde, "Characterization of the ion beam neutralization of plasma thrusters using collecting and emissive Langmuir probes," *Contributions to Plasma Physics*, vol. 53, no. 1, pp. 57–62, 2013. DOI: 10.1002/ctpp.201310010.

[180] J. Polk et al., "In-flight performance of the NSTAR ion propulsion system on the deep space one mission," in *2000 IEEE Aerospace Conference. Proceedings (Cat. No. 00TH8484)*, IEEE, vol. 4, 2000, pp. 123–148. DOI: 10.1109/AERO.2000.878373.

[181] J. W. Dankanich, M. Walker, M. W. Swiatek, and J. T. Yim, "Recommended practice for pressure measurement and calculation of effective pumping speed in electric propulsion testing," *Journal of Propulsion and Power*, vol. 33, no. 3, pp. 668–680, 2017. DOI: 10.2514/1.B35478.

[182] G. C. Soulas, "Modeling neutral densities downstream of a gridded ion thruster," *Journal of Propulsion and Power*, vol. 27, no. 3, pp. 538–552, 2011. DOI: 10.2514/1.B34094.

[183] J. Polansky, J. Wang, and N. Ding, "Experimental investigation on plasma plume potential," *IEEE Transactions on Plasma Science*, vol. 41, pp. 3438–3447, 2013. DOI: 10.1109/TPS.2013.2277724.

[184] J. Van Noord and G. Soulas, "A facility and ion thruster backsputter survey for higher power ion thrusters," in *41st AIAA/ASME/SAE/ASEE Joint Propulsion Conference & Exhibit*, 2005, p. 4067. DOI: 10.2514/6.2005-4067.

[185] T. J. Topham, S. E. Bergmann, A. C. Alves Almeida, J. A. Judge, and J. E. Foster, "Evaluation of facility effect impacts on gridded ion engines at high power densities," in *AIAA SCITECH 2025 Forum*, 2025, p. 1100. DOI: 10.2514/6.2025-1100.

[186] J. Wang, J. Polk, and D. Brinza, "Ion thruster modeling: Particle simulations and experimental validations," in *AIP Conference Proceedings*, American Institute of Physics, vol. 663, 2003, pp. 525–532. DOI: 10.1063/1.1581590.

[187] K. Keil, M. Guaita, M. Merino, E. Ahedo, K. Holste, and P. J. Klar, *Experimental data from: Numerical and experimental study of facility effects on a gridded ion engine's plasma plume*, version 1.0.1, Zenodo, Dec. 2025. DOI: 10.5281/zenodo.17858866.

[188] M. Guaita, K. Keil, K. Holste, P. J. Klar, M. Merino, and E. Ahedo, *Numerical data from: Numerical and experimental study of facility effects on a gridded ion engine's plasma plume*, version 1.0.1, Zenodo, Dec. 2025. DOI: 10.5281/zenodo.17858773.

[189] H. Leiter, C. Altmann, J. Porst, D. Lauer, M. Berger, and M. Rath, "Six decades of thrust-the ariane group radiofrequency ion thrusters and systems family," in 35th *International Electric Propulsion Conference*, Atlanta, GA, October 8-12: Electric Rocket Propulsion Society, Fairview Park, OH, 2017. [Online]. Available: http://electricrocket.org/IEPC/IEPC_2017_27.pdf.

[190] H. Leiter, J. Gonzalez del Amo, and D. Feili, "A nouvelle neutralization concept for RIT-μX miniaturized radio frequency ion thruster systems template," in 36th *International Electric Propulsion Conference*, Vienna, Austria, September 15-20: Electric Rocket Propulsion Society, Fairview Park, OH, Oct. 2019. [Online]. Available: http://electricrocket.org/2019/806.pdf.

[191] B. T. Nauschütt, L. Chen, K. Holste, and P. J. Klar, "Non-invasive assessment of plasma parameters inside an ion thruster combining optical emission spectroscopy and principal component analysis," *EPJ Techniques and Instrumentation*, vol. 8, no. 1, p. 13, 2021. DOI: 10.1140/epjti/s40485-021-00070-x.

[192] K. Holste, K. Keil, O. Dörr, C. Winklmeier, P. J. Klar, and M. Guaita, "Towards standardized ion thruster diagnostics: Calibration of energy analyzers," in 39th *International Electric Propulsion Conference*, London, United Kingdom, September 14-19: Electric Rocket Propulsion Society, Fairview Park, OH, 2025. [Online]. Available: https://www.electricrocket.org/IEPC_2025/London/submission_310.pdf.

[193] B. E. Dowd, W. H. Greene, and E. C. Norton, "Computation of standard errors," *Health services research*, vol. 49, no. 2, pp. 731–750, 2014. DOI: 10.1111/1475-6773.12122.

[194] S. Scharmann et al., "Thrust measurement of an ion thruster by a force probe approach and comparison to a thrust balance," *AIP Advances*, vol. 12, no. 4, 2022. DOI: 10.1063/5.0066401.

[195] A. Marín-Cebrián, E. Ahedo, and A. Domínguez-Vázquez, "Two-dimensional kinetic analysis of a Hall thruster discharge with a null-magnetic point at the anode," *Journal of Physics D: Applied Physics*, vol. 58, no. 37, p. 375 201, Sep. 2025. DOI: 10.1088/1361-6463/adfce0.

[196] S. Dalle-Fabbriche, J. Zhou, and E. Ahedo, "An axisymmetric hybrid model of the plasma in a radio-frequency ion thruster chamber," *Plasma Sources Science and Technology*, vol. 34, no. 8, p. 085 007, 2025. DOI: 10.1088/1361-6595/adf5e3.

[197] P. Dietz et al., "Global models for radio-frequency ion thrusters," *EPJ Techniques and Instrumentation*, vol. 8, no. 10, 2021. DOI: 10.1140/epjti/s40485-021-00068-5.

[198] S. Jahanbakhsh, M. Satir, and M. Celik, "Study of electron current extraction from a radio frequency plasma cathode designed as a neutralizer for ion source applications," *Review of scientific instruments*, vol. 87, no. 2, 2016. DOI: 10.1063/1.4935015.

[199] R. B. Lobbia and B. E. Beal, “Recommended practice for use of langmuir probes in electric propulsion testing,” *Journal of Propulsion and Power*, vol. 33, no. 3, pp. 566–581, 2017. DOI: 10.2514/1.B35531.

[200] M. Guaita, A. Marín-Cebrián, M. Merino, E. Ahedo, F. Cipriani, and K. Dannenmayer, “A full PIC study of the neutralization of the RIT10-EVO’s plasma beam,” in 38th *International Electric Propulsion Conference*, Toulouse, France, June 23-28: Electric Rocket Propulsion Society, 2024. [Online]. Available: https://electricrocket.org/IEPC_2024/472.pdf.

[201] J. S. Krueger and M. S. Lewis-Beck, “Goodness-of-fit: R-squared, see and ‘best practice’,” *The Political Methodologist*, vol. 15, no. 1, pp. 2–4, 2007.

[202] G. Lim and D. A. Levin, “Understanding in-chamber plasma behavior using a dimensionally scaled gridded ion thruster in three-dimensional kinetic particle-in-cell simulations,” *Journal of Applied Physics*, vol. 139, no. 8, p. 083 305, Feb. 2026. DOI: https://doi.org/10.1063/5.0311887.

[203] Z. Huang, Y. Hu, J. Geng, C. Yang, and Q. Sun, “Kinetic investigation of discharge performance for Xe, Kr, and Ar in a miniature ion thruster using a fast converging PIC-MCC-DSMC model,” *Plasma Sources Science and Technology*, vol. 33, no. 9, p. 095 006, Sep. 2024. DOI: 10.1088/1361-6595/ad75b2.